Les Diagnostics faisceau de IFMIF / LIPAc. Les moniteurs de profils et de pertes du faisceau

Jan Egberts

PhD THESIS

Université Paris Sud

Ecole Doctorale 534 MIPEGE

Subject: Physics

IFMIF-LIPAc Beam Diagnostics: Profiling and Loss Monitoring Systems

---

put forward by

Dipl.-Phys. Jan EGBERTS

born in Mülheim / Ruhr

Defended on September 25th, 2012

Jury members:

Président du jury :	Prof. Patrick PUZO	(Université d'Orsay)
Rapporteurs de thèse :	Dr. Étienne BURTIN	(CEA Saclay - SPhN)
	Dr. Peter FORCK	(GSI)
Directeur de thèse :	Dr. Olivier NAPOLY	(CEA Saclay - SACM)
Responsable de thèse :	Dr. Jacques MARRONCLE	(CEA Saclay - SEDI)
Examinateur :	Dr. Mariusz SAPIŃSKI	(CERN)

Les Diagnostics faisceau de IFMIF / LIPAc :
les moniteurs de profils et de pertes du faisceau

This thesis was carried out at:

CEA Saclay
DSM/IRFU
Gif-sur-Yvette
91191 cedex
France

Abstract

The IFMIF accelerator will accelerate two 125 mA continuous wave (cw) deuteron beams up to 40 MeV and blasts them onto a liquid lithium target to release neutrons. The very high beam power of 10 MW pose unprecedented challenges for the accelerator development. Therefore, it was decided to build a prototype accelerator, the Linear IFMIF Prototype Accelerator (LIPAc), which has the very same beam characteristic, but is limited to 9 MeV only. In the frame of this thesis, diagnostics devices for IFMIF and LIPAc have been developed. The diagnostics devices consist of beam loss monitors and interceptive as well as non-interceptive profile monitors.

For the beam loss monitoring system, ionization chambers and diamond detectors have been tested and calibrated for neutron and γ radiation in the energy range expected at LIPAc. During these tests, for the first time, diamond detectors were successfully operated at cryogenic temperatures. For the interceptive profilers, thermal simulations were performed to ensure safe operation. For the non-interceptive profiler, Ionization Profile Monitors (IPMs) were developed. A prototype has been built and tested, and based on the findings, the final IPMs were designed and built. To overcome the space charge of accelerator beam, a software algorithm was written to reconstruct the actual beam profile.

Key words: diagnostics, IFMIF, LIPAc, nuclear fusion, residual gas, non-interceptive, profiler, IPM, space charge, loss monitor, ionization chamber, diamonds, SEM-grids

Resumé

IFMIF sera constitué de deux accélérateurs de deutons délivrant des faisceaux continus de 125 mA et d'énergie 40 MeV qui bombarderont une cible de lithium liquide. Face à cette très haute puissance faisceau de 10 MW, de nouveaux défis doivent être relevés pour le développement de tels accélérateurs. C'est pour cette raison qu'a été prise la décision de construire un accélérateur prototype, LIPAc (Linear IFMIF Prototype Accelerator) ayant les mêmes caractéristiques faisceau qu'IFMIF, mais avec une énergie limitée à 9 MeV. Dans le cadre de cette thèse, des instruments de diagnostics faisceau ont été développés pour IFMIF et LIPAc. Ces diagnostics concernent des moniteurs de pertes faisceau ainsi que des profileurs transverses de faisceau travaillant en mode intercepteur ou non.

Pour la surveillance des pertes faisceau, des chambres à ionisation et des détecteurs au diamant ont été testés et calibrés en neutrons et en γ dans la gamme en énergie de LIPAc. Lors de ces expériences, pour la première fois des diamants ont été testés avec succès à des températures cryogéniques. Pour les profileurs interceptant le faisceau, des simulations thermiques ont été réalisées afin d'assurer leur bon fonctionnement. Pour les profileurs n'interceptant pas le faisceau, des moniteurs basés sur l'ionisation du gaz résiduel (IPM) contenu dans le tube faisceau ont été développés. Un prototype a été construit et testé, puis s'inspirant de ce retour d'expérience les IPMs finals ont été conçus et construits. Pour contrecarrer la charge d'espace générée par le faisceau, un algorithme a été élaboré afin de reconstruire le profil réel du faisceau.

Mots clés : diagnostics, IFMIF,LIPAc, fusion nucléaire, gaz résiduel, non-interceptif, profileur, IPM, charge d'espace, moniteur de pertes, chambre à ionisation, diamants, SEM-grids

"So let's get down to business now. Well, there's nothing more difficult than getting down to this business ...

... or, for that matter, to any business ..."

F. M. Dostoyevsky

Contents

Chapter 1

Introduction

Ce chapitre présente le contexte de cette thèse portant sur la conception des réacteurs de fusion nucléaire, le projet IFMIF (International Fusion Material Irradiation Facility) et son prototype LIPAc (Linear IFMIF Prototype Accelerator) pour lequel les diagnostics sont développés, le fonctionnement de tels accélérateurs et les diagnostics préconisés pour LIPAc ainsi que les raisons de leurs choix.

Dans cette période de pénurie d'énergie, le développement de nouvelles sources d'énergie est d'une grande importance. Les réacteurs de fusion nucléaire sont potentiellement capables d'assumer la charge de base du réseau électrique du futur. À la différence des réacteurs nucléaires actuels basés sur la fission, les réacteurs de fusion sont intrinsèquement sûrs tout en produisant de faibles niveaux de radioactivité. Hormis les réactions de fusion qu'il faut pouvoir maintenir de façon permanente, l'un des plus grands défis auxquels ces réacteurs seront confrontés est le bombardement neutronique diluvien que subissent les matériaux constituants ces réacteurs. Les réactions nucléaires induites par les neutrons dans ces matériaux fragilisent rapidement leurs structures et ceci de façon irréversible. Actuellement il n'existe pas de matériaux capables de soutenir de tels flux radiatifs sur une durée de temps raisonnable. Trouver des matériaux résistants à de telles conditions est l'un des objectifs sine qua non pour la construction des réacteurs de fusion du futur : relever ce défi est le but et l'ambition de IFMIF !

Pour caricaturer, IFMIF sera une source de neutrons extrêmement intense ($\sim 10^{17}$ neutrons/s) couplée à des cellules de tests d'irradiation neutronique dans lesquelles seront placées des échantillons de matériaux soumis également à des contraintes mécaniques (torsion...), thermiques... afin de tester leurs résistances à ces conditions extrêmes. La source de neutrons est constituée de 2 accélérateurs continus de deutons (E=40 MeV et I=125 mA) sur une cible de lithium liquide. Des réactions nucléaires se produisent sous l'impact des deutons sur les noyaux de lithium libérant de nombreux neutrons. Cette source neutronique s'apparentera de par son spectre en énergie et son intensité à l'environnement des réacteurs de fusion.

L'accélérateur IFMIF consistera en une source d'ions de deutérium extraits à 100 keV qui seront mis en paquets (175 MHz) et accélérés jusqu'à 5 MeV par le RFQ (Radio Frequency Quadrupole), avant d'être injectés dans 4 modules accélérateurs constitués de cavités supraconductrices jusqu'à 40 MeV, pour enfin être acheminés jusqu'à la cible de lithium. Un des plus grands défis pour le développement d'un tel accélérateur est la très haute puissance de son faisceau de 10 MW et le fort courant continu de

125 mA. C'est pour cette raison qu'une étape de validation a été décidée; elle consiste, côté accélérateur, en la construction de LIPAc qui est un prototype à l'échelle 1 de IFMIF n'intégrant que les premiers éléments jusqu'au premier module accélérateur : l'énergie délivrée par les deutons ne sera donc que de 9 MeV.

Les diagnostics pris en charge par le Commissariat à l'Énergie Atomique et aux Énergies Alternatives (CEA) de Saclay sont :

- des profileurs de faisceau non intercepteurs basés sur l'ionisation du gaz résiduel,
- des profileurs intercepteurs qui mesurent les courants d'ionisation générés par les deutons sur des fils interceptant une faible fraction du faisceau,
- des transformateurs de courant qui mesure le courant du faisceau en mode pulsé ou continu,
- des moniteurs de pertes pour assurer la sécurité de l'accélérateur en mesurant les pertes du faisceau dans des chambres à ionisation,
- des moniteurs de micro-pertes constitués par des détecteurs en diamant placés dans les modules cryogéniques accélérateurs et dont le but est le réglage fin du faisceau.

Tous ces diagnostics, hormis les mesureurs du courant faisceau seront présentés dans le cadre de cette thèse.

1.1 Fusion Power Plant Development

In this section, the basic principles of nuclear fusion is presented and the development of fusion power plants is motivated. The current development strategy for nuclear power plants is depicted and within this framework, the International Fusion Material Irradiation Facility (IFMIF) is presented.

In the face of the increasing global demand of energy and diminishing fossil fuels, the search for reliable, secure and sustainable energy sources can be considered as one of the most urgent issues of our society. Nuclear fusion has the potential to provide the base load of such a future energy supply system [1].

1.1.1 Fission & Fusion

Future fusion power plants are in many aspects similar to conventional nuclear plants. Both are thermal power stations where nuclear reactions heat water, that turns into steam and spins a steam turbine which drives an electrical generator. The energy released in the case of fission as well as fusion is based on the different binding energies of nuclei in the periodic table. The binding energy is defined as the energy required to split a nucleus into its parts. The binding energy per nucleus is therefore a measure of how strongly the nucleons are bound. During transitions of a nucleus with a low to an high binding energy per nucleon, energy is released. In general, very light as well as very heavy elements have a low binding energy per nucleus and a maximum is reached on the level of iron. Energy is therefore released by fusion of light elements to heavier ones, or by fission of very heavy elements, as it is illustrated in Fig. 1.1. On this illustration, one can already see that fusion can potentially release much more energy than fission.

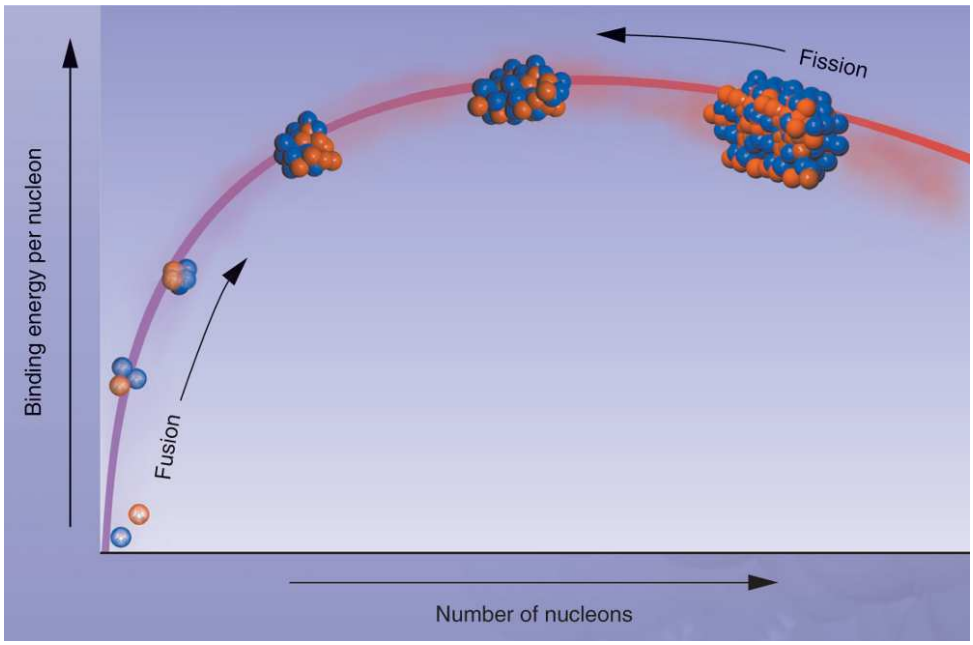

Figure 1.1: Illustration of the nuclear binding energy per nucleon versus the atomic mass number [2]

.

Despite their similarities, fission and fusion reactors have conceptual differences as

well. Main issues of commercial fission reactors are the limited abundance of the fuel, the disposal of the nuclear waste, and the potential catastrophic impact on the environment in case of an incident. All three issues do not apply, or at least not to this extend, to fusion reactors.

Fusion Reactions

Processes to be employed in fusion reactors must fulfill a number of criteria.

- First of all, they must obviously be exothermal, i.e. they release energy, which restricts potential fusion fuel to light elements.
- Since the Coulomb barrier of the nucleus must be overcome for fusion to happen, low Z reactants are mandatory, with Z being the atomic number.
- To ensure a high interaction cross section, the fusion process should have two or more products to provide more possibilities to fulfill energy and momentum conservation.
- And they should abstain from weak interactions, like the transition of a proton into a neutron.

There is a vast number of fusion processes that fulfill these criteria. For some important fusion processes, the energy release and the cross sections at 10 keV and 100 keV are given in Table 1.1 [3].

Table 1.1: Energy release Q and cross sections at 10 keV and 100 keV center of mass energy for some important fusion reaction that can be employed in future fusion reactors. Values in brackets are calculated theoretically [3].

Reaction	Q [MeV]	σ (10keV) [barn]	σ (100keV) [barn]
$p + p \rightarrow D + e^+ + \nu$	1.44	$(3.6{\cdot}10^{-26})$	$(4.4{\cdot}10^{-25})$
$D + D \rightarrow T + p$	4.04	$2.81{\cdot}10^{-4}$	$3.3{\cdot}10^{-2}$
$D + D \rightarrow {}^3He + n$	3.27	$2.78{\cdot}10^{-4}$	$3.7{\cdot}10^{-2}$
$D + T \rightarrow \alpha + n$	17.59	$2.72{\cdot}10^{-2}$	3.43
$D + {}^3He \rightarrow \alpha + p$	18.35	$2.2{\cdot}10^{-7}$	0.1
$T + T \rightarrow \alpha + 2n$	11.33	$7.9{\cdot}10^{-4}$	$3.4{\cdot}10^{-2}$
$p + {}^6Li \rightarrow \alpha + {}^3He$	4.02	$6{\cdot}10^{-10}$	$7{\cdot}10^{-3}$
$p + {}^12C \rightarrow {}^{13}N + \gamma$	1.94	$(1.9{\cdot}10^{-26})$	$2.0{\cdot}10^{-10}$

There are a few points worth noting in Table 1.1.

- First, the fusion cross sections for high Z reactants, like Li or C in this table, decrease exponentially with higher Z. The Coulomb barrier is commonly of the order of MeV and could never be penetrated according to classical mechanics. In quantum mechanics, however, the nuclei can tunnel through the barrier with a certain probability. This probability decreases exponentially with the product of the atomic numbers of the two reactants.

- Also the fusion of two proton to a deuteron has a very low cross section even at high energies since it requires the transition of a proton into a neutron, which involves a weak interaction.
- Finally, it is remarkable that the most energy is released, if ^{4}He is created in the process. Since ^{4}He is the lightest double magic nucleus, i.e. with two protons and two neutrons, it is bound particularly strongly which results in a tremendous energy release in its creation [3].

The temperatures required to trigger fusion process are tremendous. In table 1.1, the cross sections are given for reactant energies of 10 keV and 100 keV. For an ideal gas, 10 keV corresponds to a temperature of 11,600,000 K and 100 keV to 116,000,000 K. This exceeds by far the melting point of any known material. The fusion plasma therefore has to be confined in a magnetic field which can be achieved by tokamaks for instance [1]. As example, a sketch of the International Thermonuclear Experimental Reactor (ITER) tokamak is given in Fig. 1.2.

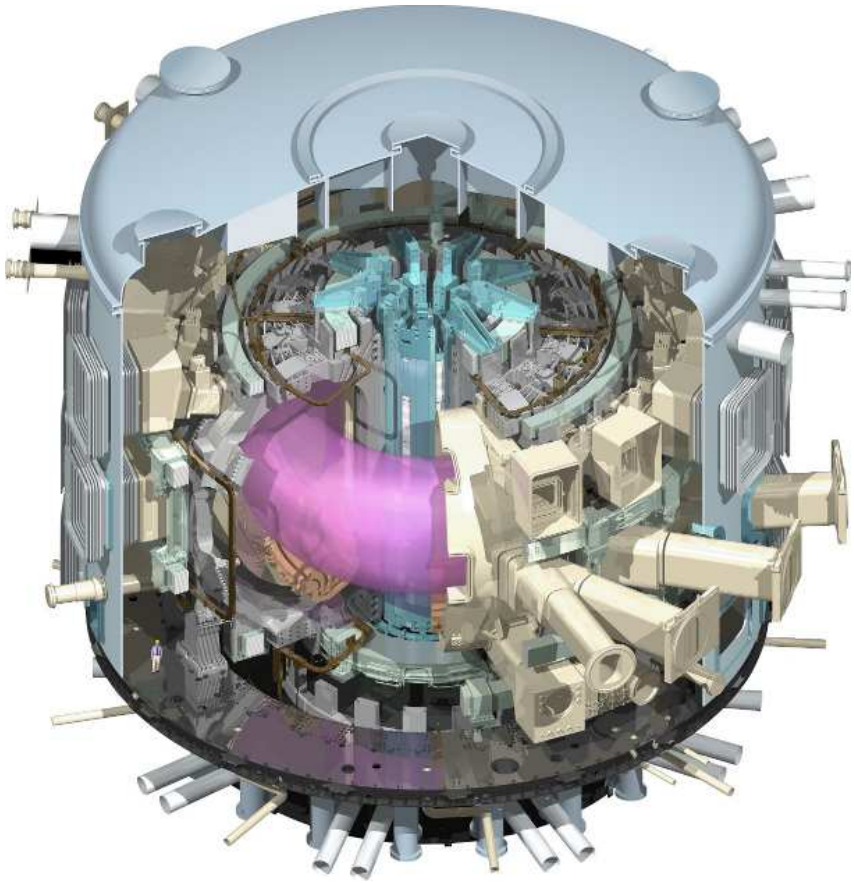

Figure 1.2: A detailed cutaway of the ITER Tokamak, with the hot plasma, in pink, in the centre [4].

From table 1.1 one can deduce that the most promising fusion process is the Deuteron (D)-Tritium (T) burn, with the highest interaction cross section and a high energy yield as well. As a stable hydrogen isotope, D exists in abundance in the oceans. T, however, is unstable and has to be produced artificially, by neutron bombardment of lithium for instance [5]. Tritium could be produced by neutrons generated in the fusion process on-site or in an external facility. Lithium and deuterium are commonly available in nature and it was estimated that easily accessible lithium resources on the earth would suffice for the next 1000 years [6].

Advantages of Fusion over Fission

The fusion products, listed in table 1.1, are all stable or short-lived. In contrast to fission, fusion fuel does therefore not require any nuclear reprocessing or long-term storage. Materials of the reactor itself, however, will be activated during the fusion process and have to be replaced during the lifetime of the reactor. The life-time of most of the created radio-isotopes is below 10 years and could possibly be further reduced by developing "low-activation" materials [6]. Even though the issue of nuclear waste disposal is still present for future fusion power plants, the issue is much less severe than for commercial fission reactors.

In addition to the low impact on the environment with virtually no radioactive waste nor any emission of greenhouse gases, fusion power plants are inherently safe [1]. The amount of fuel in the fusion core is just sufficient for a few-second burn. As soon as the fuel supply is stopped, the fusion will stop within seconds. Since it is difficult to achieve conditions under which nuclear fusion can occur, the reaction will cease immediately if the confinement by the tokamak is lost for whatever reasons, e.g. an earthquake. If control of the plasma is lost and the plasma is released, the heat could result in superficial damage of plasma-facing components. Catastrophic incidents, as they have happened in fission reactors, are impossible to occur [6].

A Roadmap to Fusion Power

The Joint European Torus (JET) currently holds the world record of producing 16 MW of fusion power during 3 s. JET has a power amplification smaller than 1, which means that less power is released by fusion than is required to maintain it. The next step will be the International Thermonuclear Experimental Reactor (ITER) which aims to be the first fusion reactor capable of sustaining itself. The objectives of ITER are to provide a thermal power of 500 MW over 300 s with a power amplification between 10 and 20. ITER is currently constructed at Cadarache, France. The first true fusion power plant, however, will probably be the Demonstration Power Plant (DEMO). The objectives of DEMO are

- to provide a level of thermal fusion power relevant for commercial applications,
- to have the capability of net electricity production,
- to prove tritium self-sufficiency,
- and to demonstrate high reliability and the performance of low-activation materials [7].

In February 2007, European Atomic Energy Community (Euratom) and Japan signed the Broader Approach (BA) agreement. This agreement aims to complement the ITER Project and to accelerate the realization of fusion energy by carrying out R&D and developing some advanced technologies for DEMO. Within the Broader Approach, three main projects are being implemented:

The first project is the Japan-EU Satellite Tokamak Programme (JT60-SA). During ITER construction, major experimental facilities will be required to develop operating

scenarios and address key physics issues for an efficient start-up of ITER experimentation and for research towards DEMO. The JT60-SA in Japan has been identified as a device which could fulfill these objectives. It will therefore be upgraded to an advanced superconducting tokamak and used by Europe and Japan as a "satellite" facility to ITER [8].

The second project is the International Fusion Energy Research Centre (IFERC). The missions of the centre include the coordination of DEMO Design and R&D activities, large scale simulation activities of fusion plasmas by super-computer and remote experimentation activities to facilitate a broad participation of scientists into ITER experiments [8].

Finally, the third project will consist of the International Fusion Material Irradiation Facility (IFMIF). Fusion as a major energy source will require materials which maintain their essential physical and mechanical properties under huge neutron fluxes and which do not remain highly radioactive for extended periods of time after exposure to the harsh thermal and irradiation conditions inside a fusion reactor. IFMIF will allow for the testing and qualification of advanced materials in an environment similar to that of a future fusion power plant.

1.1.2 IFMIF

The primary mission of IFMIF will be to generate a material irradiation database for the design, construction, licenzing and safe operation of a Demonstration Power Plant (DEMO). This will be achieved through testing and qualifying material performance under neutron irradiation that simulates service up to the full lifetime anticipated for DEMO. Tests of blanket elements will be an important use of the facility, and will complement the tests of blanket test modules in the International Thermonuclear Experimental Reactor (ITER) [9].

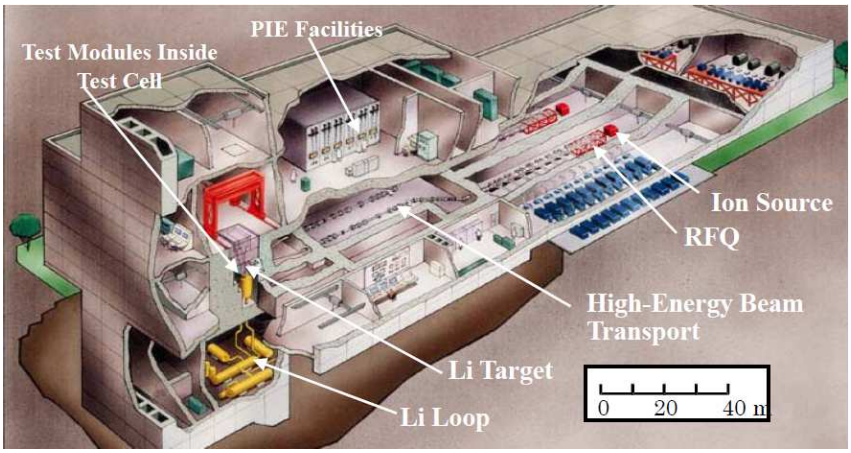

Figure 1.3: Three dimensional view on IFMIF with major subsystems identified [9].

While charged fusion products, like p^+ or α, will be well confined by the magnetic field, uncharged particles, neutrons and γ's, will be able to penetrate the magnetic field and bombard the first wall they encounter. On the one hand, these particles can be used to extract energy from the fusion reactor, on the other, this first wall they bombard must be able to withstand a huge neutron irradiation. At the International Fusion Material Irradiation Facility (IFMIF), material samples will be tested on their neutron irradiation hardness for future generations of fusion power plants, i.e. after

ITER. An outline of the IFMIF facility is given in Fig. 1.3. The ions sources, the Radio Frequency Quadrupoles (RFQs) and the High Energy Beam Transport lines (HEBTs) of the accelerator are indicated in the figure, as well as the liquid lithium target with the lithium loop and test facility.

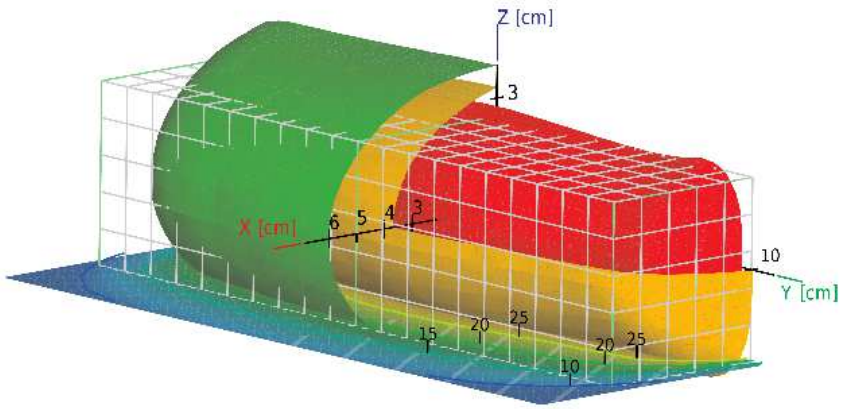

Figure 1.4: Available IFMIF irradiation volumes with specific damage rate criteria (Green: 20 dpa/fpy, Yellow: 30 dpa/fpy, Red: 40 dpa/fpy) [10].

The main objective of IFMIF is to evaluate the irradiation performance of structural materials under fusion typical conditions (first wall/blanket) for the DEMO engineering design. A sensible measure for the damage that a neutron irradiation has inflicted on a sample is the number of temporary or definite displacements each atom has performed due to the irradiation. For a facility with variable irradiation intensity, the maximum damage rate achievable at this facility is therefore measured in displacements per atom per full power year (dpa/fpy).

To achieve its objective, IFMIF must achieve damage rates by neutron irradiation comparable to the ones estimated for DEMO in a sufficiently large volume to allow for an irradiation of more than 1000 test samples [11]. Since the neutron flux density decreases with the distance from the source, regions of different irradiation intensity are generated. The different irradiation regions at IFMIF are shown in Fig. 1.4. In green, the least irradiated region with 20 dpa/fpy damage rate is marked, in yellow, the intermediate region with 30 dpa/fpy, and in red, closest to the source, the highly irradiated region with over 40 dpa/fpy. As comparison, for ITER, a damage rate of 3 dpa over its entire lifetime [12] and for DEMO, a rate of 30 dpa/fpy is expected [10].

Material irradiation experiments require stable, continuous irradiation with high availability. The IFMIF neutron source thus consist of two separate linear accelerators to provide not only the tremendous neutron flux of 10^{17} n/s, but also the maximum possible redundancy which increases its reliability. The high availability of the accelerators combined with temperature control of the material samples provides very stable irradiation conditions. To account for the mechanical stresses in fusion reactors, test modules are foreseen to test the creep fatigue of the samples [9].

The neutron energy spectra of IFMIF and DEMO, however, are quite diverse. The spectra for DEMO and IFMIF are given in Fig. 1.5, normalized on a total flux of 10^{15} n/s/cm^2. For the two fusion reactors, one can nicely see the peak at 14.1 MeV that corresponds to the neutron energy released in the fusion of D and T, compare Table 1.1 (neutron (14.1 MeV) + α (3.5 MeV)) [3].

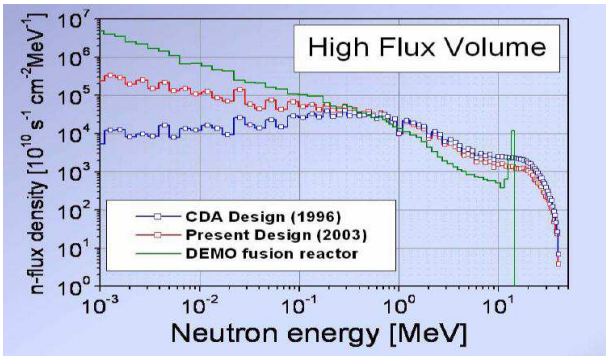

Figure 1.5: Neutron spectra expected for DEMO and two design phases of IFMIF [13].

Despite the deviation in the neutron energy spectra of IFMIF and DEMO, the neutron radiation appears to cause similar damage in the irradiated samples. Simulations have been performed in the frame of the IFMIF project to investigate the effect of the irradiation on natural iron for IFMIF and DEMO spectra. The results are summarized in Table 1.2. The activation products for IFMIF and DEMO differ only slightly. The main deviation is the different ratio of ^{54}Mn and ^{56}Mn production [10]. One can therefore conclude that IFMIF will provide a suitable environment for testing materials for future fusion power plants.

Table 1.2: Activation products of ^{56}Fe due to neutron irradiation at IFMIF and DEMO energies after 1 hour of cool down [10].

	IFMIF	DEMO
Total [10^{14} Bq/kg]	10	8.7
^{55}Fe	68 %	64 %
^{56}Mn	16 %	26 %
^{54}Mn	14 %	8.6 %
^{51}Cr	1.6 %	1.3 %
Total	99.0 %	99.8 %

IFMIF will achieve such characteristics by an accelerator based neutron source. A linear accelerator will accelerate two 125 mA continuous wave (cw) deuteron beams up to an energy of 40 MeV and then burst them onto a liquid lithium target. To minimize the heat load on the target and to increase the irradiated volume, the deuteron beam has been shaped to a rectangular flat-top distribution of $(50\times200)\,\mathrm{mm}^2$. In the target, the beam impact will trigger nuclear reactions that, in turn, release neutrons; typical reactions are: [14]

- D + ^{7}Li → ^{7}Be +2n
- D + ^{6}Li → ^{7}Be +n
- n + ^{6}Li → ^{4}He +T

1.2 Accelerator Physics

As the development of accelerator diagnostics is the scope of this thesis, physics involved in an accelerator need to be discussed in more detail. This section serves to provide a better understanding of the physical processes involved in any accelerator and to introduce some essential terms and definitions.

In its simplest design, a linear accelerator consists of a source, where the particles are created, an accelerating structure, where these particles are accelerated to design energy, and some kind of target where the beam is finally put to use. For a real accelerator, one requires various components in addition, like focusing and shaping elements, vacuum pumps, valves, diagnostics of course and many more.

Each single component of the accelerator has to be designed and optimized in order to obtain the expected beam characteristics at given positions. Beam characteristics required for the accelerator design include not only rather obvious quantities like beam current or transverse position and size, but also quantities like its longitudinal size, angular dispersion, energy spread , or the number of lost particles in the accelerator that have to be known with astonishing precision. In this chapter, techniques are presented how to calculate such beam properties that are required to properly design accelerator components.

1.2.1 Beam Dynamics

By applying Maxwell's equations, one can, in principle, calculate the trajectory of each single particle in the accelerator. However, since a treatment of the $7.8{\cdot}10^{17}$ deuterons that are accelerated by the IFMIF accelerator each second is practically not feasible, an alternate approach is required.

One option is to combine a certain number of beam particles to a single macro-particle and to have the system solved numerically by computers. The properties of this macro-particle, e.g. charge or mass, have to be scaled for the system to keep its original properties. By setting the number of beam particles to be combined to a macro-particle, one can either reduce the calculation time by having less macro-particles, or improve statistics by having more of them. One thereby has to find a good balance between accuracy and calculation run time.

While such a numerical approach provides reliable and accurate results of the beam dynamics, it grants only very little insight into the matter which is essentially required for an accelerator development. A better insight into accelerator beam dynamics based on statistical considerations is granted by a more analytic approach that is shortly depicted in the following chapter.

Single Particle Dynamics

As a first step one can analyze the motion of a single particle in a constant force field. The equation of motion for a particle of mass m in a force field $\vec{F}$ is then given by

$$m\ddot{\vec{x}} = \vec{F} \tag{1.1}$$

The inertia equals the sum over all external forces. These external forces are commonly applied by electric or magnetic fields. If these forces are constant, the equation can be easily solved by integrating it twice and using the initial position, $\vec{x_0}$, and the initial momentum, $\vec{p_0}$, as constants of integration.

$$m \cdot \dot{\vec{x}} = \vec{F} \cdot t + \vec{p_0} \tag{1.2}$$

$$m \cdot \vec{x} = \frac{1}{2}\vec{F} \cdot t^2 + \vec{p_0} \cdot t + m \cdot \vec{x_0} \tag{1.3}$$

For an accelerator which is segmented into sections of given constant fields, the trajectory of an arbitrary particle is fully determined by the two constants of integration, $\vec{x_0}$ and $\vec{p_0}$. The vector space spanned by $\vec{x_0}$ and $\vec{p_0}$ is called phase space in analogy to Hamiltonian mechanics. Here as well, it will prove to be a handy tool for the description of the particle dynamics. If the classical momentum, used in Eq. (1.2), is replaced by the relativistic momentum, the concept of the phase space will still hold in the high-energy regime.

Up to now, the system is considered to be fully symmetric, which is, of course, not the case for an accelerator. Particles traverse in the accelerator along the design orbit, i.e. the trajectory of an ideal particle. As suitable representation to account for this preferential direction, a coordinate system can be chosen that keeps this ideal particle in its origin. In this representation, the coordinates of a single particle automatically give its deviation from the design orbit. The z-axis may point in beam direction, while x- and y-axis are in the transverse plane. As generalized momenta of the phase space, the tilt of the particle with respect to the design orbit is commonly used in the transverse plane, and in longitudinal direction the relative momentum deviation, also called dispersion. The six coordinates commonly used to span up the phase space are summarized in Table 1.3. In a first approximation, the generalized momenta can be interpreted as the particle momenta normalized on the absolute particle momentum in the laboratory frame. One can easily check that the chosen generalized coordinates do NOT satisfy the Hamiltonian equations!

Table 1.3: Phase space representation in accelerator physics, giving the symbol, description and dimension of the coordinates commonly used [15].

Symbol	Dimension	Description
x	mm	horizontal displacement
x'	mrad	horizontal tilt
y	mm	vertical displacement
y'	mrad	vertical tilt
l	mm	longitudinal displacement
δ	‰	dispersion

If we assume an accelerator consisting of N sections where the particles are subject to given constant force fields, we can form a set of N equations of motions, each like the one given in equation (1.1). These equations of motion can be integrated using two constants of integrations per dimension, $\vec{x_0}$ and $\vec{p_0}$, as demonstrated in equation (1.2) and (1.3). By demanding the continuity of position and velocity of the particle during the transition from one accelerator section to the next, we can use the final state of a

particle in one section as the initial particle state in the following. Thereby, the entire set of equations can be solved by six initial parameters that correspond to a single vector of the phase space [15].

Transport Matrix Formalism

In a linear approximation, we can now assume that the transition of the initial particle state to the final particle state within an accelerator section can be described by a matrix. The phase space vector $\vec{x}(s)$ of an arbitrary particle at the position s can then be written as:

$$\vec{x}(s) = R(s)\vec{x}(0) \tag{1.4}$$

with $R(s)$ being the transport matrix from the chosen origin to the position s. If this particle traverses several accelerator sections during this drift, the transport matrix $R(s)$ is given by the ordered product of the matrices of all these accelerator sections. If the particle traverses N sections, each having a designated transport matrix R_i, with $i = 1$ being the first and $i = N$ being the last, the final phase space vector of the particle is given by

$$\vec{x}(s) = R(s)\vec{x}(0) = R_N R_{N-1} \cdots R_2 R_1 \vec{x}(0) \tag{1.5}$$

If one assumes that the three spatial coordinates, x, y and z, are decoupled, the six-dimensional phase space becomes decomposed into three two-dimensional phase spaces, one longitudinal and two transverse. To illustrate the concept of transport matrices, some simple examples in the transverse phase space will be discussed below.

As the trajectory of a free particle without any forces acting on it, is easiest to calculate, the evolution of the particle in a single transverse phase space, x and x', is discussed for this simple case first. The transport matrix for a free drift of the distance L is given in equation (1.6).

$$R = \begin{pmatrix} 1 & L \\ 0 & 1 \end{pmatrix} \tag{1.6}$$

This matrix can be plugged into equation (1.4), to achieve:

$$\begin{pmatrix} x \\ x' \end{pmatrix} = \begin{pmatrix} 1 & L \\ 0 & 1 \end{pmatrix} \begin{pmatrix} x_0 \\ x'_0 \end{pmatrix} = \begin{pmatrix} x_0 + Lx'_0 \\ x'_0 \end{pmatrix} \tag{1.7}$$

As one can nicely see, the particle still moves in the same direction, i.e. with the same angle x'_0, but has moved forward by $Lx'_0 \approx L\tan(x'_0)$ as one would have expected.

Another rather simple example is the transport matrix for focusing quadrupole in the thin lens approximation. As it is done in optics, one assumes that a thin lens gives the particle a short kick in one direction and thereby changes its tilt angle without affecting its position. The transport matrix for such thin lens is given in equation (1.8) with f being the focal length of the lens.

$$R = \begin{pmatrix} 1 & 0 \\ -\frac{1}{f} & 1 \end{pmatrix} \tag{1.8}$$

As it was done above, this matrix as well can be plugged into equation (1.4) to see that this time the position x_0 remains constant while the angle was reduced to $(x_0' - \frac{x_0}{f})$ rad. One can easily validate that a particle at position x_0 is deflected by a lens of focal strength f by an angle $\Delta x' = \arctan(\frac{x_0}{f}) \approx \frac{x_0}{f}$ which is well consistent with this matrix representation.

These are just two examples of the probably most simple transport matrices. However, this technique can be applied on more complex systems as well. For many cases, accelerator components effect various quantities of the phase space at once. For example, quadrupoles are intrinsically focussing in one direction, but defocussing in the other; as the Lorentz-Force is velocity dependent, magnets in general have a dispersion relation, etc. However, quadrupoles still keep both transverse directions separate, there is ideally no coupling between x and y. That means that in an ideal quadrupole the focal strength in x only depends on the x component of the particle position, not on the y component. The xy components of the transport matrix will thus be zero, and one can treat both directions independently, as it was done above. This is not the case for a solenoid that rotates the entire beam and thereby inflicts a strong coupling in the transverse plane [15].

Multi-Particle Dynamics

Up to now, we have only discussed the transport of a single particle. For an accelerator beam this does, of course, not suffice but a formalism capable of handling multiple particles is required. If interactions between particles of the beam can be neglected, the dynamics of a beam can be considered as a superposition of various single particle tracks. It therefore suffices to know the particle distribution in the six-dimensional phase space along the accelerator to understand the beam dynamics as well.

We assume a certain distribution of particles that traverse along the accelerator design orbit. Due to the proper choice of the coordinate system, we can assume that the coordinates of all particles are distributed around the origin. Without making any further demands on this actual distribution, we define an ellipse within phase space that contains the entire, or at least a given fraction of the distribution.

In general, an ellipse whose axes coincide with the Cartesian axes can be described by the ellipse equation:

$$\frac{x^2}{a} + \frac{y^2}{b} = 1 \tag{1.9}$$

For a tilted ellipse, one has to add an additional xy-mixing term $\frac{2xy}{c}$ to equation (1.9). It can be easily verified that this equation can be elegantly rewritten as a matrix product where a matrix σ_x is multiplied from both sides by the position vectors of the ellipse. The parameters a and b are thus expressed by the diagonal elements of the matrix σ_x, while the mixing parameter c is given by its off-diagonal elements.

With $\vec{x}$ being the vectors pointing onto the edge of the phase space ellipse, one can define an ellipse matrix σ_x such that its inverse matrix σ_x^{-1} fulfills the ellipse equation (1.10).

$$\vec{x}^T \sigma_x^{-1} \vec{x} = 1 \tag{1.10}$$

$$\sigma_x = \begin{pmatrix} \sigma_{11} & \sigma_{12} \\ \sigma_{12} & \sigma_{22} \end{pmatrix} \qquad \sigma_x^{-1} = \frac{1}{\det(\sigma_x)} \begin{pmatrix} \sigma_{22} & -\sigma_{12} \\ -\sigma_{12} & \sigma_{11} \end{pmatrix}$$

The descriptive meaning of these matrix elements for the phase space ellipse is depicted in Fig. 1.6 using the correlation parameter $r_{12} = \frac{\sigma_{12}}{\sqrt{\sigma_{11}\sigma_{22}}}$. One can see that the extension of the ellipse in x only depends on σ_{22} and that the extension of the ellipse in x' only depends on σ_{11}.

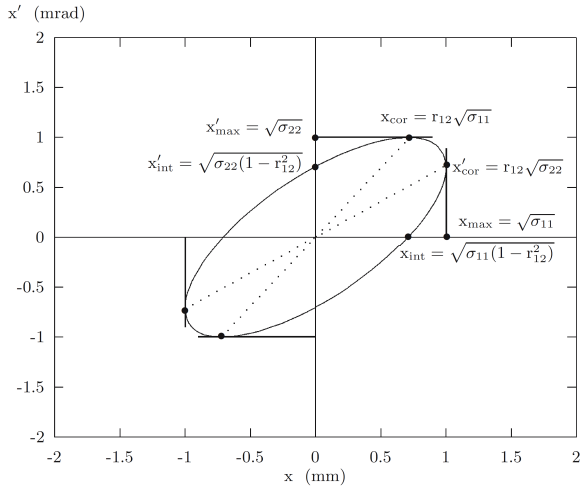

Figure 1.6: Illustration of the phase space ellipse [15].

The quantity $\epsilon_x = \det(\sigma_x)$ is called the emittance and is a measure for the size the phase space ellipse. If the emittance ellipse is fitted on the phase space distribution to assume the best representation of all the particles, the emittance can be written as

$$\epsilon_x = n^2 \cdot \sqrt{\langle x^2 \rangle \cdot \langle x'^2 \rangle - \langle x \cdot x' \rangle^2}. \qquad [16] \tag{1.11}$$

The emittance matrix elements are thus given as $\sigma_{11} = \langle x^2 \rangle$, $\sigma_{22} = \langle x'^2 \rangle$ and $\sigma_{12} = \langle x \cdot x' \rangle$. The quantity defined in equation (1.11) is commonly referred to RMS-emittance since it is given by the RMS values of the particle distribution in x and x'. The parameter n provides the means to enlarge the emittance ellipse such that is includes more particles. For $n = 1$, one commonly refers to the 1σ-emittance, with σ being the RMS size of the distribution, for $n = 2$ to the 2σ-emittance, etc. Which n-value is chosen, is mostly a matter of convention that differs for different accelerator types.

According to Liouville's theorem, the phase space volume remains constant under the effect of conservative forces. However, since we have normalized all the momenta on the total particle momentum and thereby picked generalized coordinates that do not fulfill the Hamiltonian equations, Liouville's theorem only holds true for the normalized emittance, the emittance that is rescaled with the particle momentum.

We have not yet addressed how the particles are distributed within the phase space ellipse. One can assume a constant density, but such a rough assumption will hardly be a proper model for any accelerator beam. A more adequate approach might be to assume a Gaussian particle distribution. For this case, the particle density can be written as

$$\rho(\vec{x}) = \rho_0 \exp\left(-\frac{1}{2}\vec{x}^T \sigma_x^{-1} \vec{x}\right). \tag{1.12}$$

For the transport matrix formalism, the actual distribution is, however, irrelevant as only the evolution of the emittance matrix σ_x is calculated.

The previous considerations are done for a two-dimensional phase space only; they can, however, easily be extended to six dimensions as well. Under the assumption of a given particle distribution, the emittance matrix fully determines the beam dynamics. As it is proven in common accelerator text books [15], the matrix formalism derived for a single particle can be generalized for multi-particle systems described by an emittance matrix. In this multi-particle formalism, equation (1.4) becomes

$$\sigma_x(s) = R_x(s)\sigma_x(0)R_x^T(s). \tag{1.13}$$

As done for the single particle formalism, the case of a free drift and a quadrupole in the thin lens approximation will be discussed for illustration in the multi-particle dynamics. As a simplification we can just assume the off-diagonal elements of the emittance matrix to be zero.

$$\begin{aligned}\sigma_x(L) &= \begin{pmatrix} 1 & L \\ 0 & 1 \end{pmatrix} \begin{pmatrix} \sigma_{11}(0) & 0 \\ 0 & \sigma_{22}(0) \end{pmatrix} \begin{pmatrix} 1 & 0 \\ L & 1 \end{pmatrix} \\ &= \begin{pmatrix} \sigma_{11}(0) + L^2\sigma_{22}(0) & L\sigma_{22}(0) \\ L\sigma_{22}(0) & \sigma_{22}(0) \end{pmatrix}\end{aligned} \tag{1.14}$$

The effect of a free drift is a shearing of the emittance ellipse in x direction, since σ_{22}, as a measure for the x' component of the phase space distribution, remains constant. The shearing of the phase space ellipse as effect of a free drift is illustrated in Fig. 1.7. It is indicated in Fig. 1.7 that the projection of all the phase space ellipses over x result in the original velocity distribution as it is expected for a free drift.

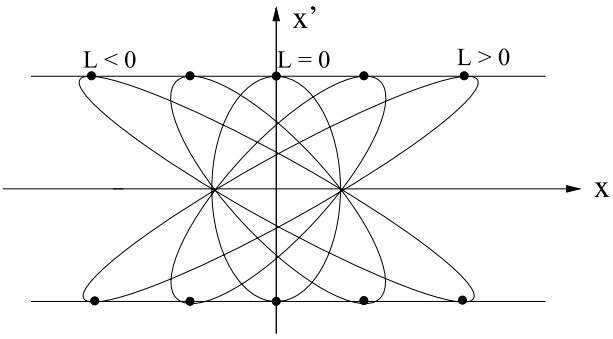

Figure 1.7: Illustration of the development of the phase space ellipse during a free drift [15].

The situation is similar for the focusing in the thin lens approximation.

$$\begin{aligned}\sigma_x\left(\frac{1}{f}\right) &= \begin{pmatrix} 1 & 0 \\ \frac{1}{f} & 1 \end{pmatrix} \begin{pmatrix} \sigma_{11}(0) & 0 \\ 0 & \sigma_{22}(0) \end{pmatrix} \begin{pmatrix} 1 & \frac{1}{f} \\ 0 & 1 \end{pmatrix} \\ &= \begin{pmatrix} \sigma_{11}(0) & \sigma_{22}(0)/f \\ \sigma_{22}(0)/f & \sigma_{22}(0) + \sigma_{11}/f^2 \end{pmatrix}\end{aligned} \tag{1.15}$$

In the thin lens approximation, the particles receive an instant kick and thereby change their velocity, but not their position. In accordance, the emittance ellipse is sheared in x' direction. The shearing of the phase space ellipse as effect of a focussing by a thin lens is illustrated in Fig. 1.8. Here as well, all projections over x' result in the original spatial distribution as it is expected for the thin lens approximation. [15]

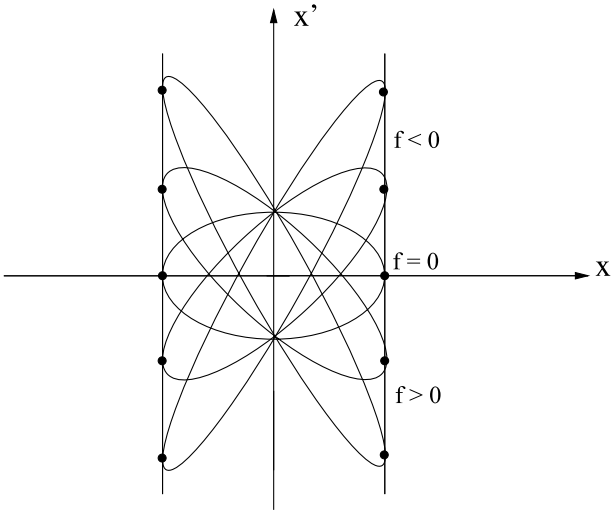

Figure 1.8: Illustration of the development of the phase space ellipse during a focussing in the thin lens approximation [15].

Such a multi-particle formalism is well suited to simulate accelerator beam dynamics and thereby allows for a proper design of the accelerator. The formalism depicted here is only a very short introduction into the subject. It is far from being complete and only serves the only purpose to define terms commonly used in accelerator physics and to give an insight in the techniques used to simulate accelerator beams. For further information, the inclined reader may be referred to the web-page of the CERN Accelerator School (CAS) http://cas.web.cern.ch/cas/ where detailed information on the CERN Accelerator Schools of the last three decades is available.

The formalism used for real accelerators development includes well more detail than discussed here. One major issue for the LIPAc accelerator is, for instance, beam particle-particle interactions due to the very high beam current. Since all the beam particles carry the same charge, they repel one another which effectively results in an enlargement of the beam. This is commonly referred to as Space Charge (SC) effect.

In addition to such an analytical approach, also numerical simulations are commonly performed by calculating single particle trajectories. An advanced particle tracking code, SOLMAXP [17, 18], was developed at CEA Saclay for this purpose. It implements electric or magnetic field maps calculated either by SOLMAXP itself or by another Finite Element Method (FEM) software. Despite the very high detail level of such simulations and their good accuracy, there will always remain a certain degree of uncertainty in the simulations, partially due to material errors of accelerator components, partially due to unforeseen or underestimated effects. This is why a solid commissioning strategy as well as good diagnostics elements have to be developed for each accelerator.

1.3 IFMIF Accelerator

Following the theoretical concepts of accelerators, this section presents the practical implementation of the IFMIF accelerator. Each accelerator subsystem is discussed briefly and issues are raised that are of importance for the diagnostics development.

The IFMIF accelerator will be a high-power accelerator aiming for total beam current of 250 mA and a total beam power of 10 MW. These characteristics pose unprece-

dented challenges for the accelerator development to such an extend that it appears impossible to achieve requirements in a single accelerator, but two separate accelerators will be build instead. Even then, each single accelerator driver will hold a total of 4 world records:

- The highest beam power at given energy
- The highest space charge effect at given energy
- The highest intensity
- The longest RFQ

Each driver of the IFMIF accelerator accelerates an 125 mA cw deuteron beam up to 40 MeV. Each driver can be subdivided in three accelerating subsystems, the ion source, the Radio Frequency Quadrupole, and the SRF-linear accelerator (linac). In between the subsystems there are beam transfer lines:

- the Low Energy Beam Transport line (LEBT) between ion source and RFQ
- the Medium Energy Beam Transport line (MEBT) between RFQ and SRF-linac
- and the High Energy Beam Transport line (HEBT) between the SRF-linac and the lithium target.

The outline of a single driver if the IFMIF accelerator is given in Fig. 1.9.

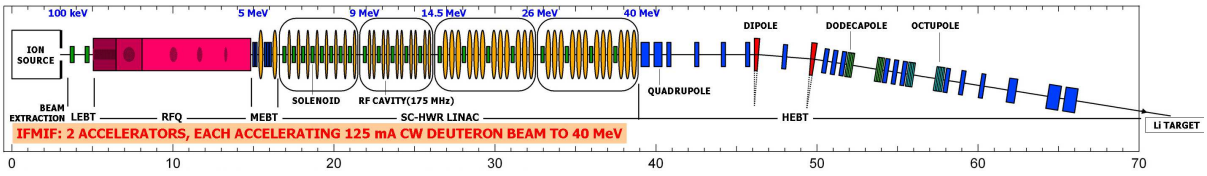

Figure 1.9: Sketch of a single driver of the IFMIF accelerator indicating the ion source, the LEBT, the RFQ, the MEBT, the SRF-linac, and the HEBT [19].

The Ion Source

In the ion source, a plasma of deuteron particles is created from which deuterons are extracted at an energy of 100 keV. At this energy, they can then be accelerated by the accelerator.

It is foreseen to use a SILHI (Source d'Ions Légers de Haute Intensité)-type source currently developed at CEA Saclay [20]. The SILHI source is an Electron Cyclotron Resonance (ECR) source, i.e. it generates an ion plasma by injecting electromagnetic-power at the electron cyclotron frequency of 2.45 GHz that ionizes the initially neutral gas. The deuteron ions can then be extracted from the plasma and are accelerated by an electric field to 100 keV.

The ion source has been tested for deuterons in 2001 and was found to be able to deliver beam currents up to 170 mA. A major issue of such an ion source is the contamination of the particle beam with equally charged molecules, since these cannot

be accelerated properly and will be lost. The species fractions were measured to be 96.9 % D^+ and 3.1 % molecular D_2^+. The normalized emittance of the beam from the source was found to be below 0.2 π·mm·mrad [21]. The concept of the emittance was discussed in detail in Section 1.2.1.

The RFQ

The ion source delivers a continuous particle beam at very low energy. This beam cannot be accelerated directly by classical accelerating structures consisting in separated RF cavities and beam focusing elements. At this low energy, the repulsive forces between the beam ions themselves, called space charge forces, are so high that it would make the beam explode if transverse focusing forces are not applied nearly permanently. For this purpose, a special device called Radio Frequency Quadrupole (RFQ) is needed [22, 23].

In the RFQ, electric fields are successively applied longitudinally and transversally on short distances of a few cm only. This allows to accelerate and focus the beam nearly simultaneously. The RFQ has to accelerate the beam to an energy high enough where space charge energy is no more dominant.

The RFQ also bunches the beam first in order to prepare it to be accelerated by RF accelerating devices. To summarize, the RFQ provides three effects: [15]

- It compresses the beam transversally, i.e. it provides transverse focusing.
- It compresses the beam longitudinally, i.e. it creates bunches and provides longitudinal focusing.
- It accelerates the beam.

The IFMIF RFQ is designed to accelerate a deuteron current of up to 130 mA from 100 keV up to 5 MeV and imposing a bunching frequency of 175 MHz. During this process, the RFQ is expected to lose only 1.1 % of the particles, which results in a total transmission of 98.9 % [22]. One of the optimization criteria for the RFQ was the minimization of high energy particle loss to reduce material activation. The very high beam current of the IFMIF beam imposes unprecedented challenges for the beam dynamics and the RFQ design. The strong space charge forces present in a 125 mA deuteron beam at low energies make the focussing and bunching of the beam very challenging. Consequently, long bunching and focussing sections are required in the RFQ before the beam can be accelerated which makes the IFMIF RFQ with 9.8 m the longest RFQ ever constructed [19].

The SRF-linac

The superconducting SRF-linac will finally accelerate the beam from the output energy of the RFQ of 5 MeV up to 40 MeV. The SRF-linac will consist of four modules contained in their own cryostat. Within each cryo-module, the cavities are arranged in groups separated by a single solenoid to refocus the beam in between acceleration [24, 25, 26, 27].

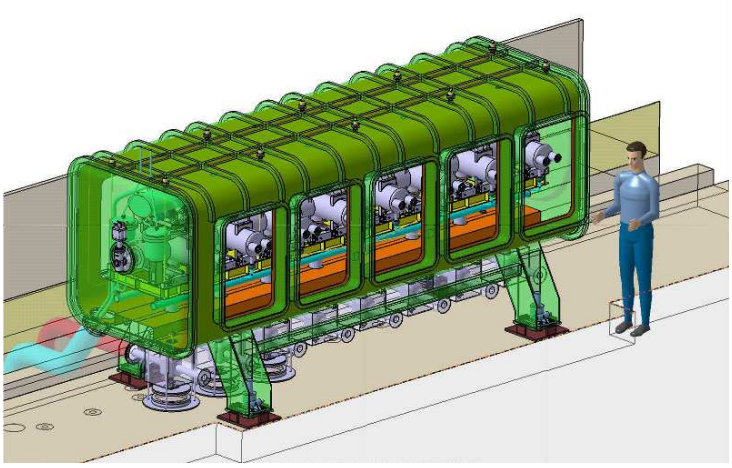

Figure 1.10: Sketch of the IFMIF first cryomodule that constitutes the SRF-linac of the prototype accelerator [28].

Solenoids are able to focus the beam in x and y at once, while quadrupoles focus in one transverse plane and defocus in the other. For high space charge beams, solenoids provide a very compact and efficient focusing tool and are thus commonly used in many space charge dominated accelerator sections [29, 30, 31]. Since a stronger refocusing is required at lower energies, more solenoids are foreseen for the first cryomodule. Detailed information on each module is given in Table 1.4 [24].

In each cavity oscillates an electro-magnetic field in such a way that the electric field at the point where the beam passes through is either parallel and in the same direction as the beam direction. The phase between the field oscillation in the cavity and the beam bunches must be tuned according to the bunch velocity. The cavities are thus characterized by their physical parameter $\beta = \frac{v}{c}$ given in Table 1.4.

Since the accelerating cavities are superconductive, it is one of the main design issues to prevent quenches, i.e. the (partial) transition of the superconductor into a normal conducting state. Quenches can occur, if the critical field or the critical temperature of the superconductor is exceeded.

Table 1.4: Characteristics of the IFMIF SRF-linac cryomodules [24].

Cryomodule	1	2	3 & 4
Cavity β	0.094	0.094	0.166
Cavity length [mm]	180	180	280
Nb of solenoids	8	5	4
Nb of cavities / module	8×1	5×2	4×3
cryostat length [m]	4.64	4.30	6.03
Output energy [MeV]	9	14.5	26 / 40

The em-field in the cavity will induce currents in the cavity surface. Even at 0 K, superconductors still show a non-zero surface resistance, called residual resistance, which results in a heat deposition on the surface. The deposited heat must be conducted through the superconducting layer towards the helium bath, where it is evacuated by the cryostat. Since both, the surface resistance and the thermal conductivity of the superconductor are rapidly varying with the temperature, the equilibrium is commonly unstable. Therefore, already a single tiny defect in the surface can induce premature quenches of the cavity. During the cavity manufacture, utmost heed is payed

to the material treatments like, thermal treatments, rinsing, electropolishing or the application of chemical baths [32].

The Lithium Target

In addition to the accelerator subsystems, there will be the lithium target. The accelerator beams are projected into a liquid lithium stream flowing perpendicularly to the accelerator beams. The Li stream is a free-surface flow of 25 mm depth, produced by a nozzle, and flows through a vacuum of $\sim 10^{-5}$ mbar. The concept of the lithium flow is shown in Fig. 1.11. The depth was chosen to be the D^+ penetration depth at 40 MeV plus a margin of 3 mm.

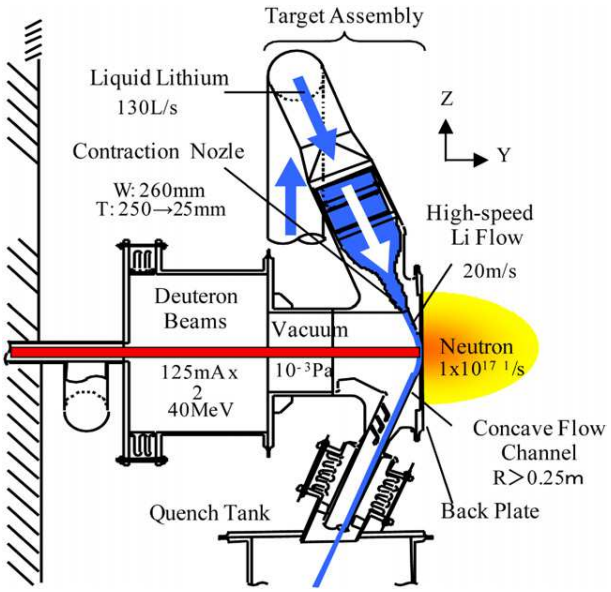

Figure 1.11: Concept of the IFMIF lithium target [33].

Due to the low pressure, the boiling point of lithium is reduced to 344 °C. Despite the huge power deposition of 10 MW in the lithium target by the accelerator beams, the lithium surface temperature must never reach the boiling point. For this reason a velocity of the lithium stream of 10 - 20 m/s is foreseen. Within the lithium target, temperatures will exceed 344 °C at the Bragg-peak, the boiling point is, however, elevated as well due to a pressure increase by centrifugal forces. A lithium test loop for the IFMIF target has been constructed at the O-arai site of the Japan Atomic Energy Agency (JAEA) in Japan. A photo of this test loop in given in Fig. 1.12 [33].

Transport Lines

Located in between the subsystems, beam transport lines serve as interface between them. They do not only connect the subsystems with one another, but they also shape the beam in such a way that it can be properly injected into the following section [19]. They do also house all the devices that are essential for the accelerator operation, but cannot be included in the subsystems itself for various reasons, e.g. pumps, focusing and shaping magnets, or beam diagnostics. Most of the diagnostics discussed in this thesis will be located on the MEBT or the HEBT.

Figure 1.12: Photo of the IFMIF lithium test loop constructed at the O-arai site of the JAEA in Japan [33].

1.4 LIPAc

The tremendous beam current of $2 \times 125\,\mathrm{mA}$ in continuous wave (cw) mode and its resulting very high beam power of 10 MW, poses unprecedented challenges for the IFMIF accelerator design particularly in the low energy regime. It was therefore decided to construct a prototype accelerator, LIPAc, at Rokkasho in Japan. In this section, the LIPAc accelerator will be discussed in more detail including a full list of diagnostics and their general conditions under which they will have to operate, e.g. radiation in the vault, or the different beam settings during the commissioning. [34]

LIPAc consists of a single IFMIF driver up to the first cryostat. LIPAc therefore has the very same beam characteristics as IFMIF, it is, however, limited to 9 MeV only. The accelerator subsystems of LIPAc and IFMIF will be virtually identical [19]. A sketch of the LIPAc is given in Fig. 1.13, indicating the ion source, the RFQ, the cryostat of the SRF-linac, and finally, downstream to the bending dipole, the beam dump.

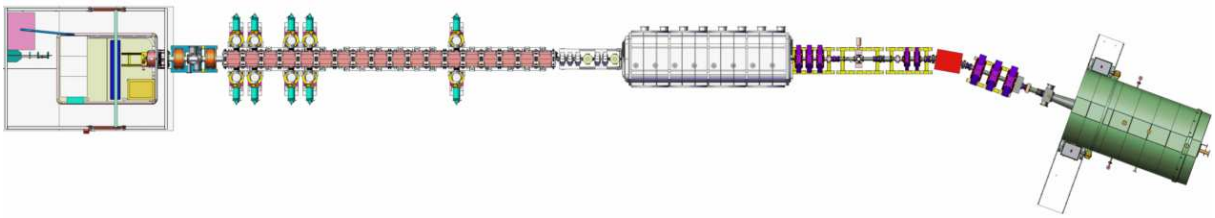

Figure 1.13: Sketch of the LIPAc accelerator [35].

As indicated in Fig. 1.13, LIPAc will not accelerate the beam onto a lithium target, but the beam will just be dumped. While the purpose of the beam dump is just to dispose of the beam energy, it will emit a huge amount of radiation in the process, similarly

to the IFMIF lithium target. A consistently thick wall is foreseen in order to isolate the accelerator from this radiative environment as well as possible.

Radiation in the LIPAc Vault

Since radiation generated within the beam dump is emitted virtually isotropically, it will also be absorbed by the dump itself. The only direction where no absorption can occur is towards the accelerator itself. This kind of radiation is commonly referred to as back-scattering. This effect can be nicely seen in the radiation map of the vault shown in Fig. 1.14. The bright red spot on the right hand side of the map indicates the beam dump as major source of the radiation. For this simulation all other sources have been neglected. Along the beam line two quadrupole triplets and, in between, one quadrupole doublet and a dipole are indicated. For more detail on the accelerator components in this region, please see Fig. 1.13.

The numbers in Fig. 1.14 indicate specific points of interest for which the neutron flux at full duty cycle has been calculated explicitly. The neutron flux and the accumulated fluence after six months of continuous full-power operation for some of these points are given in Table 1.5.

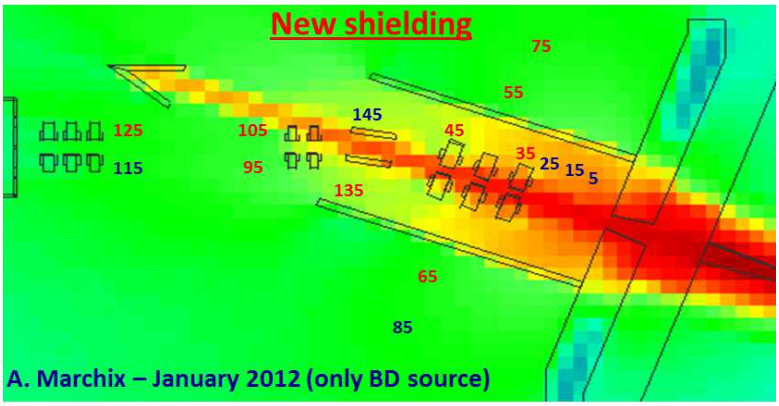

Figure 1.14: Neutron radiation map for the LIPAc vault, by courtesy of Anthony Marchix (CEA Saclay)

To prevent this backscattering from irradiating the entire accelerator, the beam is deflected by a 20° - bending magnet upstream to the beam dump. This allows for a "V" like shielding that can absorb the radiation backscattered from the beam dump. This way, only a short part of the HEBT is directly irradiated and the rest of the accelerator only suffers from secondary particle irradiation. However, the irradiation by secondary particles already suffices to pose significant challenges to the accelerator design. Materials must be chosen to be radiation hard and electronics have to be placed at remote distance or must be well shielded, if remote handling is impossible.

In spite of walls and shieldings erected to attenuate the radiation, the high background radiation level in the vault remains a major issue for the accelerator development. It makes the use of radiation hard materials imperative and requires intrinsically radiation weak components, like electronics, to be placed at remote distance or to be carefully shielded. This will have a huge impact on the diagnostics development presented later on in this thesis.

Table 1.5: Neutron radiation in the LIPAc vault at some points indicated in Fig. 1.14, giving the neutron flux at full duty cycle and the accumulated fluence after six months of continuous operation.

Point	Flux [n/cm^2/s]	Fluence [n/cm2]
5	$7 \cdot 10^8$	$1 \cdot 10^{16}$
15	$6 \cdot 10^8$	$1 \cdot 10^{16}$
25	$5 \cdot 10^8$	$8 \cdot 10^{15}$
145	$4 \cdot 10^7$	$6 \cdot 10^{14}$
115	$6 \cdot 10^6$	$9 \cdot 10^{13}$
85	$4 \cdot 10^6$	$7 \cdot 10^{13}$

1.4.1 LIPAc Commissioning

The commissioning strategy for the LIPAc is structured in three main phases, the injector, the RFQ and finally the full accelerator including the SRF-linac. In each phase, the accelerator setting will be varied around its nominal values and the properties of the resulting beam measured before the next subsystem is mounted.

As the LIPAc is built in Europe, but will be operated in Japan, the injector will be first commissioned in Europe and then again in Japan. At the end of the injector, a low-power beam dump will be installed to stop the beam. To avoid activation of the injector components, it is foreseen to perform the commissioning in Europe mainly with protons instead of deuterons.

To activate the accelerator, the proton must penetrate the Coulomb barrier which can be estimated to be

$$\Phi = \frac{1}{4\pi\epsilon_0} \cdot \frac{q}{r} \tag{1.16}$$

with r being the radius of the nucleus that can be approximated to be $r = (1.25\,\mathrm{fm}) \cdot \mathrm{A}^{1/3}$. For iron, this calculation grants a peak value of the Coulomb potential of about 8 MeV which is far higher than the injector energy of 90 keV.

For deuterons, however, the dominant effect is another. Due to its very low binding energy, the deuterium core can dissociate even at very low energies. The previous considerations concerning the Coulomb barrier do not hold for neutrons that carry no electric charge and that can thus penetrate the Coulomb barrier easily. Replacing deuterium by hydrogen is a very effective mean to avoid activation of accelerator components due to neutron capture.

At Rokkasho, the LIPAc injector will be commissioned with protons in the beginning as well and later with deuteron beams up to full intensity (140 mA) and full duty cycle (cw).

In a second step, the RFQ will be commissioned. It is foreseen to start with a proton beam of half the intensity and half the energy to achieve the same space charge effect, before a deuteron beam is used. The deuteron current will then be ramped up to 125 mA and the duty cycle will be increased from 10^{-4} until the power limit of the low-power beam dump, which is still used in this phase, is reached.

In the third and final phase, the SRF linac with the HEBT will be commissioned. First, a proton beam will be used, before to use deuterons. The deuteron beam current and duty cycle are then successively increased to nominal values. In this phase the real beam dump will be available instead of the low-power beam dump which will allow to ramp the beam power up to nominal conditions [36, 37, 38].

1.4.2 LIPAc Beam Diagnostics

To tune the accelerator to achieve nominal performance, a variety of beam diagnostics devices is required that can cope with the different beam settings listed above. In addition to the diagnostics mounted along the accelerating structures, in LEBT, MEBT and HEBT, it is foreseen to have a diagnostics plate (D-plate), i.e. a piece of beam line consisting virtually only of diagnostics elements, that can be mounted downstream to the accelerator section that is commissioned at that time [39].

The diagnostics element of the LIPAc accelerator are indicated in a mock-up in Fig. 1.15. The diagnostics elements foreseen for the D-plate are not displayed and are presented in more detail in Fig. 1.18.

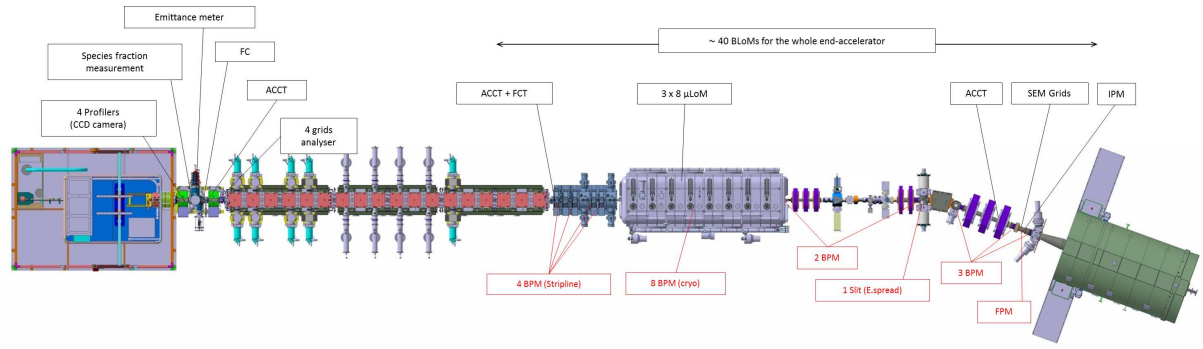

Figure 1.15: Outline of the LIPAc accelerator indicating the foreseen diagnostics elements, by courtesy of Dominique Gex (CEA Saclay). The diagnostics elements on the D-plate are not included.

LEBT Diagnostics

In the low energy regime a major issue for high intensity beam dynamics is the space charge effect. The LEBT is therefore designed in a most compact fashion to minimize the beam broadening, especially where it is not compensated, i.e. where electric fields of the beam are present, namely the source extraction and the RFQ injection regions. Consequently, the amount of diagnostics there is limited only to the most essential ones. In the middle of the LEBT, more complete diagnostics can be installed. At the end of the LEBT, a diagnostics box will be mounted during commissioning that holds additional diagnostics. An outline of the LEBT indicating some of the diagnostics foreseen is given in Fig. 1.16 [20].

An important parameter of the RFQ is its transmission, defined as the ratio of output to input current. It is therefore essential to measure the beam current at the level of the LEBT. For this purpose, a Faraday Cup (FC) and an AC Current Transformer (ACCT) are foreseen. As an interceptive device, the FC cannot be used at full beam

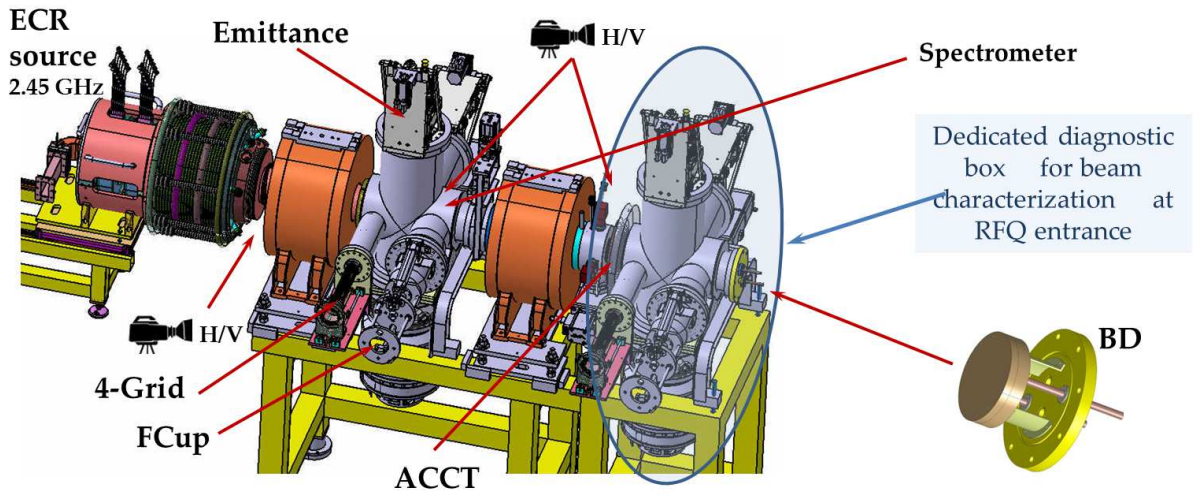

Figure 1.16: Outline of the diagnostics elements foreseen for the LEBT and the diagnostics box during commissioning [20].

intensity and since the ACCT can measure the AC component of the current only, it provides proper current readings only for pulsed beams. Neither current meter can hence be used under nominal beam condition, in cw mode at 125 mA. A DC Current Transformer (DCCT) would have been preferable over the ACCT, however, there is not enough space available.

As the normalized emittance cannot be decreased according to Liouville's theorem, the minimum achievable emittance of an accelerator is already determined on the level of the source. An emittance meter is therefore highly desirable on the LEBT.

The RFQ downstream the LEBT is designed to accelerate only one single particle type. However, the source does not generate a pure deuteron beam, but also deuterium molecules. These molecules cannot be accelerated efficiently and are lost. An optical measurement device will be mounted to measure the ratio of D^+, D_2^+ and D_3^+, based on their different Doppler shift light rays.

In addition, 4-grid analyser to measure the space charge effect and Beam Induced Fluorescence (BIF) (Fluorescence Profile Monitor (FPM)) monitors are foreseen as beam profile monitors. During the commissioning an additional diagnostics box will be mounted at the end of the beam line. With such an assortment of diagnostics, the accelerator beam can be properly characterized.

To realize short bunches, that are required not to destroy the interceptive diagnostics, a chopper was added to the LEBT retrospectively. It will be mounted in between the two solenoids and is not yet included in Fig. 1.16. By rapidly applying an electric field, a chopper can chop the beam into pulses down to 50 μs.

MEBT Diagnostics

As counterpart to the ACCT in the LEBT to determine the RFQ transmission, an ACCT and a Fast Current Transformer (FCT) will be mounted on the MEBT. The FCT is basically an ACCT with a sufficiently high bandwidth to couple to the beam bunches with the accelerating frequency of 175 MHz. It can thereby measure the beam current in the nominal cw mode as well. However, since the electric field lines of a

non-relativistic charge distribution spreads out uniformly, the field of neighboring bunches overlap which can falsify the FCT measurement.

All along the accelerator downstream the RFQ, Beam Position Monitors (BPMs) and Beam Loss Monitors (BLoMs) will be installed. In the LEBT, BPMs are not operational since the beam is not bunched, and BLoMs would not work either, since no secondary particles can escape the beam pipe at these low energies.

It was foreseen to install an additional profiler, an Ionization Profile Monitor (IPM), on the MEBT, but this profiler will not be realized due to the lack of space.

SRF-Linac

Particle loss along the SRF-linac is of particular importance since lost particles deposit their energy in the cryostat and particle losses therefore must be kept low in order to prevent quenching of the cavities. In addition to the normal BLoMs outside the cryostat, it is foreseen to place μ-loss detector close to the beam pipe that can measure even lowest losses and that thereby allow for a beam tuning by minimizing these μ-losses. These μ-loss detectors are of particular importance for the accelerator commissioning and operation, since they are the only diagnostics available at the level of the SRF-linac apart from the BPMs.

HEBT Diagnostics

The HEBT is the transport line upstream to the beam dump. A Computer Aided Design (CAD) mock-up of the entire transfer line downstream the SRF-linac is given in Fig. 1.17.

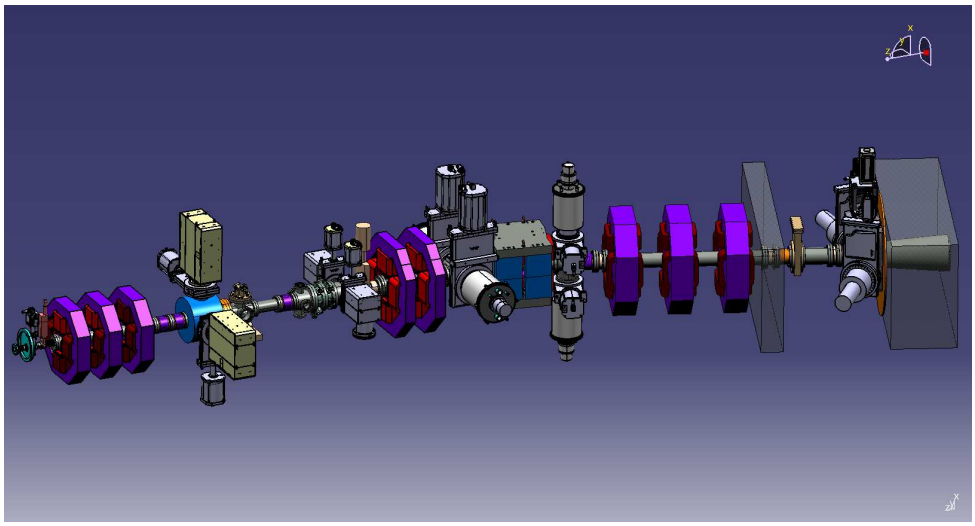

Figure 1.17: CAD Mock up of the transport line downstream the SRF-linac, containing the quadrupole triplet, the D-plate and the quadrupole doublet to the left of the bending magnet and the rest of HEBT to the right.

With a total beam power of over 1 MW in nominal beam settings, the beam can potentially damage the beam dump. On the HEBT, the beam is therefore expanded to disperse the beam power over as large a surface as possible. Along the HEBT, various profile monitors will be mounted to ensure that the energy deposition on the

beam dump is within safe limits. The profile monitors include IPM and BIF profilers as non-interceptive monitors and Secondary Electron Emission (SEM) grids as interceptive ones, if the beam intensity is below the detection limit of IPM or BIF. Since LIPAc is a prototype for the IFMIF accelerator, IPM and BIF monitors will be tested to determine which one is more suitable for IFMIF.

Diagnostics Plate

During the three main phases of the accelerator commissioning, the injector, the RFQ and finally the entire accelerator will be tuned. During the last two phases, the diagnostics plate will be installed at the end of each accelerator section to provide the diagnostics elements required for the measuring and optimizing the beam. After the commissioning, the D-plate will remain in the accelerator line downstream to the SRF-linac.

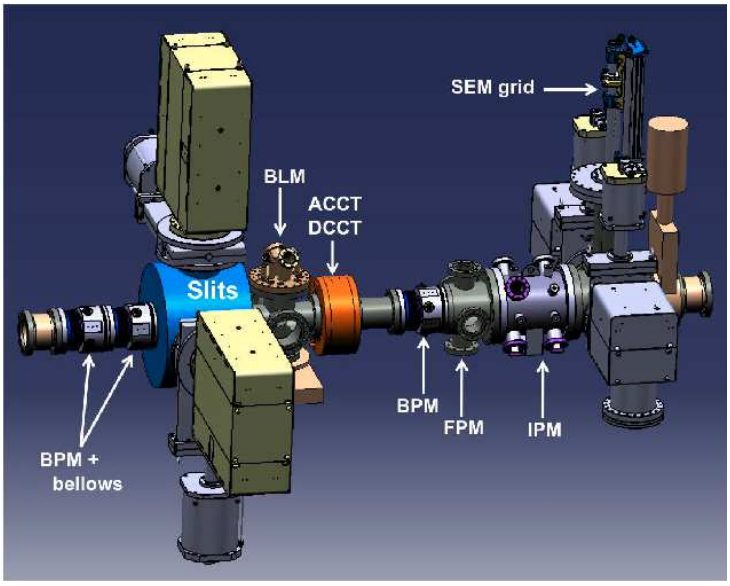

Figure 1.18: Diagnostics foreseen on the D-plate: In charge of CEA Saclay: ACCT and DCCT, SEM grid, and IPM, in charge of CIEMAT Madrid: BPMs, slits, FPM profiler, and in charge of INFN Legnaro: Bunch Length Monitor (BLM) .

The D-plate contains all the diagnostics required for commissioning, namely:

- ACCT, DCCT and FCT
- BPMs
- Bunch Length Monitor (BLM)
- Slit
- IPM profiler
- BIF profiler
- SEM grid

An illustration of the D-plate indicating each single element is given in Fig. 1.18.

In this thesis, only the diagnostics elements in charge of the CEA Saclay will be covered, i.e. the SEM grids, the IPMs, the BLoMs, and the μ-loss detectors. CEA Saclay has also taken the current transformer development in charge, however, they will be bought from Bergoz Instrumentation and will not be covered here.

1.5 Commissariat à l'Énergie Atomique

The Commissariat à l'Énergie Atomique et aux Énergies Alternatives (CEA) is one of the major institutions in France for research, development and innovation. It is involved in four main domains:

- Carbon-free energy
- Technologies for health and information
- Large scale infrastructures in research
- Defense and global security

For each of these domains, the CEA conducts an excellent fundamental research and pursues its role of supporting industry.

The CEA operates ten centers throughout France. It keeps many partnerships with other research organizations, local authorities and universities. As such, the CEA takes an active part in coordinating national alliances of French research in the fields of energy, life sciences and health, digital sciences and technologies, and environmental sciences [40].

CEA Saclay

The CEA center of Saclay was founded in 1952 and is located in the south of Paris, close to Versailles. Until now, the CEA Saclay, with more than 6000 employees, is the most versatile center of the CEA. The research conducted at Saclay does not only include research on nuclear energy, but also material sciences, health and life sciences, environmental and climate sciences, and many more [41].

Two domains of the research performed at CEA Saclay are of particular significance for this thesis: The research on alternative energy sources, like next generation fusion reactors, and the accelerator research and development.

IRFU

This thesis was performed at the division of IRFU (Institut de Recherche sur les lois Fondamentales de l'Univers). IRFU has focused its activities in eight major themes that can be subdivided in five physics topics:

- Nuclear physics

- Energetic contents of the univers
- Ultimate constituents of matter
- Structure of the universe
- Radiation detection

and three instrumental topics:

- Production and manipulation of radiation
- Simulations and data treatment
- Nuclear Energy

The choice of these themes shows how thin the boundaries between astrophysics, nuclear physics and particle physics have become. It is indeed another originality of the IRFU to have taken into account from the beginning that understanding the fundamental laws of nature requires, in particular, to study the smallest and largest scales accessible.

IRFU contributes to numerous international projects and experiments like Double Chooz for neutrino measurements, the satellite Planck to investigate dark energy, the BaBar experiment to explore the CP-violation and many more. The expertise of IRFU in accelerator projects and detector developments allows it take an active role in projects like the development of the LHC detectors CMS and Atlas or the design of micromegas [28].

DITANET

This thesis was carried out in the frame of DITANET (DIagnostics Techniques for particle Accelerators NETwork). It was an European Network installed within the FP7 Marie Curie Initial Training Network scheme. In this frame, several major research centers, leading universities, and partners from industry developed beyond-state-of-the-art diagnostic techniques for future accelerator facilities and jointly trained students and young researchers within a unique European structure [42].

Chapter 2

Beam Loss Monitors

Ce chapitre traite des deux types de moniteurs de pertes du faisceau, l'un dévolu à la sécurité de l'accélérateur et basé sur des chambres à ionisation et l'autre dont l'objectif est d'assurer le réglage fin de l'accélérateur en minimisant les pertes détectées dans des diamants. Ces deux aspects seront abordés dans les deux parties suivantes :

Les Chambres à Ionisation (IC)

Pour assurer la sécurité de LIPAc, le système de surveillance des pertes sera constitué d'un ensemble d'une quarantaine d'IC placées le long de l'accélérateur, depuis la partie aval du RFQ jusqu'à l'arrêt faisceau (Beam Dump ou BD). La forte puissance de LIPAc exige l'envoi d'un signal rapide en cas de défaillance de l'accélérateur vers MPS (Machine Protection System) en moins de 10 μs afin de stopper le faisceau rapidement ($<30\,\mu$s). Ce système de surveillance des pertes doit également pouvoir suivre l'évolution de ces pertes avec une résolution correspondant à des pertes de l'ordre de 1 W/m.

Les IC ont été choisies pour remplir cette fonction, essentiellement pour leur grande fiabilité, leur faible coût et une maintenance modeste. Ces IC sont celles utilisées au LHC (Large Hadron Collider) mais qui fonctionnent dans un tout autre domaine en énergie et avec des particules de nature différente. En effet, les seules particules qui franchiront les parois du tube faisceau sont les neutrons et les γ dans une gamme d'énergie de quelques keV à une dizaine de MeV.

Pour montrer que ces IC étaient bien adaptées pour jouer le rôle de moniteurs de pertes, l'une d'entre elles a été empruntée au LHC afin de mesurer expérimentalement sa réponse aux neutrons et aux γ. Ces calibrations ont été réalisées auprès d'un irradiateur de ^{60}Co, CoCase à Saclay (Cobalt Casemate) délivrant des γ d'énergie 1.25 MeV et auprès d'un "faisceau de neutrons" au CEA de Valduc (3 et 14.7 MeV). Les résultats sont en accord avec les réponses simulées des IC par les physiciens du LHC sur le domaine en énergie de LIPAc. Des courants de l'IC inférieurs à 2 pA ont pu être mesurés lors de ces tests, correspondant dans le pire des cas à des pertes de 1 W/m et garantissant ainsi cette possibilité. Pour les courants élevés, une bande passante proche de 50 kHz a été obtenue pour l'arrêt d'urgence du faisceau ($<10\,\mu$s pour MPS).

La possibilité d'augmenter la sensibilité de ces IC a été étudiée. Pour cela des simulations avec Geant4 donnent des gains variant de 10 à 100 selon le gaz qui remplit

l'IC comme par exemple le trifluorure de bore (BF_3). Ce type de gaz étant par ailleurs toxique et corrosif, nous avons décidé de ne pas suivre cette piste.

L'électronique et le système d'acquisition qui piloteront ces moniteurs de pertes sont également présentés.

Détecteurs au Diamant

Le pilotage de LIPAc est d'une grande difficulté essentiellement due à la grande charge d'espace du faisceau de deutons. L'une des nouveautés envisagées par l'équipe de la dynamique faisceau pour mener à bien le réglage fin du faisceau est de minimiser son halo plutôt que d'optimiser la taille du cœur du faisceau. C'est pour cette raison que des moniteurs de micro-pertes de faisceau vont être installés pour la première fois dans un accélérateur.

Ces détecteurs au diamant seront placés dans le cryostat de l'accélérateur supraconducteur, à raison de 3 pour chacune des 8 mailles constituées d'une cavité, d'un solénoïde et d'un moniteur de position.

Le fonctionnement des diamants n'a jamais été testé à température cryogénique, nous les avons donc plongés dans de l'azote et de l'hélium liquides au CEA Saclay tout en mesurant leurs réponses à une source de ^{252}Cf. En conclusion, l'utilisation des diamants à 77 K ainsi qu'à 4.2 K semble être possible.

De même que pour les IC, nous avons calibré les diamants en neutrons au CEA de Bruyères-le-Châtel. Un Van de Graaff accélère des protons et des deutons qui bombardent diverses cibles produisant des neutrons mono-énergétiques. Des γ sont également créés dont on s'affranchit par une mesure de temps de vol. Les résultats obtenus sont en bon accord avec les simulations réalisées au CEA Saclay.

Le calcul des taux de comptage attendus lors du fonctionnement de LIPAc, ainsi que des bruits de fond, sont présentés et montrent la faisabilité de la détection des micro pertes par des diamants.

L'électronique rapide associée à un système d'acquisition est aussi abordée.

2.1 Requirements

The purpose of beam loss monitors in a high-power machine like the LIPAc is threefold, they will have to

- trigger the Machine Protection System (MPS) in the case of a fatal beam loss,
- monitor losses down to 1 W/m,
- and serve as diagnostics element to tune the accelerator.

As each of these applications has different requirement on the beam loss monitoring system three different beam loss monitors are, in principle, required to cope with these demands.

If a high-power beam gets lost for some reasons, the accelerator has to be switched off as fast as possible. Calculations performed in Japan indicate that the IFMIF beam has to be stopped within less than 30 μs to prevent severe damage to the accelerator. Since the source itself has a shut-down time of approximately 20 μs, the response time of the beam loss monitors must be well below 10 μs [43].

Since it is to be expected that such a fatal beam loss will result in a tremendous rise of lost particles, the sensitivity of this kind of monitor does not need to be too high. For safety reasons however, this beam loss monitoring system must be very reliable and it must be able to cover the entire accelerator not to have any blind spot where fatal beam losses can occur without warning. The latter demand implies that many beam loss monitors will have to be mounted all along the accelerator and that therefore each single one of them must not be too expensive [44].

Hands-on maintenance of an accelerator is highly desired as it allows access to the machine without any costly and time-consuming cool-down periods to let the radiation level in the accelerator vault attenuate to acceptable limits. It is commonly considered that hands-on maintenance of the accelerator can be ensured, if particle losses are kept below a level of 1 W/m. In addition to the accelerator beam loss monitors, this threshold will also be monitored by the Personal Protection System (PPS) that guarantees the radiation protection of people working on the accelerator. For a 1 MW machine like LIPAc, 1 W/m is only 10^{-6} of the total beam power. To achieve this very demanding requirement, an extremely sensitive beam loss monitor is required. It has, however, virtually no limitation on its integration time, as only average values over the time of operation are of interest.

On the level of the SRF-linac, the only diagnostics available are Beam Position Monitors (BPMs). It is foreseen to tune the beam in the SRF-linac by minimizing the beam losses. A beam loss monitor is thus required that can identify local beam losses. One therefore needs a monitor that is sensitive to radiation resulting from beam losses only and that has a decent position resolution.

All three demands cannot be satisfied by a single device. But the beam loss monitor required for the MPS and for measuring 1 W/m losses have rather similar characteristics. Their main difference is that the one requires a low sensitivity at a short response time, and the other a high sensitivity at long response time. This matter can be easily achieved by using an integrating electronics with variable integration time. For this purpose, an Ionization Chamber (IC) is foreseen to be used.

To tune the accelerator, a good sensitivity and a read-out rate of a few Hz is required. In addition, this beam loss monitor requires a rather good position resolution as well. As losses at the low beam energies of the LIPAc emit secondaries isotropically in 4π, these beam loss monitors consequently have to be placed close to the beam pipe. For the SRF linac, this means to place them inside the cryostat. Since gaseous detectors like ICs are not deployable in cryogenic environments, a solid state device is required. Due to its intrinsic radiation hardness, it was decided to use diamond detectors for this purpose.

2.2 Ionization Chambers

This section covers the tests and calibrations of Ionization Chambers (ICs) to be used as beam loss monitors. Beam loss monitors are essential for the safe operation of any high power accelerator, since they are commonly used to trigger the MPS. The effect that fatal beam losses can have in high-power accelerators is illustrated in Fig. 2.1.

(a) Damaged inflicted to the beam pipe by the high-power electron beam of the ELBE accelerator [45].

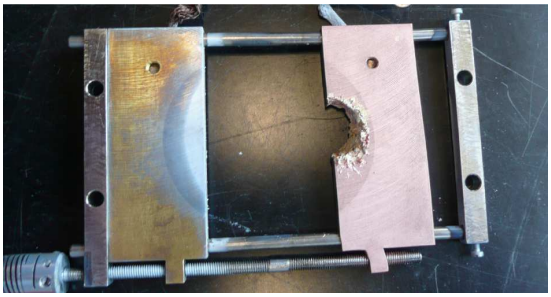

(b) A piece of a diagnostics prototype destroyed during a high-current beam test at the SILHI source at CEA Saclay; $I_{Beam} = 10\,mA$, E=100 keV, pulse length: 1 ms

Figure 2.1: Photos of accelerator subsystems after a fatal beam loss without any beam loss monitors available.

It is therefore desirable to use a very reliable detector that can be mounted in large quantities, to avoid blind spots and to achieve a certain level of redundancy. Being inexpensive, reliable and radiation hard devices, ICs are used as beam loss monitors in many accelerators [45, 46, 47, 48].

The tests and calibration of the IC, described in this section, were performed by my supervisor Jacques Marroncle (CEA Saclay) and myself. My main tasks were the Geant4 simulations for an increased neutron sensitivity and I also contributed to the experimental tests, their preparation and execution.

2.2.1 Principle of Operation

ICs are gaseous detectors that measure the ionization of primary particles in the gas that the IC is filled with. An IC in its simplest form consists of two parallel metallic electrodes separated by a gap of width D. The gap is filled with a gas or a liquid and defines the sensitive volume of the chamber. High voltages, V, commonly several kV, are applied between the anode and cathode. Charged particles traversing the sensitive volume ionize the gas or liquid and produce electron-ion pairs. The electric field E

= V/D causes electrons and positive ions to drift in opposite directions toward the anode and cathode, respectively.

The fraction of the created electrons reaching the anode, as well as their drift time, depends on the applied voltage. If the voltage is very small, the electrons produced by ionization recombine with their parents. If the electric field is larger than the Coulomb field in the vicinity of the parent ion, the electrons can escape this initial recombination. The number of electrons collected at the anode increases with the voltage up to saturation where all charges are collected. In this ionization region the created charge should not depend on the applied voltage. At higher electric fields, the electrons gain enough energy to produce additional charge carriers by ionization on their path. This is called the proportional region. In the Geiger-Müller region, saturation of the ionization current is reached [45]. Such high electric fields can commonly only be achieved close to a thin charged wire as it is the case in a Geiger-Müller counter. The different operating regions of an ionization chamber are given in Fig. 2.2 [49].

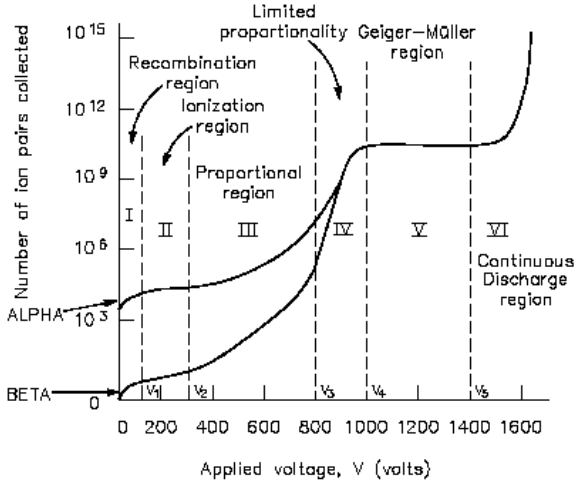

Figure 2.2: Regions of operation for Ionization chambers. The voltages given on the abscissa are voltages for ICs where the voltage is applied on a central wire and are nor comparable with the ones required for ICs like the LHC IC based on parallel plates [49].

As beam loss monitors, ICs are operated in the ionization region. In this regime, an electric field is required that is sufficiently strong to separate the ionization products and to thereby prevent recombination; however, the electric field must not exceed the gas amplification threshold.

The electric field in between two parallel plates is particularly useful for this purpose since it is constant in the entire active volume. Since the IC output signal corresponds then only to the ionization current generated by the ionizing particle, neglecting any recombination effects, the output is constant over large voltage range. This makes ICs very reliable detectors. The ionization current depends on the ionization cross section of the incident particle σ, the active range d and the average particle density in the gas n. The ionization current I_{Ion} generated by current of single-charged particles I is then given by

$$I_{Ion} = \sigma \cdot n \cdot d \cdot I \tag{2.1}$$

The ionization cross section σ depends only on the incident particle type and energy. The average active particle range d is given by the IC geometry for a certain particle type at given incidence angle. As the IC is hermetically sealed, average particle

density inside remains constant. The IC signal is thus independent of the ambient temperature or pressure. All this grants ICs a very stable signal output that can be considered independent of any external influence for a given particle type, energy and incidence. ICs are therefore commonly used for applications that require reliable and stable signal outputs, like beam loss monitoring systems.

2.2.2 The LHC IC

We intend to use the ICs of the LHC for LIPAc. The properties of this IC are discussed in this section.

A photo of the internal structure of the IC used at the Large Hadron Collider (LHC) as beam loss monitor is given in Fig. 2.3(b). The sealing of the IC that normally confines the gas inside has been removed for this photo to allow for a view inside. The IC consist of several plate electrodes as they are described in section 2.2.1. By applying alternately ground and a high voltage on these plates, an electric field is generated to extract the ionization products.

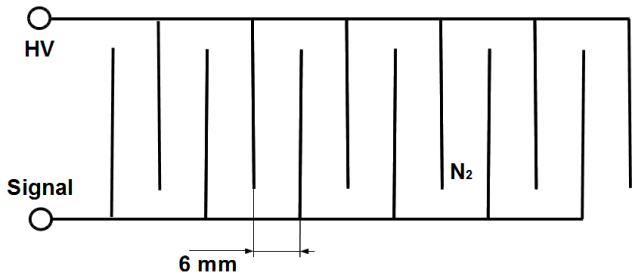

(a) Schematic view on the interior of the LHC IC illustrating the electrodes, the fill gas and the HV and signal connectors.

(b) Photo of the interior of the LHC IC [47].

Figure 2.3: Photo and schematic view on the interior of the LHC IC.

Materials

The rather simple design of the LHC ICs allows for the use of radiation hard materials, like metals or ceramics exclusively which in turn render the IC radiation hard itself. The actual materials used for the LHC IC are

- stainless steel for all mounts and the outer coverage,
- aluminum for the electrode plates,
- ceramics for all insulating materials.

At the front end of the IC, an electronics is mounted that consists only of passive elements, resistors and capacitors, to provide a low-pass filter to smoothen the applied

high voltage [47]. Due to the capacitance of the IC, fluctuations in the applied high voltage will cause fluctuations of the charge deposited on the capacitor plates, i.e. its current. To read the ionization current properly, this low-pass filter smooths the applied HV.

Relevant properties of the LHC ICs are summarized in Table 2.1.

Table 2.1: Design and standard operating parameters of the LHC IC [47].

	LHC IC
length	50 cm
diameter	9 cm
sensitive diameter	7.5 cm
gas	N_2
pressure	1.1 bar
sensitive volume length	38 cm
number of electrodes	61
electrode spacing	5.75 mm
electrode diameter	75 mm
standard bias voltage	1500 V

Signal Shape

When an ionizing particle traverses the IC, it will generate electron-ion pairs that are then separated and extracted by the electric field applied. The electric field acting on ion and electron is the same. The accelerating forces are hence equal but opposite. However, since the ion is much a heavier particle than the electron, the resulting acceleration experienced by the electron is far higher than for the ion. The time required to extract all electrons is therefore much shorter than for ions.

The resulting current of the IC, approximated as deposited charge divided by extraction time, is accordingly much higher for electrons than for ion. The signal current of the IC from a short proton bunch measured at CERN (Conseil Européen pour la Recherche Nucléaire) is given in Fig. 2.4 [50].

In Fig. 2.4, one can nicely see the very strong but also short electron contribution of the IC signal as well as the rather low and long tail from the ions slowly drifting towards the electrodes. Since for each electron one ion must be created, the electron and ion currents integrated over their proper drift times must match as well.

Charge Mobility

The previous argument based on the higher acceleration of electrons is strictly only valid in vacuum or low gas pressures where collisions with gas atoms are negligible. At higher gas pressures, the mean free path length between collisions with gas molecules/atoms will decrease. During such collisions the particle will transfer some fraction of its gained energy on the gas molecule/atom, and reach an equilibrium

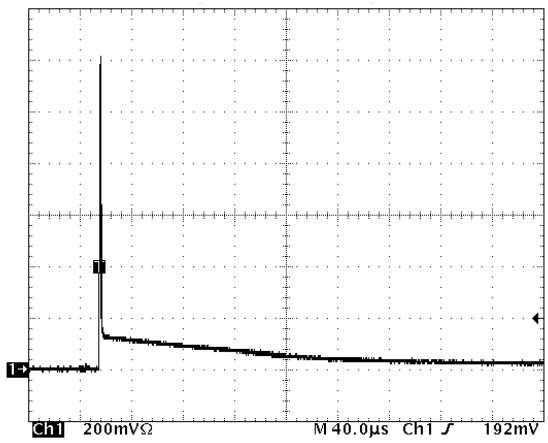

(a) Oscilloscope display of the LHC IC for a short proton bunch. The fast electron signal corresponds to the narrow peak, the slow ion signal results in a long tail over several 100 μs.

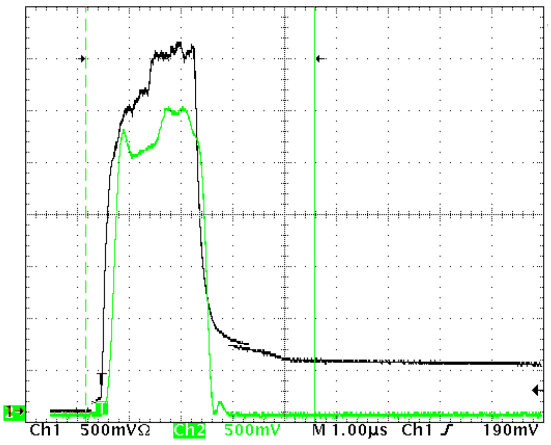

(b) Zoom of the electron signal (black) in comparison with the actual beam signal (green).

Figure 2.4: The LHC IC signal for a short bunch of protons of 1.7 μs [50].

average drift velocity after a short time. This velocity is proportional to the electric field applied E and inversely proportional to the gas pressure. Using the mobility μ as proportionality factor, the average drift velocity can be written as

$$v = \frac{\mu E}{p} \tag{2.2}$$

Typical ion mobilities in nitrogen gas at atmospheric pressure are between 1.0 and $1.5 \cdot 10^{-4}\,\mathrm{m^2 atm/Vs}$ [47]. With the IC parameters given in Table 2.1, the ion drift velocity can be calculated to be approximately 30 μm/μs, and the drift time to be about 200 μs accordingly. The mobility for electrons is circa 1000 time larger. Assuming a value of 5 cm/μs, the drift time becomes approximately 100 ns [50]. Such values are in good agreement with the measured signal shape given in Fig. 2.4. The peak width in Fig. 2.4(b) is given by the initial proton pulse length, not by the electron drift time that is much shorter.

Response Function

The IC output signal is given by the ionization current of the incident primary particle, as explained in section 2.2.1, where equation (2.1) gives the ionization current. In this equation, the average active range of the ionizing particle depends on the particle type and its incidence angle. The ionization cross section still depends on the incident particle type and its energy. Both dependencies can be covered by a response function which gives the average charge deposited in the IC by a single particle traversing the IC.

Simulations of the response function of the LHC IC have been performed by Mariusz Sapiński at CERN [51]. Results of his simulations for a transverse particle impact (w.r.t. the IC axis) is given in Fig. 2.5 [47].

Particularly for protons, but also for electrons and positrons, there is a sharp edge at about 35 MeV, 2-3 MeV respectively. Below this energy, the primary particles are stopped in the IC cover and cannot deposit any energy in the gas. This edge is followed by a small peak which can be identified as Bragg-peak at low energies [47].

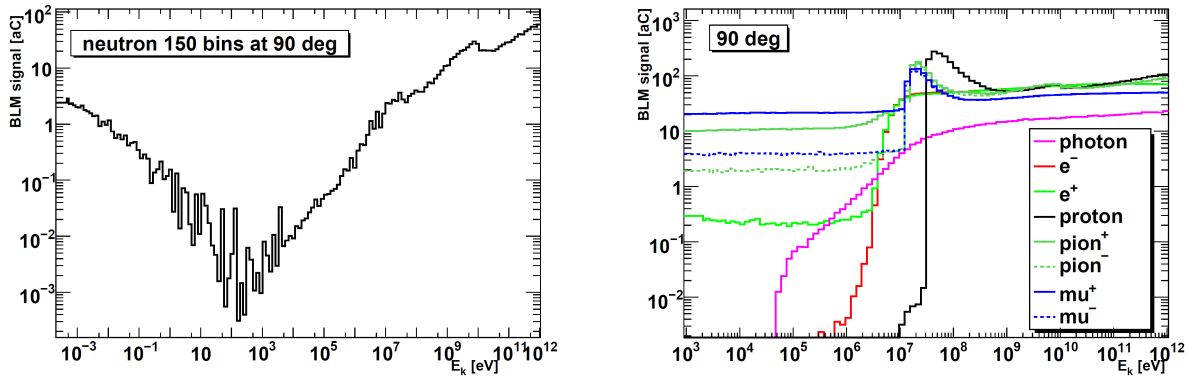

Figure 2.5: Response function of the LHC IC for various primary particles and energies [51].

A major difference between the LHC and the LIPAc is the particle design energy which is with 7 TeV for the LHC almost 10^6 times higher than the 9 MeV of the LIPAc. As a consequence, primary particles with some TeV of energy will contribute to the IC signal at the LHC, while at the LIPAc primary particles will not even be able to escape the beam pipe, since deuterons of 9 MeV (5 MeV) have a penetration depth of 136 μm (53 μm) in iron [52]. For the LHC, the response functions of the IC for many different particles at various energies and incidence angles are required to properly estimate the IC response. For the LIPAc, only γ and neutrons of energies well below 9 MeV will be able to escape the beam pipe.

As shown in Fig. 2.5, the response function of the LHC IC for γ and neutrons at $\sim$1 MeV, that are expected at LIPAc, is several orders of magnitude smaller than for the high energetic protons, that are available at the LHC. In spite of the very high beam current of the LIPAc, the reduced sensitivity of the IC results in a very low signal current which is in fact a major issue for the beam loss monitor system of the LIPAc.

The IC current is required to measure 1 W/m losses. The IC current resulting from 1 W/m losses was estimated for different distances to the beam pipe and is displayed in Fig. 2.6. The IC current drops rapidly at greater distances to the beam pipe. Outside the cryostat of the SRF-linac, the IC is estimated to be even below 2 pA [44].

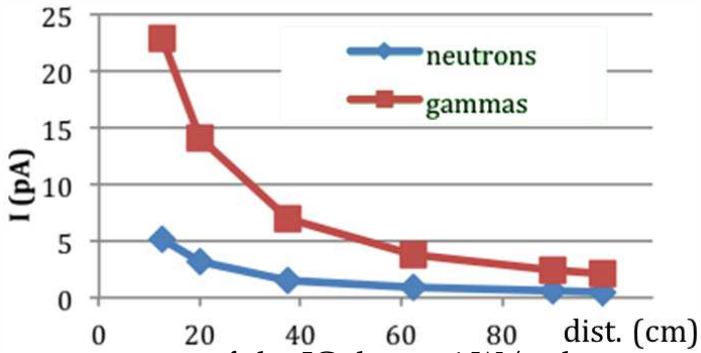

Figure 2.6: The output current of the IC due to 1 W/m losses versus the distance to the beam pipe.

2.2.3 Positioning of the IC

As beam loss can occur anywhere, the entire accelerator should ideally be covered by a system of beam loss monitors to avoid any blind spots. However, as it was pointed in section 2.2.2, since primary particles cannot escape the beam pipe one has to measure secondary particles, neutrons and γ, instead. Since the response function of the IC is very low for such particles at low energies, see Fig. 2.5, in the low energy parts of the accelerator, ICs cannot effectively be used as beam loss monitors, but they will only be used in the high-energy regions downstream the RFQ.

Starting from the end of the RFQ down to the beam dump, it is foreseen to place about 40 ICs along the accelerator, 4 at the far end of the RFQ, 4 on the MEBT, at least 16-24 along the SRF linac, and another 8-10 on the HEBT. On MEBT and HEBT, the ICs can be placed close to the beam pipe, on the level of the SRF linac however, they must be placed outside the cryostat, i.e. about 1 m away from the beam. The IC signal will be greatly reduced due to the large distance and the absorption of secondary particles by the cryostat as well.

In particular for the ICs located on the HEBT, but also for the other locations, the background signal due to neutrons or γ coming from the beam dump can be orders of magnitude higher than the signal expected from the beam losses at design settings with beam losses of 1 W/m only. The IC current close to the beam dump is expected to be $\sim$7 nA, in comparison to $\sim$20 pA due to 1 W/m losses close to the beam pipe.

However, under nominal beam conditions the background signal from the beam dump should be rather constant and its variation should be well below the signal by the 1 W/m beam losses [44].

The ICs should thus be able to measure currents below 2 pA to monitor 1 W/m losses in the SRF linac and well above 10 nA to trigger the MPS. The IC electronics must therefore have a total dynamic range of $\sim 10^5$.

2.2.4 Neutron Calibration at CEA Valduc

In spite of the fact that the LHC ICs have been well tested at CERN and extensive Geant4 simulations have been performed, the very different beam conditions at the LIPAc require additional tests and calibrations. At the low energies of the LIPAc, only neutrons and γ can escape the beam pipe and only these particles can be used to trigger the ICs. It was therefore decided to perform a neutron calibration at the SAMES accelerator at CEA Valduc and a γ calibration at the Cobalt Casemate (CoCase) at CEA Saclay. For this purpose, an IC was borrowed from CERN to be tested. The test at CEA Valduc is presented in this section.

SAMES at CEA Valduc

CEA Valduc was founded in 1957 in the north-west of Dijon. It is a military center that was strongly involved in the construction of the French nuclear weapons. The SAMES accelerator at CEA Valduc serves as neutron source by accelerating 400 keV deuterons onto a deuterium or tritium target. This triggers D-T or D-D fusion reaction that release mono energetic neutrons of 14.7 MeV or 3 MeV respectively [53].

Experimental Setup

The IC is mounted close to the D/T-target of the SAMES accelerator. The experimental setup is shown in the photo in Fig. 2.7. The yellow pipe in the foreground is the IC, in the background one can see the SAMES accelerator beam line entering the vault through a sealed hole. At the end of the beam line, the target is mounted having a brass like color. As tritium is a highly radioactive gas, the accelerator vault must be sealed during the measurements to avoid tritium contamination in the case of an accident.

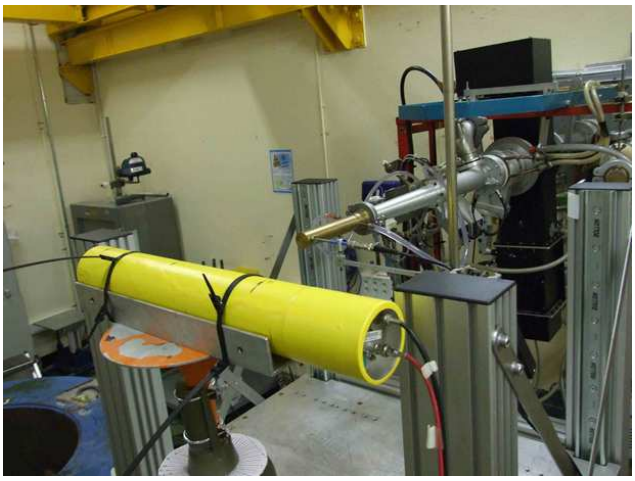

Figure 2.7: Photo of the experimental setup at the SAMES accelerator at CEA Valduc, in yellow the IC in the background the accelerator with the D/T-target.

Ionization Regime Check

For an ionization chamber operated in the ionization regime it is to be expected that the output current is independent of the extraction voltage. As the LHC IC applies the electric field over parallel plates, the electric field should be constant in virtually the entire active range. If the applied high voltage is slowly decreased, the electric field will reach a point where it does not suffice any more to prevent the recombination of the ionization products. A rapid drop in the IC output is expected once the recombination starts. Under constant neutron irradiation, the IC current was measured for decreasing high voltages. The data is given in Fig. 2.8.

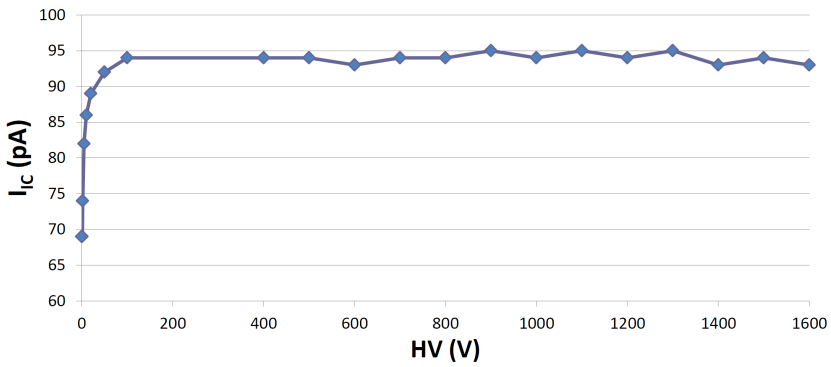

Figure 2.8: IC output current versus the applied high voltage under constant irradiation, by courtesy of the SAMES operators.

At higher voltages, one can nicely see a long plateau that corresponds to the ionization region, discussed in section 2.2.1. At about 100 V, the IC output collapses and drops rapidly to zero, as it expected due to the recombination.

The IC output signal was also measured at a variable neutron flux at 14.7 MeV to check its linearity. The IC current measured by a picoammeter plotted versus the neutron flux in arbitrary units is presented in Fig. 2.9. The measured current rises linearly with the neutron flux, as it is expected in the ionization regime.

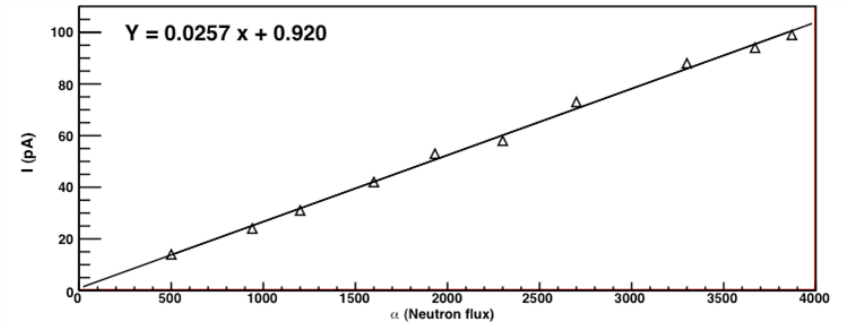

Figure 2.9: IC current measured by a picoammeter plotted versus the neutron flux.

At the nominal voltage settings of ∼1600 V the IC is thus safely operated in the ionization regime. The stable operating conditions and its high signal linearity in the ionization region make the IC a very reliable diagnostics element.

Response Function Measurement

During the test, the IC distance from the source as well as its orientation have been varied for both neutron energies available, 3 MeV and 14.7 MeV. The HV applied on the IC was chosen to be 1600 V for all measurements. We have calculated based on the IC current the response function of the IC for the given neutron energy and angle. The resulting response function, in aC/n, for the different angles and distances are given in Fig. 2.10. They are compared with results from simulation performed at CERN, presented as red / green lines.

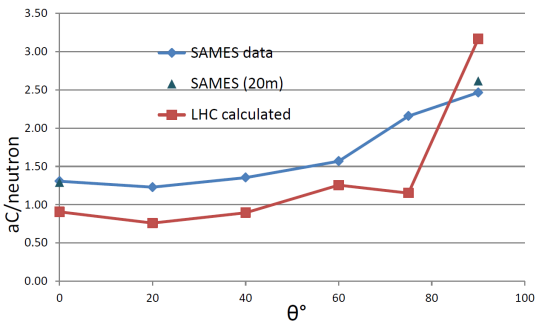

(a) Response Function for 3.0 MeV neutrons.

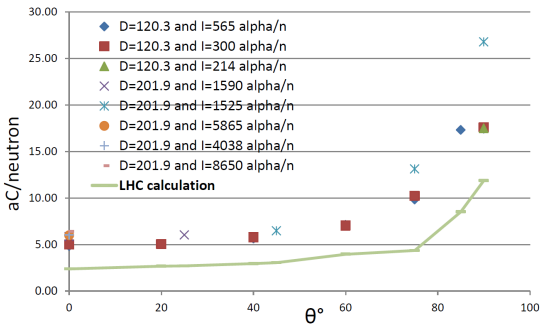

(b) Response Function for 14.7 MeV neutrons.

Figure 2.10: Response function of the IC for neutrons measured for various incident angles at the SAMES accelerator at CEA Valduc.

The simulation results from CERN appear to be underestimated, but the signal shape is in good agreement.

At 3 MeV, the test was performed with 8 m long cables connecting the IC with the electronics. For comparison, two measurements were taken at 0° and 90° with 20 m long cables. No significant differences were seen.

Wall Effects

It is assumed that the neutrons are emitted isotropically in 4π. The neutron flux density then drops with $1/r^2$. By scaling the measured IC current on the total neutron flux and the decreased solid angle at larger distances, we have defined a quantity R_Ω that is normalized on the measurement done at 80 cm. This value is plotted versus the distance between IC and neutron source in Fig. 2.11. For an $1/r^2$ drop in the neutron flux density, the R_Ω value should remain constant. This is, however, clearly not the case.

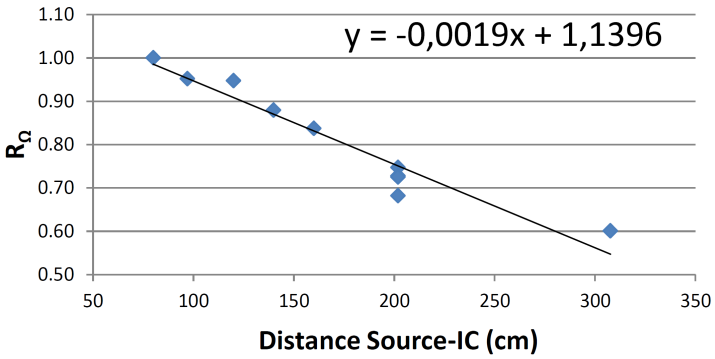

Figure 2.11: The quantity R_Ω, the IC current scaled by the total neutron flux and decreased solid angle that the IC occupies at larger distances, normalized on the measurement at 80 cm plotted versus the distance between IC and neutron source.

Such a drop in the intensity for larger distances between the IC and the neutron source, could be explained by neutrons that are reflected by the walls of the vault or by neutrons that are losing some part of their energy in collisions with air molecules which would decrease the IC current due to its lower response function at lower energies. To evaluate these options, the IC current in the vault was simulated using Geant4. Mariusz Sapiński (CERN) kindly provided us with the Geant4 model of the IC used for the calculation of the IC response functions at CERN.

In Geant4, the vault was implemented and the neutron source was assumed to emit neutrons isotropically in 4π. Within this Geant4 script, the IC model was placed at the same positions used during the measurement and the resulting current was determined. The IC signal normalized on the reading at 80 cm and the resulting R_Ω-value, as defined above, are presented in Fig. 2.12. Since the neutrons are emitted in 4π and the solid angle covered by the IC is rather small, only a small fractions of the emitted neutrons contribute to the IC current. The errors of the IC in this simulation are therefore significant.

According to the Geant4 simulations, the IC decreases with the distance roughly with $1/r^2$, as the value R_Ω remains constant over a rather long range. Only the last data point indicates an increased reading which might be due to reflection from the back wall of the vault. However, an undue decrease in the IC signal at larger distances as measured at CEA Valduc could not be confirmed by simulation. As possible explanation, a non-uniform neutron emission by the source remains.

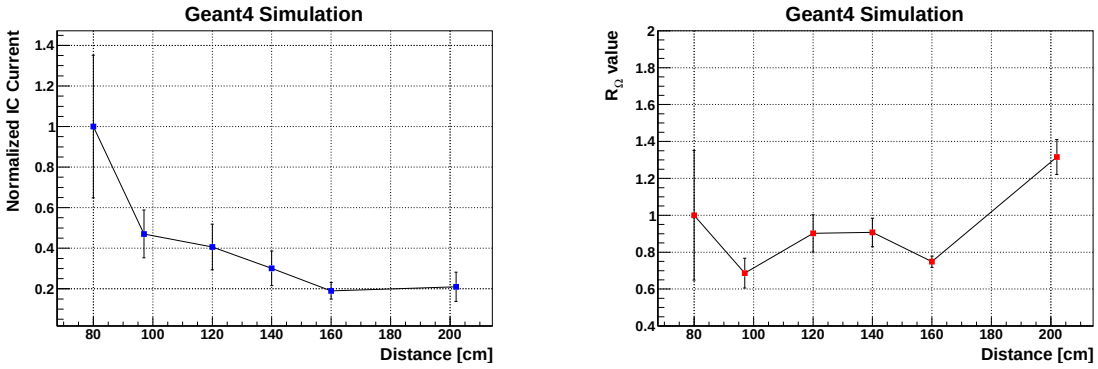

(a) The IC current normalized on the current reading at 80 cm.

(b) Normalized R_Ω value of the IC.

Figure 2.12: Investigation of the assumed wall effect in the CEA Valduc vault by Geant4 simulations. The IC current / R_Ω-value is plotted for various distances to the neutron source normalized on the current reading at 80 cm.

Conclusion

The IC was tested and calibrated at the accelerator driven neutron source SAMES at CEA Valduc. It was verified that the IC operates well in the ionization region and that the signal output remains constant over a large voltage range. The calculated response function of the IC is in good agreement with LHC simulations. At larger distances, an undue drop in the IC signal was observed that indicates a non-uniform neutron emission by the source.

2.2.5 Sensitivity Improvement

The low sensitivity of the IC for secondary particles expected at the LIPAc is one of the major issues of the LHC IC. Finding possibilities of increasing the IC sensitivity for LIPAc secondaries, i.e. mainly neutrons and some γ, was of great interest. For this purpose Geant4 simulations have been performed of the IC bombarded by neutrons and γ that presented in this section.

In these simulations, the IC filled with various different gases was irradiated by neutrons and γ of the spectrum expected from LIPAc. Neutrons and γ have been launched isotropically from a large source in 2π. This way, the IC will be bombarded uniformly from all directions and under all incident angles as it is expected to be the case during operation at the LIPAc. Simulations using Argon, Krypton and CO_2 as fill gas did not show any significant difference to the original nitrogen, neither for neutrons nor for γ.

Simulations of the IC response with boron trifluoride (BF_3) as fill gas showed a great signal increase for neutrons. Boron, in its natural occurrence consists to 80.1 % of ^{11}B and to 19.9 % of ^{10}B. ^{10}B has a very high neutron capture cross section particularly for thermal neutrons, as shown in Fig. 2.13. After the neutron capture, the excited $^{11}B^*$ nucleus decays under the emission of a high-energetic α. In this process, a total energy of 2.79 MeV is released [54].

Since a $\sim$ 1.5 MeV α has a penetration depth of less than 10 mm in nitrogen at atmospheric pressure, it is certainly stopped within the IC and deposits its entire energy inside. As the energy transfer takes place mostly via electronic collisions, a high energy

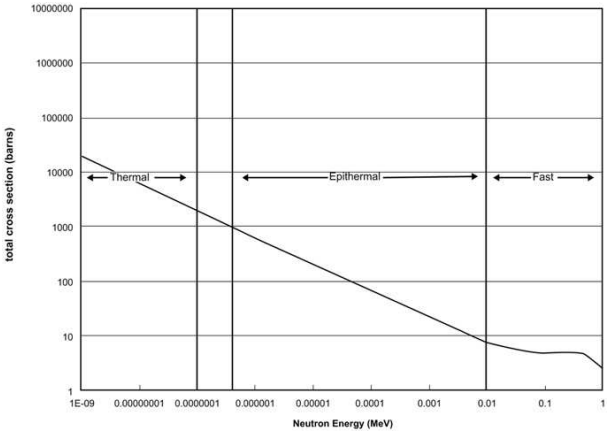

Figure 2.13: Neutron capture cross section of ^{10}B [54].

deposition results in a high ionization and thus a high IC output signal. However, the very short penetration depth of the α requires the ^{11}B* decay to take place within the fill gas itself. Otherwise, if the ^{11}B* nucleus decays in a solid, the α will be most likely absorbed by the very same material and cannot ionize the fill gas. Just placing some pieces of boron in the IC therefore not suffice, but the ^{10}B must be dissolved in the gas somehow. Possible candidates are the already mentioned boron trifluoride (BF_3) gas or diborane (B_2H_6). Geant4 simulations have been performed with BF_3 only.

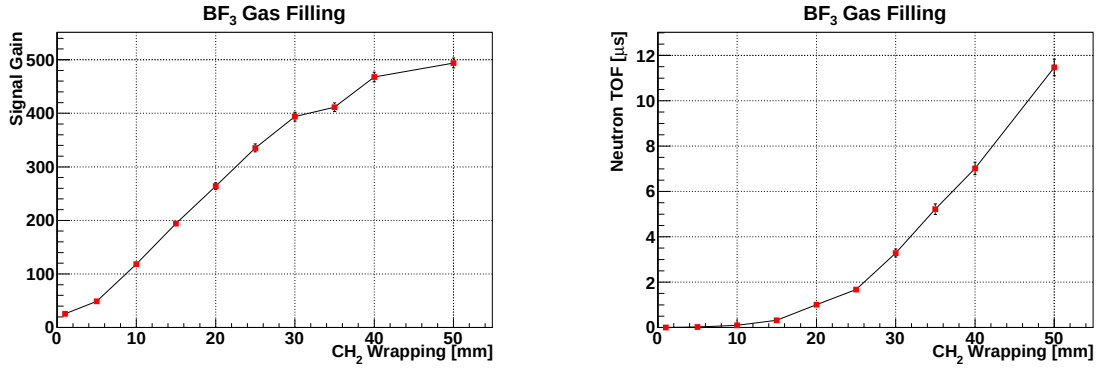

(a) Signal gain w.r.t. the IC filled with nitrogen.

(b) Neutron time of flight.

Figure 2.14: Geant4 simulation results using BF_3 as fill gas for the IC.

Since the neutron capture cross section of ^{10}B rapidly rises at lower neutron energies, the IC sensitivity can be increased even further by thermalizing the neutrons. For this purpose, the IC can be wrapped in a moderator, like CH_2. The resulting signal gain of an IC with BF_3 fill gas wrapped in a layer of CH_2 is given in Fig. 2.14(a). For the simulation, it was assumed that the boron in the BF_3 gas consists to 100 % of ^{10}B. For lower concentration, the gain will be lower as well.

When the neutrons get thermalized, they will be slowed down which in turn delays the signal of the IC. The neutron time of flight versus the width of the CH_2 wrapping is presented in Fig. 2.14(b). To cope with the MPS requirement to provide a trigger in less than 10 μs, the neutron time of flight should not exceed 2 μs to leave sufficient time for signal integration and data post-processing. This limits the possible CH_2 width to approximately 25 mm. With 25 mm of CH_2 wrapped around the IC and BF_3 as fill gas inside, its signal output can be increased by a factor of 330. For a BF_3 gas with the natural abundance of ^{10}B, this factor is reduced by approximately a factor of five, but this still grants a huge improvement.

There are, however, also some severe issues related to a boron containing fill gas. BF_3 is toxic and corrosive. As the ICs will be built in Europe and will then be shipped to Japan where the LIPAc will be commissioned, a toxic fill gas is of particular concern as it will make a safe transport to Japan more complicated and thus costly. Since BF_3 is corrosive as well, all aluminium parts in the IC will have to be replaced by stainless steel. This is well possible, but will also increase the IC price. An alternative might be diborane (B_2H_6). However, while this gas is not corrosive, it is still toxic and due to its large fraction of hydrogen also highly flammable. This makes B_2H_6 probably even a worse candidate than BF_3.

Conclusively, the IC sensitivity for neutrons can be greatly increased by using boron trifluoride (BF_3) or diborane (B_2H_6) as fill gas. However, since these gases are toxic and corrosive, or flammable respectively, they will complicate the manufacture and safe transport and operation. The use of one of these gases in the ICs is therefore currently only considered as option, if such a greatly increased sensitivity of the IC is truly required. Otherwise, the normal LHC IC filled with nitrogen will be used.

2.2.6 γ Calibration at CoCase

In addition to the neutron calibration of the IC and the Geant4 simulations of the neutron response, calibrations of the IC for γ irradiation were performed at the Cobalt Casemate (CoCase) at CEA Saclay that are presented in this section. The LHC IC was irradiated twice at CoCase, once in January 2010 and the second time in October 2011.

CoCase

The Cobalt Casemate (CoCase) at CEA Saclay is an intense γ source based on ^{60}Co decays. ^{60}Co decays by a β process to an excited ^{60}Ni* nucleus. During the transition to the Ni ground state, the nucleus releases two γ, one at 1.333 MeV and the other at 1.173 MeV [55]. These γ are used at CoCase to irradiate material samples, or the IC in our case.

CoCase was built in 1994. Since the half-life of ^{60}Co is 5.27 years [55], the source was stopped after ten years in 2003. To continue the successful operation of CoCase, a new ^{60}Co source of an activity of 629 GBq was set-up in mid 2004. To account for the attenuation of the activity of the source due to nuclear decays, it is measured frequently to provide users with proper values on the emitted radiation dose [56].

Experimental Setup

In January 2010, the IC was positioned right in front of the γ source. The general setup of the experiment can be seen on the photo presented in Fig. 2.15. The current of the IC was read over ca. 10 m of BNC cables by a picoammeter of the model Keithley 648 [57].

The source activity at CoCase in January 2010 was attenuated to 350 GBq. As each ^{60}Co decay releases two γ that are emitted isotropically in 4π, the γ flux at CoCase is $5.57{\cdot}10^7\,\gamma/s\cdot\mathrm{msr}$. The electrons emitted during the β decays have an energy of 318 keV [55] only. Electrons at such low energies have a very low response function, as can be seen in Fig. 2.5, and its contribution to the IC can therefore be neglected.

Figure 2.15: Photo of the experimental setup at CoCase. The IC (yellow) is located in front of the CoCase source (orange).

IC Response Function Measurement

During the test, the IC distance from the source as well as its orientation have been varied. Based on the IC current, we have calculated the response function of the IC for the given γ energy and angle. The resulting response function, in aC/γ, for the different angles and distances compared with results from simulation performed at CERN, presented as red stars, is given in Fig. 2.16. Apart from a factor of 1.8, the experimental results are in good agreement with the simulations performed at CERN.

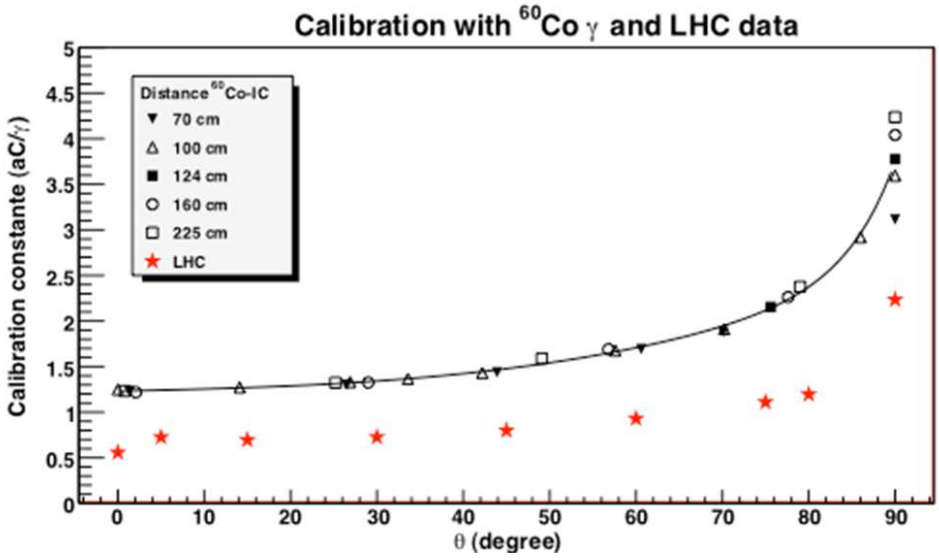

Figure 2.16: Response function of the IC for γ measured at CoCase for various angles, simulations performed at CERN are given as red stars [58].

IC Electronics

The second IC test at CoCase in October 2011 was dedicated to the choice of the proper electronics. The ICs are supposed to be used as fast trigger for the MPS,

but it is also supposed to measure 1 W/m losses. The very high sensitivity at a low bandwidth required to detect such low losses and the reasonable sensitivity at a very high bandwidth could be achieved either by integrating electronics with variable integration times, or by a fast transimpedance amplifier combined with an averaging of the data. To cover the high dynamic range ranging from a total beam loss, i.e. 1 MW within in few mm^2, down to 1 W/m, one could use a logarithmic amplifier.

Electronics Design

All electronics to be used are based on operational amplifiers. The desired properties of the different electronics are in principle just realized by changing the feedback loop of the operational amplifier. This way, linear, logarithmic or even integrating amplifiers can be designed.

An operational amplifier will generate an output voltage that causes the feedback current to annihilate the input current. For a linear amplifier that feedback consists of a simple resistor. The output voltage of such a linear amplifier is then $V_{\mathrm{Out}} = R \cdot I_{\mathrm{In}}$.

For a logarithmic amplifier, a diode is used in the feedback loop instead of the resistor. In contrast to a resistor, a diode does not have a linear current-voltage characteristic, but can be estimated according to the Shockley equation by an exponential function.

$$I_{\mathrm{D}} = I_{\mathrm{S}} \left(e^{V_{\mathrm{D}}/V_T} - 1 \right) \tag{2.3}$$

In the Shockley equation (2.3), $V_T = \frac{\mathrm{kT}}{\mathrm{e}}$ is the thermal voltage, V_{D} and I_{D} the diode voltage and current, and I_{S} the saturation current of the diode. For large diode voltages $V_{\mathrm{D}} \gg V_T$, this becomes

$$I_{\mathrm{D}} = I_{\mathrm{S}} \cdot e^{V_{\mathrm{D}}/V_T}. \tag{2.4}$$

By the same considerations as for the linear amplifier, the output voltage of a logarithmic amplifier is then given by

$$V_{\mathrm{Out}} = V_T \cdot \ln \left(\frac{I_{\mathrm{In}}}{I_{\mathrm{S}}} \right). \tag{2.5}$$

An integrating electronics can be built in a similar fashion by placing a capacitor in the feedback loop. The capacitance is defined as $C = \frac{Q}{V} \Leftrightarrow V = \frac{Q}{C}$. The output voltage of the operational amplifier has to compensate the input current $I = \dot{Q}$ and is therefore given by

$$V_{\mathrm{Out}} = \frac{1}{C} \cdot \int I(t) dt \tag{2.6}$$

All the electronics used in the tests at CoCase have been designed at IRFU (CEA Saclay) by Philippe Abbon.

Electronics Test at CoCase

The experimental setup for the IC test in October 2011 was the same as in January 2010. In contrast to the previous measurement, the IC was now placed at various positions within the vault to achieve a wide range of different output currents. In

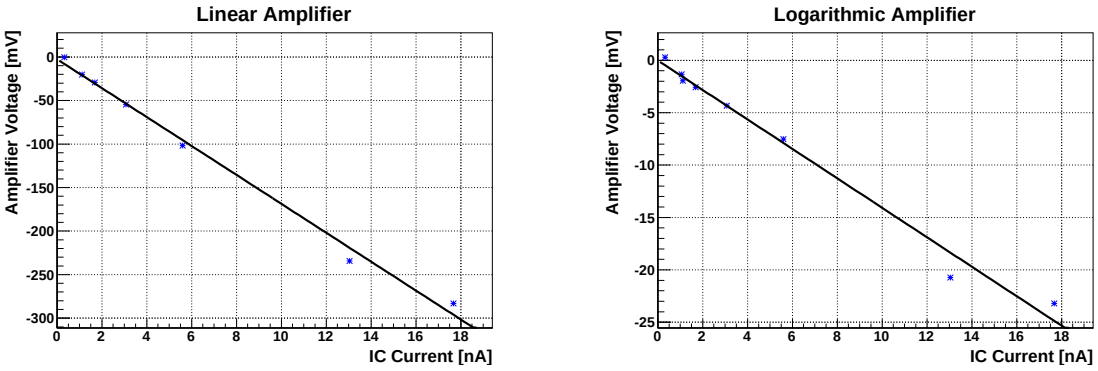

(a) Output of the linear electronics.

(b) Output of the logarithmic electronics.

Figure 2.17: Electronics voltage output versus the IC current measured by a picoammeter at CoCase.

addition to the IC current measurement by a picoammeter, in December 2010 the current was also measured by a linear, a logarithmic and an integrating electronics.

In Fig. 2.17, the measured current-voltage characteristic is given for the linear and the logarithmic amplifiers. The IC measured by the picoammeter was taken as reference.

Both appear highly linear which might be surprising for the logarithmic amplifier. However, as shown above, the "logarithmic" amplifier only grant a logarithmic voltage output for $V_D \gg V_T$, otherwise the full Shockley equation (2.3) holds. At room temperature, the thermal voltage can be calculated to be $V_T \approx 25.8\,\mathrm{mV}$, which is higher than all the voltages recorded during the measurement. This measurement is in good agreement with a test measurement performed by Ph. Abbon.

The Shockley equation (2.3) can be expressed by a complete Taylor expansion

$$I_D = I_S \left(\sum_{k=0}^{\infty} \frac{(V_D/V_T)^k}{k!} - 1 \right). \tag{2.7}$$

For $V_D \ll V_T$, a first order approximation may grant a good approximation of the full expansion and thus grants a linear correlation between current and voltage, just like an ohmic resistor. In addition, a real diode still has a certain ohmic resistance that is probably not negligible at low input currents either. In the current regime investigated in the test, a linear correlation therefore had to be expected.

The sensitivity of the integrating electronics strongly depends on the integration time and the feedback capacitor, as shown in equation (2.6). The signal output for two different feedback capacitors, $C_1 = 40\,\mathrm{pF}$ and $C_2 = 100\,\mathrm{pF}$, is shown in Fig. 2.18(a). A linear fit is performed that indicates a slope of $4.29\,\mathrm{mV}/\mu\mathrm{s}$ and $1.57\,\mathrm{mV}/\mu\mathrm{s}$ respectively. The ratio $4.29/1.57 = 2.73$ is in good agreement with the expected factor of $2.5 = C_2/C_1$.

In a second measurement, the linearity between output voltage and integration time was verified. For a constant input current, the output voltage of an integrating electronics is expected to rise linearly with the integration time, as shown ind equation (2.6). This linearity was tested for three different IC currents, $I_{IC} = 0\,\mathrm{pA}$, $I_{IC} < 1\,\mathrm{pA}$, and $I_{IC} \approx 2\,\mathrm{pA}$. The resulting data fitted linear plot is given in Fig. 2.18(b). The data points scarcely scatter around the linear fit and the zero crossing of the fit is well below 1 mV.

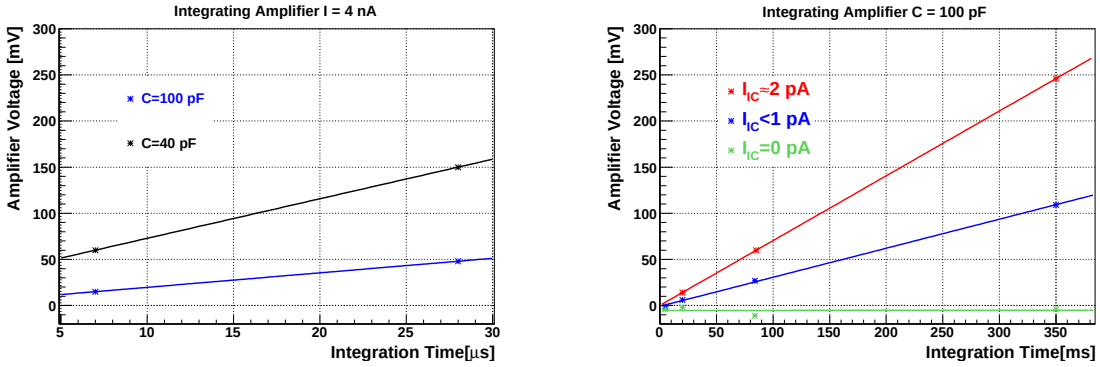

(a) Comparison of two integrating electronics with different feedback capacitors, $C = 40\,\mathrm{pF}$ and $C = 100\,\mathrm{pF}$.

(b) Comparison of three different IC currents, $I_{IC} = 0\,\mathrm{pA}$, $I_{IC} < 1\,\mathrm{pA}$, and $I_{IC} \approx 2\,\mathrm{pA}$.

Figure 2.18: Integrating amplifier output versus integration time measured by a picoammeter at CoCase.

This measurement indicates a good linearity between the output signal and the integrating time. As the high dynamic range required for a beam loss monitoring system could be achieved by varying the integration time, this linearity is of utmost importance. In addition, one can nicely see that the electronics are capable of measuring currents well below the 2 pA that are expected from 1 W/m losses at LIPAc within reasonable integration time of below one second.

2.2.7 Interface to MPS / Control Display

One can therefore conclude that this kind of electronics is well capable of detecting 1 W/m losses, if it is above the background noise fluctuations in the vault. The integrator is thus a good choice to monitor 1 W/m losses. However, it appears not feasible to implement an integrating time short enough to trigger the MPS within less than 10 μs. As the linear electronics does not provide a sufficiently large dynamic range, it is currently foreseen to use logarithmic pre-amplifiers.

In a second step, the voltage output of the pre-amplifier will be duplicated by a unity gain buffer amplifier and both signals are then post-processed by VME cards. One of the cards will serve the MPS including only passive elements, like comparators. The other card will contain an integrating electronics to provide a signal for a display in the control room. A sketch of a possible solution of such an electronics is presented in Fig. 2.19. The detailed design of this electronics is still under investigation.

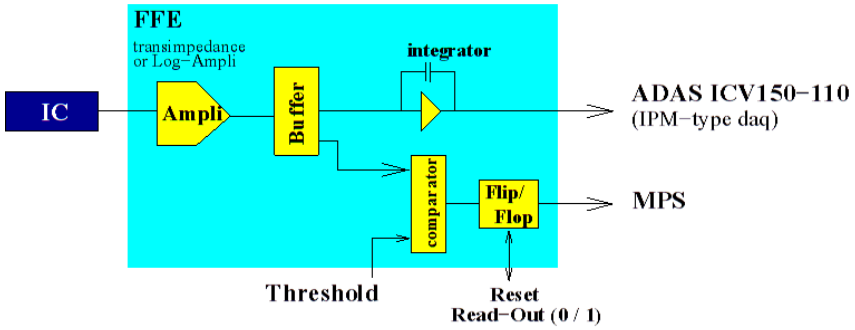

Figure 2.19: Sketch of a possible solution for the MPS electronics.

Control Room Display

In the VME card for the operator, the signal will be accumulated and averaged over a sufficiently long time span to safely read the IC with a precision better than 2 pA. According to the test measurements performed with integrating cards at CoCase, see Fig. 2.18(b), this should be feasible within less than one second. The limit of 2 pA allows to resolve beam losses that exceed the 1 W/m limit all over the accelerator.

The issue of the high radiation background from the beam dump still remains which is several orders of magnitude above the limit of 1 W/m. However, it is assumed that once the beam is stable, this background will be virtually constant with fluctuations well below the PPS limit [44]. Under such conditions, this offset can be easily subtracted. As the background radiation varies for different positions within the vault, each IC must be calibrated separately.

Machine Protection System

For the MPS, a trigger is required to stop the beam rapidly in case of fatal beam loss. In contrast to circular high-power machines like the LHC, no sophisticated dumping system is required, since the beam is already directed onto the beam dump anyway.

The signal coming from the ICs will be compared with a series of thresholds in the VME card. Every time one of these thresholds is exceeded, it is foreseen to write an entry into a circular buffer and possibly send an advance warning to the operator. If the final threshold is exceeded, a signal will be send directly to the MPS stopping the beam. This will also stop the circular buffer that can be used for a postmortem analysis.

2.2.8 Detailed Design Review

In June 2012, the Detailed Design Review for the LIPAc instrumentation was held at CIEMAT Madrid. During this review, all diagnostics elements have been presented to an international expert committee and their development stage was evaluated. In a preliminary feedback, the expert committee acknowledged that the ICs are well suitable to protect the accelerator and can be used to trigger the MPS. However, they expressed their doubt that the ICs might not be able to measure 1 W/m losses. In addition, the committee pointed out the importance of low-noise cables and remarked a possible noise background due to X-rays emitted from the cavities.

We agree that we cannot measure the absolute values of 1 W/m losses. However, we have demonstrated that the ICs have a sufficiently high resolution to measure 1 W/m losses and that we thus measure the evolution of those losses, if the fluctuations of the background are sufficiently low.

We have already foreseen to use coaxial low-noise and see our decision conformed by this recommendation. It is also foreseen to measure the response of the ICs to cavity X-rays. During a SPIRAL2 cavity test, we will place one IC next to a cavity and measure the IC signal.

2.2.9 Conclusion

The LHC Ionization Chambers (ICs) have proven reliable and robust beam loss monitors. They were found able to measure fast losses and thereby serve as trigger for the Machine Protection System (MPS) as well as to measure very low losses to monitor the losses down to 1 W/m.

A LHC IC has been calibrated for γ at the Cobalt Casemate (CoCase) at CEA Saclay and for neutrons on the SAMES accelerator at CEA Valduc. In spite of the fact that a read-out electronics will have to measure IC signal currents below 2 pA to cope with PPS requirements, it was shown that this can be achieved by integrating the signal over less than one second. Even though boronated gases improve the sensitivity of the IC for neutrons significantly, boron trifluoride (BF_3) and diborane (B_2H_6) are both toxic and corrosive or flammable respectively. As these complicate a safe transport to Japan as well as a safe operation on the accelerator, we prefer to abstain from this solution.

For the electronics, it is foreseen to use logarithmic amplifiers, since it is not feasible to design integrating electronics with integration times short enough to trigger the Machine Protection System (MPS) within 10 μs. The electronics will include a circular buffer that allows for a postmortem analysis of the beam losses in case of a beam abord due to fatal losses.

2.3 Diamond Detectors

While Ionization Chambers (ICs) prove to be very reliable high-bandwidth beam loss monitors they cannot provide any localized loss information on the level of the SRF linac. For this purpose it is foreseen to place diamond detectors within the cryostat to measure even lowest losses and to thereby tune the accelerator. This type of beam loss monitor is therefore also called μ-loss detector.

Diamond detectors are in principle solid state Ionization Chamber (IC). The fill gas in a common IC is replaced by diamond as solid state material. This grants the advantage that such detectors can be placed in the cryogenic environments and that they are much smaller than gaseous detectors, since a solid is much dense than a gas.

The test and characterization of diamond detectors as μ-loss detectors, presented in this section, were performed together with my supervisor Jacques Marroncle (CEA Saclay). My main tasks were the data analysis of the data acquired at CEA Bruyères-le-Châtel and I also contributed to the experimental tests, their preparation, execution and analysis.

The properties of diamond detectors and the tests performed to evaluate their capability to be used as μ-loss detector in the cryostat are discussed in this section.

2.3.1 Diamond Properties

The advantages of diamond detectors over ICs, their size and their ability to operate in cryogenic environments, apply also for other solid state detectors, like silicium or germanium detectors. The differences of the three semi conducting detectors and the reasons why diamonds have been chosen are presented in this sections.

The diamond structure is equivalent to a face-centered cubic (FCC) lattice, with a motif of two atoms at each lattice point: one at (0,0,0) and the other at $(\frac{1}{4},\frac{1}{4},\frac{1}{4})$, where the coordinates are fractions along the cube sides. This is equivalent to two interpenetrating FCC lattices, offset from one another along a body diagonal by one-quarter of its length. The cubic unit cell of normal diamond has a side length a = 3.567 Å. Fig. 2.20 illustrates the unit cell of a diamond crystal.

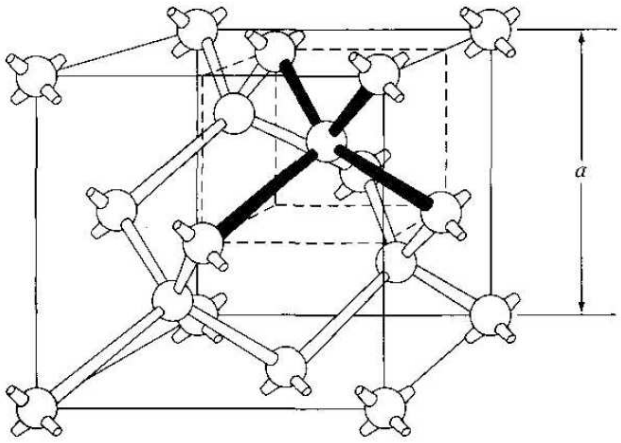

Figure 2.20: The unit cell of diamond, where a = 3.567 Å is the cubic lattice constant [59].

The closest carbon atoms covalent bond length is equal to one-quarter of the cubic body diagonal, that is 1.54 Å. The unit cell contains the equivalent of eight C atoms, and the atomic number density is therefore $1.76 \cdot 10^{23}\mathrm{cm}^{-3}$. It is interesting to mention that this is the highest atomic density of any matter on earth. Multiplying the atomic density by the average atomic mass of the C atom results in a theoretical mass density for diamond of $3.52\,\mathrm{g/cm}^3$. A unique feature of carbon atoms in the diamond lattice is the strength of their bonds. That is the reason for the relatively high energy necessary to displace an atom from its site under particle irradiation. A concise summary of diamond properties in comparison with other common semiconductors and the resulting effect on detectors based on diamonds is given in Table 2.2 [59].

Table 2.2: Comparison of different semiconductor properties and the resulting property of diamond detectors w.r.t. the other semiconductors [59].

	Diamond	Si	Ge	Diamond Detector Property
Band gap [eV]	5.48	1.12	0.67	high T operation
Dielectric strength [V/cm]	10^7	$3 \cdot 10^5$	10^5	high voltage operation
Intrinsic resistivity[Ω/cm]	$\gg 10^{11}$	$2.3 \cdot 10^5$	50	low leakage current
Electron mobility [cm^2/Vs]	1900 - 4500	1350	3900	fast signal
Hole mobility [cm^2/Vs]	1800 - 3500	480	1900	fast signal
Electron lifetime [s]	$10^{-10} - 10^{-6}$	$> 10^{-3}$	$> 10^{-3}$	full charge collection
Hole lifetime [s]	$10^{-10} - 10^{-6}$	10^{-3}	$2 \cdot 10^{-3}$	full charge collection
Density [$\mathrm{g/cm}^3$]	3.52	2.33	5.33	
Dielectric constant	5.72	11.9	16	low capacitance
Displacement energy [eV]	43	13 - 20	28	radiation hardness
Thermal conductivity [W/m/K]	2000	150	60.2	heat dissipation
Energy to create e-h [eV]	11.6 - 16	3.62	2.96	lower signal

It is purpose of the μ-loss detectors to detect lowest particle losses. The μ-loss detector thus needs a good sensitivity to secondary particles resulting from beam losses and a low sensitivity to background particles. Secondary particles from losses are mostly high-energetic neutrons and γ ($\sim$1 - 10 MeV). In the LIPAc vault, the major background component will be thermalized neutrons, in the cryostat, however, it is to be expected that x-rays from the super-conductive cavities are dominant. Due to its rather low atomic number, diamond is less sensitive to photoelectric emission of electrons and thus less sensitive in the low energy range than silicon. In addition, diamonds have a better sensitivity for neutrons, since they can transfer a greater recoil on the light carbon atoms. Both effects lead to a an increased signal to noise ratio of diamonds compared to silicon detectors.

Due to the very high radiation level in the LIPAc vault, the radiation hardness of the detectors in use is a great concern as well. Since the displacement energy of diamond is higher than of any other semiconductor listed in Table 2.2, diamonds are considered the material best suited for the harsh environment of LIPAc.

Modern diamonds are grown by Chemical Vapor Deposition (CVD). This technique allows to grow single crystalline CVD (sCVD) diamonds of several mm in size. Polycrystalline ones are commonly referred to polycrystalline CVDs (pCVDs). pCVDs consist of several crystals that have grown into one another. This technique allows for

much larger diamonds, however it also changes their physical properties. The border between two crystals can trap charge carriers which greatly reduces electron and hole life time and in turn reduces the effective charge collection.

2.3.2 Principle of Operation

Like any other semi-conducting detector, diamonds as well work in principle like solid state ionization chambers. As described in more detail in section 2.2.1, a simple IC consists of two parallel plates. When a charged primary particle passes through, it will ionize the gas in between the plates. By applying proper voltages on the plates, one can collect the ionization products and read the ionization current. Fig. 2.21 illustrates the principle of operation of a diamond detector.

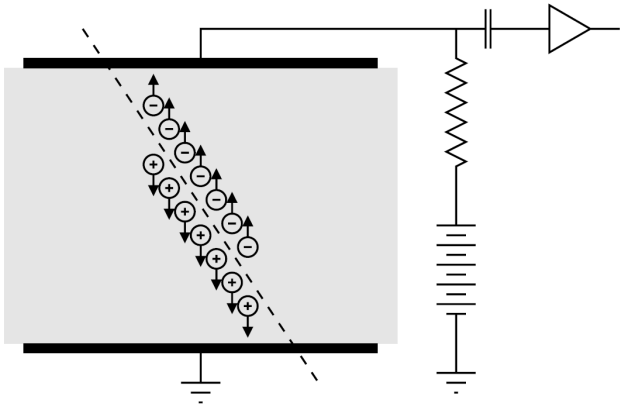

Figure 2.21: An ionizing particle passes through a diamond detector. It generates electron-hole pairs that are extracted by an electric field applied over electrodes on top and on bottom [60].

In a diamond detector, the gap between the two plates is not filled by a gas, but by diamond. Accordingly, a diamond detector is much smaller. Diamond detectors commonly have a size of a few mm^2 times a few 100 μm in depth. On each side of such a flat sCVD diamond plate, a thin metal layer is deposited that is used as electrode. In spite of the very little effective volume of a diamond detector, it still has a significant response signal as a solid has a much higher density than a gas which results in an increased energy deposition per volume. This allows for very small particle detectors that have due to their size a good position resolution, response time and a sensitivity that even enables single particle counting.

While molecules or atoms will have to be ionized to generate charge carriers in a gas, in a solid semiconductor it suffices to lift an electron from the valence band to the conducting band. This can be triggered by a primary particle hitting the detector, but it could also be due to thermal excitation. Silicon detectors are therefore sometimes used at cryogenic temperatures to decrease this thermal noise. The higher band gap of diamond between the valence band and the conducting band reduces the detector signal, since more energy must be deposited in the crystal for the same amount of charge carriers to be created, but it also decreases the thermal noise to virtually nothing, since thermal energies do not suffice to generate electron-hole pairs.

The high dielectric strength, presented in table 2.2, allows to apply several 100 V over a distance of few 100 μm only. This results in a huge electric field which in turn allows for a very fast and efficient charge collection.

Ramo's Theorem

As the distance between the charge carriers and the electrode is much smaller than the actual electrode size, mirror charges must be taken into account for the output current calculation. This can be done handily by Ramo's theorem describing the current induced in a metal by an approaching charged particle. Ramo's theorem states

$$I = E_v \cdot q \cdot v, \qquad [61] \tag{2.8}$$

with I being the induced current, q the charge and v the velocity of the particle, and E_v the weighted electric field. E_v is defined as the electric field at the position of the particle under the following condition:

- charged particle is removed,
- electrode potential is set to unity,
- all other conductors in proximity are grounded. [61]

The weighted potential is therefore an auxiliary field that does not exist in reality, that only depends on the detector geometry, and that must not be mistaken with the actual electric field applied on the electrodes.

Ramo's theorem indicates that a current is induced in the electrodes as soon as the charge carriers start moving. It is not required for them to actually reach the electrodes and to deposit their charge there. This effect is of particular importance for polycrystalline diamonds where charge carriers can be trapped at the borders of the single crystals.

While the charge carriers drift towards the electrodes, the current induced by a single electron / hole is approximately constant. This becomes clear considering Ramo's theorem, equation (2.8). The induced current is proportional to the velocity and the weighted field. The velocity of all ions and electrons is given by their mobility and the electric field applied. Since the electric field is constant in a plate capacitor, the velocities of all ions and electrons respectively are the same. Since the same argument holds for the weighted field, the current induced by all electrons / holes is constant over the drift.

Signal Shape

Particles passing through the diamond, like high-energy protons, will generate electron-hole pairs all along their way that in turn drift towards the electrodes where they are absorbed. The diamond detector current therefore rises rapidly while the electron-hole pairs are created and then drops linearly, as the charge carriers are absorbed by the electrodes. The resulting signal has a triangular shape.

Particles with a very low penetration depth, like α's or heavy ions, will generate electron-hole pairs along their trajectories as well, but since their trajectories are very short, they generate charge carriers basically only on the surface of the diamond very close the one of the electrodes. Either electrons or holes are absorbed virtually immediately, the oppositely charged charge carriers, however, will have to drift over the entire diamond detector depth before being absorbed. Over this drift, they will

induce a constant current. The resulting output signal of the diamond detector in this case has a rectangular shape.

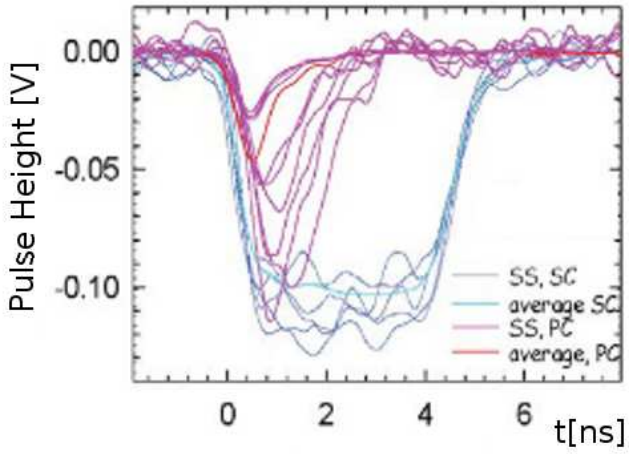

Figure 2.22: Diamond detector signal shapes for the collection of 4.78 MeV α particles with a penetration depth of $\sim 11\,\mu$m of single crystalline CVD (blue) and polycrystalline CVD diamonds (magenta) [59]

In reality, the signal shapes will, of course, be superimposed by a finite rise / fall time and possibly an exponential decay due to the finite lifetime of the electrons / holes. Such an exponential decay will in fact dominate the signal shape for pCVD diamonds as most charge carriers are trapped at the borders between single crystals. A signal comparison for sCVD and pCVD generated by 4.78 MeV α is given in Fig. 2.22 [59]. In blue, one can nicely see the rectangular signal shape of the sCVD. In magenta, the signal of the pCVD rises in a similar fashion, however, it decays exponentially.

For the LIPAc beam loss monitors, mostly neutrons and γ will be measured. While neutrons will not be stopped in the diamond, they do deposit energy mostly in rare collisions with the carbon atoms of the diamond crystal. As this results in a very localized energy deposition the diamond signal shape due to a neutron impact rather resembles the one of an α.

2.3.3 Positioning of the Diamond Detectors

The beam loss monitors based on diamond detectors for the LIPAc, will be located in the cryostat of the SRF linac exclusively. It is foreseen to place three diamond detectors at each solenoid. The assembly of a diamond μ-loss detector triplet is illustrated in Fig. 2.23.

The μ-loss detectors are arranged uniformly around the beam pipe with a 120° gap in between. This provides not only redundancy and thus an increased reliability, but also provides some angular information on the beam loss.

They are mounted within metal boxes providing the electronics connections to the diamond and as well acts as Faraday cage to shield the diamond from external noise. The diamond detectors are set on the level of the solenoid as losses are expected to be highest here due to the large beam diameter.

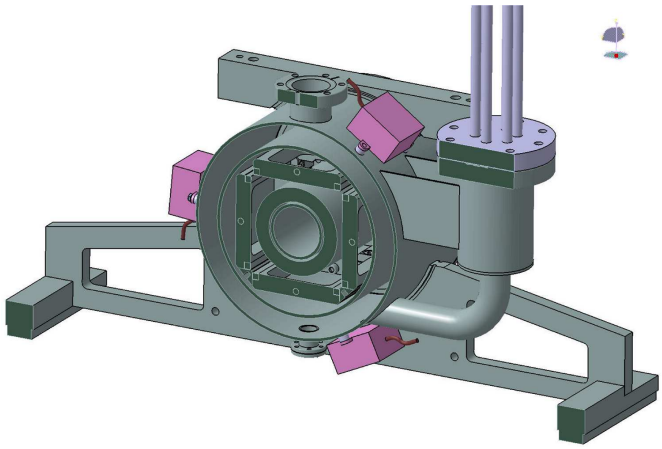

Figure 2.23: Assembly of the three μ-loss detectors (pink) around the beam pipe, by courtesy of Philippe Hardy (CEA Saclay)

2.3.4 Electronics

There are two basic groups that electronics for diamond detectors can be subdivided into:

- current amplifiers and
- charge amplifiers.

Current amplifiers grant a very fast signal with rise and fall times of commonly only a few 100 ps [62]. This allows, for instance, to measure particle losses with a time resolution sufficiently high to resolve the accelerating bunch structure of the beam; the IFMIF and LIPAc will have pulses every 5.7 ns that could be easily resolved by such electronics.

While charge amplifiers commonly have signal rise and fall of ≈ 10 ns, they provide a very good sensitivity and signal to noise ratio. This is particularly desirable for applications like ours, where a feeble amount of energy is deposited in the diamond by the incident particle and the particle flux is so low that single particle counting is required [63].

Diamond Operation during the Tests

For the μ-loss detectors, single crystalline diamonds are used. They have a size of $4 \times 4 \times 0.5\,\mathrm{mm}^3$ and a voltage of 300 V is commonly applied. This results in an electric extraction field within the diamond of 6 kV/cm. The active surface of the diamond is given by the metalized region which is $\sim 9\,\mathrm{mm}^2$. The diamond is mounted within a little aluminum box that supports the diamond as well as ensures a proper contact of the high voltage (HV) and output signal connections. The output current is amplified by a front-end charge amplifier that allowed for single particle counting.

The voltage output of the front-end electronics is recorded by an oscilloscope. If the signal exceeds a certain threshold, the oscilloscope adds an entry for the measured voltage in a histogram. This threshold determines the cut-off energy under which no events will be recorded any more. The histogram, giving a spectrum of the energy

deposited in the diamond, can be extracted from the oscilloscope after the measurement. To allow further data post-processing, it is also possible to save the entire signal shape for each event.

2.3.5 Tests with a ^{252}Cf Source

The properties of diamond detectors are well-understood and extensive studies on their response for various particles have been performed [59, 60, 64, 65, 66, 67, 68, 69, 70]. However, diamond detectors have not yet been tested in cryogenic environments before. It was therefore decided to perform such a test by placing the diamond in liquid nitrogen (LN_2), i.e. at 77 K, and in liquid helium (LHe), i.e. 4.2 K. Both tests have been performed at CEA Saclay.

Californium (^{252}Cf) was used as neutron source to irradiate the diamond. ^{252}Cf has two decay channels, with a probability of 97 %, it will decay to Curium (^{248}Cm) by emitting a $\sim$ 6 MeV α particle, and with 3 %, it will perform a spontanuous fission in which 3.77 neutrons are in average released. γ emitted during these decays have commonly energies $\lesssim$ 150 keV and are thus below the energy cut-off of the diamond electronics. The lifetime of ^{248}Cm is with 348,000 a much longer than the 2.647 a of ^{252}Cf. The contribution of ^{248}Cm to the radiation spectrum should therefore be negligible. For these reasons, ^{252}Cf was considered a good choice as neutron source to test diamonds in cryogenic environments [71].

Liquid Nitrogen

For the test, the CVD diamond detector was placed inside a Dewar filled with liquid nitrogen (LN_2). The ^{252}Cf source was positioned outside the Dewar, but as close to the diamond as possible. A photo of the experimental setup showing the Dewar filled with LN_2 and the aluminum box that contains the diamond detector is given in Fig. 2.24.

Figure 2.24: Photo of the CVD diamond test in liquid nitrogen with a ^{252}Cf source outside the Dewar.

To compare the performance of the diamond at cryogenic and ambient temperatures, spectra of the diamond with and without LN_2 in the Dewar were recorded as well as a background measurement with neither source nor LN_2. The recorded spectra are

given in Fig. 2.25(a). No significant deviation of the two spectra is visible. The count rate in LN_2 is slightly reduced w.r.t. to the measurement at ambient temperature, but this could be due to absorption in the LN_2. In the spectra one can nicely see the edge of the energy cut-off at around Analog-to-Digital Converter (ADC) channel number 50.

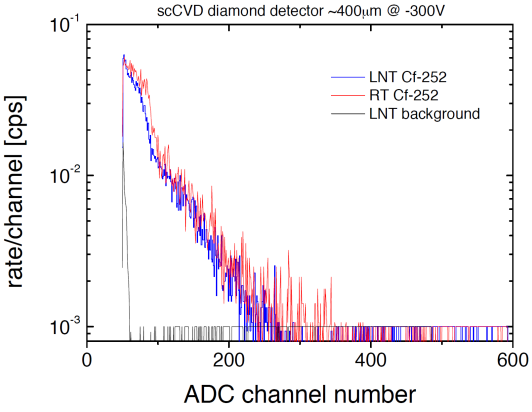

(a) Spectra at ambient temperature (red) and in liquid nitrogen (blue) with source and the background measured without source shown in black.

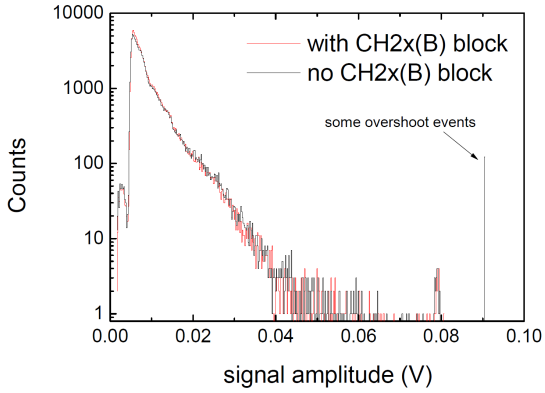

(b) Spectra of a ^{252}Cf source at ambient temperature with and without a block of CH_2 acting as neutron moderator.

Figure 2.25: Spectra of the energy deposited by radiation of a ^{252}Cf source in the diamond, by courtesy of Michał Pomorski (CEA Saclay).

It remains to evaluate, what kind of radiation is really emitted by the ^{252}Cf source and if our assumption of a neutron source is valid or not. For this purpose, the radiation of the ^{252}Cf source was measured by the diamond detector at ambient temperature with and without a block of CH_2 between the source and the detector. As neutron-proton collisions have a large cross section, materials with a high hydrogen density, like H_2O or CH_2, are commonly used as neutron moderators. If we detect mainly neutrons, it is expected to measure different spectra with and without the moderator, since the neutron energy changes.

The diamond spectra with and without the CH_2 block are presented in Fig. 2.25(b). As there is virtually no difference to be seen, one must conclude that we measured not neutrons, but probably mostly γ. The prior reasoning why ^{252}Cf should be a good neutron source appears to be not valid for an old source where fission products contribute significantly to the total emitted radiation.

Nonetheless, one can conclude that diamonds can be operated at cryogenic temperatures down to 77 K.

Liquid Helium

As the μ-loss detectors will be placed in the cryostat of the LIPAc, the test at 77 K in liquid nitrogen does not suffice, but the diamonds must be tested in liquid helium (LHe) as well. The experimental setup for LHe is more complicated than for LN_2 as the Dewar must be kept close to prevent a rapid evaporation of the helium. A photo of the experimental setup is shown in Fig. 2.26.

In Fig. 2.26, one can see the white Dewar filled with LHe in the foreground and in the background, one can see the oscilloscope connected to the diamond inside the Dewar

Figure 2.26: Photo of the experimental setup of the diamond test in LHe. The white Dewar filled with LHe is in the foreground.

by signal cables. Apart from the Dewar, the measurement was performed in the same way as the measurement in LN_2. The recorded spectrum of the energy deposited in the diamond is given in Fig. 2.27. The energy scale on the abscissa corresponds to the energy deposited in the diamond, not the particle energy.

As already observed during the test in LN_2, the count rate is reduced, but the spectrum shape remains unchanged. It can hence be concluded, that diamond detectors can be operated at cryogenic temperatures at 77 K as well as at 4.2 K.

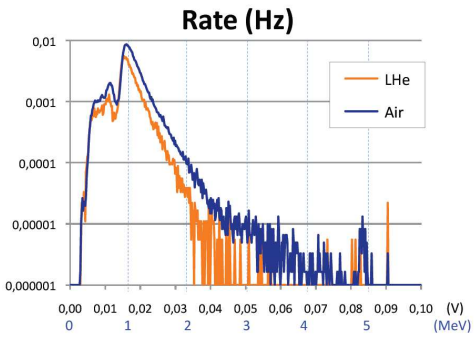

(a) Spectra of the energy deposited in the diamond in LHe and at ambient temperature, by courtesy of Michał Pomorski (CEA Saclay).

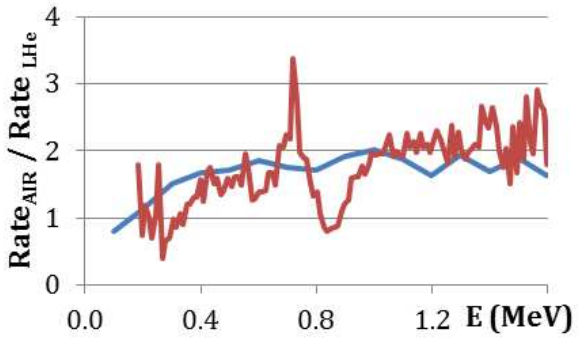

(b) Experimental (red) and simulated (blue) ratio of the count rates in LHe and at ambient temperature, by courtesy of A. Marchix (CEA Saclay).

Figure 2.27: Comparison of the diamond tests under irradiation of a ^{252}Cf source in LHe and at ambient temperature.

2.3.6 Calibration at CEA Bruyères-le-Châtel

The tests in liquid nitrogen and liquid helium have demonstrated that diamond detectors can be used in cryogenic environments. The second goal, to test the diamond response for neutrons was not achieved. It was therefore decided to measure the response for neutrons and its basic properties under neutron irradiation at the accelerator driven neutron source at CEA Bruyères-le-Châtel (B3).

CEA Bruyères-le-Châtel

The CEA center at Bruyères-le-Châtel is located in the south of Paris and belongs like Valduc to the sites dedicated to military applications.

Figure 2.28: Photo of the Van de Graaff accelerator at CEA Bruyères-le-Châtel [72].

The accelerator driven neutron source works similarly as the SAMES accelerator in Valduc. The Van de Graaff electrostatic accelerator is able to accelerate a particle beam of up to 200 μA to various energies ranging from 400 keV up to 4 MeV. A fast chopper allows for pulse lengths down to 10 ns. By an additional magnetic bunch compression, pulses of 1 ns can be realized. The very short pulses allow for accurate time of flight (TOF) measurements.

A photo of the Van de Graaff accelerator is shown in Fig. 2.28. On the photo one can see the large accelerating structure of the Van de Graaff in the background. A transport line, splitting in two, brings the accelerated particles from the accelerator to the various experimental stations [72].

The accelerated particles are shot on a target where neutrons are produced. By choosing proper projectile type and energy as well as the proper target material, virtually mono-energetic neutrons of various energies can be generated. Some examples of typical combinations are given in table 2.3.

Table 2.3: Typical reaction that can be triggered by the Van de Graaff accelerator at B3 [72].

Reaction	Neutron Energy [MeV]	Projectile Energy [MeV]
p + Li $\rightarrow$ ^{7}Be + n	$0.03 < E_n < 0.70$	$1.9 < E_p < 2.4$
p + T $\rightarrow$ ^{3}He + n	$0.7 < E_n < 3.0$	$1.3 < E_p < 4.0$
D + D $\rightarrow$ ^{3}He + n	$4.0 < E_n < 7.0$	$1.0 < E_D < 4.0$
D + T $\rightarrow$ ^{4}He + n	$15.0 < E_n < 20.7$	$0.5 < E_D < 4.0$

We have taken data at accelerator settings that correspond to neutron energies of 200 keV, 600 keV, 750 keV, 1.2 MeV, 2.1 MeV, 3.65 MeV, 6 MeV and 16 MeV.

Experimental Setup

In contrast to the experimental setup during the cryogenic tests at CEA Saclay, at CEA Bruyères-le-Châtel the test takes place in an accelerator vault which is a radiation protected area. The experiment had therefore to be controlled remotely. The preferred solution would have been to place only the diamond in the vault and to connect the electronics by a long cables. This has the advantage that the electronics do not get irradiated. However, due to the very low capacitance of the diamond detector, such a solution is not feasible. The capacitance of the long cables ($\sim 100\,\mathrm{pF/m}$) is larger than the capacitance of the detector ($\sim 2\,\mathrm{pF}$) which results in severe signal distortions. It was therefore decided to place everything, electronics, power supplies and the oscilloscope, in the accelerator vault and handle the oscilloscope from remote distance via an Ethernet connection.

To avoid any unnecessary background signal, the oscilloscope receives a trigger from the accelerator. This trigger opens a gate that is just long enough that all neutrons emitted from the source can reach the detector in time. Using a logical AND function between this gate and the detector signal input, random events that clearly cannot be correlated with the pulsed source are suppressed.

Another complication arises from γ that will be emitted during the nuclear reactions as well. It is foreseen to perform a neutron - γ discrimination by a time of flight (TOF) measurement. To allow for a proper discrimination, the TOF difference for neutrons and γ must be larger than the neutron and γ pulse width. By increasing the distance between the neutron source and the diamond, the TOF difference can be increased which allows for a better event discrimination, but it also reduces the count rate as neutrons and γ are emitted in 4π.

As START time for the TOF, the trigger coming from the accelerator was used. The front-end electronics provide for such applications a fast output channel that was used to determine the arrival time of the particles in the diamond and thus the STOP time of the TOF. All three signals traces were saved on the oscilloscope hard drive for the data analysis in binary format for a faster data acquisition.

Data Analysis

The objective of the data analysis is to discriminate neutrons from γ by comparing their TOF. Event with a TOF shorter than a predefined threshold can be correlated with γ, events with a TOF longer than this threshold with neutrons. A ROOT [73] script was written to read the saved data files and to perform the analysis automatically.

The accelerator trigger and the timing signal are not synchronized. The reference time that the START and STOP times are based on is, in general, not the same. It depends on various parameters like cable lengths used, but remains constant during a measurement. What is here called TOF is therefore not an absolute TOF value, but only correct down to a additive constant. It is therefore well possible to have even negative TOFs in this sense.

In a 2D histogram, where the number of events are plotted versus the energy deposited in the diamond and the TOF of the particles, the timing threshold to dis-

Table 2.4: Results of the data analysis of the B3 measurements. The table includes the total number of neutrons and their percentage, the number of γ and their percentage, the acquisition time, the accelerator current, and the distance between source and diamond.

E_n [MeV]	N_γ	N_n	T_{acq} [min]	I_{acc} [nA]	Distance[mm]
0.6	439 (9.0 %)	4421 (91.0 %)	24	600	345
0.75	1237 (9.6 %)	11617 (90.4 %)	37	700	300
1.2	518 (3.7 %)	13329 (96.3 %)	69	900	425
2.1	885 (6.2 %)	13312 (93.8 %)	52	800	425
3.6	289 (6.0 %)	4512 (94.0 %)	102	—	450
6.0	8134 (64.0 %)	4580 (36.0 %)	77	1200	810
16.0	1700 (26.2 %)	4785 (73.8 %)	105	550	795

criminate neutrons from γ can be nicely seen. An example of such a histogram for a neutron energy of 2.1 MeV with a cut performed at 25 ns is shown in Fig. 2.29(a).

Once the discrimination threshold is known, the spectrum for the energy deposited in the diamond by all particles, neutrons and γ, can be deconvolved in a γ and a neutron spectrum. An example for the neutron spectrum at 2.1 MeV as well is presented in Fig. 2.29(b).

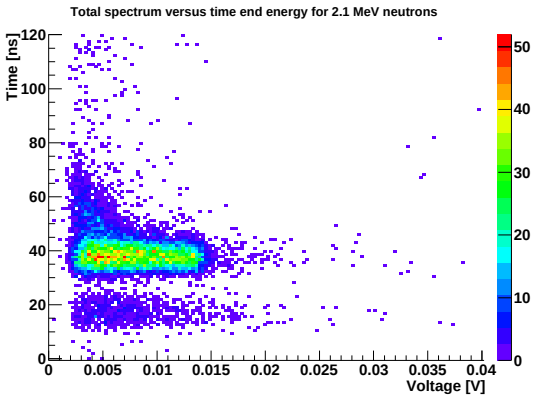

(a) Number of events plotted versus the energy deposited in the diamond and the TOF in a 2D histogram.

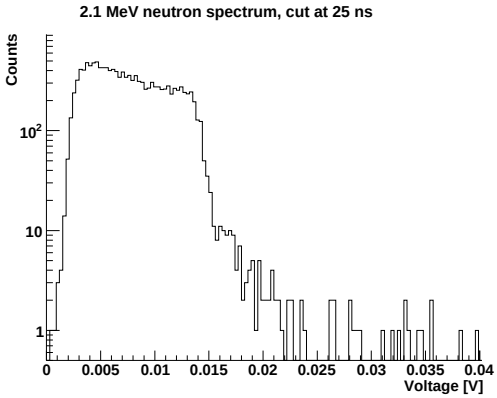

(b) Example of the spectrum of the energy deposited in a diamond by 2.1 MeV neutrons.

Figure 2.29: Results of the B3 data analysis.

Table 2.4 contains the count rates for all measurements at the different neutron energies. The table includes the total number of neutrons and their percentage, the number of γ and their percentage, the acquisition time, the accelerator current, and the distance between source and diamond. These information was of interest for the operators of the accelerator driven neutron source as well, since such a measurement has not yet been done before. The accelerator current at 3.6 MeV was by accident not recorded.

The γ and neutron spectra of the measurements are given in Appendix A.

Comparison with Simulation

To compare the experimental results with simulation, Anthony Marchix (CEA Saclay) has simulated the energy deposition of neutrons of the given energy in a diamond crystal. Both, the experimental neutron spectra as well as the results of the simulation are presented in Fig. 2.30.

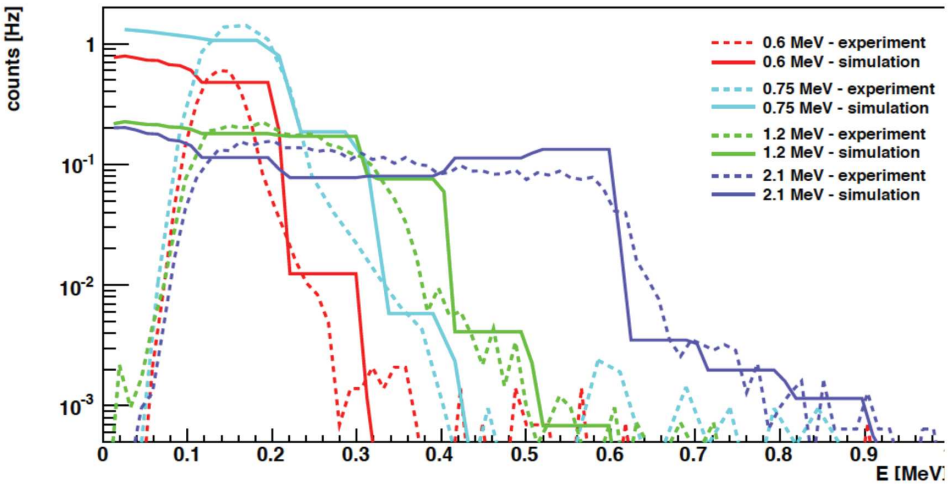

Figure 2.30: Comparison of the energy loss spectra of neutrons of various energies measured at B3 with Simulation.

The simulation is in good agreement with the measurement. There are some deviations in the count rates for the different energies, but the general shape of the spectra matches well. One can conclude that the measurements as B3 have well confirmed simulation results and can be used as a benchmark for future simulations.

2.3.7 Exptected Count Rates

The neutron and γ spectra expected for 1 W/m losses on the level of the SRF linac have been simulated by Anthony Marchix (CEA Saclay) considering cavity and solenoid material. For a diamond of 0.5 mm thickness and an active surface of 9.2 mm^2, he has also simulated the energy deposition in the diamond due to neutrons and γ. The spectra are presented in Fig. 2.31.

Based on these data, one can estimate the expected count rate due to 1 W/m losses. The expected count rates of the diamond detector for various detection thresholds are presented in Table 2.5.

Table 2.5: Expected count rates of the diamond detectors in the cryostat of the SRF linac.

Threshold [keV]	70	100	200	300	400	500	600	700	800
Neutrons (kHz)	3.7	3.2	1.8	1.3	1.1	0.9	0.7	0.6	0.5
γ (kHz)	1.2	1.1	0.9	0.8	0.7	0.6	0.6	0.5	0.5

During our tests at CEA Saclay and B3, we commonly had a detection threshold of $\sim$50 keV. Since these tests have been performed under ideal conditions, it appears

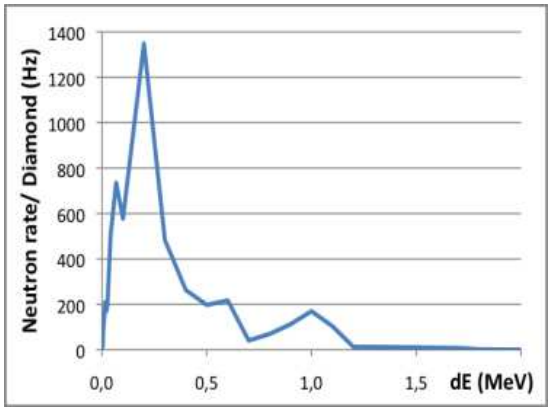

(a) Energy deposition in the diamond due to neutrons

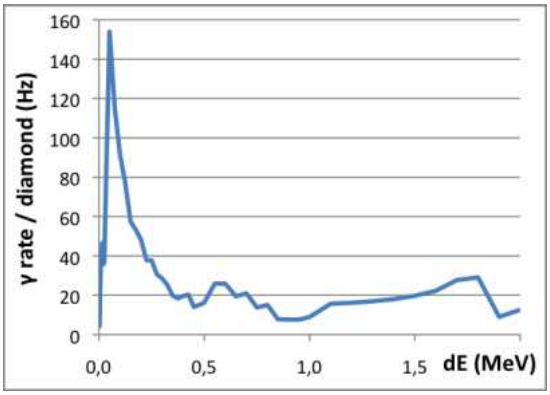

(b) Energy deposition in the diamond due to γ.

Figure 2.31: Simulated results of the energy deposition in the diamond detector due to 1 W/m losses, by courtesy of Anthony Marchix (CEA Saclay).

reasonable to assume a threshold of $\sim$200 keV for LIPAc. At this threshold, we expect a count rate of 2.7 kHz. The background due to radiation from the beam dump at a threshold of 200 keV is expected to be $<$0.6 kHz. This value is based on the neutron and γ flux outside the cryostat. A simulation of the radiation in the cryostat itself has not yet been performed, but is foreseen. To evaluate the contribution of X-rays coming from the SRF-cavities, the diamond detectors will be tested during the test of the super-conducting cavities for SPIRAL2.

During commissioning, it is foreseen to operate the LIPAc at low duty cycle. At a duty cycle of 10^{-4}, this provides only 16 counts per minute, but during the commissioning losses are expected to be far higher than the 1 W/m limit as well.

2.3.8 Detailed Design Review

The diamond detectors to be used as μ-loss monitors were also presented during the Detailed Design Review in June 2012. The preliminary remarks of the expert committee were, that it is a very interesting and novel development. However, the X-ray sensitivity and the life time in cryogenic environments has never been tested and is questionable. The experts also expressed their concern that the diamonds might be swamped by radiation from the beam dump, similarly as for the ICs. They also proposed to install a backup system in the case that they do not operate satisfactorily.

As for the ICs, we also intend to place diamonds close to a SPIRAL2 cavity during a test to measure the X-ray sensitivity of the diamond. Due to the close proximity of the diamonds to the beam pipe and the rather long distance towards the beam dump, we expect the radiation from the beam dump to be insignificant. Further simulations will, however, be performed as soon as reliable simulations of the background radiation is available. If the diamonds do not work, the ICs will have to help out. A third kind of beam loss monitor is not foreseen.

2.3.9 Conclusion

Diamonds have been tested on their neutron and γ response at CEA Saclay and at CEA Bruyères-le-Châtel. At CEA Saclay, it was demonstrated that diamond detectors

work well at cryogenic temperatures, at 77 K in liquid nitrogen as well as at 4.2 K in LHe.

At the accelerator based neutron source at CEA Bruyères-le-Châtel, the diamond detectors were calibrated for neutrons of various energies. A comparison with simulations indicates a good agreement and provides confidence in simulation results.

The count rates of the diamond detectors have been estimated for LIPAc. For nominal beam conditions, count rates of several kHz are expected. During commissioning the count rate is greatly reduced at low duty cycle, but even at a duty cycle of 10^{-4}, 1 W/m losses can still be reasonably monitored, if the signal is integrated over a minute.

Chapter 3

SEM-Grids

La mesure des profils transverses du faisceau en mode pulsé est l'objet de ce chapitre. Une grande sensibilité est requise pour de tels moniteurs puisque la longueur du pulse faisceau peut être aussi faible que 50 μs. Une des solutions est d'intercepter une faible proportion du faisceau tout en veillant à définir la plage de fonctionnement pour ne pas brûler ou vaporiser les composants actifs du détecteur.

Pour cette raison, les moniteurs envisagés sont des Secondary Electron Emission grids (SEM-grids) basés sur l'émission d'électrons secondaires lorsque une faible proportion des deutons du faisceau est interceptée par les fils de ces moniteurs. Les principes et le fonctionnement de ces moniteurs seront d'abord décrits. Ensuite, une étude thermique permettant de définir les diamètres des fils selon la taille du faisceau, donc de l'emplacement du moniteur, sera présentée. Une argumentation donnera les limites de ces études en comparant par exemple les courants créés par émission secondaire et ceux qui apparaissent à haute température par émission thermique (ou thermo-ionique). Des hypothèses simplificatrices de calculs seront commentées, comme l'absence du traitement du pic de Bragg, la connaissance ou la méconnaissance du coefficient d'émissivité ϵ incitant à la prudence et donc à prendre des marges de sécurité dans la définition des fils de tungstène.

Une table résumant les températures maximales en fonction de la taille du faisceau permettra de rester lors de l'exploitation de LIPAc, dans les possibilités de fonctionnement des SEM grids, évitant par exemple de casser un fil sous l'effet d'une densité de puissance déposée trop importante.

Pour terminer, les 2 SEM-grids qui prendront place dans la Diagnostic Plate (DP) et en amont de l'arrêt faisceau seront décrits brièvement.

3.1 Motivation

It was discussed in section 1.2.1 that the beam is fully described by its six dimensional phase space distribution, three dimensions for the spatial coordinates and another three for the momentum distribution. Profile monitors, like SEM-grids or Ionization Profile Monitors (IPMs), measure the projection of the spatial distribution of the beam. One commonly differentiates between longitudinal and transverse profile monitors. The profile monitors presented in this thesis measure the transverse beam profile. If not further specified, profiles are hence considered to be transverse only.

A profile monitor does not provide the full phase space distribution, but at least a spatial projection. Projections of the momentum distributions can be acquired by profile monitors using additional techniques. During the particle drift along the accelerator, their spatial distribution will change. This change in the spatial distribution depends in a first approximation only on the momentum distribution. The profile evolution can then be described by the transport matrices. For a given set of transport matrices, one can calculate the momentum distribution based on the corresponding spatial distributions.

To determine the emittance, one therefore needs to measure profiles with different transport matrices. One way is to measure profiles at different positions along the accelerator. If only one profiler is available, one can also vary the transport matrix of the accelerator in front of this profile monitor. For this purpose, the focal strength of quadrupole magnets are commonly varied [45].

Beam profile monitors do not only grant the probably most descriptive measure of the accelerator beam which allows for an easy accelerator operation and tuning, but they also provide the means to measure the beam emittance, which is of great interest to understand the beam dynamics.

The work on the SEM, presented in this section, was performed by my supervisor Jacques Marroncle (CEA Saclay) and myself. My main task was the simulations of the energy deposition in the different wire materials.

3.2 Requirements

As LIPAc is designed as a prototype accelerator for IFMIF, the commissioning will take up most of its time in operation. During the commissioning the beam intensity might vary over six orders of magnitude, from 1 mA at a duty cycle of 10^{-4} up to 125 mA in cw mode. If the diagnostics is supposed to provide profile measurements with a dynamic range of no more than 8 bits, it would already require a profiler with a dynamic range of about $1{:}10^8$. Since profilers with such dynamic ranges are virtually impossible to design for LIPAc conditions, it was decided to build two profilers instead, one for the low-intensity and one for the high-intensity regime.

SEM grids are interceptive profilers that can be driven in the beam line, if required. When passing through, beam particles deposit a certain fraction of their energy in the wires. The SEM grid heats up and may eventually melt. This is particularly challenging for low-energetic particles since they may be stopped by just some μm of matter. Since the energy deposited in the wires increases linearly with the beam intensity, SEM grids can only be safely used at low beam intensities.

The SEM grid material and design must be chosen to withstand the huge heat load due to the accelerator beam and the highest beam intensities must be determined in which the SEM grids are still safely operational.

3.3 Principle of Operation

Secondary Electron Emission (SEM) grids belong to the family of wire scanners. An entire harp of wires can be driven into the beam to measure its profile. Thus, SEM grids are inteceptive profilers. When passing through the wire, beam particles release electrons from the wire. This results in a current that can be measured to deduce the beam profile.

The lowest beam intensity at which a SEM grid can still be operated is determined by the noise of the read-out electronics. A SEM grid cannot provide any reasonable beam profile any more, if the current induced in the SEM grid wires is of the same order as the electronics noise. In the ideal case, this would be the thermal noise. At the rather high intensities at LIPAc, this is not an issue, and we can assume to have always a sufficiently high signal.

As the beam current increases, the wire heats up. In the mean time, there are, in principle, three basic cooling processes:

- cooling by radiation
- cooling by conduction over the wire
- cooling by conduction over the residual gas

In contrast to what we observe under atmospheric pressure, the cooling over the residual gas is fully negligible, since the residual gas pressure is so low. The dominant process actually is cooling by radiation. The power emitted by thermal radiation is given by the Stefan-Boltzmann law:

$$P = \epsilon \sigma A T^4 \tag{3.1}$$

For a continuous beam, the wire temperature will reach an equilibrium state after some time when the power deposition of the beam equals the power dissipated by thermal radiation.

For a pulsed beam, however, the temperature rises in the pulse duration and drops rapidly afterwards. When the next pulse approaches, the wire will possibly not have fully cooled and will be heated accordingly to a higher peak temperature. According to equation (3.1), the power dissipation by thermal radiation is greatly increased, and the wire cools down faster. After a few bunches of constant power deposition, the peak temperature reaches an equilibrium.

This equilibrium peak temperature limits the use of SEM grids at high intensities. If this temperature rises too high, the wire can melt which, of course, destroys the profiler. But already at lower temperatures, above 2000 K, thermionic electron emission may occur which can affect the profile measurement [45].

3.4 Secondary Electron Emission

When a charged projectile collides with a metal surface, it may release electrons. This process is called Secondary Electron Emission (SEM). In principle, two different mechanisms contribute to the emission of secondary electrons, one is generally referred to as potential emission, the other as kinetic emission. Other effects, like secondary emission due to excited valence electrons [74] or due to decaying surface or volume plasmons [75] are considered of minor importance and will not be discussed.

Potential Emission

When an ion hits the metal surface, it can be neutralized, if the neutralization energy of the ion exceeds the work function of the metal. However, if the neutralization energy of the ion exceeds twice the metal work function, an additional electron may be released from the metal in analogy to the Auger effect. This process is commonly referred to as potential electron emission and is independent of the incident particle energy. Kishinevsky has derived a simple formula to calculate the contribution of the secondary electron emission due to potential emission by a theoretical model. His formula is given in equation (3.2), with γ being the secondary electron yield, E_i the ionization energy of the ion, Φ the work function and ϵ_F the Fermi energy of the metal [76].

$$\gamma = \frac{0.2(0.8E_i - 2\Phi)}{\epsilon_F} \tag{3.2}$$

Baragiola et al. have confirmed this equation experimentally. On a series of different SEM yield measurements, they have performed a fit and the empirical equation to be [77]

$$\gamma = 0.032(0.78E_i - 2\Phi) \tag{3.3}$$

Given the Fermi energy for aluminum of 11.6 eV [78], this is in good agreement with the equation predicted by Kishinevsky.

Kinetic Emission

The second process considers ionization by the primary particle, but also ionization by secondary electrons, recoils or photons. It is commonly called kinetic electron emission. This kind of process is strongly energy dependent and governs the electron emission at higher energies. Sternglass [79] has derived a theory for fast ion impact that well describes the kinematic electron emission.

When a fast ion passes through a material, it will interact with the electrons in the material and will thereby lose energy. One can assume two discrete processes, distant collision where the ion transfers only a small amount of energy to the electrons and thereby creates slow secondary electrons, and close collision where a significant amount of energy is transferred and fast electrons are created, so-called δ-ray electrons. This process is illustrated in Fig. 3.1(a).

The number of slow secondaries generated directly by the ion and originating in a certain unit layer dx at depth x, $n_{se}^{(1)}(v_i, x)$, is then given by the average energy loss of the ion going into the generation of slow secondaries per unit length, $\left\langle \frac{dE_i}{dx} \right\rangle^{(1)}$,

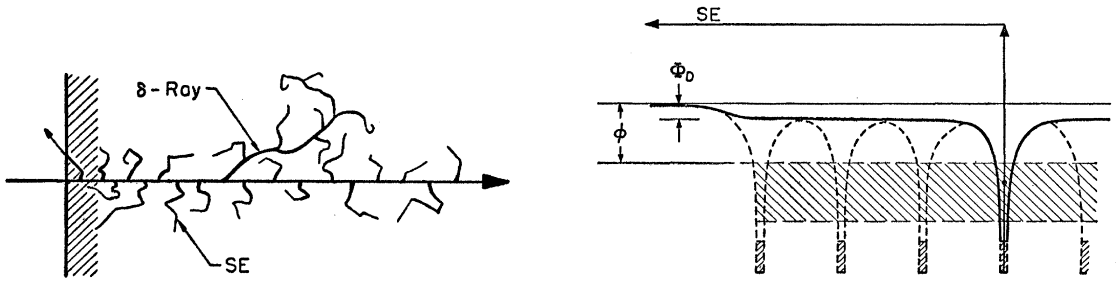

(a) Formation of secondary electrons (SE) and high-energetic δ-rays by fast ions.

(b) Schematic diagram to illustrate the formation of a fast SE in the interior of a metal and its escape across the surface potential barrier.

Figure 3.1: Figures illustrating the generation of secondary electrons [79].

divided by the mean energy loss suffered by the ion per slow secondary formed, $\bar{E}_0$. With v_i being the initial ion velocity, one receives

$$n_{se}^{(1)}(v_i, x) = \frac{1}{\bar{E}_0} \left\langle \frac{dE_i}{dx} \right\rangle^{(1)} . \tag{3.4}$$

For the total secondary emission yield, one still has to add the contribution of the δ-rays that in turn have a sufficiently high energy to generate further slow secondaries. Assuming that the energy loss of the ion is equally distributed on slow electron and δ-ray production leads to

$$n_{se}(v_i, x) = \frac{1}{2\bar{E}_0} \left\langle \frac{dE_i}{dx} \right\rangle [1 + f(v_i, x)] , \tag{3.5}$$

with $f(v_i, x)$ being the factor that represents the fraction of δ-ray energies available for the creation of slow secondaries in higher order processes.

Equation (3.5) gives the total number of secondary electrons released in a certain unit layer at depth x. For the total number of secondary electrons emitted by the metal surface under ion bombardment, it remains to multiply this value with the probability that the emitted electron can escape, and to integrate this product over the entire penetration depth of the ion. For the escape probability, Sternglass assumes an exponentially decaying density. The path that an electron has to take in order to escape the material is illustrated in Fig. 3.1(b). As the escape probability of the secondaries rapidly decreases at larger penetration depths, the Secondary Electron Emission can be considered to be surface effect only [79].

Thermionic Emission

At high temperatures, electrons can be released from metal surfaces as it is the case for hot cathodes. This effect is commonly called thermionic electron emission. It was studied in detail and the thermionic current can be properly described by the Richardson-Dushman-equation (3.6) which has been found to be in good agreement with experimental measurements: [80, 81]

$$j = AT^2 e^{-\Phi/kT} \qquad \text{with} A = \frac{4\pi m k^2 e}{h^3} = 1.20 \times 10^6 \,\mathrm{Am^{-2}K^{-2}} \tag{3.6}$$

Since the thermionic emission does not rise linearly with the beam current, it can result in profile distortions. For tungsten, the work function Φ is 4.5 eV [81]. In conservative estimation , we assume a constant wire temperature of 2000 K over 20 mm. The current on the central SEM-grid wire due to thermionic emission is then calculated to be $\sim 28\,\mu$A for a wire of 20 μm diameter, and $\sim 140\,\mu$A for a wire of 100 μm diameter.

These values can be compared with the expected signals from secondary electron emission. The number of secondary electrons per incident ion and unit layer emitted from a single surface is given by the Sternglass equation (3.5). We assume that only such electrons are released that are created within 1 nm of the surface and that 25 eV is required per released electron in average. We also neglect the effect of δ-electrons, i.e. we assume $f(v_i, x) = 0$. Under these assumptions, equation (3.5) becomes

$$I_{SEM} = \frac{d}{2\bar{E}_0} \left\langle \frac{dE_i}{dx} \right\rangle \Delta I_{Beam}, \tag{3.7}$$

with ΔI_{Beam} being the fraction of the beam hitting the SEM-grid wire and $d = 1\,$nm being the width of the layer from which electrons can escape.

The energy loss $\left\langle \frac{dE_i}{dx} \right\rangle$ of a deuteron in tungsten is calculated by SRIM to be 59 eV/nm at 9 MeV and 82 eV/nm at 5 MeV. For a 125 mA beam at 9 MeV and an RMS beam size of 4.5 mm, the current due to secondary electrons on a 20 μm thick wire will be 520 μA. At small wire diameters, the passes through the wire and electrons are emitted twice, once when the beam particles enter and once when they leave the wire.

At larger wire diameters, beam particles can be stopped in the wire. Secondary electrons can thus only be emitted on a single surface, but the beam current is deposited in the wire as well. Assuming that all beam particles are stopped inside a 100 μm wire, the previously considered beam will generate a current of 2.4 mA. Both values are significantly larger than the current due to thermionic emission at 2000 K. No significant profile distortion are thus to be expected up to wire temperatures of 2000 K.

3.5 Positioning of the SEM-Grids

For LIPAc, two SEM-grids are foreseen. One will be mounted on the D-plate where the beam pipe diameter is 100 mm, the other on the HEBT upstream to the beam dump to ensure a proper power distribution on the beam dump where the beam pipe diameter is 150 mm.

A major issue for all the diagnostics on the HEBT is the very limited space available to mount diagnostics. Originally, 250 mm have been foreseen to mount three different types of profilers, a BIF, an IPM and a SEM-grid. By optimizing the HEBT assembly, an additional 110.5 mm could be liberated. The profilers must still be designed in a very compact fashion to mount all of them in the available 360.5 mm.

3.6 Thermal Simulations

One of the major demands on the SEM-grid development, apart from the limited space available, is to reduce the maximum temperature of the wires. For this pur-

pose, materials with high heat capacity, high melting point and good heat conductivity are required. Good candidates for the wire material are commonly tungsten or carbon. In the frame of this thesis, the energy loss of 5 MeV and 9 MeV deuterons in carbon as well as in tungsten were simulated in SRIM (Stopping and Range of Ions in Matter) [52] and the resulting wire temperature is calculated.

SRIM

SRIM is a software that calculates the energy loss of particles in matter based on the Bethe-Bloch-equation (3.8) [45].

$$-\frac{dE}{dx} = 4\pi N_A r_e^2 m_e c^2 \frac{Z_t}{A_t} \rho_t \frac{Z_p^2}{\beta^2} \left[\ln \frac{2m_e c^2 \gamma^2 \beta^2}{I} - \beta^2 \right] \tag{3.8}$$

In the equation, the index t denotes target quantities, while p stands for projectile. In this form, the Bethe-Bloch equation does not include any density or radiative corrections.

SRIM allows for energy loss calculations of fast ions in matter. The lower energy threshold of the incident ions is given by a few keV. Projectile mass, energy and direction can be chosen freely. For the target, an extensive material library is available that can, however, be adjusted to individual needs. The graphical user interface of SRIM is given in Fig. 3.2.

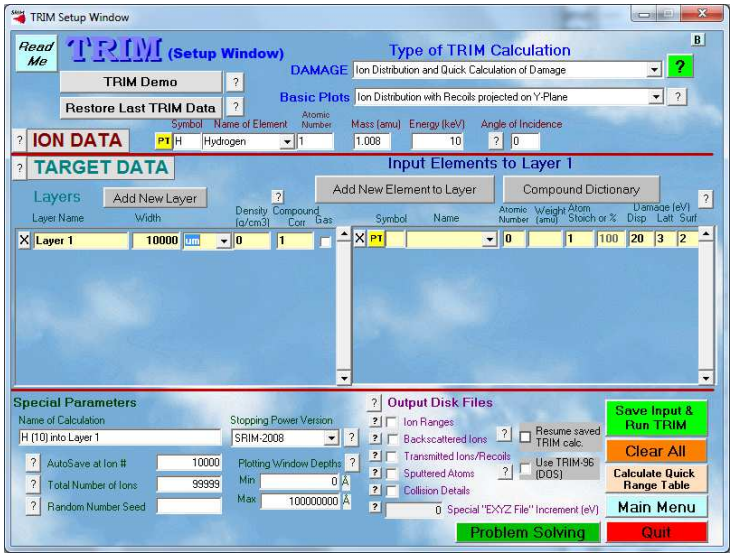

Figure 3.2: Graphical user interface of the SRIM simulation software [52].

The user can define a certain number of particles that will be tracked while they penetrate the target material. After the simulations, various information like energy loss distribution in electronic or nuclear collisions, energy distribution of recoil atoms, damage rate in the material, etc. are automatically calculated and can be extracted for further treatment.

Thermal Model

Using the energy deposition calculated in SRIM, one can determine the SEM-grid wire temperature. To estimate the particle trajectory inside the wire, the curvature of the

round wire is neglected and a rectangular cross section is assumed as a simplification, as illustrated in Fig. 3.3(a). For the wire depth, one can then use the full wire diameter in a conservative approximation. This implies to assume a wire cross section of a significantly larger surface than the wires actually have. A more realistic approach is to assume a rectangular wire that has the same width and a cross section of the same surface. The resulting depth can then be calculated to be $d = \pi/4 \varnothing_{wire}$. The power deposited in the wires according to the two models is thus given by

$$\Delta P_{mean} = \dot{N} \int_0^d \frac{dE}{dx}^{SRIM} dx$$

$$\Delta P_{Tot} = \dot{N} \int_0^{\varnothing} \frac{dE}{dx}^{SRIM} dx$$

with $\dot{N}$ being the number of beam particles hitting the wire per second. The integration effectively averages the energy deposition along the wire diameter. Localized effects like the Bragg-peak are thus not taken into account.

If thermal conduction is neglected, one can easily calculate the heat flow into the wire by adding up the power deposited in the wire by the beam, given above, and subtracting the power dissipated by radiation according the Stefan-Boltzman law (3.1). From the heat flow, one can then determine the wire temperature. An example of the resulting temperature of a wire hit by several beam pulses is given in Fig. 3.3(b). One can nicely see that the wire reaches an equilibrium peak temperature after a few pulses.

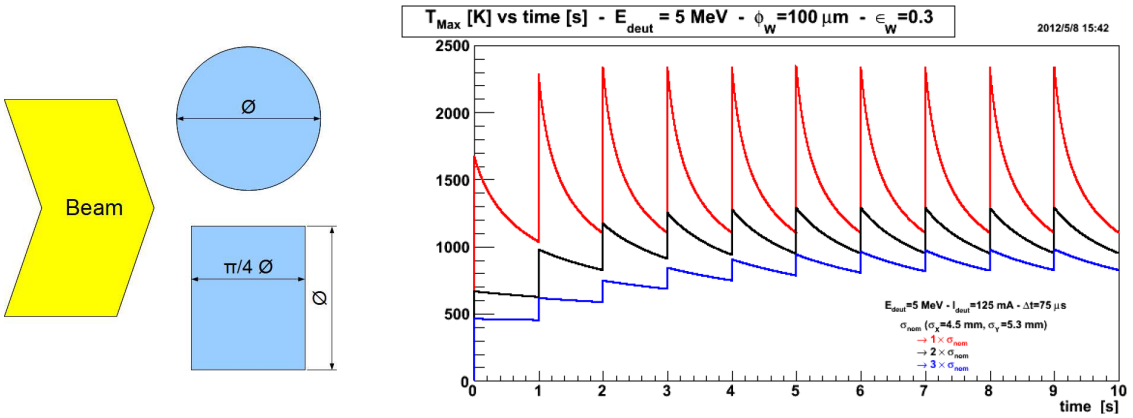

(a) Approximation of a rectangular wire cross section of the proper surface.

(b) Example of a temperature evolution for several beam pulses. After a few pulses the peak temperature stabilizes.

Figure 3.3: Illustrations of thermal model.

The emissivity ϵ in the Stefan-Boltzmann law remains unknown in this equation and is assumed to be 0.3 for tungsten in the following calculations. Decreasing this factor to 0.1 can increase determined temperatures by more than 200 K. The heat capacity of tungsten, required to convert the heat deposited in the wire into a temperature, has a strong temperature dependency, which is, however, well known.

For the beam on the D-plate, we assume a Gaussian shape with $\sigma_x = 4.5\,\text{mm}$ and $\sigma_y = 5.3\,\text{mm}$. The highest wire temperature will be reached in the center of the

Gaussian. Since we neglect any kind of heat conduction in our model, we only need to consider the center of the Gaussian distribution which simplifies the calculation and thus allows to easily estimate maximum wire temperatures.

The results of this model have been cross-checked with the FEM-solver Ansys [82] by Sandrine Cazaux (CEA Saclay). The temperatures calculated based on our simplified model are slightly higher than the temperatures calculated by Ansys, as it was expected since we neglected heat conduction.

Tungsten Wires

The maximum temperature of a tungsten wire was calculated twice, once by such an average (denoted as ΔP_{mean}) and once by using the whole wire diameter (denoted as ΔP_{Tot}). The wire temperatures versus the wire diameter are presented in Fig. 3.4 for both models. The calculation was performed for a 9 MeV (5 MeV) deuteron beam of 125 mA, $\sigma_x = 4.5$ mm and $\sigma_y = 5.3$ mm, and a pulse length of 50 μs.

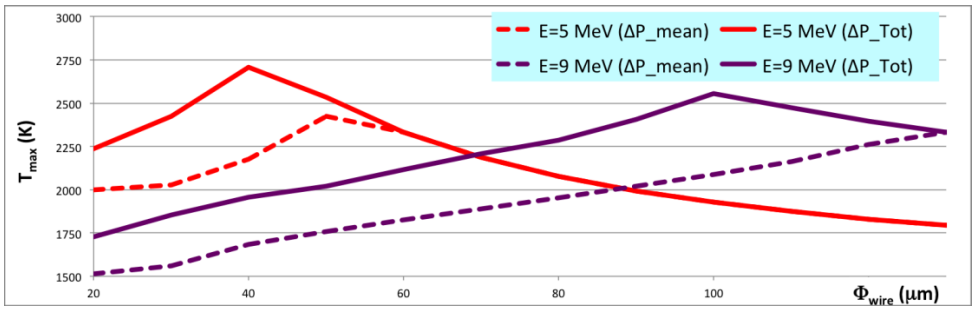

Figure 3.4: The maximum wire temperature versus the wire diameter at E = 9 MeV (5 MeV) I = 125 mA Δt = 50 μs.

The penetration depth of 9 MeV (5 MeV) deuterons in tungsten is 103 μm (44 μm). The beam particles are thus able to traverse very thin wires, but are absorbed by thicker wires which leads to a very high power deposition and thus a high temperature. At even higher wire diameters the maximum wire decreases again as the power is deposited in more material.

Table 3.1: SEM-grid wire temperatures on the HEBT at nominal beam conditions with $\sigma_0^x = 11.5$ mm & $\sigma_0^y = 8.5$ mm beam size for different pulse lengths. The wire diameter (100 μm) is chosen to be the effective wire size, the values in brackets are for the average diameters $d = \pi \varnothing_{wire}/4$

$\varnothing_W$ [μm]	E [MeV]	σ/σ_0	T_{max}[K] for various Δt [μs]				
			50	60	75	100	150
100	9	1.0	1321 (1143)	1415 (1217)	1546 (1319)	1745 (1472)	2101 (1742)

The SEM-grid on the D-plate must be able to cope with 5 MeV as well as 9 MeV beams. As one can see in Fig. 3.4, the optimum wire diameter for both energies is either 20 μm or $\sim$70 μm. 20 μm wires have, however, the advantage that the beam is not stopped in the wire and that the Bragg peak, neglected in this calculation, cannot result in any hot spots on the wire.

It is thus foreseen to use 20 μm for the D-plate SEM-grid and 100 μm wires for the HEBT grid where the wire temperature is much lower due to the larger beam size. The peak temperatures calculated for nominal beam settings are presented in Table 3.1 for the HEBT SEM-grid and in Table 3.2 for the D-plate SEM-grid.

On the D-plate, the beam is much narrower than on the HEBT which results in a greater heat deposition on the wires. If the thermal stress is too high at the nominal beam size, it is possible to expand it to distribute the beam power over a larger surface and thereby reduce the heat load of the wires. In Table 3.2, the nominal beam is exemplarily expanded by 25 % and 50 %.

Table 3.2: SEM-grid wire temperatures on the D-plate at nominal beam conditions with $\sigma_0^x = 4.5\,\text{mm}$ & $\sigma_0^y = 5.3\,\text{mm}$ beam size for different pulse lengths. The effective wire is chosen to be the wire diameter, the values in brackets are for the average diameters $d = \pi \varnothing_{wire}/4$

$\varnothing_W$ [μm]	E [MeV]	σ/σ_0	T_{max}[K] for various Δt [μs]				
			50	60	75	100	150
20	5	1.0	2235 (2001)				
		1.25	1701 (1535)	1898 (1706)	2178 (1951)		
		1.5	1375 (1261)	1520 (1388)	1729 (1571)	2059 (1861)	
	9	1.0	1729 (1513)	1929 (1679)	2215 (1920)		
		1.25	1345 (1194)	1485 (1310)	1687 (1478)	2007 (1744)	
		1.5	1119 (1006)	1224 (1093)	1374 (1218)	1613 (1416)	2058 (1787)

Carbon Wires

A simulation was performed for carbon wires of 30 μm diameter in a 5 MeV deuteron beam. At a pulse length of 200 μs the wire temperature rises to 1255 °C and even at a pulse length of 300 μs the temperature is just risen to 1700 °C. It is evident that carbon wires are superior to tungsten wires in terms of heating. However, carbon wires must not be used in superconducting accelerators.

In contrast to tungsten, carbon has no melting point, but it sublimates. If that happens, some dust of carbon particles of variable size might be emitted. If these particles get into a superconducting cavity, they can cause it to quench and thereby shut down the entire accelerator. For safety reasons, we therefore have to abstain from carbon wires and will have to use tungsten in spite of its inferior heat performance.

3.7 Design

The SEM-grids will be built based on the design of the SEM-grids of SPIRAL 2, an accelerator project currently under construction at Ganil (Grand accélérateur national d'ions lourds). Some adjustments will have to be performed to adapt the grids to the needs of LIPAc. However, the number of wires per plane, 47, will remain unchanged to allow for the use the electronics of SPIRAL 2 as well.

HEBT SEM-grid

The beam pipe on the HEBT has a diameter of 150 mm. Based on the thermal simulations it was decided to use tungsten wires with a diameter of 100 μm. For the SEM-grid on the HEBT, it was decided to have wires of variable spacing, with a smaller distance between the wires in the central region and a larger distance in the halo, to achieve a good resolution in the center of the profile while covering a wide active range nonetheless. The spacing foreseen is:

- 13 wires at 2.0 mm spacing
- 12 wires at 2.5 mm spacing
- 12 wires at 3.0 mm spacing
- 10 wires at 4.5 mm spacing

This results in total of 47 wires that are spread over 137 mm.

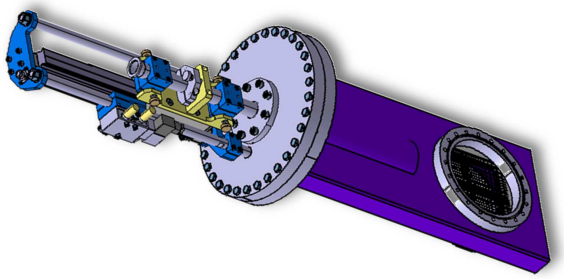

Figure 3.5: Design drawing of the SEM-grid for the HEBT. Design was done by Henry Przybilski (CEA Saclay).

Since space is limited on the HEBT, the SEM-grid will be mounted in a rectangular chamber. A design drawing is given in Fig. 3.5. This way, the SEM-grid will require only 82 mm of space including all flanges required for the assembly.

D-Plate SEM-grid

The beam pipe on the D-plate has a diameter of 100 mm. Based on the thermal simulations it was decided to use tungsten wires with a diameter of 20 μm. As for the HEBT, a variable wire spacing is foreseen:

- 17 wires at 1 mm spacing
- 20 wires at 2 mm spacing
- 10 wires at 3 mm spacing

This results in total of 47 wires that are spread over 87 mm.

A design drawing of the D-plate SEM-grid is given in Fig. 3.6. To save space in the D-plate SEM grid will share the vacuum chamber with 2 ionic pumps. On the HEBT, it is under consideration to place the SEM-grid and the BIF monitor on a single joint chamber.

All the engineering design of the SEM-grid was performed by Henry Przybilski (CEA Saclay).

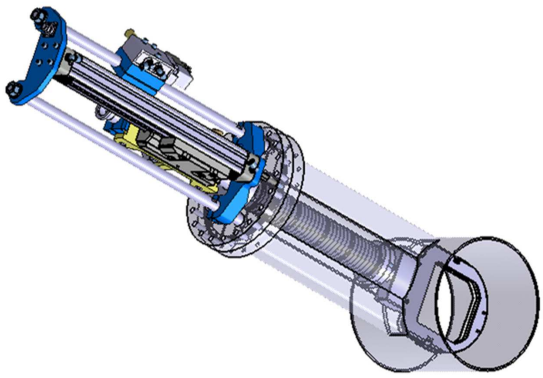

Figure 3.6: Design drawing of the SEM-grid for the D-plate. Design was done by Henry Przybilski (CEA Saclay).

3.8 Detailed Design Review

The SEM-grids were presented during the Detailed Design Review in 2012. In their preliminary evaluation, the expert committee pointed out the limited dynamic range of 12 bits that is currently foreseen and that the wire spacing of the SEM-grids will not suffice for an accurate emittance measurement.

We, as well, have only learned a few days before the Detailed Design Review about the very hard requirements asked for the emittance measurement which are not fulfilled by the foreseen SEM-grid. The emittance can be measured by letting the beam pass through a slit and thus select only one point in x/y. Downstream to the slit, the beam starts to diverge according its transverse momentum distribution. By measuring the profile a few m downstream the slit, one can thereby determine the phase space distribution, i.e. the emittance. Due to the slit size of $\sim 100\,\mu$m, the beam is very narrow and thus cannot be accurately measured by the SEM-grid with a wire spacing > 1 mm.

Currently two options to overcome this issue are foreseen:

- Mounting the SEM on a stepper motor and achieve the required resolution by scanning the beam. As the beam must be scanned in x and y, the SEM-grid will have to be mounted on an actuator that is tilted by 45°. This requires a complete redesign of the SEM-grid chamber and will greatly increase the price.
- Mounting the SEM-grid downstream the qudrupole doublet such that the beam can expand further ($\sigma \approx 2$ mm) and the steerers in the quadrupole can be used to scan the beam over the fixed SEM-grid.

To cope with the higher dynamic range required to perform emittance scans as well, we consider to either use some integrating electronics or to use a 16-bit ADC instead.

3.9 Conclusion and Outlook

Thermal simulations of the wire heating indicates that carbon is the better material choice for the SEM-grid wires. However, carbon is prohibited in superconducting

machines, since a single broken wire can result in a cavity quench which will shut down the entire accelerator. For the LIPAc SEM-grids, tungsten wires with a diameter of 100 μm will be used on the HEBT and tungsten wires of 20 μm diameter on the D-plate. For both SEM-grids, thermal simulations were performed indicating beam settings at which SEM-grids are still operational.

A test is foreseen at the IPHI with 3 MeV protons of 10 - 100 mA to determine if the 20 μm wires are able to handle the thermal shock.

Chapter 4

Ionization Profile Monitors

Cette partie est le fruit d'une recherche très poussée concernant la mesure de profils transverses du faisceau non intrusif. Ce type de moniteur est absolument essentiel pour la conduite du faisceau. Il doit être capable à la fois de mesurer des profils en mode pulsé, par exemple pour des longueurs de pulse d'une centaine de μs afin de prendre le relai des SEM-grids, mais aussi en mode continu : une dynamique de 10 000 apparaît déjà en supposant une intensité de faisceau constante.

Ce type de moniteurs représente un défi pour LIPAc et IFMIF expliquant les 2 programmes de R&D entrepris dans 2 laboratoires sur ce sujet :

- au CIEMAT de Madrid, où la technologie choisie est basée sur la fluorescence du gaz résiduel. On parle alors de Fluorescence Profile Monitor (FPM).
- Au CEA de Saclay, où l'on a privilégié l'ionisation du gaz résiduel ou IPM pour Ionization Profile Monitor.

L'IPM se présente sous l'aspect d'un détecteur à "plaques parallèles". Entre ces 2 plaques est établi un champ électrique. Sur l'une de ces plaques (mise à la masse) sont gravées des bandes conductrices (strips) reliées individuellement à une électronique. Lorsque le faisceau passe entre les 2 plaques, les ions et les électrons résultants de l'ionisation des molécules du gaz résiduel par les deutons dérivent sous l'effet du champ électrique vers les plaques. Des courants proportionnels à la taille transverse du faisceau sont alors mesurés sur les strips.

L'un des ingrédients essentiels pour la construction d'un IPM est l'uniformité du champ électrique. Celle-ci a été obtenue en concevant des dégradeurs de champ latéraux et 2 paires d'électrodes supplémentaires implantées à proximité des 2 plaques. Les paramètres de ces composants ont été déterminés en simulant l'IPM par une approche en éléments finis qui est développée dans cette partie. Un premier prototype de taille modeste $6\times6\,\mathrm{cm}^2$ d'ouverture intégrant les résultats de ces études a été testé au GSI Darmstadt en mai et novembre 2010 et a donné d'excellents résultats comme :

- la bonne uniformité du champ électrique,
- la résolution de la position du profil : inférieure à 100 μm
- une bonne superposition des profils mesurés avec l'IPM et avec un FPM de GSI

- l'extrapolation de ces résultats aux conditions de LIPAc montrant que la mesure avec l'IPM est réalisable pour une intensité de deutons de 4.2 mA pour une pression de 10^{-7} mbar.

Ensuite, l'IPM a été testé sur la source SILHI de IPHI (proton de 90 keV pour un courant maximal de 100 mA) fin 2010 et a montré que l'on pouvait mesurer des profils en mode continu pour des intensités de 10.5 mA. Deux IPM doivent être installés sur LIPAc, l'un sur la Diagnostics Plate (DP) et l'autre en amont du Beam Dump (BD) correspondants à des ouvertures de 10×10 et 15×15 cm^2 respectivement. De nouveaux calculs d'optimisation de champs électriques ont dû être développés ; la tâche étant rendue ardue du fait des grandes ouvertures et du peu d'espace axial dont nous disposons sur LIPAc. De nouvelles formes d'électrodes en arc de cercles ont été étudiées pour améliorer la configuration du champ électrique.

À partir de ces études, un prototype pour le BD a été construit et testé à IPHI. Ce profileur sera installé dans un environnement hautement radiatif (7 kSv/h pour les seuls neutrons), il est donc constitué de matériaux résistants aux radiations comme la céramique, le cuivre, époxy... Des profils ont été mesurés en courant continu jusqu'à 20 mA.

Un des problèmes auxquels ces profileurs seront confrontés est la forte charge d'espace du faisceau. Concrètement, cela se traduit par le fait que le champ électrique engendré par le faisceau n'est plus négligeable et va se superposer au champ électrique d'extraction. Il en résulte que les trajectoires des ions et des électrons ne sont plus linéaires, mais courbées. Dans notre cas, le profil du faisceau apparaitra donc plus étalé qu'il ne l'est en réalité. Cet effet est d'autant plus grand que la taille du faisceau est faible et que son intensité est grande.

Il existe des solutions pour contrecarrer cet effet comme augmenter le champ électrique, superposer un champ magnétique au champ électrique de façon à guider la trajectoire des électrons... mais elles requièrent dans le premier cas des valeurs beaucoup trop grandes et dans le second des encombrements spatiaux qui nous sont interdits. Un algorithme a donc été développé afin de faire une correction quasiment en ligne du profil mesuré en s'appuyant sur des paramètres de faisceau donnés par la dynamique faisceau. Cet algorithme est présenté en détail ainsi que sa sensibilité aux conditions initiales. Un premier test expérimental mené à SILHI a donné des résultats très encourageants.

Ce chapitre se conclura sur des perspectives et d'éventuelles améliorations.

4.1 Introduction

The very high beam power of the LIPAc accelerator at the rather low energy of 9 MeV poses unprecedented challenges for the accelerator development and the beam diagnostics in particular. To complement the set of transverse beam profile monitors foreseen for the LIPAc, two non-interceptive types of profilers are foreseen, Ionization Profile Monitors (IPMs) and Beam Induced Fluorescence (BIF) monitors, also called Fluorescence Profile Monitors (FPMs). The non-interceptive profilers are the only devices for which such a redundancy is foreseen. This emphasizes their complexity and importance for LIPAc as well as for IFMIF. Both are residual gas monitors that measure the beam profile based on interactions with the residual gas in the accelerator beam pipe. They are thus fully non-interceptive devices which allows them to measure profiles at beam intensities at which SEM-grids are no longer operational.

The development of the IPMs, presented in this section, was performed together with my supervisor Jacques Marroncle (CEA Saclay). My main tasks were the electric field simulations of the IPM field boxes, their design and optimization, the preparation, execution and analysis of the test measurements, the interpretation of the test results, and the development and implementation of the SC correction algorithm.

4.1.1 Requirements

While SEM-grids can be used at low beam intensities and low duty cycles only, the IPMs aim to fill the gap up to highest beam currents in continuous wave (cw) and pulsed beam mode. The IPMs therefore must be able to measure accurate profiles particularly in the high-intensity beam regime where SEM-grids are no longer operational. To achieve a certain level of redundancy, the IPMs should, however, also be able to measure beam profiles at low and intermediate beam intensities. This calls for a very robust device with a large dynamic range.

As high-intensity accelerator, the LIPAc is designed in a very compact manner and leaves hardly any space for beam diagnostics. The few diagnostics elements, that may be mounted, have to be designed in a very compact fashion as well. This has a huge impact on the IPM development and the achievable performance.

Finally, the IPMs must be able to withstand a huge radiation level. One of them will be mounted close to the beam dump and will there suffer a huge amount of neutron radiation. During the design, only radiation hard materials may be used to achieve the required radiation tolerance of the IPM.

IPMs are commonly used as beam profile monitors in high power hadron machines [83, 84, 85]. However, the conditions at the LIPAc pose unprecedented challenges on the IPM and require the development of new particle detection and profile correction techniques.

4.1.2 Residual Gas Profile Monitors: A BIF / IPM Comparison

When the accelerator beam passes through the residual gas which is always present in any vacuum tube, collision with the residual gas atoms / molecules can occur. During such collisions, the atoms / molecules can get excited and / or ionized. Beam Induced

Fluorescence (BIF) monitors and IPMs take advantage of these two effects to measure the beam profile non-destructively. Since they are both based on similar physical interactions, i.e. collisions with the residual gas, they share both common characteristics like a strong signal dependency on the residual gas pressure or a vulnerability to the space charge effect of the beam.

Both techniques have certain advantages / disadvantages which are summarized in Table 4.1. The data in the table are for 200 keV protons in nitrogen gas which is one of the rare configurations for which comparable data for ionization and fluorescence is available in literature.

Table 4.1: Comparison of IPM and BIF properties for 200 keV proton beams.

Property	IPM	BIF
Cross section (200 keV p^+)	$\sim 4 \cdot 10^{-20}\,m^2$ [86]	$\sim 5 \cdot 10^{-21}\,m^2$ [87]
Detection angle	4π	$\lesssim 10^{-3}$ [88]
Drift duration / Life time	$\sim 600\,ns$	$\sim 50\,ns$ [87]
Radiation hardness	medium / good	bad / medium
Installation	in the beam pipe	outside the beam pipe
Price	expensive	inexpensive

A major advantage of IPMs is their greater sensitivity. The cross section for ionization is commonly larger than for fluorescence. In addition, an IPM extracts virtually all ionization products in its active area and thus covers effectively the entire solid angle. A BIF monitor only utilizes light that is collected by the camera. The covered solid angle is thus commonly very small, $\lesssim 10^{-3}$ [88]. Due to the higher cross section and the full solid angle coverage, IPMs will commonly be 10^5 times more sensitive than BIF monitors, if both monitor allow for single particle counting, i.e. electrons, ions or photons.

A major issue of IPMs is their intrinsic vulnerability to the space charge effect of the beam. The electric field of the beam repels ions / attracts electrons and thereby affects the ionization particle distribution on their drift to the read-out plate. This can result in strong profile distortions and has to be compensated somehow for high current accelerators like the LIPAc.

BIF monitors suffer this effect as well, since excitation and ionization of residual gas molecules often occur in parallel. However, this effect is less problematic for the BIF monitors as the excited molecules have a life time which is commonly shorter than the drift inside an IPM field box. In addition, one can implement a wavelength filter to reject light emitted from long-lived or charged excited states that would provide wrong profiles. Such a filter will, however, again reduce the already low signal. A detailed study on the use of beam induced fluorescence for beam profile measurements has been performed at GSI [89].

For the LIPAc, a huge issue is the radiation hardness of the profile monitor. IPMs can be designed to be very radiation hard. Techniques to design a radiation hard IPM are presented in section 4.5.3. For a BIF monitor, one can substitute the camera by radiation hard CID cameras or photomultiplier tubes. One can even use optical systems to place them in less irradiated regions of the accelerator vault, but all these

measures render the originally simple and cheap BIF monitor more complicated and expensive.

However, apart from the lower price, the greatest advantage of BIF monitors over IPMs is that no parts have to be mounted inside the beam pipe. This allows for a very compact assembly, where two, or possibly even more cameras, measure profiles in the same plane. It makes BIF monitors also very flexible devices, since only a view port on the accelerator is required to mount the camera on.

4.2 Principle of Operation

In spite of complex pumping systems applied in modern accelerators, a certain level of residual gas always remains in the beam pipe. For LIPAc, a residual gas pressure of $10^{-8} - 10^{-5}$ mbar is foreseen. When the beam passes through the residual gas, collisions with the residual gas molecules or atoms will occur. During such collisions, the residual gas atoms / molecules can get ionized or excited. By applying an electric field, one can extract the ionization products, i.e. ions or electrons. They are accelerated towards some read-out plate, where the ionization current density is measured. Based on the ionization current density, the actual beam profile can be determined. A sketch of the principle of operation of an IPM is presented in Fig. 4.1.

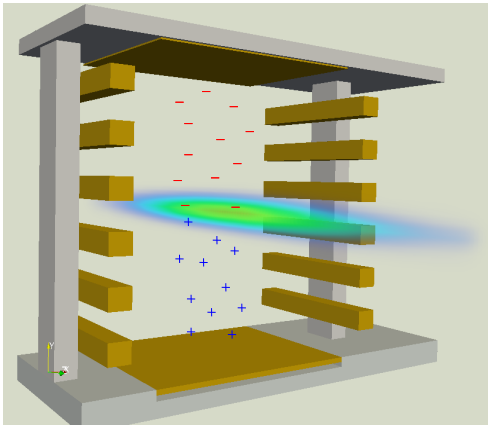

Figure 4.1: A sketch of an Ionization Profile Monitor (IPM) with a beam passing by. Ions and electrons are created by the beam and extracted by an electric field applied by the IPM field box.

The IPM signal is directly proportional to the ionization current, if no recombination occurs. The ionization current in turn can be calculated by

$$I_{Ioniz} = n \cdot d \cdot \sigma_{Ioniz} \cdot I_{Beam}, \tag{4.1}$$

with n being the particle density in the beam pipe, d being the active depth in which ionization occurs, σ_{Ioniz} the ionization cross section and I_{Beam} the beam current.

Assuming deuterium as residual gas, the ionization current will mostly consist of deuterium molecules. In principle, there are two processes possible: Pure ionization where the deuterium molecule remains intact but loses an electron and dissociative ionization where the molecule itself dissociates into two atoms / ions. However, the cross section for dissociative ionization is about two orders of magnitude below the pure ionization cross section. Fig. 4.2 gives measured ionization cross sections for

hydrogen molecules that are bombarded by 6 MeV protons. The cross sections are plotted versus the energy of the released electron. The solid lines are theoretical calculations.

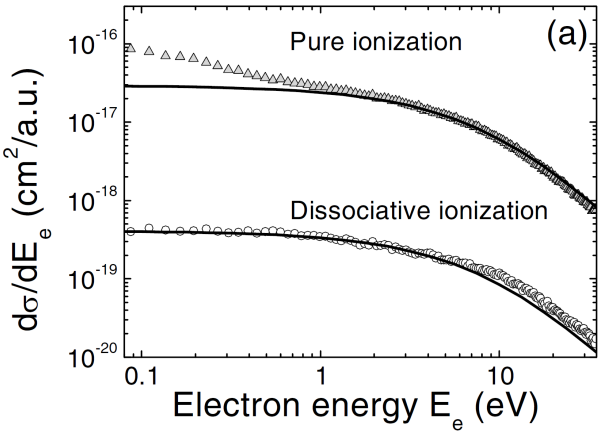

Figure 4.2: Measured cross sections for pure and dissociative ionization of hydrogen molecules under 6 MeV proton bombardment are plotted versus the energy of the released electron. The solid lines are theoretical calculations.[90]

Bohr Ionization Cross Section

Based on a classical theory, the Bohr ionization cross section can be derived [91]. One can assume a charged projectile on a straight trajectory interacting with a hydrogen-like atom. The perpendicular electric force component of this projectile on an electron is given as

$$F_{\perp} = \frac{e^2 Z_p \rho}{(\rho^2 + v^2 t^2)^{3/2}} \tag{4.2}$$

with Z_p being the projectile charge, v the velocity of the projectile and ρ the impact parameter. Integrating the force over all time will average out the longitudinal component yielding a momentum transfer of

$$\Delta p(\rho) = \frac{2e^2 Z_p}{v\rho} \tag{4.3}$$

For an ionization to take place, the energy transfer corresponding to this momentum transfer on an electron has to be larger than the ionization energy I_{nl}. This defines the minimum impact parameter ρ_{min} at which an ionization can still occur. The ionization cross section can thus be calculated to be

$$\sigma^{Bohr} = \pi \rho_{min}^2 = 2\pi Z_p^2 a_0^2 \cdot \frac{v_0^2 E_0}{v^2 I_{nl}} \tag{4.4}$$

with a_0, v_0, and E_0 being scaling constants. The Bohr ionization cross section, and thus the IPM signal, therefore scales with Z^2 and $1/v^2$ of the beam, and with $1/I_{nl}$ of the residual gas.

Profile Distortion Effects

An intrinsic issue of such a profile monitor is the fact that the beam profile is not measured directly, but over the ionization current. If the ionization current changes, for whatever reason, its profile during the drift towards the read-out plate, the measured profile will no longer correspond to the actual beam profile. During the design of an IPM this must be taken into account and measures must be taken to prevent changes in the ionization current density. In an ideal IPM, the ionization products follow linear trajectories on their way to the read-out plate. Such an ideal case can, however, never be achieved in reality due to various distortion mechanisms that are listed below.

The ionization particles are not created at rest, but they do have a certain initial velocity. This initial velocity will result in a parabolic trajectory. The velocity component of a deuterium molecule in one direction at ambient temperature can be calculated by

$$\bar{v} = \sqrt{\frac{k_B T}{m_{deuterium}}}. \tag{4.5}$$

to be 787 μm/μs. Assuming an electric field of 500 V/cm and a drift distance of 75 mm, a deuterium ion requires 350 ns to reach the read-out plate. This results in an ion displacement of 280 μm which is well negligible in our configuration.

Even if one considers the possibility that the beam heats the residual gas up by a few 100 °C, the displacement due to the thermal ion velocities remains small due to its $\sqrt{T}$ dependency.

However, during the ionization process, a certain fraction of the projectile momentum is transferred onto the ion. The momentum transfer on ions during the ionization process was measured with great accuracy using a reaction microscope at the Max-Planck-Institute for Nuclear Physics [90]. In a reaction microscope a supersonic gas jet collides with a projectile beam. By an assembly of electric and magnetic field, virtually all ionization products are collected and their momenta are measured. This way, the collision can be fully reconstructed.

The momentum transfer of 6 MeV protons onto hydrogen molecules during the ionization process was found to be about $\lesssim 1$ a.u., i.e. a velocity transfer of below 600 m/s. As this value is still below thermal velocities, it can be fully neglected for ions.

As shown in Fig. 4.2, ionization electrons commonly have an energy of several eV. Due to their low mass, electrons of 1 eV energy already have a velocity of $\sim$600 km/s. However, electrons are also extracted faster by the electric field of the IPM and they reach the read-out plate in $\sim$4 ns for the above mentioned IPM characteristics of 500 V/cm electric field strength and a drift distance of 75 mm. Nonetheless, the displacement of electrons due to the momentum transfer is $\sim$2.5 mm. Without a proper confinement of the electrons, it is therefore imperative to collect ions in order to measure the beam profile.

The commonly most dominant source of ionization current deformations is the effect of electric fields in the IPM field box. The electric field in the IPM field box can be considered as superposition of

- the electric field generated by the field box itself and

- the electric field generated by the accelerator beam.

Additional sources of electric fields like the ionization current itself or mirror charges on the beam pipe are neglected.

4.3 Electric Field Calculations

The electric field of the beam cannot be overcome by any mean without affecting the beam. The electric field of the field box, however, is given by the field box geometry. By properly designing the IPM field box, one can realize a uniform electric extraction field that does not distort the ionization current and thus allows for a proper beam profile measurement.

4.3.1 Physics Background

Electric and magnetic fields are fully determined by Maxwell's equations. They are given in their differential form, expressed in natural units, in equation 4.6 [92].

$$\begin{aligned} \vec{\nabla} \cdot \vec{D} &= 4\pi\rho \\ \vec{\nabla} \cdot \vec{B} &= 0 \\ c\vec{\nabla} \times \vec{E} &= -\dot{\vec{B}} \\ c\vec{\nabla} \times \vec{H} &= \dot{\vec{D}} + 4\pi\vec{J} \end{aligned} \tag{4.6}$$

The electric field inside the IPM field box can be calculated electrostatically and the polarization density of the vacuum inside the beam pipe can be assumed to be zero, i.e. $\vec{D} = \vec{E}$. In this case all time derivatives vanish and only two equations remain:

$$\begin{aligned} \vec{\nabla} \cdot \vec{E} &= 4\pi\rho \\ \vec{\nabla} \times \vec{E} &= 0 \end{aligned} \tag{4.7}$$

In such a static case, an electric potential can be defined such that the electric field is given by its gradient.

$$\vec{\nabla}\Phi(\vec{r}) = -\vec{E}(\vec{r}) \tag{4.8}$$

Equation (4.7) can then be rewritten for the electric potential. This yields the Poisson equation, given in equation (4.9).

$$\begin{aligned} -\vec{\nabla} \cdot \vec{E} = \vec{\nabla} \cdot \vec{\nabla}\Phi(\vec{r}) &= -4\pi\rho \\ \Rightarrow \qquad \Delta\Phi &= -4\pi\rho \end{aligned} \tag{4.9}$$

From the Poisson equation, one can derive the electric potential inside an arbitrary volume V using Green's theorem. Green's theorem for differentiable scalar functions ϕ and ψ states

$$\int_V \left[\phi\Delta'\psi + \vec{\nabla}'\phi\vec{\nabla}'\psi\right] dV' = \oint_{\partial V} \phi \frac{\partial\psi}{\partial n'} dA' \tag{4.10}$$

or in another representation

$$\int_V [\phi\Delta'\psi - \psi\Delta'\phi]\, dV' = \oint_{\partial V} \left(\phi\frac{\partial\psi}{\partial n'} - \psi\frac{\partial\phi}{\partial n'}\right) dA' \tag{4.11}$$

with

$$\frac{\partial\phi}{\partial n} \coloneqq \vec{\nabla}\phi \cdot \vec{n}$$

In this equation, $\vec{n}$ is the unity normal vector on the boundary surface ∂V. Choosing $\phi(\vec{r}') = \Phi(\vec{r}')$ and ψ such that

$$\Delta'\psi = -4\pi\delta(\vec{r} - \vec{r}'),$$

the second volume integral of equation (4.11) yields the electric potential $\Phi(\vec{r})$, due to the property of the Dirac function:

$$\int_V \Phi(\vec{r}')\delta(\vec{r} - \vec{r}')dV' = \Phi(\vec{r})$$

To determine the electric potential in an arbitrary volume, one just needs to solve the remaining integrals in equation (4.11).

For two cases of boundary conditions, equation (4.11) can be significantly simplified. It can be shown that for a given charge distribution inside the volume V the potential $\Phi(\vec{r})$ is clearly defined by either

- the potentials Φ on the boundary ∂V of the volume V or by
- the derivatives of the potentials $\partial\Phi/\partial n$ on the boundary ∂V.

$\partial\Phi/\partial n$ can here be interpreted as the electric field component perpendicular to the boundary. The former are called Dirichlet boundary condition and the latter Neumann boundary condition.

It can be shown that potentials that satisfy one of the boundary conditions are physically indistinguishable. One can conclude that if a solution is found by a Finite Element Method (FEM) algorithm, there is no different solution possible. Using the Poisson equation (4.9) to substitute the $\Delta\Phi(\vec{r})$ by the charge density $\rho(\vec{r})$ in the volume, the potentials are given for Dirichlet boundary conditions by

$$\Phi(\vec{r}) = \int_V \rho(\vec{r})G_D(\vec{r},\vec{r}') - \frac{1}{4\pi}\oint_{\partial V} \Phi(\vec{r}')\frac{\partial G_D(\vec{r},\vec{r}')}{\partial n'}dA' \tag{4.12}$$

and for Neumann boundary conditions, the potentials are given by

$$\Phi(\vec{r}) = \int_V \rho(\vec{r})G_D(\vec{r},\vec{r}') - \frac{1}{4\pi}\oint_{\partial V} G_D(\vec{r},\vec{r}')\frac{\partial\Phi(\vec{r}')}{\partial n'}dA' + \langle\Phi\rangle_{\partial V}\,, \tag{4.13}$$

with $\langle\Phi\rangle_{\partial V}$ being the average potential on the boundary ∂V.

$G_D(\vec{r},\vec{r}')$ is called the Green's function that is commonly used to solve such problems in physics and is here defined as by

$$\Delta G_D(\vec{r},\vec{r}') = -4\pi\delta(\vec{r}-\vec{r}').$$

The definition of the Green's function is thus consistent with the function chosen above for ψ to solve Green's theorem. In physics, it can be considered as the potential of a point-like charge at position $\vec{r}'$ plus an arbitrary function $f(\vec{r},\vec{r}')$ that fulfills the Laplace equation (4.14).

$$\Delta f(\vec{r},\vec{r}') = 0 \tag{4.14}$$

By solving equations (4.12) or (4.13), one can calculate the potential of an arbitrary charge distribution within any volume once the Green's function is known. However, the Green's function can hardly be determined by a software algorithms and an analytical solution is in general not calculable by computers [92].

4.3.2 Finite Element Method

One of the most versatile methods to determine the electric potential inside a given volume with given boundary conditions is the Finite Element Method (FEM). The Finite Element Method, in its presently accepted forms, can be credited to Richard L. Courant who called it at first Method of finite differences [93]. This name actually describes well the mathematical concept of FEM. Instead of trying to solve differential equations, one converts differential quotients into difference quotients and integrals into sums in accordance with the original motivation of the infinitesimal calculus.

While differentials and integrals are applicable on continuous space, a space discretization is required to comply with sums and differences of discrete values. For this purpose the geometry in which the electric potentials are to be solved is meshed. A mesh for a 1D line of length l could consist in n uniformly distributed points with a spacing of l/n. A mesh of a 2D surface could consist of the corner points of triangles or rectangles and the like for a 3D object. Examples of possible 3D meshes, based on prisms, tetrahedra and cuboids are shown in Fig. 4.3 [94].

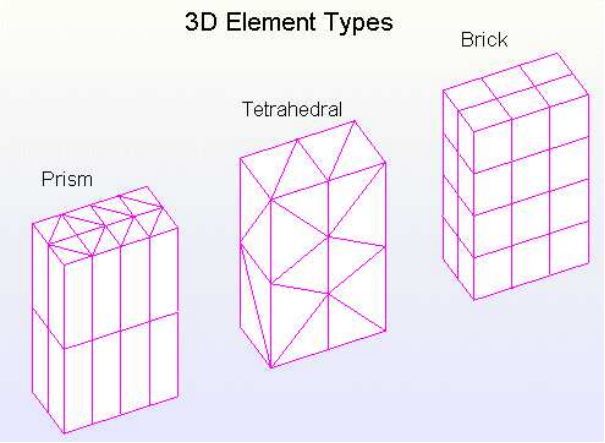

Figure 4.3: Different possible mesh types for 3D geometries.[94]

The mesh points do not have to be distributed uniformly, in the contrary, modern FEM solvers generate a mesh that is optimized for each particular geometry shape.

To each point of the mesh, a potential value can be assigned. For a 1D mesh of N mesh points the Poisson equation (4.9) can be discretized into $N-2$ equations, since each point requires two neighbors to express the second derivatives of the Laplacian by difference quotients. The electric potentials of two mesh points, or their derivative must be given as boundary condition to solve the system of $N-2$ equations. This system of linear equations is commonly solved using a matrix formalism. This formalism can be applied to meshes of higher dimensions as well.

By increasing the number of mesh points and thus decreasing the mesh size, the acquired solutions should converge towards the solution of the Poisson equation as the difference quotients converge towards differential quotients [93]. To improve the performance of such algorithms, modern FEM often assume not a fixed value for each mesh point, but easily calculable functions over the distance between two points [95].

4.3.3 Boundary Element Method

One of the major disadvantages of the FEM method occurs for 3D applications where the number of mesh points to achieve a given point spacing d increases with $1/d^3$. To reduce the distance between two points in a 3D mesh by a factor of 2, 8 times more mesh points are required, i.e. the calculation takes much longer.

An interesting solution to this problem offers the Boundary Element Method (BEM). It was shown in section 4.3.1 that the electric potentials inside an arbitrary charge-free volume can be calculated by solving an integral over the boundary of this volume, see equations (4.12) and (4.13). For problems, on which Green's theorem can be applied, it therefore suffices to perform a FEM approximation on the volume boundary only. Since much less points are required for a 2D mesh of the boundary than of the entire 3D volume, the performance of such an algorithm can be greatly improved for many applications.

4.3.4 Electric Field Solver

For the electric field calculations presented in this thesis, the FEM solver packages included in the particle tracking software Lorentz-3E of Integrated Engineering Software [96] are used. It includes FEM as well as BEM solvers. Due to the better performance, BEM calculations were used in this thesis exclusively.

In a first step, the geometry in which the electric potential is to be calculated is implemented in a Computer Aided Design (CAD) software. In a second step, a meshing of the geometry is performed. In a third step, the mesh is then read by the FEM solver and for each mesh point the material properties and possibly boundary conditions are defined before the resulting system of equations can be solved. Finally, the calculated potentials must be visualized and possibly post-processed. The Lorentz-3E package provides a Graphical User Interface (GUI) that allows performing all four tasks in a user-friendly fashion.

As a benchmark, the horizontal electric field components of the IPM prototype field were calculated by Lorentz-3E and compared with results of different solvers, SOLMAXP [17, 18] and COMSOL Multiphysics [97]. The resulting field components in the central IPM plane are presented in Fig. 4.4. The calculated electric fields are in good

agreement for all three solvers. Only in the calculation performed by SOLMAXP, a Frisch-grid, to reduce the effect of secondary electrons, was implemented which results in a slightly different field configuration in the bottom corners of the IPM field box.

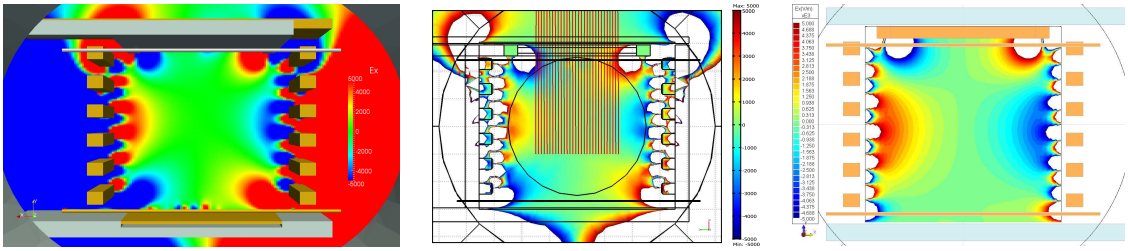

(a) Horizontal electric field component in the range of $\pm$ 50 V/cm calculated by SOLMAXP.

(b) Horizontal electric field component in the range of $\pm$ 50 V/cm calculated by COMSOL, ion trajectories in the field are given as red lines.

(c) Horizontal electric field component in the range of $\pm$ 50 V/cm calculated by Lorentz-3E.

Figure 4.4: FEM results of the horizontal electric field component in the central plane of the IPM prototype field box calculated by different electric field solvers.

Just like Lorentz-3E, COMSOL is also a commercial software package, which allows performing all the above mentioned tasks using a single GUI. SOLMAXP, however, is a FEM solver that is developed at CEA Saclay. Geometries have to be defined in an external CAD software and are imported into SOLMAXP in a *.stl format. The meshing consists in simple cuboids of constant size. The size of the cuboids are defined by the user. Thereby, the resolution can be adjusted for each direction separately. The solver output consists in the calculated potentials which can be post-processed by another software, e.g. ROOT [73], to get the electric field values.

Considering the slightly different color representation of the electric field values, the results of the three different solvers, presented in Fig. 4.4, are all in a good agreement. Such a consistency check in combination with experimental validation of the electric field uniformity, presented in section 4.4.2, provide confidence in the FEM results of the Lorentz-3E software package.

4.4 IPM Prototype

To investigate the basic properties of IPMs, a prototype was build. FEM field calculations are presented to optimize the electric field uniformity inside the field box as well as results of test measurements performed at GSI (Helmholtzzentrum für Schwerionenforschung) in Darmstadt, Germany, and at the SILHI source of the IPHI (Injecteur de Protons à Haute Intensité) injector at CEA Saclay, France. [98]

4.4.1 Prototype Design

An IPM commonly consists of three subsystems:

- the field box

- the front-end electronics
- the data acquisition system

In this thesis a strong focus is set on the electric field box, the electronics were designed by Philippe Abbon (CEA Saclay) and for the data acquisition, commercial systems were used.

IPM Electric Field Box

As described in section 4.2, it is the purpose of the IPM field box to generate an uniform electric field that is required to avoid any significant distortions during the extraction of the ionization products from the beam region. Once the ionization products are extracted from the beam, they are measured by the read-out plate which is included in the field box.

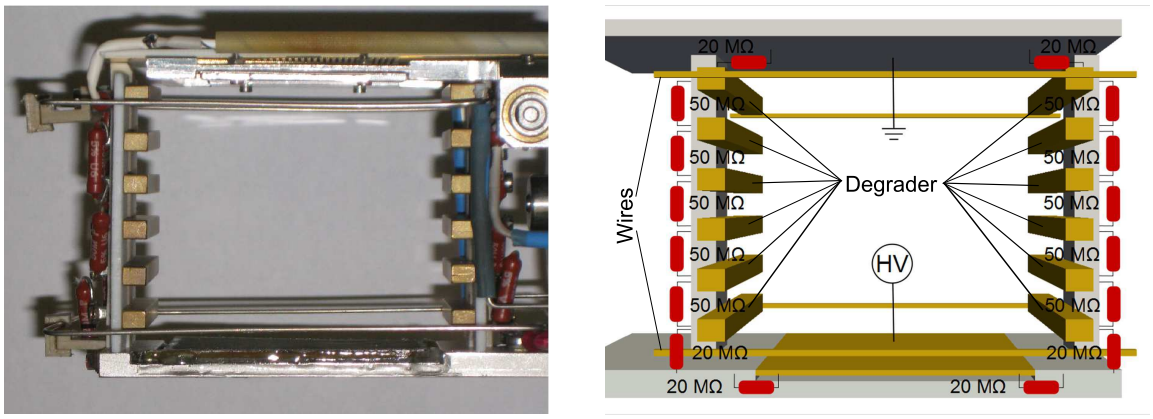

(a) Photo of the IPM prototype field box.

(b) Sketch of the IPM with the resistor values indicated.

Figure 4.5: Photo and sketch of the IPM prototype field box.

A photo of the field box of the IPM prototype is presented in Fig. 4.5(a). On the bottom plate a high voltage is applied that repels the ionization products towards the read-out plate on top. The design value of the high voltage for the field box is 5 kV. For higher voltages, sparks can occur. The read-out plate, where ions or electrons deposit their charge, consist of 32 single strips. The deposited current on the strips is then read by the front-end electronics. The strips are realized by a copper deposition on a ceramic board. They have a spacing of 1.25 mm and a total length of 20 mm. A photo of such a ceramic board with the strips upon is shown in Fig. 4.6.

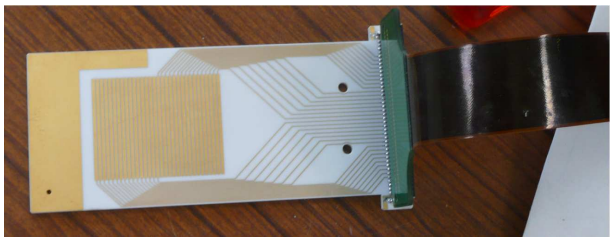

Figure 4.6: Photo of the read-out strips of the IPM prototype.

When ions or electrons impinge on a metal surface, they can emit secondary electrons, as explained in more detail in section 3.4. If electrons are collected on the strips, ions

will release secondary electrons from the HV plate that will also be accelerated by the extraction field towards the read-out strips. The signal of these electrons will result in a distorted profile. To avoid such distortions a Frisch-grid is mounted in front of the HV plate to repel secondary electrons back to the HV plate. This grid is set on an even higher voltage than the HV plate. A few 100 V between the grid and the HV plate is sufficient to overcome the kinetic energy of the secondary electrons. The Frisch-grid was embedded in the resistor chain of the degraders to avoid an additional power supply.

To allow for the evaluation of the electric field uniformity in beam direction, a mechanism to reduce the active depth of the IPM has been installed on the prototype. Two movable copper plates are mounted above the strips in such a way that they form a slit. Since ions cannot penetrate the plates, they can only reach the strips through the slit. By moving the copper plates towards one another, one can close the slit and thus reduce the active depth of the IPM. The steel frame of this slit can be seen in Fig. 4.5(a) below the top plate.

To avoid fringe fields of the IPM perpendicularly to the beam, on both hands side of the IPM, six degraders are mounted in the form of small copper blocks. Appropriate voltages are applied on the degraders to reduce the fringe fields and to improve the electric field uniformity. To avoid additional high voltage supplies, the degrader voltages are applied over a resistor chain. The red resistors, outside of the IPM field box can be seen in Fig. 4.5(a).

Unfortunately, fringe fields in beam direction cannot be overcome by such degraders as they would block the beam itself. Instead, correction electrodes close to the top read-out plate and the bottom high-voltage plate are mounted in the form of wires. A similar technique was already applied by Giacomini et al. [83]. By applying high voltages on these wires, the fringe fields can be pushed back in the IPM field box. The position and voltage of the correction electrodes and the resistors to be used in the resistor chain of the degraders were determined by FEM calculations in Lorentz-3E.

Electric Field Optimization

It is difficult, if not even impossible, to achieve a perfect electric field uniformity in the entire field box. Instead, only the electric field components in the central IPM plane are considered. The electric field box of the IPM prototype was designed by minimizing the electric field component in direction of the profile, i.e. if the profile in x is measured, the electric field component in x direction will be minimized. It is assumed that variations in the absolute value of electric field strength do not affect the profile shape.

Non-uniformities of the electric field component in beam direction can focus particles onto the strips. Variations of these non-uniformities can therefore have an impact on the profile shape. As a second order effect, this effect is virtually neglected during the field box design. Due to the symmetry of the field box, the electric field component in beam direction vanishes in the central IPM plane. Possible distortions can therefore be minimized by reducing the active depth, i.e. the read-out strip length.

The best electric field uniformities were achieved for an acceleration voltage on the bottom plate of 5 kV, 8 kV on the lower electrode wires and 1.2 kV on the upper wires close to the read-out strips. The electric potentials and horizontal field components

Table 4.2: Resistor values of the resistor chain for the degraders in the IPM field box.

Degrader	1	2	3	4	5	6	plate	Frisch-grid
Voltage [V]	323	1129	1935	2742	3548	4355	4677	5000
Resistor [MΩ]	20	50	50	50	50	50	20	20

for this configuration are presented in Fig. 4.7. The degrader voltages and the resistor values of the resistor chain are given in Table 4.2. The last elements of the degrader chain are the high-voltage plate and the Frisch-grid where 5 kV are applied. The color scale in Fig. 4.7(b) is limited to $\pm 5\,\mathrm{kV/m}$, i.e. $\sim 6\,\%$ of the average extraction field.

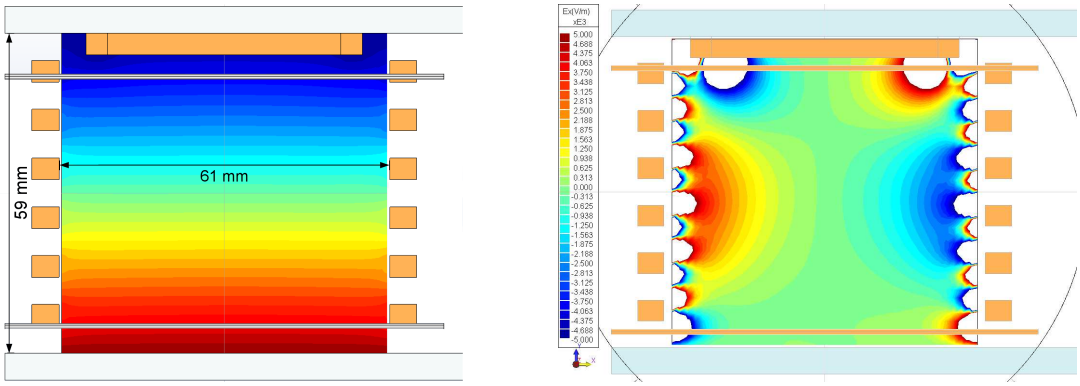

(a) Equipotential lines.

(b) Horizontal electric field components within $\pm 5\,\mathrm{kV/m}$.

Figure 4.7: Electric field simulations of the IPM prototype field box calculated by Lorentz-3E.

Front-End Electronics

The basic concepts of the electronics used have already been discussed in section 2.2.6. As for the Ionization Chamber, electronics based on linear and logarithmic amplifiers and based on charge integration have been foreseen to be tested.

Each electronics card gives a continuous multiplexed voltage output of the signal. The linear and logarithmic transimpedance amplifiers provide a signal every 2.133 μs, for the integrating electronics this time, of course, depends on the integration time. To ensure a proper synchronization with the Data Acquisition System (DAQ), each electronics card provides a trigger signal to be sent to the DAQ.

Data Acquisition System

For the data acquisition, a commercial Acqiris card from Agilent Technologies [99] was used. The card has an 8 bit ADC, a sampling frequency of up to 1 GHz, and a memory of 2 MB. A 2.133 μs long profile signal, provided by the front-end electronics, digitized at 1 GHz has thus 2133 data points. Each data point has a size of 8 bit, i.e. 1 Byte. The Acqiris card memory of 2 MB can therefore store approximately 800 profiles before it must transfer the data to the computer memory.

Due to a dead time in the Acqiris card after each reading, it discarded every second trigger coming from the front-end electronics. Effectively, profiles were read every 4.266 μs. Accelerator pulses of up to 3.4 ms can thus be continuously read. For longer pulses, a dead time during the data transfer to the computer memory occurs, or the sampling frequency must be reduced.

4.4.2 Prototype Tests at GSI

The IPM prototype was tested at GSI (Helmholtzzentrum für Schwerionenforschung) in two campaigns, one in May 2010 and the other in November 2010. The tests were performed at a branch of the UNILAC that is called X2 and that is dedicated for beam diagnostics development. Photos of the UNILAC accelerating structure and the X2 branch are given in Fig. 4.8.

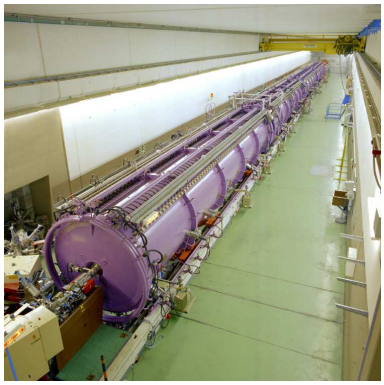

(a) Photo of the UNILAC accelerating structure [100].

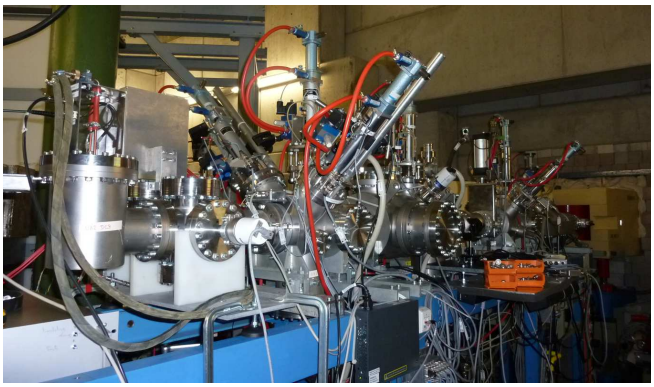

(b) Photo of the X2 branch with the IPM prototype mounted on the cross upstream the beam dump.

Figure 4.8: Photos of the GSI accelerator beam lines.

To place the Ionization Profile Monitor (IPM) at the GSI beam line, it was mounted on a cross with 6 flanges of 100 mm internal diameter. Two of them were used to mount the cross on the X2 beam line in front of the beam dump, as can be seen in Fig. 4.8(b). On one horizontal flange, the IPM is mounted, and on the remaining horizontal flange, a vacuum gauge to monitor the residual gas pressure. The two remaining vertical flanges are left for spare.

In order to move the IPM in and out of the beam line, it was mounted on a stepper motor granting a precise positioning of the detector. The motor controller can be connected via the GSI internal network to a computer which allows for a remote control by a Labview code of the detector positioning without need to enter the cave. This is important for fast position scans, when opening / closing the cave to adjust the detector position manually would cause major delays.

Table 4.3: Parameters of the beams available at GSI.

Particle	Charge State	Energy [A·MeV]	Pulse Current [μA]	Pulse Length [μs]
Ca	10	4.8 (4.6)	< 33	5000
Xe	21	4.8	< 1100	200
U	28	4.8	< 1700	100

The X2 beam line is equipped with a gas inlet system that allows for a regulation of the residual gas pressure from $5 \cdot 10^{-7}$ up to $5 \cdot 10^{-4}$ mbar. By injecting a certain gas, not only the pressure but also the residual gas type itself can be varied. This is a very advantageous feature for our prototype test as it allows for an easy adjustment of the ionization signal strength independently of the beam properties.

Three different beam types were available during the test period, a low-current, long-pulses Ca^{10+} beam, a high-current, short-pulses U^{28+} beam, and a high-current, short-pulses Xe^{21+} beam. The detailed beam parameters of each beam are presented in Table 4.3.

Data Analysis

As discussed in section 4.4.1, each profile acquired at 1 GHz consists of 2133 data points. By distributing these data points uniformly over the 40 mm active width of the IPM prototype, one can easily display the measured profile. An example of such a profile measurement is given in Fig. 4.9(a).

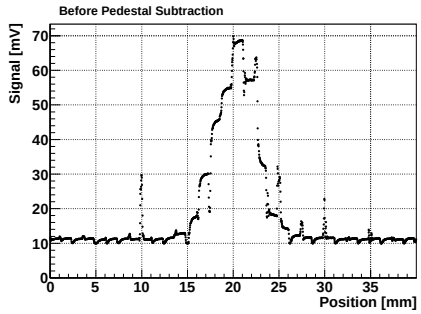

(a) Raw data of the profile.

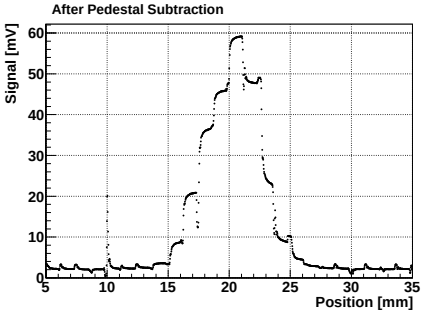

(b) Profile after pedestal subtraction.

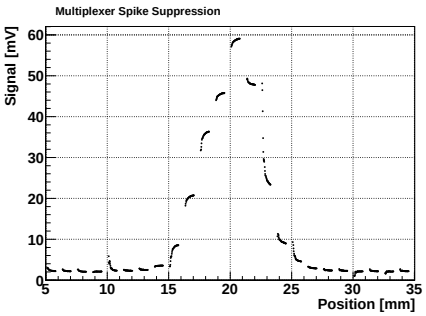

(c) Profile after suppression of the multiplexer spikes.

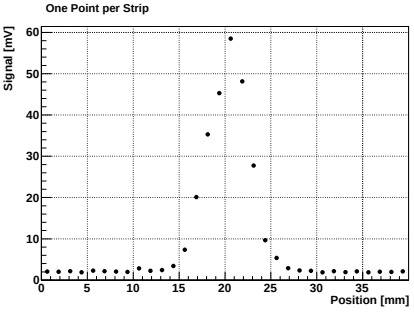

(d) Only a single point is displayed per read-out strip.

Figure 4.9: Corrections of an acquired profile.

One can nicely see the different strips where the readings are approximately constant. In between each strip there is a spike which can be explained by the switching of the multiplexer. In addition, the profile has a strong offset. Both effects can be greatly reduced by a pedestal subtraction. A pedestal profile is acquired while the beam is switched OFF and subtracted from beam profile. This way, the systematic offset of the amplifiers can be eliminated. Also the multiplexer spikes can be reduced. The same profile after such a pedestal subtraction is shown in Fig. 4.9(b). To reduce the effect of the multiplexer even further, the data points close to the strip edges are rejected. 960 out of the 2133 data points were rejected. By adjusting the size of the acceptance

window, one can either further improve either the accuracy or one can improve the available statistics. The fully corrected profile is given in Fig. 4.9(c). In the following profiles, only one single point will be displayed per strip that is averaged the readings still displayed in Fig. 4.9.

Pressure Scaling

The profiles of a 30 μA Ca^{10+} beam have been acquired at different residual gas pressures. According to equation (4.1), a linear correlation between the IPM output signal and the residual gas pressure is to be expected. The IPM signal plotted over the residual gas pressure is presented in Fig. 4.10. A linear fit is performed that matches the data points nicely.

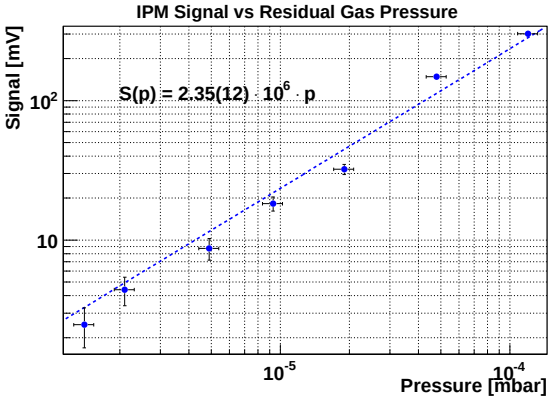

Figure 4.10: IPM signal versus the residual gas pressure.

For this test the IPM was operated at the nominal voltage of 5 kV, i.e. 833 V/cm. Unless stated otherwise, all measurements are performed at this extraction field.

Charge State Scaling

According to equation (4.1), the IPM signal should also scale with the ionization cross section. In a classical approximation, the ionization cross section for a single particle is given by the Bohr cross section (4.4) that scales with Z^2, with Z being the charge state. If the electric current of the accelerator beam is kept constant, the ionization current rises linearly with Z.

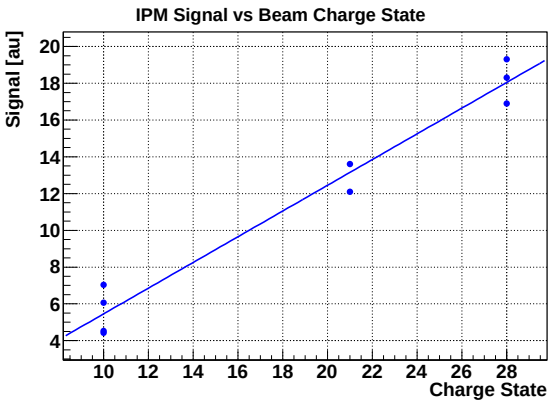

Figure 4.11: IPM signal versus the charge state of the beam particles.

Integrated IPM signals, scaled on residual gas pressure, beam current and IPM slit opening, versus the charge state of the beam particles are presented in Fig. 4.11. The spread in the displayed data points is due to errors in the residual gas pressure, beam current and slit opening measurement. It can be concluded that the IPM signal rises linearly with the charge state. This is of particular importance to extrapolate the IPM response measured at GSI for highly charged beams to LIPAc that accelerates deuterons of $Z = 1$ only.

LIPAc Signal Estimation

Based on these scaling properties, the measurable current at LIPAc can be estimated. At GSI, the IPM prototype was able to measure profiles of 30 μA 4.8 A·MeV Ca^{10+} beams in $1.4{\cdot}10^{-6}$ mbar residual gas pressure by integrating over 5 ms. The corresponding profile is presented in Fig. 4.12.

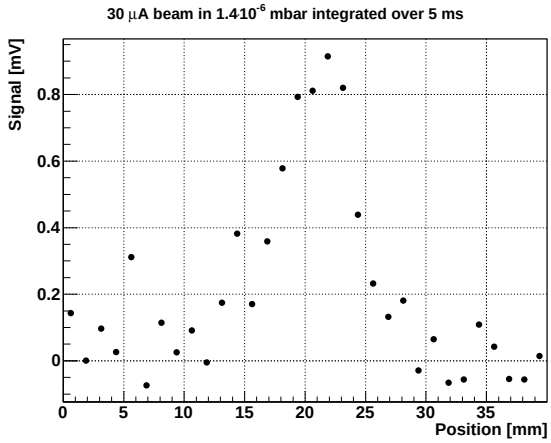

Figure 4.12: Lowest measurable IPM signal integrated over 5 ms at 30 μA beam current and $1.4 \cdot 10^{-6}$ mbar residual gas pressure.

By the scaling laws, verified above, such a beam generates a comparable ionization current as a 300 μA 4.8 A·MeV proton or deuteron beam. If we take this value as the minimum measurable current, the IPM should be able to measure beam profile down to 8.4 mA in 5 ms integration time at $5 \cdot 10^{-8}$ mbar at LIPAc.

Table 4.4: Number of pulses required to achieve a reasonable signal for various duty cycles and beam currents.

T_{Pulse} [ms] \ I_{Beam} [mA]	125	75	40	10	1
0.05	28	44	88	336	3360
0.1	14	22	44	168	1680
0.2	6.8	11	21	84	840
0.5	2.8	4.4	8.4	34	340
1.0	1.2	2.4	4.0	17	168
2.0	0.6	1.2	2.0	8.4	84
5.0	0.3	0.4	0.8	3.4	34

Different ionization cross sections of nitrogen and hydrogen are not considered in this estimation. Cross sections for deuterium beam are not available, but the ionization cross sections for protons of 5 MeV in nitrogen are about a factor four higher than in hydrogen [86]. The IPM should be able to measure beam profile down to 34 mA in 5 ms integration time in $5 \cdot 10^{-8}$ mbar of the deuterium residual gas at LIPAc. Table 4.4 summarizes the number for pulses that have to be accumulated for a proper IPM signal for different beam currents and pulse lengths.

Ionization Current

The ionization current measured on the IPM at a residual gas pressure of 10^{-5} mbar has been compared with theoretically calculated values. For this calculation, the ionization cross section of 5 MeV proton in the specific residual gas were used and scaled by the charge Z of the accelerator beam particle, Z = 21 for the Xe^{21+} beam used for this calculation. The results are presented in Table 4.5.

Table 4.5: The ionization current measured by the IPM at 10^{-5} mbar in different residual gases in comparison with calculated values.

	N_2	He	Ne	Ar	Kr
Measurement [nA]	354	76	123	272	456
Theory [nA]	199	29	83	157	250
Ratio	1.8	2.6	1.5	1.7	1.8

The ionization current measured on the IPM strips was determined based on the conversion of the front-end electronics. The scaling of the vacuum gauge for the different gases and the effect of the secondary electrons, discussed in section 4.4.2, have been considered. The measured ionization currents are systematically higher than the calculated values by about 70 %. This might indicate a pressure gradient within the IPM chamber due to the gas inlet system with a $\sim$70 % higher pressure on the level of the IPM field box.

Long Cable Effect

At the tests at GSI, the front-end electronics were mounted on the accelerator itself. For the LIPAc, this will be impossible due to the radiation level in the vault. The front-end electronics will have to be placed at remote distance, either completely outside the vault or within, protected by extra shielding. At GSI, co-axial cables of up to 465 cm were available to test the effect of longer cables. Two effects are expected:

- an attenuation of the signal
- an increased noise level.

An attenuation effect can be easily evaluated by comparing the IPM signal of beam profiles acquired at different cables lengths, but with the same beam settings. As presented in Fig. 4.13(a), a signal attenuation due to the longer cables cannot be observed.

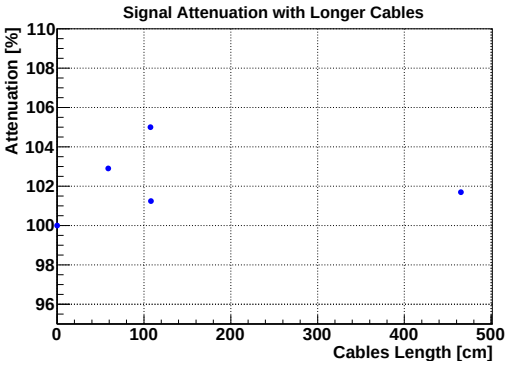

(a) IPM signal attenuation with increased cables length.

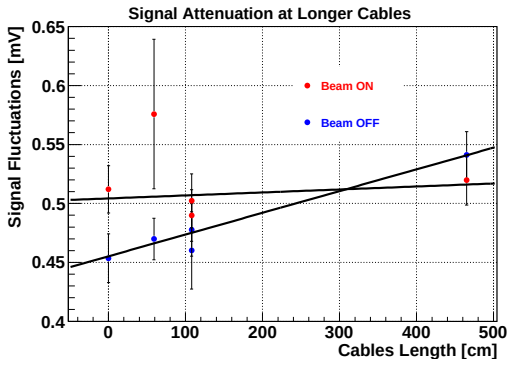

(b) IPM signal noise with increased cables length.

Figure 4.13: The effect of longer cables between the IPM and the front-end electronics.

For the signal noise evaluation, the fluctuations of the signals measured on single read-out strips were calculated for the actual profiles with the beam ON and for the pedestal data when the beam was switched OFF. It can be seen in Fig. 4.13(b) that the fluctuations of the data with the beam OFF rise constantly with longer cables, while the fluctuations of the data with the beam ON remain constant. This fluctuation of the data with the beam OFF can therefore be considered as the noise contribution of the cables. At about 465 cm of cables between the IPM and front-end electronics the noise of the cables starts to dominate the total noise.

It can be concluded that cables between the IPM and front-end electronics of less than 5 m do not affect profile acquisitions.

Electric Field Uniformity

It was the focus of the IPM development to achieve a highly uniform electric field. It was therefore a primary objective of the GSI tests to measure the field uniformity. This was done in two different ways:

- By opening and closing a slit above the read-out strips (as described in section 4.4.1) and comparing the resulting profiles, the field uniformity longitudinal to the beam can be evaluated.
- To evaluate the field homogeneity transverse to the beam, the detector can be moved transversally by a stepper motor.

For different slit openings, beam profiles are acquired and Gaussian fits are performed to determine width and total signal strength. The product of the Gaussian peak and the RMS width is taken as a measure for the total signal strength. When the slit is opened the signal rises linearly as the active area increased and more charge carriers can reach the strips. The total signal plotted versus the slit opening is shown in Fig. 4.14(a). The profile width increases slightly at larger slit openings, as it is shown in Fig. 4.14(b). This could indicate electric field inhomogeneities that increase closer to the detector edge. It can however also be explained by tilted strips with respect to the beam direction.

The IPM field box was designed to provide a good electric field uniformity only if proper voltages are applied on degraders and correction wires. By varying the electric

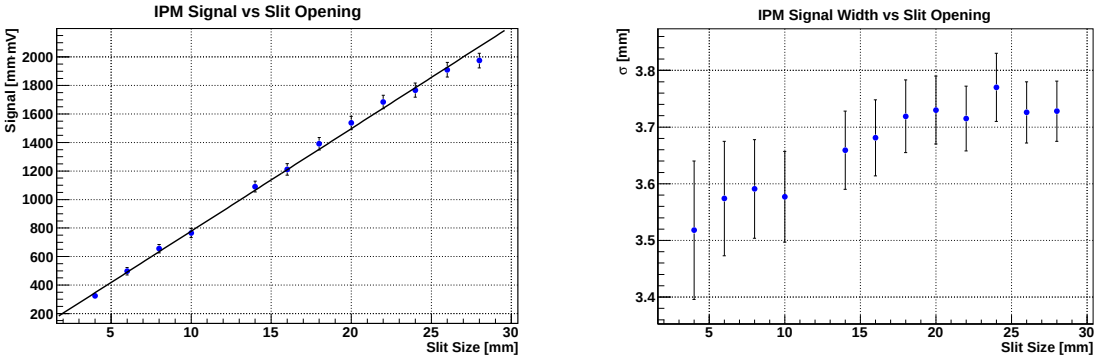

(a) Signal Intensity versus slit opening.

(b) Profile width versus slit opening.

Figure 4.14: Electric field uniformity check by varying the slits above the read-out strips and thereby reducing the active width of the IPM.

potential on the bottom wire, one can easily de-tune the field box. FEM simulations indicate a focusing effect for reduced voltages on the bottom wires. The beam profile width plotted versus the bottom wire voltage is presented in Fig. 4.15. For a slit opening of 5 mm, as shown in Fig. 4.15(a), no significant variation of the profile can be seen. For larger slit openings, as shown in Fig. 4.15(b), the expected focusing effect at lower wire voltages is nicely visible. The larger slit opening results in a better statistics and increases the effect field distortions as the field uniformity decreases rapidly towards the edges of the IPM field box.

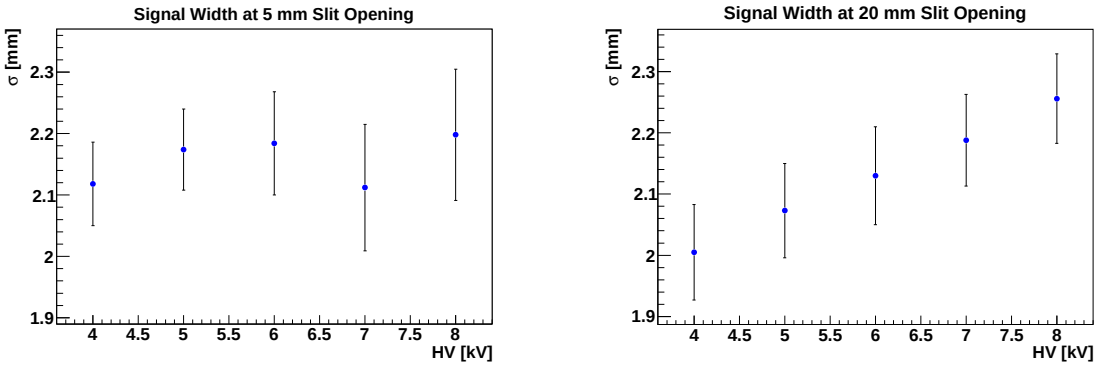

(a) 5 mm slit opening.

(b) 20 mm slit opening.

Figure 4.15: Effect of different high voltages on the bottom wire on the profile measurement.

The second approach to test the electric field uniformity is to move the IPM stepwise through the beam. The IPM was moved from -12 mm up to +8 mm out of its central position hitting the limits of the active area of the strips and the furthest extension of the stepper motor respectively. The center of the peak was determined by a Gaussian fit and plotted vs. the actual detector position. A linear fit, given in Fig. 4.16(a), yields a conversion ratio of (0.97 ± 0.01) mm of profile movement for each mm the detector was moved. The deviation from the unity slope expected might be due to an insufficient calibration of the stepper motor.

During the scan the profile width changes slightly, as shown in Fig. 4.16(b). The variation in the profile width is not significantly larger than the error bars, but its "W" shape indicates a systematic effect probably due to field errors. This shape can be explained by electric field lines that are slightly tilted towards the field box center which results in a net focusing of large profiles. In the exact center of the IPM field

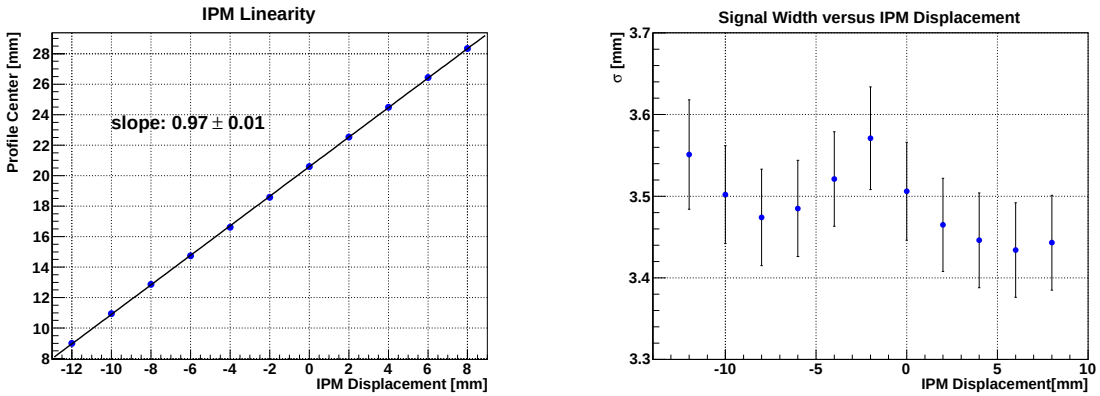

(a) Profile displacement versus IPM displacement.

(b) Profile width versus IPM displacement.

Figure 4.16: Displacement of the measured beam profile versus the IPM position at nominal IPM voltages, HV=5 kV.

box, the field lines are hence parallel and the proper profile is measured for small beam sizes. Outside of the center the focusing effect becomes stronger which reduces the measured profile width. At the very edge of the active width field distortion close to the slit holder above the read-out strips bend the electric field lines back. This field configuration can be seen in Fig. 4.7(b).

It can be concluded that the measures taken to optimize the electric field homogeneity did have their desired effect. Only by observing the profile width at different IPM displacements, an effect of the electric field errors was seen that is in good agreement with the FEM simulations and is still not significantly larger than the fit error.

Position Resolution

In the same experimental setup, also the position resolution of the IPM prototype was tested by reducing the step size of the stepper motor to 100 μm. As presented in Fig. 4.17(a), the IPM prototype was well capable of resolving 100 μm beam displacements.

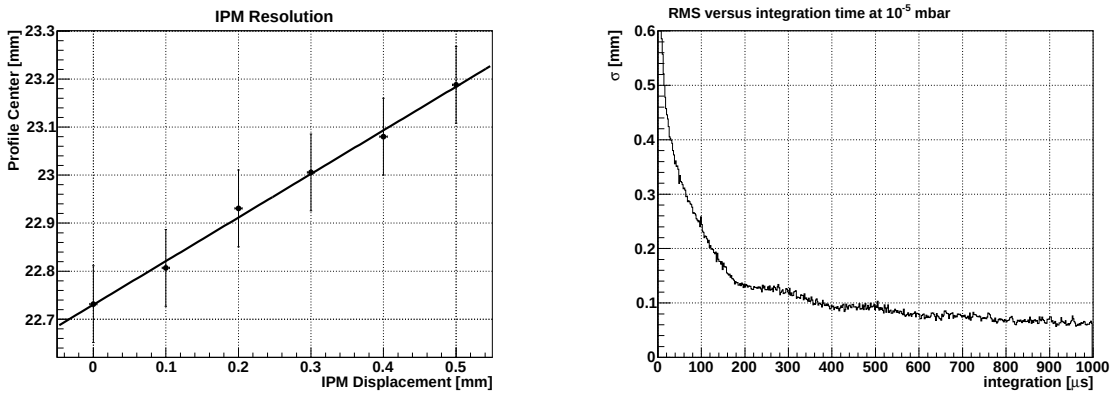

(a) Displacement of the measured beam profile versus the IPM position at 100 μm steps.

(b) Jitter of the profile center versus integration time.

Figure 4.17: The IPM position resolution determined in two different ways.

The resolution of the IPM strongly depends on the statistics available and thus on

beam current, integration time and residual gas pressure. For this reason, the position resolution as a function of the integration time was determined.

Under stable beam conditions, beam profiles were acquired using the linear transimpedance front-end electronics card over a long time. At first, the center of the beam profile was calculated for each reading of 2 μs duration separately and the standard deviation of this distribution was calculated. In a second step, the number of reading used to calculate the profile center was successively increased which allowed for a simulation of higher integration times which results in more precise calculations due to better statistics.

The result of this calculation method are given in Fig. 4.17(b) for a beam of 120 μA and a residual gas pressure of 10^{-5} mbar. The standard deviation reaches a plateau of about 100 μm after less than 1 ms. This measurement is in good agreement with the previous claim to be able to resolve beam shifts below 100 μm.

SEM Grid Profile Comparison

The resolution of 100 μm is only valid for the profile center. There are effects that can change the profile shape without affecting the profile center, e.g. the space charge of the beam or initial ion velocities. One way to effectively consider such effects is by comparing the acquired profiles with profiles acquired by other diagnostics devices that are less sensitive to such effects.

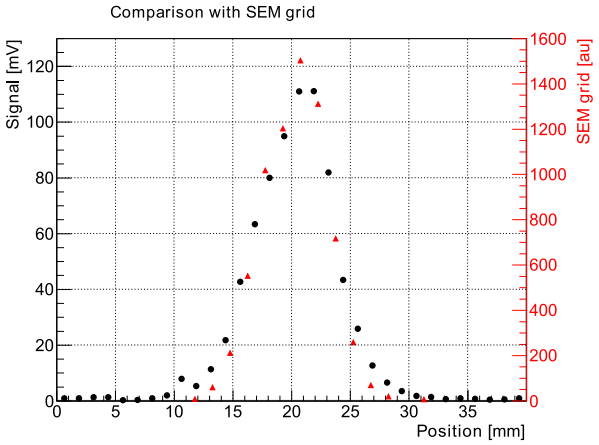

Figure 4.18: Comparison of the IPM profile with a SEM grid profile

Approximately 1 m upstream the IPM, a SEM-grid was mounted to compare the acquired profiles. Since a SEM-grid is an interceptive device that cannot withstand high beam powers, the pulse length of 5 ms was reduced to 200 μs not to damage the grid. The IPM profile over the entire 5 ms shows strong deviation from the SEM-grid profile. When the acquisition time of the IPM was reduced to the first 200 μs that were measured by the SEM-grid, both profilers provide similar profiles. In Fig. 4.18, the IPM profile is presented in black and in comparison the profile acquired by a SEM-grid in red.

The IPM profile appears to be slightly broadened w.r.t. the SEM-grid profile. Based on these measurements it is, however, impossible to determine, if this deviation is due to systematic error in the IPM or SEM-grid, or if the beam has changed its profile during the 1 m drift between SEM-grid and IPM.

This is why we decided to perform an additional profile comparison with a Beam Induced Fluorescence (BIF) monitor that can be mounted on the IPM chamber and can thus measure the beam profile in the same plane as the IPM.

BIF Profile Comparison

A BIF monitor of GSI [89], was mounted on the IPM cross in such a way that it can record the same beam profiles as the IPM. A sketch of the experimental setup is given in Fig. 4.19. The beam penetrates the cross perpendicular to the image plane. On top, the BIF camera is mounted on an image intensifier, and from the right side the IPM can be moved in.

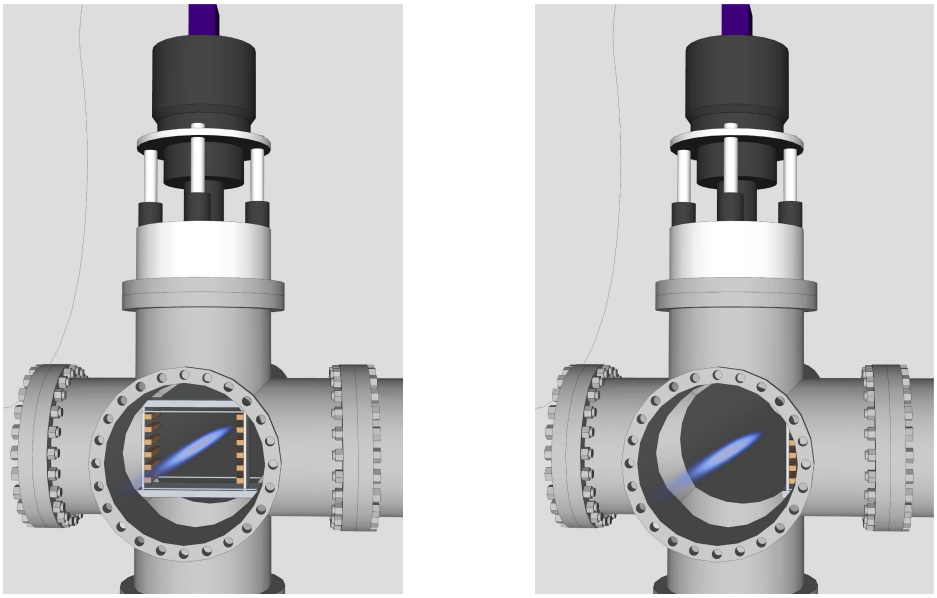

(a) The IPM is in the beam line and can measure the beam profile (IPM FEE on the right flange).

(b) The IPM is out of the beam line and the BIF can measure the beam profile (BIF camera mounted on the top viewport).

Figure 4.19: Sketch of the experimental setup with the IPM and the BIF monitor mounted on the same cross.

Since the IPM field box blocks the sight on the beam, it has to be moved out of the beam for BIF profile measurements. Profile measurements at the same time are therefore not possible. We assume, however, that the beam does not vary within the short time between the IPM and BIF measurements.

Since both profile monitors, BIF and IPM, derive their profiles from the residual gas, it is to be expected that the residual gas has an impact on the profile measurement. For an 1 mA Xe^{21+} beam, we have measured and compared beam profiles in nitrogen, helium, neon, argon, krypton, and xenon. In Fig. 4.20, the profile comparison in nitrogen is presented exemplarily. In Fig. 4.20(a), the profiles at a residual gas pressure of 10^{-6} mbar and in Fig. 4.20(b) for 10^{-5} mbar gas pressure are shown. While the statistics is lower at 10^{-6} mbar, the BIF and IPM profiles match nicely at both residual gas pressures.

The detailed profiles of all the different residual gases are included in Appendix B. Table 4.6 summarizes the beam profile widths measured by the IPM and the BIF

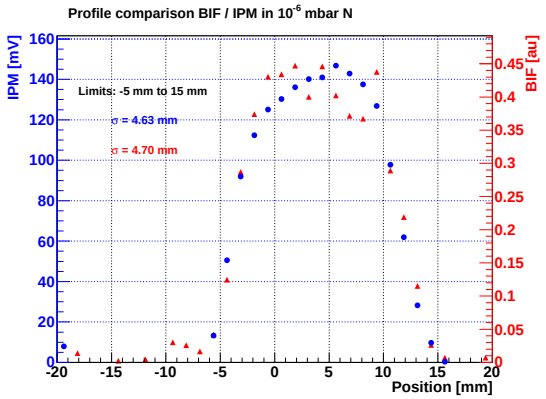

(a) Profiles at 10^{-6} mbar nitrogen.

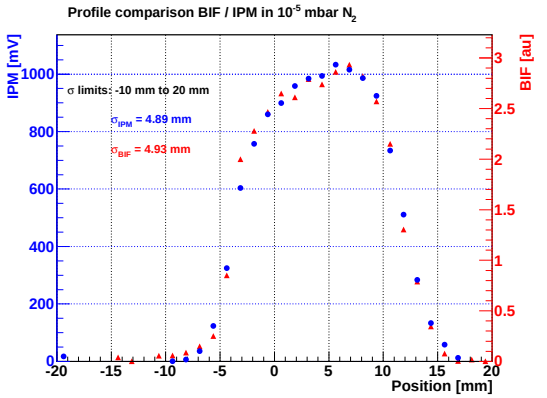

(b) Profiles at 10^{-5} mbar nitrogen.

Figure 4.20: Comparison of beam profiles acquired by the IPM (blue) and the GSI BIF monitor (red).

monitor in the different residual gas types and pressures. After each measurement with one residual gas type, the accelerator was flushed with the new gas to avoid any contamination of the previous residual gas. This was normally done within one or two hours. The entire measurement took thus more than seven hours.

While the beam was very stable, it was still observed that the beam current during the measurement dropped from 1.1 mA down to 750 μA and the profile shrunk from 5 mm in RMS (N_2) to 4.2 mm (Xe). The profiles acquired at different residual gases can therefore not be compared. However, the IPM and BIF profile measurements commonly match for all gases and all pressures within $\sim 100\,\mu$m. At 10^{-6} mbar, the fluctuations are systematically higher due to the lower statistics available.

Table 4.6: Comparison of the IPM and BIF profile widths at different residual gases.

	10^{-5} mbar						10^{-6} mbar			
	N_2	He	Ne	Ar	Kr	Xe	N_2	He	Ne	Xe
IPM [mm]	5.01	4.76	4.30	4.21	4.16	4.17	4.63	4.61	4.19	4.03
BIF [mm]	4.93	4.74	4.28	4.03	4.20	4.24	4.70	4.70	4.43	4.15

The calculation of the RMS is strongly influenced by the background noise. To reduce this effect the RMS was only calculated in the actual profile region. For all gases, except for nitrogen, a region from -5 mm to +15 mm was used. Due to the already large profile in nitrogen that still greatly increased at lower extraction fields, a region from -10 mm to +20 mm was chosen.

By varying the extraction voltage, one can estimate profile distorting effects, like space charge or initial velocities of the ions. At lower extraction fields, these effects will have a larger impact and thus larger profiles will be measured. Voltage scans for all the residual gases are presented in Fig. 4.21. The dashed lines are the measured BIF profile widths.

With increased extraction fields the profiles shrink since space charge effect and initial particle velocities become less and less significant. When the extraction field is strong enough to dominate any other effect, the measured profile should be the actual beam

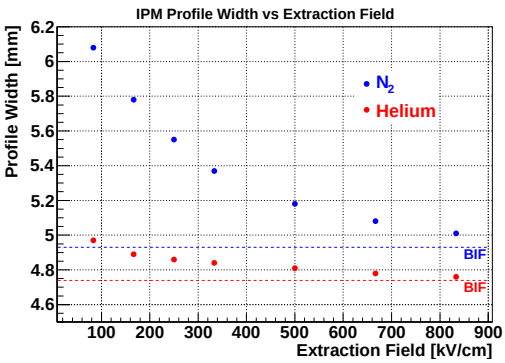

(a) Profile widths in N_2 and helium.

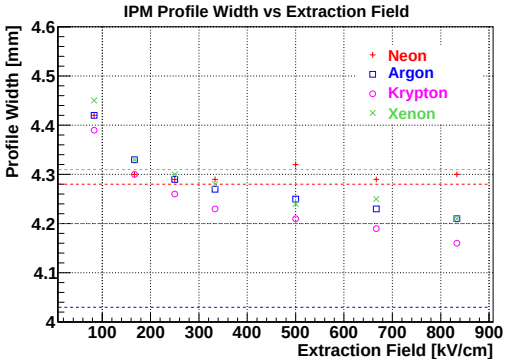

(b) Profile widths in the other tested noble gases.

Figure 4.21: Profile width in different residual gases versus the IPM extraction field.

profile, if the extraction field is uniform, as it was simulated, see section 4.4.1, and experimentally verified, see section 4.4.2.

IPM Profile Broadening in Nitrogen

For the noble gases, see Fig. 4.21(b), the measured beam profiles hardly shrink any more at high extraction fields, i.e. the state is achieved where the extraction field is dominant and the actual beam profile is measured. For nitrogen in Fig. 4.21(a), however, the profile shrinks by over 1 mm and appears to keep shrinking even at the IPM nominal extraction field of 833 V/cm.

A possible explanation for this effect might be the dissociation of the nitrogen molecule in two nitrogen atoms, an effect that cannot occur for the atomic noble gases. In literature, the kinetic energy of the dissociated nitrogen atoms was found to be roughly independent of projectile types and energy [101, 102, 103]. The kinetic energy of nitrogen ions emitted under 90° w.r.t. the projectile incidence has a continuous spectrum from 2 - 10 eV with a peak at 4 eV.

A 4 eV nitrogen atom has a velocity of $v = \sqrt{2E/m} = 7.4\,\mathrm{mm}/\mu\mathrm{s}$. At nominal extraction field strength of 833 V/cm, this results in a displacement of 2.4 mm during the 324 ns long drift towards the read-out strips. At a reduced extraction field of 83 V/cm, this displacement increases to even 7.6 mm.

For a profile width of ~ 5 mm, dissociated nitrogen ions even from the central beam region will be collected far outside the actual profile. It is to be expected that at weaker extraction fields, the IPM profile shows tails that effectively increase the RMS profile width. This effect can be seen in Fig. 4.22. In Fig. 4.22(a), the IPM profile measured at a high extraction field matches nicely the BIF profile which is less sensitive to this effect. In Fig. 4.22(b), the actual profile broadens only a little, but the already existing tails become more prominent.

Ionization cross sections for dissociative and non-dissociative ionization were not available in literature for these specific beam settings. In section 4.2, it was already stated that the single ionization cross section for 6 MeV protons on hydrogen molecules is two orders of magnitude higher than for dissociative ionization, see Fig. 4.2. For nitrogen bombarded by 100 keV protons however, Luna et al. [101] found the dissociative ionization channels to be almost as important as the non-dissociative ones.

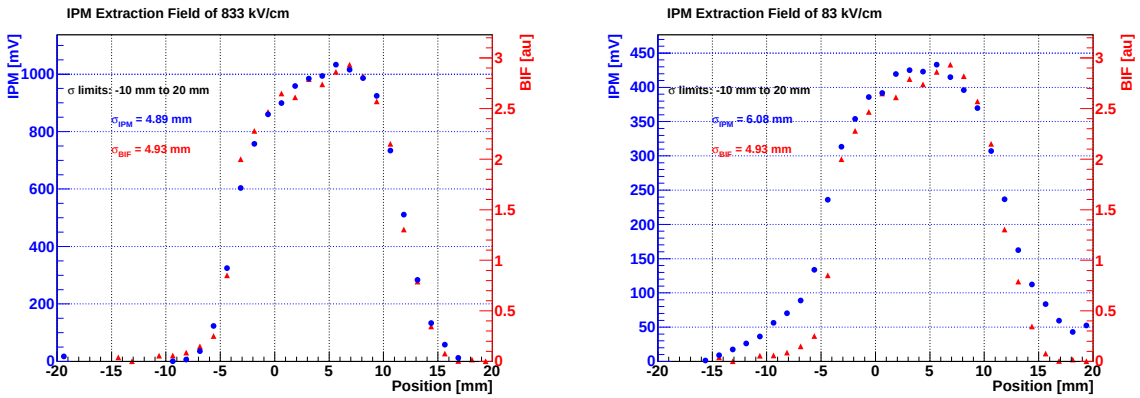

(a) IPM extraction field of 833 V/cm.

(b) IPM extraction field of 83 V/cm.

Figure 4.22: IPM profiles in nitrogen as residual gas at strong and weak extraction fields. For a better comparison, the BIF profile is plotted as well.

BIF Profile Broadening in Helium

It was already well known at GSI that helium as residual gas results in a strong profile broadening at high residual gas pressures [104, 105]. At GSI, it was assumed so far that this broadening can be explained by metastable excitation states of the helium atom.

Due to the selection rule that optical transitions are only possible between states with $\Delta l = \pm 1$, the transition from excited state 1s2s to the ground state is formally forbidden. This state consists of three degenerated states with j=1, the triplet states, and of the singlet state with j=0. The lifetimes of both metastable states have been measured by Baldwin [106] to be 19 ms for the singlet and 8000 s for the triplet state. These lifetimes are far longer than the beam pulse of 250 μs and light coming from these transitions can therefore be fully neglected.

However, at higher residual gas pressures the natural lifetime of these metastable states will be decreased by inter-atomic collisions and light coming from them will contribute to the acquired profiles. But since this light was emitted with a significant delay during which the excited atoms have drifted randomly, the acquired profiles will appear broadened.

This explanation is purely based on optical transitions and should therefore have no effect on the profile measurement of the IPM. At 10^{-6}, 10^{-5}, 10^{-4}, and $5 \cdot 10^{-4}$ mbar, beam profiles have been acquired by the IPM and the BIF. To account for the additional noise at high residual gas pressures, a supplemental offset correction has been performed. The profiles are given in Fig. 4.23.

At 10^{-4} mbar, the BIF profiles gets slightly broadened, but more remarkably, profiles from IPM and BIF show both an asymmetric tail on the left hand side which becomes even more prominent at higher residual gas pressure. Since it is observed by IPM and BIF and since it appears to be asymmetric, this tail in the profile is probably not an artifact, but a real beam property.

At $5 \cdot 10^{-4}$ mbar, the BIF profile is greatly broadened while the IPM has hardly changed apart from the asymmetric tail. The IPM profile width increases slightly from 4.8 mm at 10^{-5} mbar over 5.1 mm at 10^{-4} mbar up to 5.2 mm at $5 \cdot 10^{-4}$ mbar. This increase is probably due to the tail of the beam.

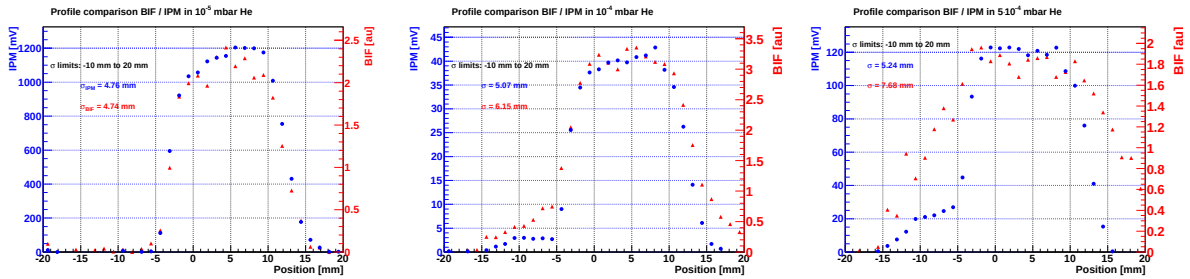

(a) Profiles in helium at 10^{-5} mbar.

(b) Profiles in helium at 10^{-4} mbar.

(c) Profiles in helium at $5{\cdot}10^{-4}$ mbar.

Figure 4.23: IPM and BIF profiles acquired in helium at different residual gas pressures.

One can conclude that the measurement is in good agreement with the above given explanation of the BIF profile broadening due to metastable excitation states, since the IPM profiles remain almost unchanged. As the residual gas at LIPAc will consist mostly of deuterium at $\sim 10^{-7}$ mbar, such effects are not to be expected at LIPAc.

Signal Amplification Effect

Another important quantity that varies for different residual gas and with the extraction voltage is the integrated signal. Since the IPM signal depends on the residual gas pressure, the vacuum gauge needs to be calibrated for an absolute signal comparison. Assuming a linear correlation between the residual gas pressure and the IPM signal, the signal can be scaled to correct for residual gas pressure variations due to the different gauge sensitivities. Conversion factors have been used according to indications of the manufacturer given in Table 4.7 [107].

Table 4.7: Pressure conversion factors to determine the actual pressure of different gases, given by the manufacturer [107].

Gas	N_2	He	Ne	Ar	Kr	Xe
Scaling factor	1	5.0	4.1	0.8	0.5	0.4

The integral signal of each profile scaled on the beam current and the corrected vacuum pressure is given in Fig. 4.24. The integrated signal is plotted versus the average kinetic energy of the ions which is directly proportional to the extraction field. For each residual gas the signal rises linearly with the ion energy, i.e. the IPM extraction voltage. Linear fits have been performed for each residual gas type indicating the fit function in the graph.

We assume that the signal amplification at higher extraction fields is due to the emission of secondary electrons from the read-out strip surface. The secondary electron yield is defined as the mean number of electrons released from a surface per incident ion. This yield is projectile, energy, and target dependent and was already discussed in detail in section 3.4.

One commonly distinguishes between kinetic and potential emission. In the case of kinetic emissions, the energy required for the electron to overcome the work function of the metal is provided by the kinetic energy of the incident ion. In the case of

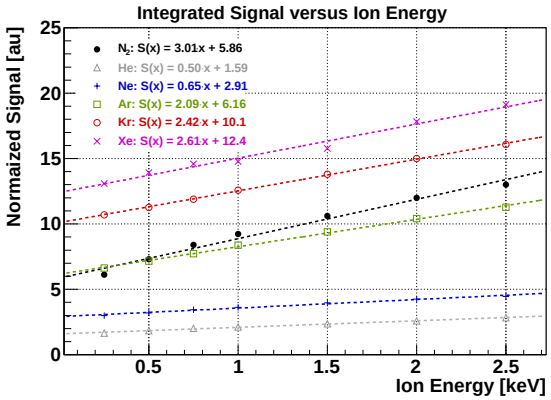

Figure 4.24: Integrated IPM Signal versus kinetic energy of the ions on the level of the read-out strips.

potential emission, the metal work function is overcome by the energy released during the neutralization of the incident ion. The kinetic emission therefore depends on the ion energy, the potential emission does not.

From the IPM signal readings, we can calculate a total electron emission yield that is required to explain this signal amplification. The y-intercept of the fit function is the charge deposition on the read-out strips, if the ions arrived at zero velocity. It can thus be considered as the actual ion current plus the contribution of the electrons due to the potential emission. The potential electron emission yields were calculated by Zalm et al. [108] and are given in Table 4.8.

Table 4.8: Potential secondary electron emission yields for copper from literature [108].

Helium	Neon	Argon	Krypton	Xenon
0.29	0.23	0.08	0.05	0.00

Based on these literature values for the potential emission yields, a total electron emission yield can be calculated. The resulting SEM yields are plotted in Fig.4.25(a). As comparison, Fig. 4.25(b) shows SEM yields measured by Magnuson et al. [109].

Electron yields from ion bombardment are available in literature for various target materials and projectile ion type and energy. Electron yields for low energy noble gases on copper have been measured by Baragiola [74, 77], Zalm [108], Magnuson [109], and Carlston [110]. Literature values and values calculated from the IPM data are given in Table 4.9 for an ion energy of 3 keV. Values are taken from graphs with an assumed reading error of 10 %.

It is obvious that the electron emission yields calculated from the IPM data exceed the literature values by a factor of $3-4$. However, for measurements dedicated for the electron yield determination, the target materials were thoroughly rinsed, etched and sputtered since it is known that surface contamination can drastically change the electron yield. Ferron et al. [111], for instance, investigated the effect of oxidation layers upon aluminum targets on the electron yield for 30 keV Argon ion bombardment. The electron yield was found that to be increased by up to 100 %. In the analysis, it was stated that this increase can be attributed to electron emission from the surface oxide layer only. A quantitative model could unfortunately not be provided. However, as

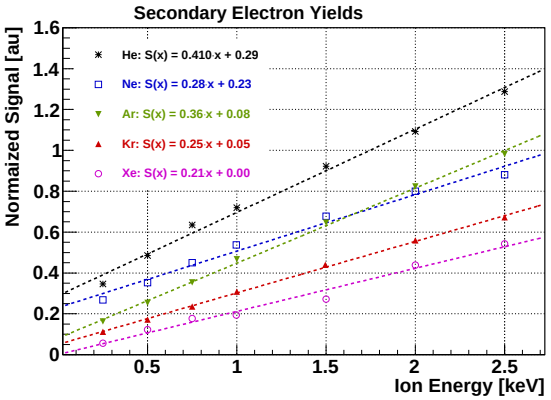

(a) Secondary electron emission yields calculated from the signal amplification of the IPM.

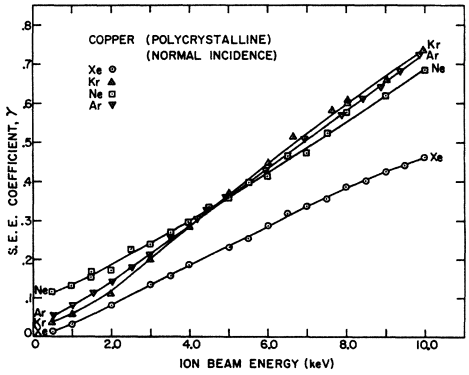

(b) Secondary electron emission yields from copper under the bombardment of noble gases [109].

Figure 4.25: Signal amplification at stronger extraction fields and the secondary electron emission yields measured by Magnuson et al. [109].

Table 4.9: Secondary electron emission yields for copper from literature and yields calculated from the IPM data [74, 77, 108, 109, 110].

	Baragiola	Zalm	Magnuson	Carlston	IPM
He	0.39	—	—	—	1.52
Ne	—	0.35	0.25	0.3	1.07
Ar	0.28	0.29	0.21	0.33	1.16
Kr	0.25	0.29	0.2	0.3	0.80
Xe	—	0.19	0.14	0.2	0.63

the penetration depth decreases at lower projectile energies, it is to be expected that such a surface effect has an even stronger impact for the 2.5 keV ions present in the IPM than for the 30 keV ions analyzed by Ferron et al.

Even though the electron yields derived from the IPM data are much higher than the literature values, the yields for different gases can be compared with respect to one another. For neon, argon, and krypton, electron yields are comparable and available in almost all sources. The mean value is therefore a good scaling quantity. In Table 4.10, the secondary electron yields are given scaled by the average yield of neon, argon, and krypton (only argon and krypton for the yields of Baragiola due to the lack of data for neon).

Table 4.10: Normalized secondary electron emission yields from literature and from the IPM data [74, 77, 108, 109, 110].

	Baragiola	Zalm	Magnuson	Carlston	IPM
He	1.47	—	—	—	1.50
Ne	—	1.13	1.14	0.97	1.06
Ar	1.06	0.94	0.95	1.06	1.15
Kr	0.94	0.94	0.91	0.97	0.79
Xe	—	0.61	0.64	0.65	0.62

The electron yield for helium is by about 50 % increased, for neon, argon, and krypton they are on the same level, and for xenon they are decreased by about 40 % which is in good agreement with the literature values. Given the experimental setup which was not designed for such a measurement, the acquired values are in good agreement with the literature values and confirm the theory of a charge amplification effect due to secondary electron emission.

The result might encourage considering the use of new strip materials to take advantage of this amplification mechanism and to thereby maximize the IPM signal output. However, experimental values of secondary electron emission yields from metals with oxidation surface layers are scarce and extrapolations from rinsed and etched materials hardly admissible.

Conclusion

The IPM prototype was thoroughly tested at GSI for low and intermediate beam currents between 30 μA and 1.7 mA. One can conclude that the IPM prototype performs very well and that most properties are well understood in this current regime.

However, since beam current of up to 125 mA are expected at the LIPAc, additional tests at high intensities and high space charge beams have been performed at CEA Saclay.

4.4.3 Prototype Tests at CEA Saclay

The SILHI source of the IPHI injector at CEA Saclay is able to deliver a pulsed or continuous 95 keV proton beam of up to 100 mA [112]. Due to the low energy, very high space charge effects can be realized even at moderate beam currents, since the linear charge density is given by I_{Beam}/v. A proton beam of 10 mA at 90 keV has thus the same charge density as a 71 mA deuteron beam at 9 MeV. A photo of the IPHI injector with IPM prototype upstream the beam dump is shown in Fig. 4.26.

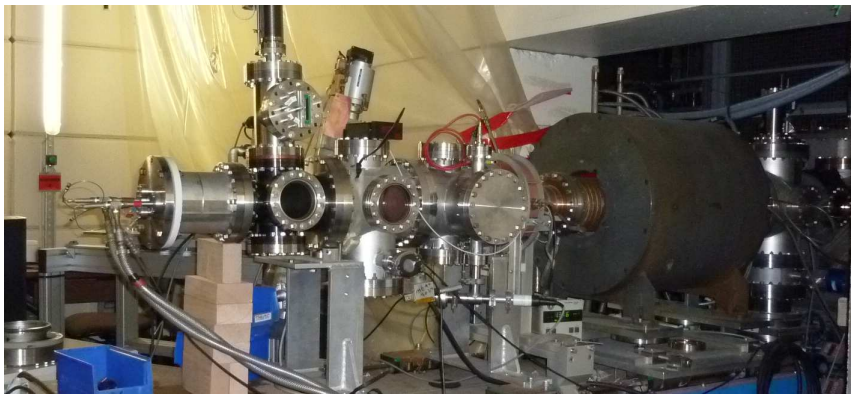

Figure 4.26: Photo of the IPM prototype mounted on the SILHI beam line.

A major problem during the test was an increased current on the HV power supply. For a cw beam of 3 mA, the current consumption of the HV power supply of the IPM is presented in Fig. 4.27. Even at low extraction voltages on the IPM field box, the current rises rapidly and reaches a plateau at about 2 mA. We assume that this current is due to electrons generated by the beam during collisions with the residual

gas or by secondary electron emission on the beam pipe due to lost beam particles. The only way to overcome this issue was to reduce the IPM extraction field and to use power supplies capable to supply higher currents.

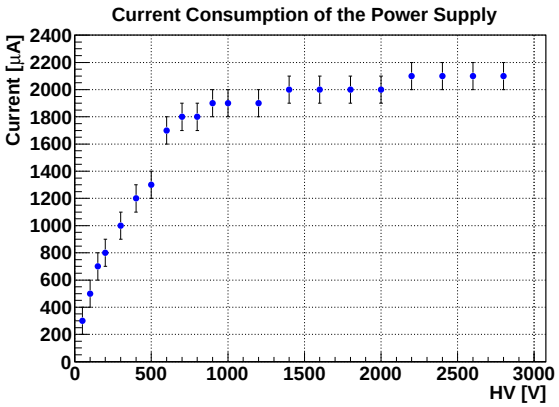

Figure 4.27: Current on the HV power supply for a cw beam of 3 mA.

With reduced extraction voltages, we were able to measure beam profiles at high beam currents, in continuous wave (cw) mode up to 10.5 mA and up to 21 mA at a reduced duty cycle of 10 %, i.e. one 100 ms pulse per second. Profiles at 3 mA and at 10.5 mA are presented in Fig. 4.28.

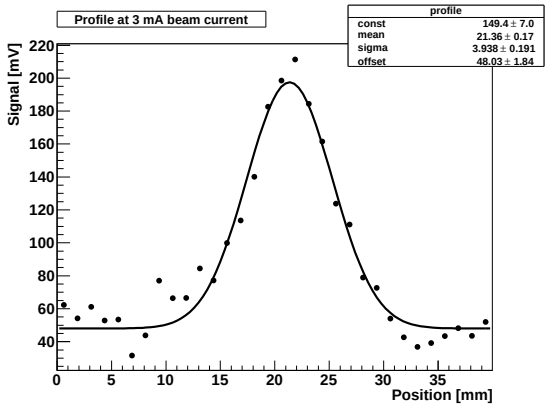

(a) Beam profile of a 3 mA cw proton beam at 90 keV.

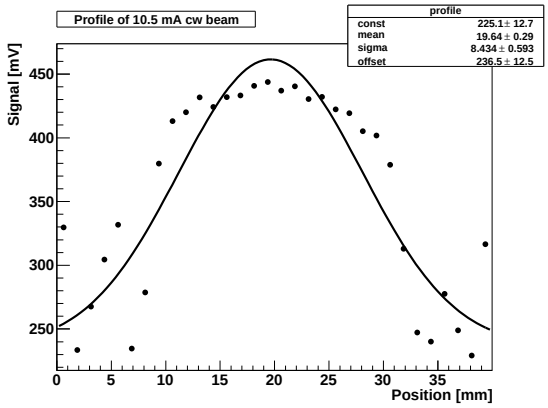

(b) Beam profile of a 10.5 mA cw proton beam at 90 keV.

Figure 4.28: Beam profiles measured during the prototype test at the SILHI source of the IPHI injector at CEA Saclay.

In both profiles one can nicely see the increased background due to the beam halo and secondaries. With reduced IPM extraction voltages, distortions due to the space charge of the beam are even more significant. A profile comparison as it was done at GSI was impossible since we could not mount any BIF cameras on our cross to measure in the same plane. BIF cameras that were mounted up- and downstream to the IPM provided incomparable profiles since the beam was highly divergent, as shown in Fig. 4.29.

The profile at 3 mA is probably already broadened by the space charge effect, but at 10.5 mA in Fig. 4.28(b), the profile shows a rectangular shape which is typical for strong space charge distortions. The effects of the space charge on the measured profiles are discussed in detail in section 4.6.

To evaluate the effect of the space charge of the beam profile, profiles have been acquired by IPM and BIF monitors for different beam currents. For each current the

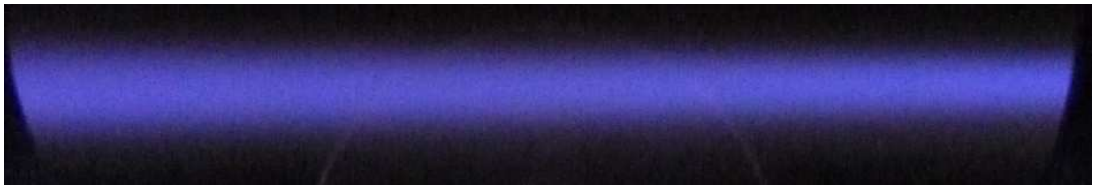

Figure 4.29: Photo of a 90 keV proton beam in the IPHI injector.

whole accelerator settings had to be changed which also affected the beam size. The RMS sizes of the acquired profiles are presented in Fig. 4.30.

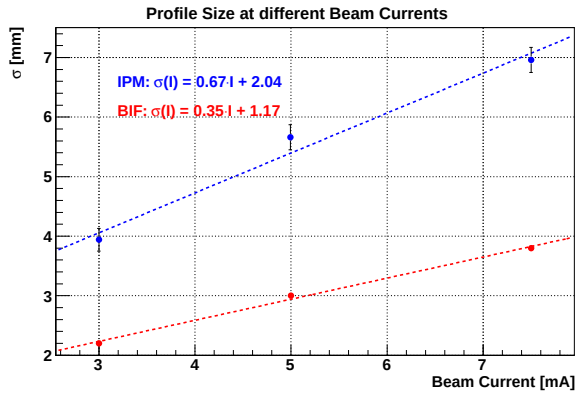

Figure 4.30: A comparison of the beam profile widths measured by IPM and BIF at different cw beam currents.

The space charge effect can be estimated by assuming

- that the BIF profilers are not affected at all and
- that the evolution of the beam during its drift from the BIF monitor to the IPM is independent of the beam current.

The y-intercept of the linear fit of the IPM data is 0.9 mm larger than for the BIF data, i.e. without any space charge the beam is 0.9 mm larger in the IPM than in the BIF. At 7.5 mA beam current, the IPM profile is 3.2 mm broader than the BIF. Assuming that the actual beam expansion between BIF and IPM does not depend on the beam current, 2.3 mm (= 3.2 - 0.9 mm) are due to space charge.

The IPM prototype was well capable of taking profiles at the high-current cw beams of the IPHI injector. The huge amount of secondary electrons in the beam pipe made it necessary to reduce the extraction voltages and to use stronger power supplies. The profile broadening due to space charge at the IPHI injector is particularly strong due to the low beam energy and the necessity to reduce the extraction voltages.

But this test proves that for high-current beam profile measurements techniques must be found to overcome the space charge effect.

4.5 Final LIPAc IPMs

The IPM prototype was designed to study the general properties of an IPM. For the design of the final LIPAc IPMs, the actual requirements and restrictions of the LIPAc must be considered.

4.5.1 Positioning of the IPMs

Originally, three IPMs were foreseen for the LIPAc accelerator, one on the MEBT, one on the D-plate, and one on the HEBT upstream the beam dump. The IPM on MEBT was finally dismissed due to a lack of space.

HEBT IPM

The LIPAc beam dump must be able to withstand the 1.1 MW beam power. The IPM upstream the beam dump is supposed to ensure that this power is deposited uniformly on the dump to prevent damage.

The space available for diagnostics on the HEBT is very limited. Originally, 250 mm have been foreseen to mount three different types of profilers, a BIF, an IPM and a SEM-grid. By optimizing the HEBT assembly, an additional 110.5 mm could be liberated. The profilers must still be designed in a very compact fashion to mount all of them in the available 360.5 mm.

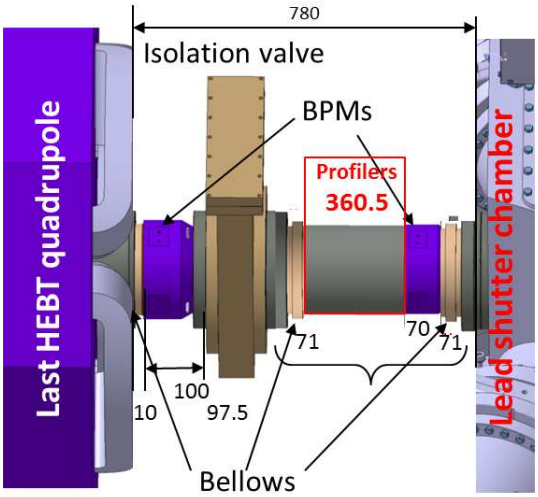

Figure 4.31: Schematic drawing of the HEBT assembly, indicating the different components and the 360.5 mm available for the profilers, by courtesy of Beatriz Brañas (CIEMAT)

Due to the beam dump, the residual gas pressure is expected to be very high in this region, $\sim 10^{-5}$ mbar. This will result in a very high IPM signal, but probably also in an increased noise level due to secondary particles from the beam dump. The dump also emits a huge level of radiation, mostly γ and neutrons. The IPM must therefore be very radiation tolerant.

D-plate IPM

The diagnostics plate will be an accelerator section that is devoted to beam diagnostics and that will be mounted at the end of each accelerator subsection during the commissioning. In the final stage of the LIPAc, the D-plate will remain in the accelerator downstream to the SRF linac.

Due to its close proximity to the SRF linac, the vacuum pressure will be quite low between 10^{-8} and 10^{-7} mbar which greatly decreases the IPM signal. Since the D-plate is devoted to diagnostics, more space for the IPM is available here than in the other sections.

4.5.2 Vacuum Conditions

Since the signal strength of a residual gas monitor scales linearly with the residual gas pressure, it is of particular importance for the IPM. At CIEMAT, simulations of the pressure along the HEBT have been performed that are presented in Fig. 4.32.

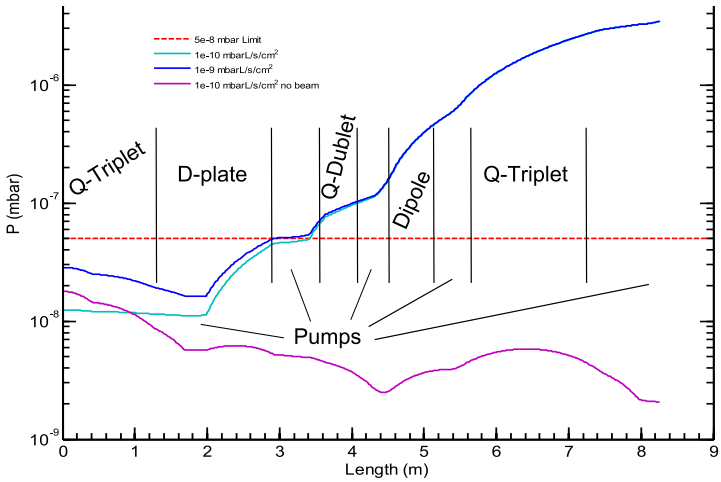

Figure 4.32: Expected vacuum pressure downstream the SRF linac indicating also the qudrupole dublet / triplets, the D-plate, and the bending dipole [113].

With the beam ON, the pressure rises up to $\sim 10^{-5}$ mbar close to the beam dump. In pulsed mode, the residual gas pressure will be lower. One can nicely see four buckles in the pressure curves that can be identified with the four pumping stations along the HEBT. The main constituent of the residual gas is expected to be deuterium gas coming from the beam dump.

4.5.3 Radiation Hard Design

A device is always only as radiation hard as its weakest component. This component is commonly the front-end electronics which has to be placed at remote distance or needs additional shielding. The design of such a shielding to ensure the protection of the electronics is costly and time-consuming. However, the alternative, to place the electronics outside of the accelerator vault and to connect them by long cables can result in strong profile distortion due to the cable capacitance.

Other commonly radiation weak components are optical read-out devices like cameras. This is why we opted for the strip read-out. γ can extract some electrons from the copper strips which will result in an increased background, but such an offset can be easily subtracted.

Multi Channel Plates (MCPs) are commonly used to amplify the signal of an IPM. While they are intrinsically radiation hard, they are sensitive to any particle that can extract electrons from its surface, i.e. also γ. This can greatly increase the noise level

and can also lead to an accelerated aging since the amount of charges that can be extracted from an MCP channel is limited.

The materials of the IPM field box themselves have to be chosen carefully. Metals are considered to be very radiation tolerant. For all insulators, ceramics have been chosen. Ceramics have the appeal of being good thermal and bad electric conductors. Heat, which might be deposited on detector by radiation, cannot disperse over the air, but has to be conducted to the beam pipe. A good thermal conductor like ceramics can effectively prevent damage from overheated detector components.

On insulating surfaces, electric charges can be deposited by radiation. These charges can generate extremely high voltages that can lead to discharges at worst, or distort the electric extraction field in the field box at best. While the low electric conductivity of the ceramics allows it to hold high voltages with only very low leak currents, it allows for deposited charges to flow off and thus to prevent dangerous charge accumulations.

A good way to reduce radiation damage is generally to reduce the amount of material that is irradiated. If there is a preferential direction where the radiation comes from, like the beam dump for LIPAc, devices can be placed in such an orientation to minimize the irradiated cross section. This way, the final IPM versions will be equipped with SMD resistors soldered on the degraders backsides, instead of the bulk resistors used for the IPM prototype.

Another significant difference to the IPM prototype is that the final IPMs are designed with an aperture larger than the actual beam pipe. This way the IPM is not only at safe distance to the accelerator beam, but the beam pipe itself acts as shielding against primary and secondary particles for the IPM field box.

4.5.4 IPM Field Box Designs

All IPMs field boxes were designed based on FEM simulations of the electric extraction field. All of them were designed to provide the best possible electric field uniformity considering the limiting factors of the environment where they will be mounted.

MEBT IPM Design

The beam diameter on the MEBT is 50 mm which allows for a rather compact IPM field box which is also necessary as the available space on the MEBT is very limited. A design drawing of the IPM is shown in Fig. 4.33(a). Since there is not enough space to place two IPM field boxes to measure x- and y-profile, it was decided to mount the IPM field box on a ring gear in the beam pipe to be able to rotate it to measure the other profile. A conceptual design drawing of this rotating mechanism is presented in Fig. 4.33(b).

On the MEBT, only very little space is available which makes the design of a good electric field box particularly challenging. The design was chosen similarly to the prototype design with nine degrader pairs on both sides and correction electrodes to minimize the effect of fringe fields. To save some space the correction electrodes were not outside the field box as for the prototype, but embedded in the field box itself, as

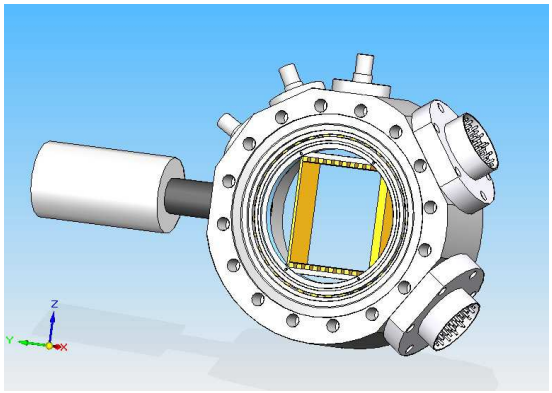

(a) Design Drawing of the MEBT IPM mounted in beam pipe.

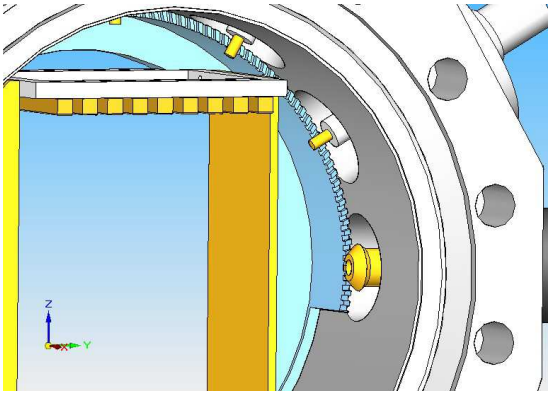

(b) Design drawing of the rotation mechanism of the MEBT IPM.

Figure 4.33: Design drawings of the MEBT IPM, by courtesy of J.-Ph. Mols (CEA Saclay).

can be seen in Fig. 4.34(b). This allows for larger and thus more effective degrader bars.

The nominal voltage on the HV-plate was 5 kV, on the correction electrodes 1 kV and 10 kV respectively. The resulting horizontal electric field component in the central IPM is presented in Fig.4.34(a) as color scale and the total extraction field as streamlines. The color scale is limited to ± 3 kV/m, i.e. 3 % of the average extraction field. The extraction field uniformity is thus even better than for the IPM prototype.

In Fig. 4.34(b), the electric potentials and the electric field lines are presented in longitudinal direction. Here, one nicely see that the extraction field of an asymmetric IPM field box, with positive HV on one side and grounded strips on the other, is strongly affected by the grounded beam pipe, which is in close proximity to the IPM.

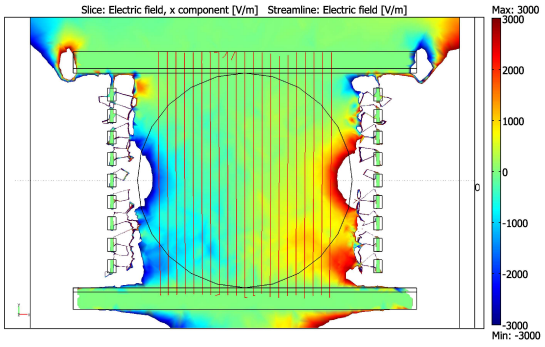

(a) Horizontal electric field component.

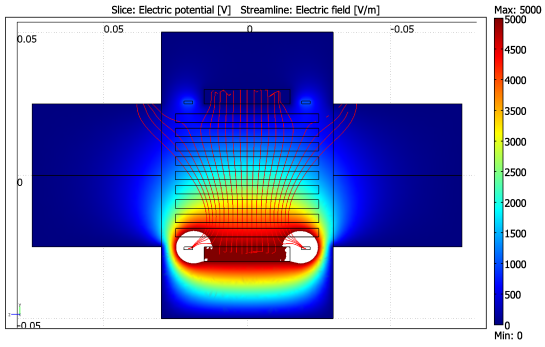

(b) Electric potentials in the field box.

Figure 4.34: FEM simulations of the extraction field of the MEBT IPM field box.

Due to the compact design of the IPM field box, sparks can occur, if the distance between two HV elements is too short. With 1 mm of distance per kV applied on the components, sparks can commonly be prevented even at ambient pressure. This is a very conservative estimation since the breakdown voltage of high vacuum is much higher than for air.

This IPM will not be built due to a lack of space on the MEBT. It remained therefore in this preliminary design phase and neither the technical design nor the electric field optimization have been finalized.

HEBT IPM Designs

The IPM on the HEBT is supposed to measure the beam profile upstream the beam dump to ensure a uniform power deposition on the beam dump. The beam pipe diameter is 150 mm and the pressure is expected to be $\sim 10^{-5}$ mbar. Due to a lack of space, only a single IPM can be mounted to measure either x- or y-profile.

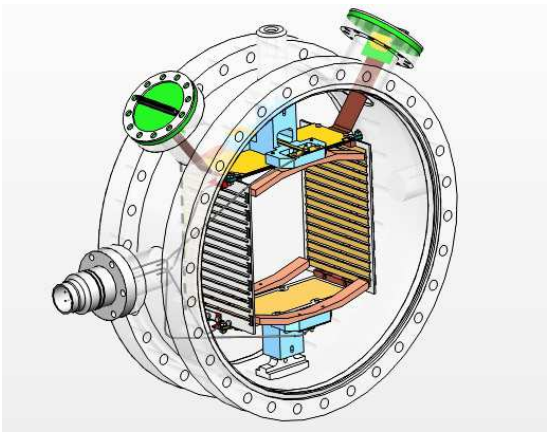

(a) Design drawing of the HEBT IPM field box, by courtesy of J.-Ph. Mols (CEA Saclay).

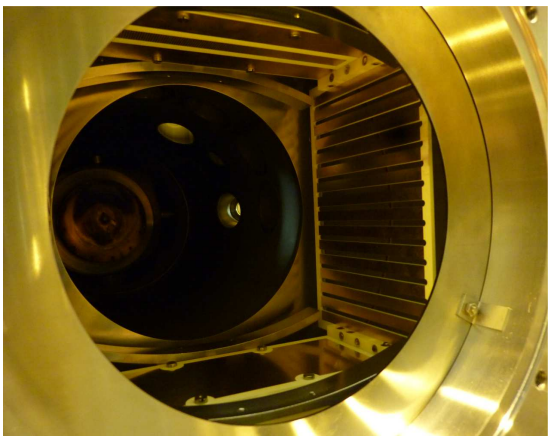

(b) Photo of the HEBT IPM field box mounted at the IPHI injector at CEA Saclay.

Figure 4.35: HEBT IPM field box.

A 3D design drawing of the IPM is presented in Fig. 4.35(a). The IPM field box has an aperture of 153 mm and is thus slightly larger than the beam pipe. This way, the IPM fulfills the beam stay-clear requirement of 150 mm within some margin and the beam pipe acts as shielding for the IPM. On the bottom plate, an HV of 7.5 kV is applied which results in an average extraction over 153 mm of 490 V/cm.

On the top plate 128 read-out strips are mounted with a spacing of 1.05 mm. The HEBT IPM has thus active range of 134.4 mm which covers almost the entire beam pipe diameter. The signal read-out is realized over two separate connectors with 64 pins each. Each connector covers one side of the read-out strips. In Fig. 4.35(a), these connectors are displayed in green. The HV connector is suitable for voltages up to 10 kV and can be seen in Fig. 4.35(a) to the left.

Table 4.11: Resistance values of the resistor chain for the degraders in the IPM field box.

Degrader	1	2	3	4	5	6	7	8	9
Voltage [V]	406	782	1082	1232	1533	1683	1984	2360	2585
Resistor [MΩ]	27	25	20	10	20	10	20	25	15

Degrader	10	11	12	13	14	15	16	HV plate
Voltage [V]	2961	3367	3742	4494	5245	5997	6748	7500
Resistor [MΩ]	25	27	25	50	50	50	50	50

The degrader consist of a metal deposition on a ceramic substrate. On the backside of the ceramic substrate, SMD resistors are soldered in as resistor chain to apply

appropriate voltages to each resistor. The resistances of the resistor chain and the resulting voltages on the 16 degrader stripes are given in Table 4.11.

The resistor values are chosen to optimize the electric field uniformity inside the IPM field box. The simulation result of the electric potential in the central IPM plane is presented in Fig. 4.36(a). The equipotentials are flat and parallel which indicates a good field uniformity.

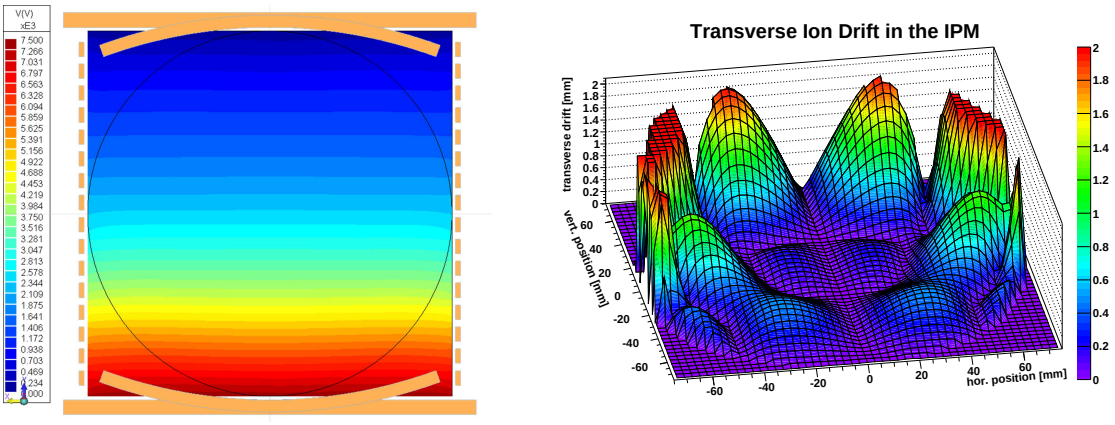

(a) Electric potentials in the central plane of the HEBT IPM field box.

(b) Displacement of ions during their drift to the read-out strips in the central IPM plane.

Figure 4.36: HEBT IPM extraction field simulation results.

The quantity of interest is, however, not the electric potential nor the extraction field, but the effect of the field on the ionization particles. When measuring a profile in x-direction, the displacement of an ion in x-direction during its drift to the read-out strips is of interest, since this displacement will result in profile distortions. For this purpose, a particle tracking in the extraction field has been performed. The ion displacement during the drift versus the initial ion position is plotted in Fig. 4.36(b). The strips are placed on the front part of the diagram, at -75 mm, where the ion displacement is minimum.

The particle tracking was implemented in Root and only considers the effect of the electric extraction field. Other effects like initial ion velocities due to thermal energy or momentum transfer during the collision or interactions with the accelerator beam are neglected.

Outside the 150 mm beam pipe, the values are set to zero, since no beam particles are expected to traverse the IPM in that region. In the center of the IPM field box, where the beam is expected, the ion displacement is only a few 100 μm. Towards the edges of the field box, the displacement rises up to 2 mm due to degrader imperfections. Close to the HV plate in the back, the drift rises as well significantly due to the long drift distance towards the read-out strips.

The technique of a particle tracking to evaluate the extraction field quality is particularly useful since some electric field non-uniformities will cancel out during the ion drift, if they are oppositely directed. The extraction field in the IPM field box has a focusing effect close to the HV plate and close to the read-out strips, and a defocussing effect in the center. In Fig. 4.36(b), one can see how the effect within the three regions cancel out and create lines of minimum displacement in some regions.

D-plate IPM Designs

The D-plate is dedicated for beam diagnostics. It is thus the only place where two IPMs can be mounted to measure x- and y-profiles. The beam pipe on the D-plate has a diameter of 100 mm and the residual gas pressure is expected to be $10^{-8} - 10^{-7}$ mbar.

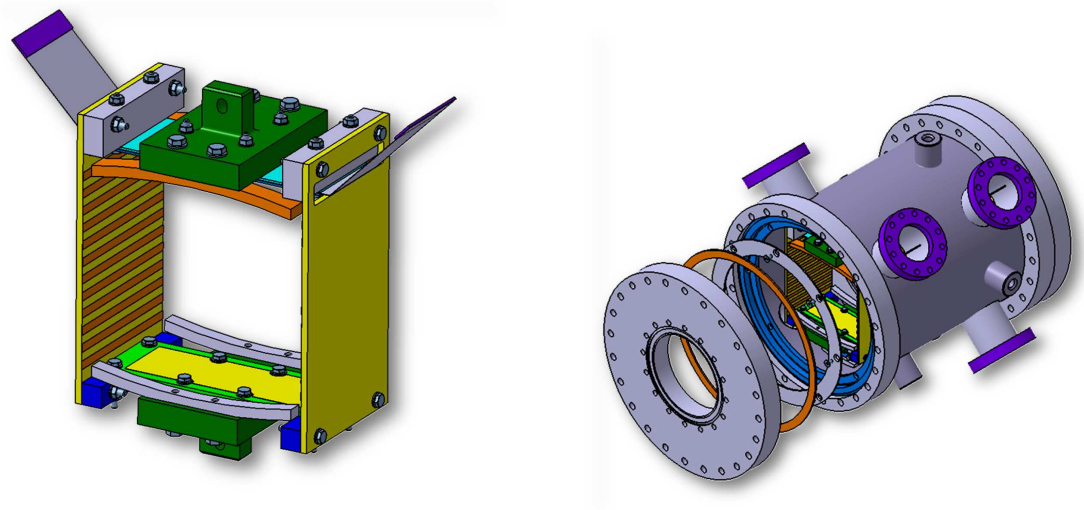

(a) Design drawing of the D-plate IPM field box.

(b) Design drawing of two D-plate IPMs mounted in one chamber

Figure 4.37: D-plate IPM design drawings, by courtesy of H. Przybilski (CEA Saclay)

A 3D design drawing of the IPM is presented in Fig. 4.37. The IPM field box has an aperture of 103 mm and is thus slightly larger than the beam pipe as it was the case for the HEBT IPM. On the bottom plate, an HV of 7.5 kV is applied which results in an average extraction over 103 mm of 730 V/cm. On the correction electrodes, 9750 V and 1100 V respectively are applied.

On the top plate 80 read-out strips are mounted with a spacing of 1.125 mm. The D-plate IPM has thus active range of 90 mm which covers virtually the entire beam pipe diameter. The signal read-out and the HV connectors are realized in the same way as for the HEBT IPM.

Table 4.12: Resistor values of the resistor chain for the degraders in the IPM field box.

Degrader	1	2	3	4	5	6	7
Voltage [V]	517	1033	1416	1932	2315	2698	3214
Resistor [MΩ]	27	27	27	20	27	27	27

Degrader	8	9	10	11	12	HV plate
Voltage [V]	3731	4688	5204	5587	6543	7500
Resistor [MΩ]	27	50	20	50	27	50

The degrader are designed as for the HEBT IPM field box as copper deposition on a

ceramic substrate. The voltages on each of the 12 copper stripes of the degrader and the resistors used to achieve these voltages are presented in Table 4.12.

The electric potentials of the D-plate IPM is presented in Fig. 4.38(a). The horizontal electric field component is within 1 % of the average extraction field. This D-plate IPM has thus the best extraction field uniformity of all the IPMs presented in this thesis.

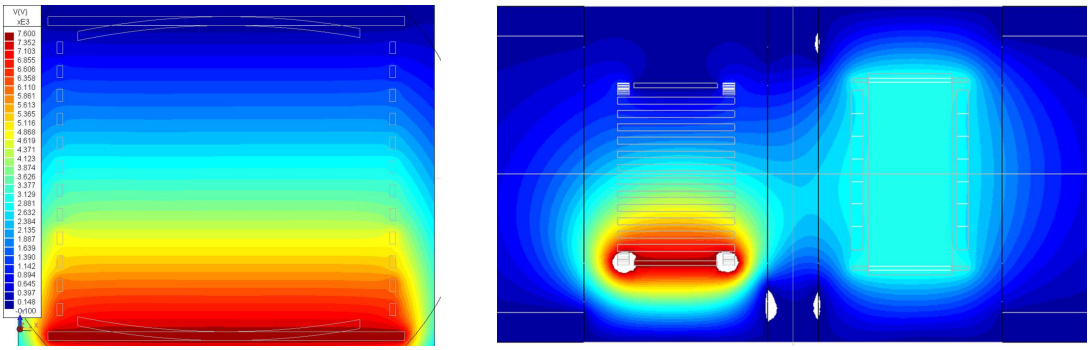

(a) Electric potentials in the central plane of the D-plate IPM field box.

(b) Electric potentials in the D-plate IPM field box in the longitudinal plane.

Figure 4.38: D-plate IPM FEM simulations of the electric extraction field.

For the D-plate IPM, there will be two IPM field boxes in close proximity to measure the x- and y-profile. The fringe fields of one IPM can distort the extraction field of the other IPM. To minimize this coupling two grounded rings are included in between the two IPMs. The resulting electric potentials in the longitudinal plane is presented in Fig. 4.38(b).

The coupling of the two IPM field boxes results in an asymmetry of the electric field distribution that dominates the electric field uniformity in spite of the grounded rings. In a second step, to reduce the effect of the coupling even further, the IPMs have been designed asymmetrically. The curved correction electrodes were shortened on one side by 5 mm. This provides a simple, but very effective measure to minimize the coupling between the two IPMs.

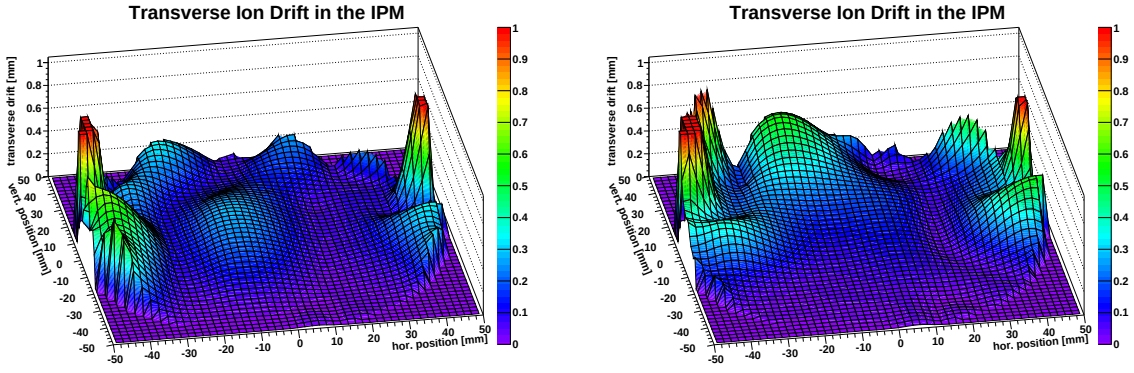

(a) Ion displacement with both IPMs ON.

(b) Ion displacement with only one IPM ON.

Figure 4.39: Ion displacement during the drift to the read-out strips of the D-plate IPM.

To evaluate the quality of the electric extraction field, a 3D particle tracking of the ionization products in the IPM field box has been performed. The ion displacement during their drift to the read-out strips versus the ionization position is presented in

Fig. 4.39(a). The bump in the central part of the IPM field box is due to the coupling of the two IPMs. The ion displacement in the entire active range is well below 300 μm.

It might be useful in some cases to measure one profile with the second IPM being switched OFF. Since the electric field was optimized with high voltages on both IPMs, the electric field uniformity will suffer, if the second IPM is switched OFF. In this case, the voltages on the correction electrodes will have to be adjusted to 10500 V and 1700 V respectively. The ion displacement for this configuration is presented in Fig. 4.39(b). One can see the asymmetric effect of the shortened correction electrode, but overall, the ion displacement is well below 500 μm.

IPM Parameters

The characteristics of both IPMs on the HEBT and on the D-plate are presented in Table 4.13.

Table 4.13: Summary of the parameters of HEBT and D-plate IPMs (values in brackets are for the operation of a single D-plate IPM).

	HEBT	D-plate
Planes	x or y	x & y
Installation length [mm]	120	268
Active length [mm]	10	10
Beam pipe ⌀ [mm]	150	100
Aperture [mm]	153	103
Read-out strips	128	80
HV plate [kV]	7.5	7.5
Extraction Field [V/cm]	490	730
Electrode 1 [V]	1200	1100 (1700)
Electrode 2 [V]	9500	9750 (10500)

4.5.5 Electronics

For the final IPMs, a front-end electronics based on charge integration will be used. The major advantage of integrating electronics is the very high dynamic range that can be realized by varying the integration time. During the commissioning of the LIPAc, the beam current will be slowly increased from 1 mA at a duty cycle of 10^{-4} up to 125 mA at full duty cycle. The average beam current will thus rise by over six orders of magnitude, a range which can hardly be covered by common electronics.

The front-end electronics consist of modules that can process 64 channels each and that were designed by Ph. Abbon (CEA Saclay). For HEBT and D-plate IPMs, the same modules are used in spite of the different channel number. For each IPM two modules are thus required. The principle of operation of integrating electronics is discussed in more detail in section 4.2.

The front-end electronics receives a trigger from the DAQ to start the charge integration. After the integration, the electronics transfer the signal reading to the DAQ. The DAQ multiplexes and digitizes the data, and allows for an online display of the profiles and for a data storage for post-processing. Unlike the ICs, no fast signals are required from the IPMs. The DAQ operates therefore at around 50 Hz only.

As the front-end electronics require a trigger from the DAQ to start the integration process, they also operate at 50 Hz only. At low integration times of a few μs only, this results in a dead time of almost 20 ms. Particularly in cw beams, the cables connecting the IPM with the front-end electronics can charge up which results in signal distortions. For this purpose, all channels are grounded over 1 MΩ resistors that prevent a charging of the cables during the electronics dead time.

4.5.6 IPM Test

The HEBT IPM was also tested at the SILHI source of the IPHI injector at CEA Saclay. A photo of the injector is shown in Fig. 4.40. The IPM is mounted in between an ACCT and a BIF tomography chamber equipped with many view ports

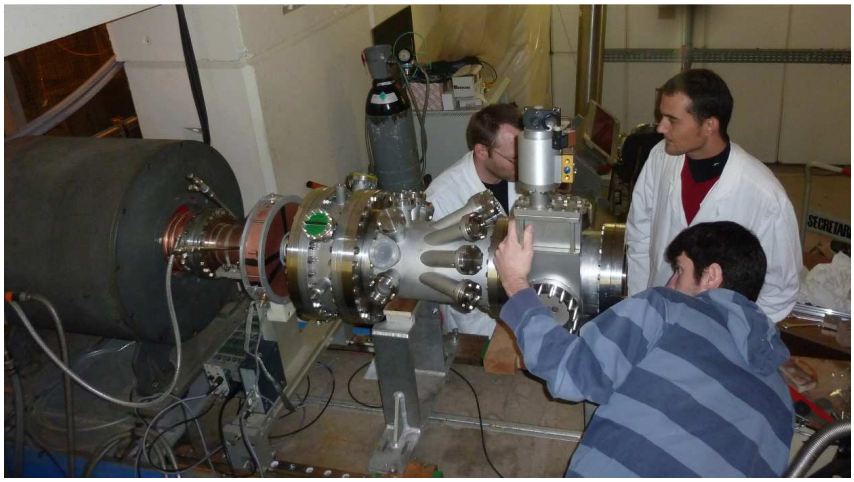

Figure 4.40: Photo of the IPHI injector where the HEBT IPM was tested.

The IPM was able to hold the nominal voltages and to measure profiles in pulsed and continuous beams of over 20 mA. After the demonstration that the IPM is operational and can measure beam profiles at high beam currents, the test had two main objectives:

- Testing the new front-end electronics and DAQ
- Investigating the effect of the beam space charge on the profile acquisition.

The results of the high space charge profile acquisition are presented in section 4.6.6.

One possibility to prevent radiation damage of the front-end electronics is to place them at remote distance. For this purpose the effect of long cables between the IPM and the electronics were tested. In Fig. 4.41(a), a beam profile of the IPHI injector is presented with short cables of only 2 m. If the cable length is increased up to 60 m, profile distortions occur as presented in Fig. 4.41(b) for 30 m in red and for 60 m in black.

At short integration times, the distortions become more prominent. In Fig. 4.42(a), profiles with cables of 30 m (red) and 60 m (black) are shown at an integration time of 892 μs. The distortions can be reduced by the use of coaxial cables, as presented in Fig. 4.42(b) for 60 m long cables. The profile acquired with coaxial cables is shown in black, the profile acquired with flat cables in red. Since the coaxial cable only had 32 channels, the first 32 channels are not connected and the corresponding data points of the profile in Fig. 4.42(b) are zero.

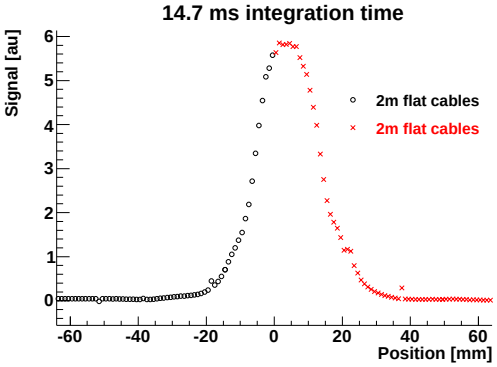

(a) Profile measurements with 2 m cable.

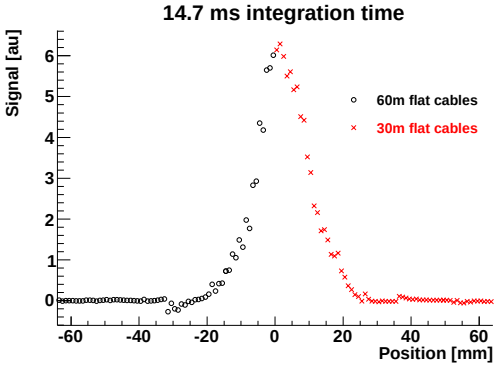

(b) Profile measurement with 60 m of cable (black) and with 30 m of cable (red).

Figure 4.41: Profile measurements at the IPHI injector with different cable lengths between the IPM and the front-end electronics.

The very strong profile distortion at long cable lengths particularly at low integration times makes it necessary to reduce the cable length between IPM and front-end electronics. Since it appears impossible to place the electronics inside the vault, we will place them outside, but as close as possible. The required cable length is estimated to be less than 20 m which appears well feasible according to the performed tests.

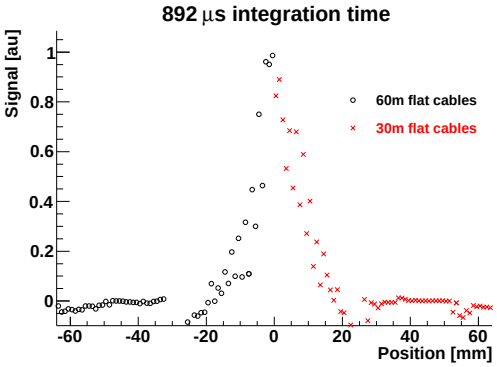

(a) Profile measurement with 60 m of cable (black) and with 30 m of cable (red).

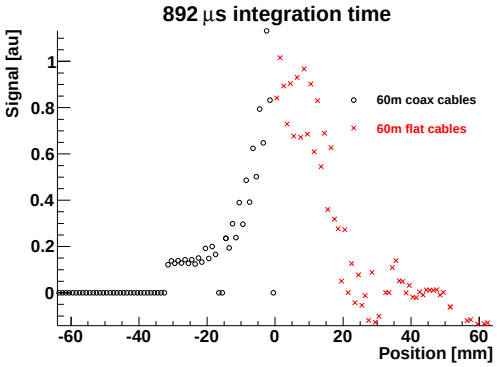

(b) Profile measurement with 60 m of cable (black) and with 30 m of cable (red).

Figure 4.42: Profile measurements at the IPHI injector with different cable lengths between the IPM and the front-end electronics.

4.6 Space Charge Correction

It was demonstrated that the IPM prototype acquired accurate beam profiles at low- and intermediate-current beams and that the final IPM version was able to acquire profiles at pulsed and continuous high currents. However, the reliability of such

profiles was not evaluated since no direct profile comparison, like the comparison with the BIF monitor at GSI, was possible.

The electric field, that the ionization products experience, is a superposition of the extraction field of the IPM field box and the space charge field of the beam itself. The electric field of the low- and intermediate-current beams, available during the tests at GSI, provides only a small contribution to the total electric field. At high beam currents, however, the electric field of the beam can easily dominate the extraction process which results in strong profile distortions.

To evaluate the space charge effect on the beam profile measurement at the LIPAc, the electric field of a beam distribution at nominal LIPAc conditions, provided by our beam dynamics group, were calculated. This field was superimposed with the extraction field of the D-plate IPM field box and a particle tracking was performed. The ion displacement during their drift to the read-out strips under nominal LIPAc conditions is presented in Fig. 4.43(a). While the ion displacement neglecting the space charge, see Fig. 4.39(a), was well below 300 μm, the ion displacement in the central beam region has risen up to 5 mm due to the space charge of the beam.

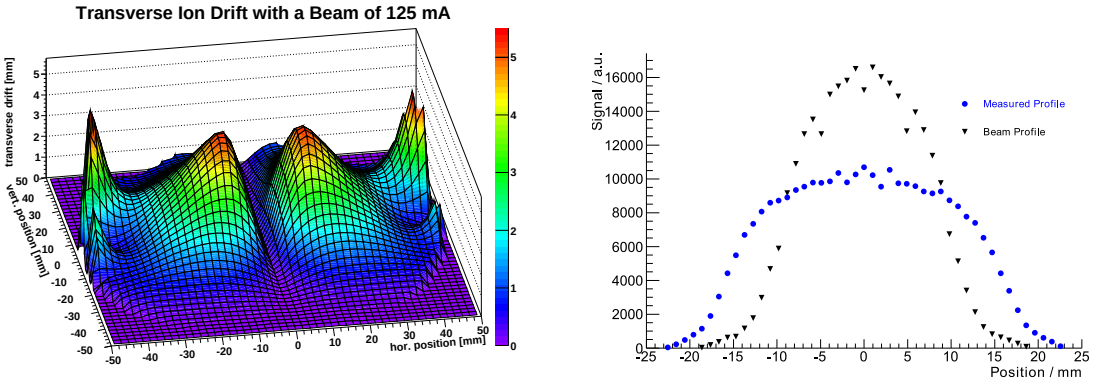

(a) Ion drift in the D-plate IPM including the space charge of the beam at nominal LIPAc conditions.

(b) Simulation of a beam profile measurement by the D-plate IPM at nominal LIPAc conditions.

Figure 4.43: Simulations of the effect of the space charge on the profile acquisition at nominal LIPAc beam conditions.

As the ions are repelled by the beam, the measured profile will be broadened. A simulation of a profile measurement at the LIPAc is presented in Fig. 4.43(b). The original beam profile is displayed in black, the simulated measurement in blue. Measured beam profiles at the LIPAc will suffer strong distortions due to space charge and means have to be developed to overcome the space charge effect.

4.6.1 Space Charge Correction Techniques

There are basically three different ways to overcome the space charge effect:

- a magnetic guidance field
- an increased electric extraction field
- a software correction algorithm

Each of the approaches has its own advantages and drawbacks that will be discussed shortly.

Magnetic Field

If a magnetic field is applied in parallel to the electric extraction field particles with a velocity component perpendicular to the magnetic field will suffer the Lorentz force and will start spiraling around the magnetic field lines. This way, the ionization particles are confined by the magnetic field and can then be directed towards the read-out strips. The highest possible displacement is given by the Larmor radius with which the particle spirals around the magnetic field. To keep this radius low, normally electrons are detected and a strong magnetic field is used.

There are three major issues of this technique:

- The magnets that are required in addition are commonly expensive as highly uniform magnetic fields are required.
- The equation of motion of a charged particle in an electric and magnetic field

  $$m \cdot \ddot{\vec{x}} = e \cdot (\vec{E} + \dot{\vec{x}} \times \vec{B})$$

  only decouples and can thus be easily solved for $\vec{E} \times \vec{B} = 0$. For $\vec{E} \times \vec{B} \neq 0$, the particle velocity perpendicular to the magnetic field will increase which ultimately increases the Larmor radius. Therefore, it does not suffice any more to demand that one electric field component vanishes, but $\vec{E} \times \vec{B}$ has to be minimized instead.

  A potential distribution with strong non-uniformities in beam direction, as shown in Fig. 4.38(b) for instance, does not suffice any more if a magnetic field is applied. To achieve a good electric field uniformity in x and z, IPM field boxes at least twice as large are required. A design as compact as it is required for LIPAc is impossible.
- Since the Lorentz force scales with particle velocity, the beam itself is strongly affected as well. For this purpose correction magnets are commonly placed up- and downstream to the IPM to correct for the beam kick. A design drawing of such assembly is shown in Fig. 4.44(a). It commonly requires an installation length of several meters [83].

Since there is hardly any space available in the LIPAc, a magnetic field guidance was dismissed as not feasible.

Increased Electric Field

It was shown that the IPM prototype measured accurate profiles at GSI, if the extraction field was sufficiently higher than the beam field. A possible solution to overcome the space charge effect is thus to increase the electric extraction field to a level where the beam field does no longer significantly contribute. However, if the same ratio between space charge field and IPM extraction field as at GSI is supposed to be applied to the LIPAc IPMs, voltages of $\sim 1\,\mathrm{MV}$ are required which is clearly not feasible.

Common HV connectors are limited to 10 kV. Applying voltages higher than 10 kV makes the IPM more spacious and more expensive. It was therefore decided to keep all HVs below 10 kV.

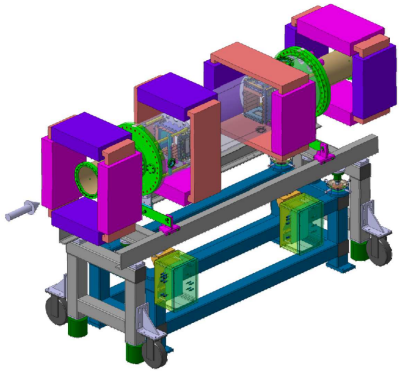

(a) Design drawing of the GSI IPM [83].

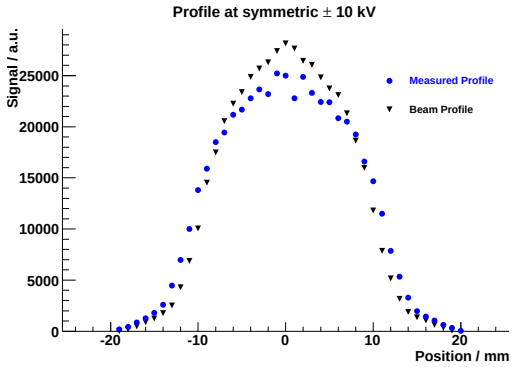

(b) Simulation of a profile measurement at LIPAc with increased extraction fields.

Figure 4.44: Techniques to overcome the space charge effect.

A presumably simple solution to effectively increase the extraction field strength is to apply the voltages symmetrically, i.e. positive HV on the HV plate and negative HV on the read-out strips. This does not only double the voltage differential, but it also reduces fringe fields and simplifies the extraction field optimization. Considering all these effects, the effective extraction field strength could be tripled without increasing the actual IPM voltages. A simulation of a profile measurement at LIPAc nominal conditions with symmetric voltages of ± 10 kV applied on the IPM is presented in Fig. 4.44(b). The measured profile is still slightly broadened, but the result is already much improved compared with the simulation presented in Fig. 4.43(b).

However, it appears to be impossible to connect the front-end electronics to read-out strips set on high voltage. It was even considered to add a Multi Channel Plate (MCP) in between the beam and the read-out strips that converts the extracted ions into electrons. This way, the MCP could be set on negative HV that is attracting ions and accelerates the created electrons towards the grounded read-out strips. The idea was dismissed due to aging issues of the MCP.

Correction Algorithm

The theoretical background of the space charge effect is well understood and it is easily possible to simulate a profile measurement with a given beam distribution. A Space Charge (SC) correction algorithm will have to reverse such simulations and will have to determine the beam distribution based on the distorted measurement. Attempts of a functional SC correction algorithm have already been made before by Graves and Amundson et al. for the IPM of the Fermilab Booster [114, 115].

The advantages of such a software correction are that no additional hardware is required. This allows keeping the very compact design of the LIPAc IPMs. All that is required is a software package in the DAQ which also greatly reduces the cost of such a solution.

The major disadvantage is that such a correction algorithm has to make certain assumption about the beam. If these assumptions are not valid, the algorithm is likely

to fail which could be an unacceptable risk for certain applications. But since the other above discussed solutions are practically not feasible, the space charge correction for the LIPAc IPMs will be performed by a software correction.

While Graves and Amundson et al. used an analytical approach to squeeze the measured profiles back to their original size, in this thesis a fully numerical approach is pursued.

4.6.2 SC Correction Algorithm

The SC correction algorithm aims

- to correct the measured profile for a wide range of possible beam distributions,
- to restore not only the beam size, but also the proper beam shape,
- and to be applied on-line or almost on-line.

The latter two aims can be realized by correction matrices. Instead of scaling the profile with a constant factor to the original beam size, a matrix A can be multiplied on the vector of the measured profile points $\vec{P}_{measured}$. The matrix A can be chosen such that the resulting vector $\vec{P}_{corrected}$ is the beam profile.

$$\vec{P}_{corrected} = A \cdot \vec{P}_{measured} \tag{4.15}$$

The matrix multiplication allows for a variation in the profile shape which is required to correct profile distortions due to the space charge effect. Since it is a simple mathematical operation, a matrix multiplication can be easily implemented in an on-line display. The calculation of the matrix remains to be challenging.

The matrix component a_{ij} represents the probability that an ion collected on strip j has been created by the beam at the position i. This probability can be determined by a particle tracking, if the beam distribution is known.

Since the beam distribution is unknown, a test distribution can be used instead. The test distribution is varied until the right distribution is found. The consistency of the test distribution and the corrected profile $\vec{P}_{corrected}$ is used as break condition of this iteration, i.e. the algorithm terminates, when the profile of the test distribution is close enough to the corrected profile $\vec{P}_{corrected}$.

Test Distribution

In a first approach, Gaussian distributions were used as test distributions. However, it was found that corrected profiles appeared to be Gaussian as well and that the actual beam profile could not be properly reconstructed.

Generalized Gaussian distributions showed greater merit. Generalized Gaussian distributions are Gaussian distributions with $(x-\mu)^\beta$ instead of $(x-\mu)^2$ as shown in equation (4.16).

$$P(x) = \frac{\beta}{2\alpha\Gamma(1/\beta)} e^{-(\frac{|x-\mu|}{\alpha})^\beta} \tag{4.16}$$

The additional degree of freedom allows varying the kurtosis, i.e. the fourth normalized moment, of a generalized Gaussian distribution as well as the RMS size. Examples of generalized Gaussian distributions with different kurtoses are given in Fig. 4.45.

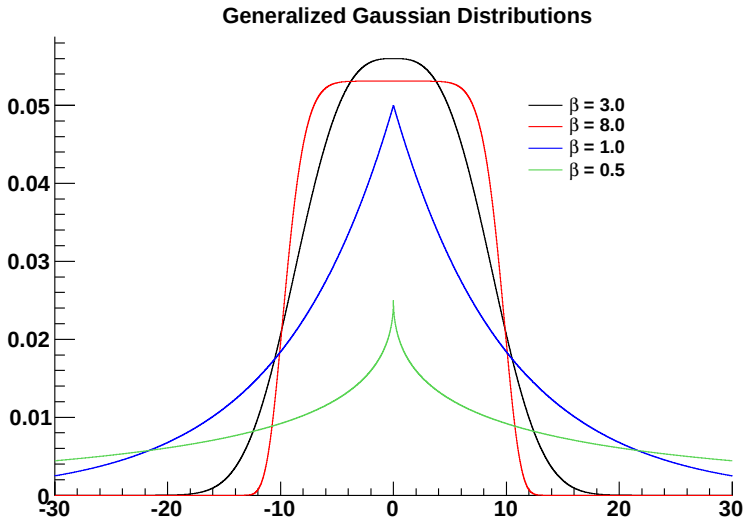

Figure 4.45: Examples of generalized Gaussian distributions.

A generalized Gaussian distribution is fully defined by the parameters α, β and μ. Since the profile center μ is independent of any space charge profile broadening, the two parameters α and β remain to check the self-consistency of the solution. For practical reasons, the second and forth normalized moments of the distribution, σ and κ, are used. They are defined by α and β.

Since the two-dimensional beam distribution is required as test function and only a one-dimensional profile is measured, it is assumed that the beam is perfectly symmetric in x and y. This might be the most significant assumption of the algorithm.

Beam Field Calculation

The electric field of an arbitrary charge distribution is given by Maxwell's equation

$$\vec{\nabla} \cdot \vec{E} = \frac{\rho}{\epsilon_0}. \tag{4.17}$$

Integrating the equation over the volume V and applying Gauss's theorem yields

$$\oint_{\partial V} \vec{E} d\vec{A} = \int_V \frac{\rho}{\epsilon_0} dV'.$$

For a continuous accelerator beam, one can assume an infinitely long, uniformly distributed charge density. The bunch structure of the beam is thus neglected in this approach. Even the lightest possible ions, H_2^+ ions, need about 60 ns to escape the $1{\cdot}\sigma$ region of the beam in the extraction field of the IPM field box. At a bunching frequency of 175 MHz, i.e. one bunch every 5.7 ns, these ions will suffer the electric field of 10 bunches. The expected D_2^+ ions will remain in the beam region even longer.

It is thus justified to average over all of them and to assume a continuous charge distribution.

For an infinitely long, uniformly distributed line charge, the integration along the line can be easily performed and cancels out on both sides of the equation.

$$\oint_{\partial A} E dl = \int \frac{\rho}{\epsilon_0} dA \tag{4.18}$$

To perform the integration over the transverse beam plate, a surface A with the edge ∂A must be chosen. The integration can be easily performed, if the electric field is perpendicular and constant on ∂A. Assuming a symmetric beam distribution, this condition is met for concentric circles. An integration over a circle with radius r yields

$$E(r) = \frac{1}{2\pi r} \cdot \int_0^r \frac{\rho(r')}{\epsilon_0} r' d\theta dr' \tag{4.19}$$

For a known charge distribution $\rho(r')$, the integral can be solved either analytically or numerically.

Boundary conditions, e.g. the grounded beam pipe, are not yet considered for this calculation. Maxwell's equation (4.17) states that the integral over an electric field on a closed surface only depends on charges inside the enclosed volume. Boundary conditions can thus only affect the shape of the chosen surface. Since the beam pipe has the same circular symmetry that is assumed for the beam field calculation, it cannot have any impact on the electric field calculation. Mirror charges on the IPM field box, however, break the symmetry and are thus not neglected in this calculation.

Equation 4.19 is only applicable for circular beam distributions. For arbitrary distributions, one can apply a point-summation-method to calculate the electric field numerically. In a point-summation-method, the charge distribution is segmented by a raster. For each raster point the electric field of a point charge is assumed. The electric field at a given point is then the sum over the electric fields of all raster points.

This technique was only used to calculate the electric field of beam distributions provided by our beam dynamics group. For analytical test functions like Gaussian or generalized Gaussian distributions, calculations by equation 4.19 are far more efficient.

Assumptions

From the choice of the test function and the electric field calculations result a number of assumptions that are made during the correction algorithm. If these assumptions are not fulfilled, the algorithm will possibly not work properly.

- The beam must have a circular symmetry. This assumption was made to expand the one-dimension beam profile to a two-dimensional distribution and for the electric field calculation.

  It is in principle possible to generalize the circular beam distribution to an elliptical one, if two IPMs are mounted. But this will increase the degrees of

freedom of the correction matrices. One already requires one correction matrix for each beam current, each beam RMS and each beam kurtosis. For an elliptical beam distribution, two more parameters are required and the total number of correction matrices to be calculated will rise exponentially. It is thus possible to overcome the limitations of this assumption, but it is not envisaged in the frame of this thesis.

- It is assumed that the beam is in the center of the IPM field box. If the beam profile is measured off center, one can be easily shift to the center, apply the correction matrix and then shift it back. This way, the space charge effect can be properly corrected. Non-uniformities of the extraction field cannot be properly corrected this way, but the resulting ion drift variations, presented in Fig. 4.39(a) for instance, are with a few μm orders of magnitude below the ion displacement due to space charge.
- If the beam is displaced in the other direction, the ions will drift a slightly longer or shorter distance from the beam region to the read-out strips. This effect cannot be detected by a single IPM.
- It is assumed that the beam can be approximated by a generalized Gaussian distribution. According to simulation results of our beam dynamics group, this assumption seems reasonable, but must be checked for each measurement.
- For the correction matrix calculation, one needs the beam current. It is assumed that the DC beam current is measured by an DCCT or ACCT in pulsed operation.

The effect of these assumptions and what errors will result in the profile correction, if they are not met, will be discussed in further detail in section 4.6.5.

4.6.3 Simulation

The feasibility of such a SC correction algorithm based in generalized Gaussian distributions was tested in simulation. For the beam distribution provided by our beam dynamics group, the electric field of the beam was calculated and a profile measurement was simulated by a particle tracking. On the resulting profile vector, a correction matrix was multiplied calculated from a generalized Gaussian distribution of the similar RMS size and kurtosis, $\sigma = 6.3\,\text{mm}$ and $\kappa = -0.5$.

In Fig. 4.46(a), the real beam profile (black), the measured profile (blue) and corrected profile (red) are compared. The corrected profile is in very good agreement with the original beam profile and its σ and κ values are well consistent with the test distribution which would have triggered the break condition of the matrix search algorithm.

The question arises what happens if due to an error in the search engine the algorithm breaks prematurely and wrong matrix is chosen. Since the space charge can only result in a broadened profile, the worst case that can reasonably happen is, if a matrix of the parameters of the uncorrected profile is chosen. In this case, that is $\sigma = 8.72\,\text{mm}$ and $\kappa = -0.81$. The corrected profile resulting from such a premature break is presented in Fig. 4.46(b). The parameters of the corrected profile, $\sigma = 7.15\,\text{mm}$ and

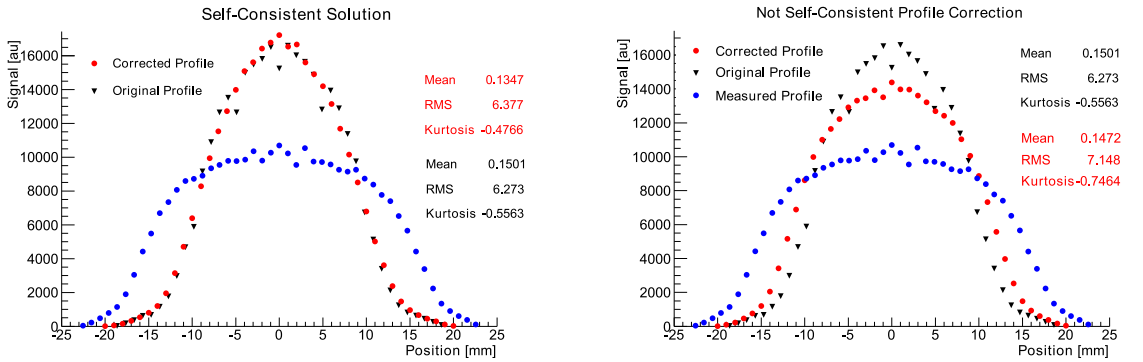

(a) Example of a self-consistent solution.

(b) Example of a not self-consistent solution.

Figure 4.46: Simulations of the SC correction algorithm.

$\kappa = -0.75$, are inconsistent with the test distribution. While the corrected profile does not match the beam profile, it is nonetheless in far better agreement than the uncorrected profile.

4.6.4 Search Algorithm

If the σ and κ values of the uncorrected profiles are used to calculate the correction matrix, the corrected profile will be somewhere between the uncorrected profile and the real beam profile, as can be seen in Fig. 4.46(b). This effect can be exploited to implement an efficient search engine. In a first step, the parameters of the uncorrected profile are used to calculate the correction matrix. In a second step, the correction matrix is calculated using the parameters of the previously corrected profile. This is repeated until the parameters converge.

With an infinite number of correction matrices and a continuous parameter distribution, the algorithm converged towards parameters that should represent the proper beam values. With a finite number of matrices however, the algorithm can converge prematurely. To avoid errors in the search engine due to the finite number of correction matrices, a local search over all matrices in the vicinity of the convergence point is performed to find the best set of matrix parameters.

This search engine has the advantage that is requires only a few iterations to find the convergence point, which limits the search area to a rather small region.

4.6.5 Error Analysis

As discussed in section 4.6.2, there are a number of assumptions to be made for the SC correction algorithm to work. If one of these assumptions is not valid, the correction algorithm might fail. To evaluate the impact of a deviation from ideal conditions, profile measurements are simulated including some errors in the beam properties.

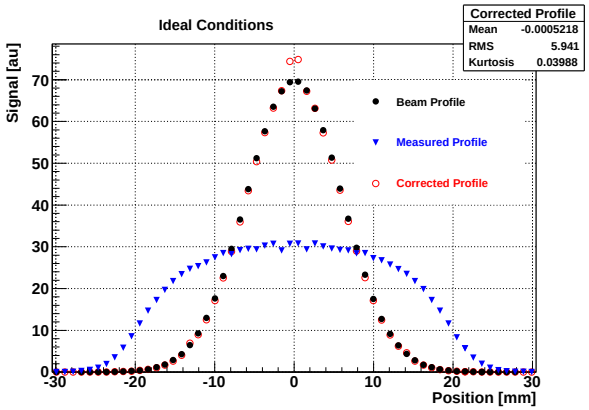

Figure 4.47: 6 mm profile at nominal LIPAc conditions corrected under ideal conditions.

In Fig. 4.47, a profile measurement of a Gaussian-shaped, 125 mA deuteron beam of 9 MeV with an RMS size of 6 mm is simulated and the acquired profile is corrected using proper beam information.

Beam Size Error

The greatest risk of this kind of algorithm is probably the failure of the search engine to find the proper parameters for a self-consistent solution. This could be due to insufficient statistics of the IPM data or a bad signal-to-noise ratio. In Fig. 4.48, the profile correction is presented, if the actual beam profile is 5.75 mm (Fig. 4.48(a)) or 5.5 mm (Fig. 4.48(b)) instead of the assumed 6 mm. The corrected profiles have an RMS size of 5.85 mm and 5.8 mm respectively, which is an error of 100 μm and 300 μm respectively.

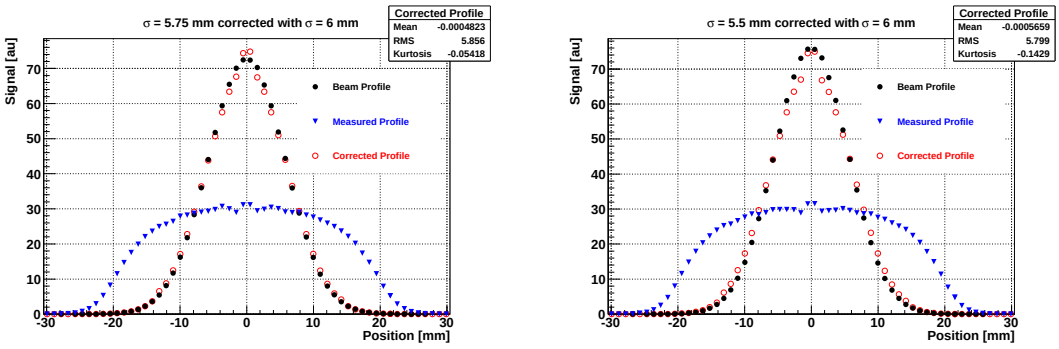

(a) Correction of a profile with a σ 0.25 mm too large.

(b) Correction of a profile with a σ 0.5 mm too large.

Figure 4.48: Effect of the wrong σ value.

Beam Position Error in x

If the IPM measures a profile which is off-center, the algorithm will shift the profile in the center, perform the correction and then shift it back to its original position. The error resulting from this technique is estimated in Fig. 4.49. One can see some spikes in the profile, which are probably artifacts from the simulation. The corrected profile is off the beam profile by 150 μm at a 15 mm beam shift and by 300 μm at a 30 mm beam shift in x-direction.

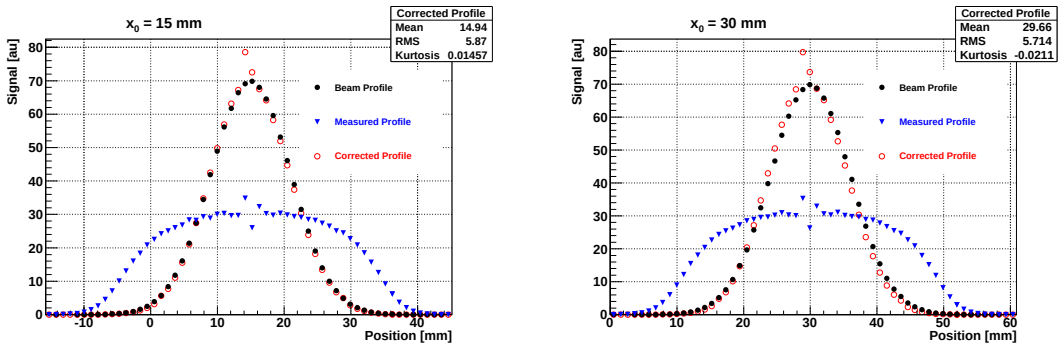

(a) Correction of a profile that is shifted by 15 mm in x.

(b) Correction of a profile that is shifted by 30 mm in x.

Figure 4.49: Effect of beam shifts in x-direction.

Beam Position Error in y

Beam shifts in y-direction, if the x-profile is measured, are not visible in the profile measurement. If the beam is shifted in y, the ion drift will be increased or decreased which can have an effect on the profile correction. In Fig. 4.50, the profile corrections are performed for beams that are shifted by 15 mm and 30 mm towards the read-out strips. Since the ion drift is shorter, the space charge effect is overestimated in this case. At a beam shift of 15 mm, there is no difference visible, but at 30 mm beam shift, the corrected profile is 45 μm too narrow.

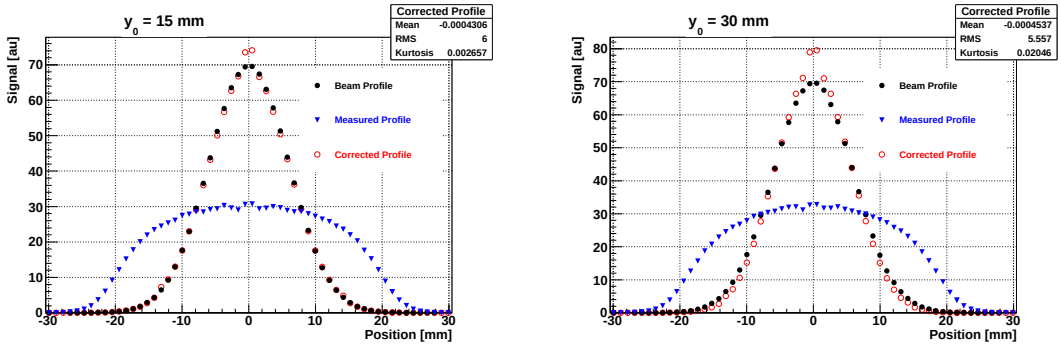

(a) Correction of a profile that is shifted by 15 mm in y.

(b) Correction of a profile that is shifted by 30 mm in y.

Figure 4.50: Effect of beam shifts in y-direction.

Beam Current Error

Finally, the beam current has a large impact on the correction algorithm, since it has a direct impact on the beam field. In Fig. 4.51, simulation results of a profile correction

are presented, if the actual beam current is 10 % or 20 % too low. The corrected profiles are 450 μm and 800 μm too norrow, since the space charge effect is overestimated in the correction.

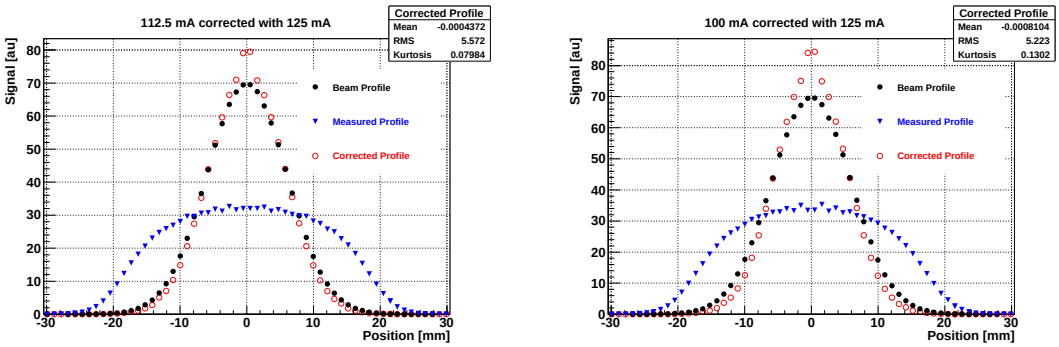

(a) Correction of profile with the beam current 10% overestimated.

(b) Correction of profile with the beam current 20% overestimated.

Figure 4.51: Effect of the beam current uncertainty.

The effect of the beam current appears to be dominant. The data base of the correction matrices should thus include enough correction matrices to ensure that the error in the current is never larger than 10 %. For a continuous current range from 1 mA to 125 mA, 27 different current values will be required to cope with this demand.

Error Coupling

These error estimations are done for a single error source, i.e. one parameter is attributed with an error and all others are assumed to be well known. A coupling between two error sources, that can lead to an amplifying effect, has not yet been considered. Such an amplification is to be expected due to the fact that the search algorithm searches for a self-consistent solution.

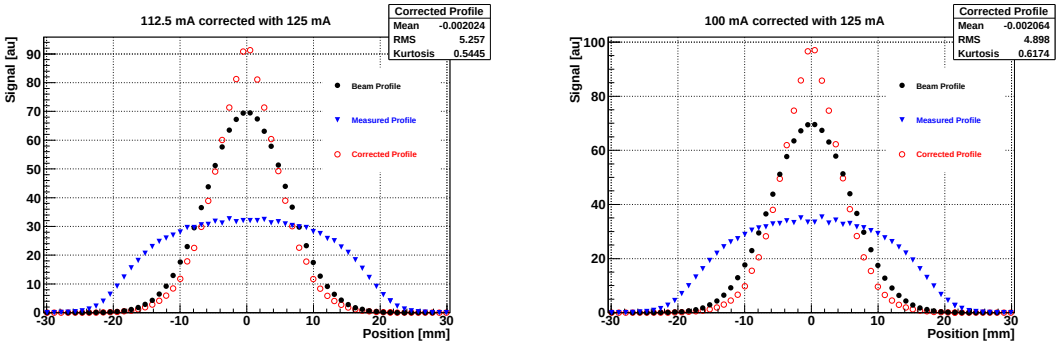

(a) Correction of profile with the beam current 11% overestimated.

(b) Correction of profile with the beam current 25% overestimated.

Figure 4.52: Effect of the beam current uncertainty considering the amplifying effect of the search algorithm.

If, for example, the beam current is overestimated, the corrected profiles are too narrow and the search algorithm will find a self-consistent solution for a too low σ value as well. Since the space charge is stronger for narrow beams, this will ultimately lead to an even narrower profile. The approach to search for a self-consistent solution thus amplifies already existing errors.

In Fig. 4.52, simulation results of the correction algorithm are presented using self-consistent matrices parameters.

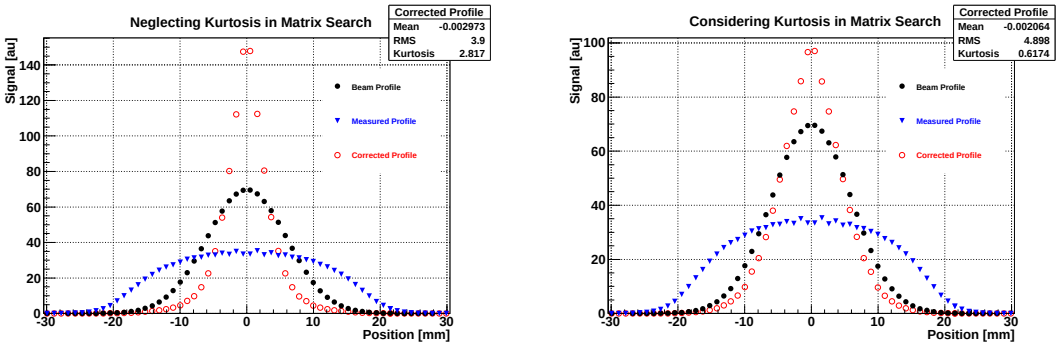

(a) Matrix search based on σ only.

(b) Matrix search considering the kurtosis κ.

Figure 4.53: The kurtosis κ of the corrected profiles diverge, if the profile is strongly overcompensated. The kurtosis must therefore always be considered.

The space charge effect results not only in a broadening of the profiles, but it also decreases the kurtosis, i.e. measured profiles in the presence of strong space charge effects appear rectangular. It is thus important to consider not only the profile width, but the kurtosis as well to find a self-consistent solution.

In Fig. 4.53(a), the result of a profile correction neglecting the kurtosis is presented. The corrected profile shows strong deviations of the actual beam profile. The kurtosis value of 2.8 already clearly indicates that the correction was not successful, since such a value is not expected from high-current beams. In comparison, considering the kurtosis, the algorithm grants reasonable results even at high beam current errors, as shown in Fig. 4.53(b).

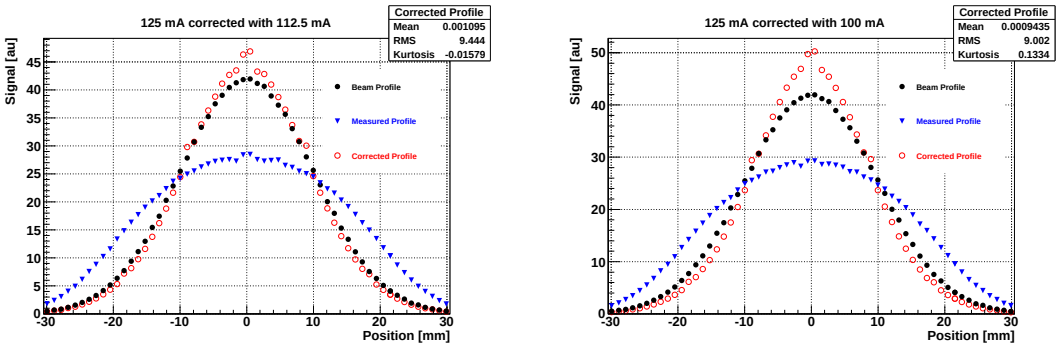

(a) Correction of profile with the beam current 10% overestimated.

(b) Correction of profile with the beam current 20% overestimated.

Figure 4.54: Effect of the beam current uncertainty on a beam of 10 mm RMS size considering the amplifying effect of the search algorithm.

All these simulations were performed using the electric field map of the HEBT to investigate the impact of error sources. On the HEBT, the beam is diverging to spread the beam power on the dump on a larger surface to avoid damage. It is thus difficult to estimate the beam diameter inside the IPM. According to our beam dynamics group, a reasonable value for the beam diameter in $\pm 3\sigma$ is 80 mm - 100 mm. In Fig. 4.54, the previous simulation is repeated for an RMS beam radius of 10 mm.

Since the charge density in the beam scales the radius squared, the effect is greatly reduced for the larger beam.

4.6.6 Experimental Test

The SC algorithm was also experimentally tested at the SILHI source of the IPHI injector at CEA Saclay. The complication in the experimental setup is that the real beam profile is unknown and hence the success or failure of the correction algorithm cannot be easily evaluated.

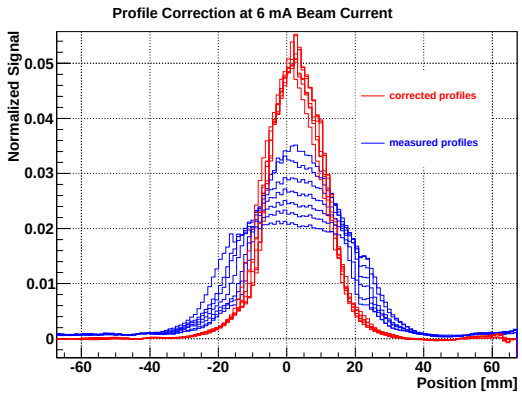

(a) SC correction test at a proton beam of 6 mA and 90 keV.

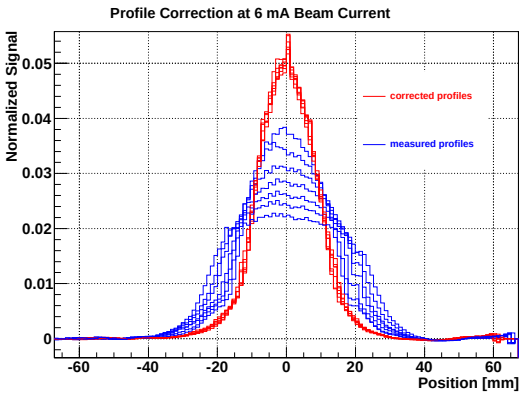

(b) Measured and corrected profiles are shifted to the center for a better comparison.

Figure 4.55: Experimental test of the SC correction algorithm. Beam profiles are measured at different extraction voltages (blue) and corrected individually for each voltage (red).

To evaluate the success of the correction, beam profiles were measured at different extraction fields. At a low extraction field strength, the ions will remain in the beam region longer and suffer a stronger effect of the beam field which increases the profile broadening due to the space charge. For each extraction field value, dedicated matrices were calculated and the correction was performed. Since the beam remained constant, it is to be expected that the corrected profiles match for all extraction field values.

In Fig. 4.55(a), profile measurements of a 6 mA proton beam of 90 keV is presented. In blue, the measured profiles at different extraction voltages are shown. The extraction voltages were reduced from 6.5 kV to 1.65 kV. At lower voltages, the profiles get broader as it was expected. In red, the corrected profiles are presented. All corrections were performed indepedently of another.

Due to a beam jitter, the measured profiles are not all concentric. For a better comparison of the corrected profiles, they are not shifted back to their original position in Fig. 4.55(b). All profiles, measured and corrected, are in the center. The corrected profiles are in a good agreement which indicates a successful profile correction.

It was shown in section 4.6.5 that a failed correction commonly results in profile which has an increased kurtosis value. In the search engine of the SC correction algorithm, high corrected profiles with high kurtosis values are therefore slightly suppressed.

The results of all the test measurements performed at the IPHI injector are added in Appendix C.

4.6.7 Practical Implementation

The SC correction algorithm should be implemented in the DAQ to provide an online correction of the measured profile. For the LIPAc prototype, it appears advantageous to execute the Root script by a compiler as it was done during the development. This allows for easy adoptions, if necessary. Once the algorithm has been tested and was found operational, the script could be compiled to launch the algorithm as executable which will improve the performance and render the system more stable.

It appears sensible to display both, the corrected and the uncorrected image on the GUI. It remains to the operator which profile to trust. Indicators, if the correction was successful, like the profile kurtosis or the minimization parameter of the search algorithm should be displayed as well.

Matrix Database

A matrix database must be implemented prior to operation. The SC correction algorithm will access this database for each profile correction process and read the required correction matrices from the computer hard drive. It is of importance to keep the database large enough to be prepared for any kind of accelerator beam. However, since the matrix calculations require a great amount of calculation time, it must be chosen as small as possible for practical reasons. A proposed arrangement of the parameters for correction matrices is given in Tab. 4.14.

Table 4.14: Proposed Arrangement of the matrix parameters of the SC correction algorithm.

Parameter	Number of matrices	Interval	Margin
I_{Beam}	35	variable	1 mA - 125 mA
σ	21	0.5 mm	5 mm - 15 mm
κ	3	0.25	-0.25 - +0.25
Total	2205	—	—

It was shown in section 4.6.5 that an error of the beam current has the largest impact on the correction algorithm. To minimize this effect, the vast number of beam current matrices should be calculated with an interval smaller than 5 mA over the entire range from 1 mA to 125 mA.

Different matrices to account for other error sources like a beam displacement in x- or y-direction could be calculated as well, but their effect was found to be insignificant compared to the effect of the beam current.

A single matrix calculation requires about two hours of calculation time. 2200 matrices could thus be calculated on a multi-core processor with 10 processor cores within 20 days. For the LIPAc, there are two different IPMs, one on the D-plate and one on the HEBT. The HEBT IPM will be operated at 9 MeV beam energy only. The D-plate IPM will be operated during the commissioning at 5 MeV as well. Since the field map in the IPM field box changes, if one of the two IPMs on the D-plate is switched OFF, a total of five sets of corrections matrices have to be calculated. This requires already 100 day, i.e. about 3 months.

4.7 Detailed Design Review

The development of the IPMs for LIPAc has been presented at the Detailed Design Review of the LIPAc Beam Instrumentation in June 2012. It was the preliminary judgment of the expert committee that the "IPM development is in a good shape" and that the "correction algorithm looks promising" [116]. However, it was recommended to perform further experimental tests of the correction algorithm and to increase the extraction voltage to $\sim 40\,\mathrm{kV}$ to reduce the impact of the space charge effect. In addition, the expert committee was concerned about the signal strength of the IPM in pulsed beam mode and pointed out the importance of comparing IPM and SEM-grid profiles. In the following, the three points:

- Increased Extraction Voltage.
- Further Experimental Tests.
- SEM-Grid Comparison.

are discussed in more detail.

Increased Extraction Voltage

At high electric extraction fields, the beam might receive a significant kick that has to be compensated by steerers along the accelerator. On our request, the beam dynamics group has estimated the maximum kick these steerers can compensated and that the IPM is thus allowed to inflict to be 0.54 mrad at 9 MeV and 0.85 mrad at 5 MeV. By an FEM particle tracking, the beam deflection by the electric field of the IPM has been determined. The detailed results of this simulation for various IPM extraction voltages on the HV-plate are presented in Table 4.15. As comparison, the maximum beam deflection that be corrected by the steerers is given in the last column.

Table 4.15: Deflection of the beam due to the electric field of the IPM in comparison to the correction limit of the steerers for various voltages on the HV-plate.

IPM voltage			7.5 kV	10 kV	15 kV	20 kV	30 kV	40 kV	limit
Deflection [mrad]	D-plate	5 MeV	0.75	1.0	1.5	2.0	3.0	4.1	0.85
		9 MeV	0.42	0.55	0.8	1.1	1.7	2.2	0.54
	HEBT	9 MeV	0.25	0.32	0.5	0.7	1.0	1.3	0.54

One can see in Table 4.15 that the current IPM voltages of 7.5 kV are already close to the limit of what the steerers can correct. However, a displacement of the beam by a few mm on the beam dump might still be acceptable during commissioning. The IPM design will thus be adjusted for a nominal extraction voltage of 20 kV, i.e. 25 kV on the HV electrodes. HV connectors for up to 25 kV are commercially available and can be implemented in the current design without too great an adjustment.

The free space between the field box and the beam pipe will have to be increased from 10 mm to 20 mm for the HEBT IPM. For the D-plate IPM the foreseen margin already suffices. The resistor chain should be tested in vacuum for the increased voltages to avoid damages due to resistor heating.

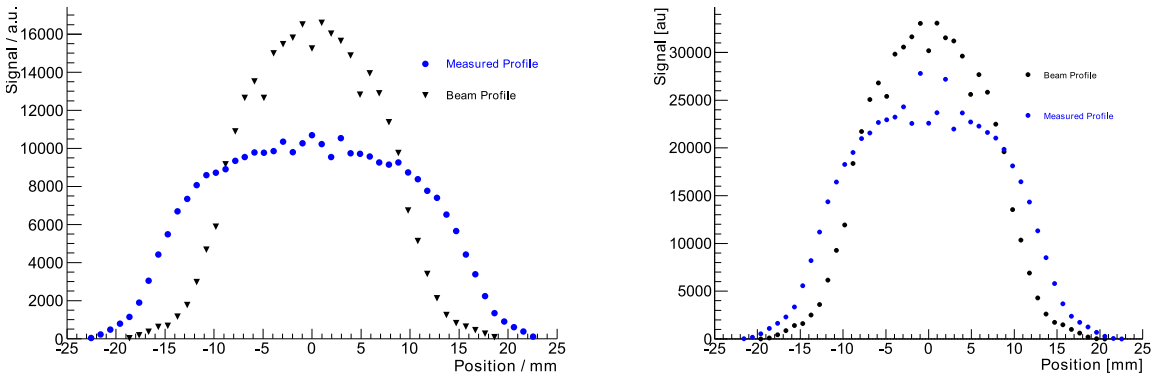

(a) Simulation of a profile measurement at 7.5 kV, i.e. an extraction field of 750 V/cm.

(b) Simulation of a profile measurement at 15 kV, i.e. an extraction field of 1500 V/cm.

Figure 4.56: Simulations of a beam profile measurement on the D-plate at extraction voltages of 7.5 kV and 15 kV, blue: measurement, black: beam

In Fig. 4.56, simulations of beam profile measurements at 7.5 kV and 15 kV are compared. While the profile broadening due to the space charge is still significant, the situation is greatly improved. The impact of the SC correction algorithm is thus reduced as well as the consequences of an algorithm failure.

Further Experimental Tests

Additional tests of the IPM and thus the correction algorithm are foreseen once the IPHI RFQ is mounted at CEA Saclay at the end of 2013. High-current proton beams of 3 MeV and up to 100 mA will be available [117]. Such an accelerator will provide the ideal conditions to test the SC correction algorithm as the current, the charge density and the energy per nucleon of the beam are comparable to LIPAc conditions. The final tests could be performed at LIPAc itself in the frame of the diagnostics commissioning on-site.

SEM-Grid Comparison

It was demonstrated in section 3, that the SEM-grids can hold beam currents of 125 mA at a pulse length of 50 μs. Based on the measurements done at GSI, the IPM signal expected at the LIPAc was estimated. As presented in Table 4.4, the IPM will require $\sim$28 pulses of 50 μs length to accumulate sufficient data for a decent profile.

Asymmetric Beam

During the presentation of the IPM, the question was asked what was going to happen, if the beam is not circular which is one of the most urgent assumptions of the algorithm, but was not discussed during the error calculation in section 4.6.5. Though it is in principle possible to generalize the presented algorithm to elliptical beams and thus consider asymmetric beam distributions as well, this is not foreseen in the current stage of the algorithm. The question thus remains if the algorithm provides sufficiently good results, even for asymmetric beam.

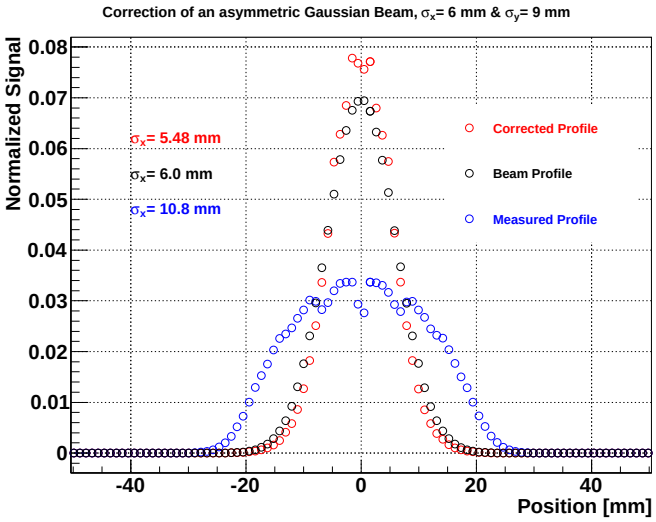

Figure 4.57: SC correction of the x-profile of a Gaussian asymmetric beam of $\sigma_x = 6\,\text{mm}$ & $\sigma_y = 9\,\text{mm}$.

To evaluate this effect, a simulation of a profile measurement of an asymmetric beam of $\sigma_x = 6\,\text{mm}$ & $\sigma_y = 9\,\text{mm}$ at full intensity by the HEBT IPM has been performed. As it is expected to be the worse case, a profile measurement in the narrower x-direction was simulated. The resulting profile measurement and the correction performed by the algorithm are presented in Fig. 4.57. The search algorithm chose a matrix with 5.5 mm RMS size and a kurtosis of -0.2, which is in good agreement with the values of the corrected profile.

The SC correction provides a slightly (500 μm) narrower profile, but given the rather strong asymmetry of a beam which is 50 % larger in y than in x, one can assume that the slight asymmetries foreseen for LIPAc will have no impact at all on the profile correction.

4.8 IFMIF IPM

At the International Fusion Material Irradiation Facility (IFMIF), the deuteron beam will be accelerated onto the liquid lithium target. The beam will have a rectangular shape to deposit the beam power uniformly on the target. Localized peaks in the power deposition can boil the lithium at one spot which can cause major damage for the target system. The IFMIF IPM is supposed to measure the beam profiles upstream the target and thus ensure safe operation of the lithium target.

The effect of space charge of the IFMIF on the IPM profile measurement has been evaluated in simulation. On the level of the lithium target, the beam will have a size of $200 \times 50\,\text{mm}^2$. Since the position of the IPM along the IFMIF HEBT is not yet defined and thus the beam shape in the IPM field box is unknown, the beam is assumed to have a size of $100 \times 25\,\text{mm}^2$. The profile measurement along the short axis is most challenging, since the impact of the space charge effect on the profile measurement is larger.

In an optimistic estimation, the IPM field box could have an aperture of 200 mm. Applying 10 kV on the HV-plate will thus provide an electric extraction field of

500 V/cm. A simulation of a profile measurement at IFMIF nominal conditions, 125 mA at 40 MeV, was performed by a particle tracking in an ideal extraction field and the beam field calculated for the rectangular distribution. The measured profile (black) in comparison to the original beam profile (blue) is presented in Fig. 4.58(a). Under the ideal conditions assumed here, the profile distortions are rather low and could be easily corrected by the SC correction algorithm discussed in section 4.6.

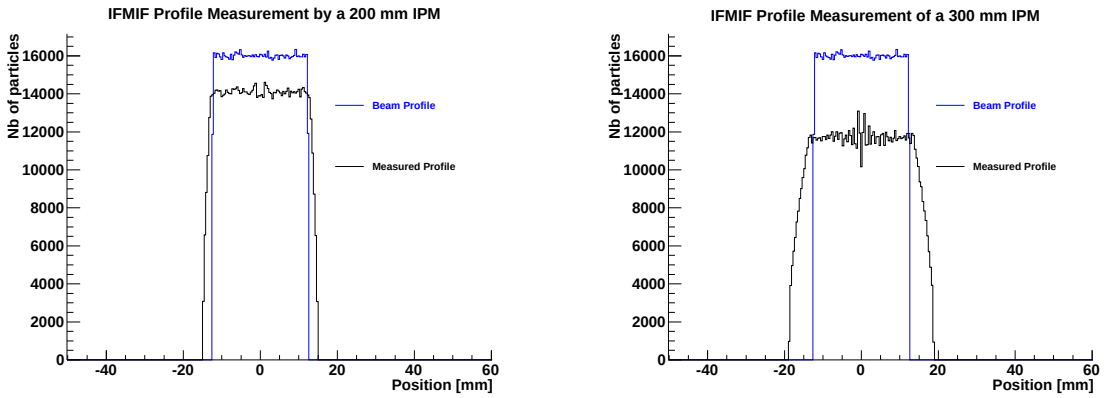

(a) IFMIF IPM under optimistic assumptions.

(b) IFMIF IPM under more realistic assumptions.

Figure 4.58: Simulation of a beam profile measurement at IFMIF nominal conditions, 125 mA deuteron beam of 40 MeV.

More realistic assumptions would probably be a field box aperture of 300 mm. As the voltages are applied asymmetrically on the IPM, even for voltages of 10 - 12 kV, the effective extraction field will be limited to 250 V/cm. Under such condition the profile broadening, presented in Fig. 4.58(b), is greatly increased.

While the space charge effect is still lower than for LIPAc, it is questionable, if the risk of a SC correction algorithm failure is acceptable for IFMIF. Alternative options to overcome the space charge effect, discussed in section 4.6.1, that have been dismissed for LIPAc due to a lack of space, should be reconsidered. If the space and the budget is available, a magnet guidance field would be advisable. Otherwise, the extraction field could be increased by either applying higher voltages, by applying the voltages in a symmetric fashion, or by enlarging the field box that allows for a more efficient use of the applied voltages.

4.9 Outlook & Conclusion

A prototype for the LIPAc IPM has been designed based on FEM electric field studies, built and tested at the IPHI injector at CEA Saclay and at the UNILAC at GSI. The IPM prototype performed very well at low - and intermediate - current beams and its properties are well understood. At higher beam currents, the space charge effect starts to dominate the ion extraction which results in strong profile distortions.

The final IPM versions for the LIPAc accelerator have been designed based on FEM studies of the electric field as well. The HEBT profiler has already been built and was successfully tested at the IPHI injector at CEA Saclay.

To overcome the space charge effect of the beam, a software algorithm was written that aims to not only scale the measured profile to the beam width, but to restore

the beam shape as well. The algorithm shows great success in simulations and also experimental tests look promising.

A detailed study of the algorithm was performed in simulation to evaluate the risk of an algorithm failure. Based on these tests, a set of parameters for correction matrices are proposed to be calculated for the SC correction algorithm.

As there is no accelerator with similar beam characteristics as LIPAc, the final test of the algorithm can only be performed during the LIPAc commissioning. It might thus be of interest to perform a series of tests at LIPAc.

- The effect of the background radiation of the profile acquisition has not yet been tested. It might become necessary to perform an extra offset correction. This could be done by subtracting a pedestal measurement with the beam ON, but the IPM HV OFF.
- The fit parameters in the search algorithm of the SC correction algorithm might have to be adjusted to the LIPAc conditions.
- Profile comparisons with the BIF monitor at different beam current should indicate the reliability of the SC correction algorithm.
- For the space charge calculation, a continuous beam has been assumed. If the beam current is underestimated due to pulse structure of the beam, an effective current could be defined that should be proportional to the beam current.
- Voltage scans, as described in section 4.4.2, should be performed to analyze the properties of deuterium as residual gas. If the initial ions velocity of deuterium is too high, this feature is already implemented in the SC correction algorithm.

Chapter 5

Conclusion and Outlook

In the frame of this thesis three diagnostics components of the LIPAc accelerator have been developed.

- Beam loss monitors, i.e. diamond detectors and ionization chambers
- SEM-grid profile monitors
- Ionization profile monitors

For the beam loss monitor system, the LHC IC has been tested and calibrated on neutrons and γ in the energy range expected for the LIPAc. For this purpose, measurements have been performed at the neutron source at CEA Valduc and at the γ source CoCase at CEA Saclay. It was found that the simulations of the response function performed at CERN can be well extrapolated to the LIPAc energies.

Since a major part of the IC signal is expected to be due to neutrons, simulations have been performed how the sensitivity of the ICs can be increased for neutron impact in the LIPAc energy range. It was found that filling the IC with a boron containing gas could significantly increase its response function. Due to safety issues, this solution was, however, dismissed.

To measure lowest losses on the level of the SRF-linac, it is foreseen to place diamond detectors inside the cryostat. Diamond detectors have never been used in cryogenic environments. In the frame of this thesis, diamonds have been successfully tested at ambient temperature and also in liquid nitrogen and in liquid helium. In addition, they have been calibrated at the CEA Bruyères-le-Châtel.

The LIPAc will be equipped with interceptive and non-interceptive profile monitors. As interceptive profilers, SEM-grids are foreseen. They will be bought from Ganil and adapted according to our needs. Thermal studies have been performed to optimize the wire diameter and to evaluate up to which beam current and duty cycle SEM-grid can be used.

As non-interceptive profiler, an Ionization Profile Monitor (IPM) will be used. A prototype was built and tested at the high - current ion source of the IPHI injector at CEA Saclay and at the UNILAC at GSI. The IPM prototype performed very well at low - and intermediate - current beams and its properties are well understood. At higher beam currents, the space charge effect starts to dominate the ion extraction which results in strong profile distortions.

The final IPM versions for the LIPAc accelerator have been designed based on FEM studies of the electric field as well. The HEBT profiler has already been built and was successfully tested at the IPHI injector at CEA Saclay.

To overcome the space charge effect of the beam a software algorithm was written that aims not only to scale the measured profile to the beam width, but to restore the beam shape as well. The algorithm shows great success in simulations and also experimental tests look promising.

A detailed study of the algorithm was performed in simulation to evaluate the risk of an algorithm failure. Based on these tests, a set of parameters for correction matrices are proposed to be calculated for the SC correction algorithm.

Acknowledgments

I would like to express my sincere thanks to all the people that have contributed to this thesis.

My particular thanks goes to the beam diagnostics group at GSI and the SILHI group at CEA Saclay that made the IPM tests at the UNILAC and the IPHI source possible and supported us continuously during the IPM development. Above all, I would like to thank Peter Forck (GSI), Frank Becker (GSI), and Raphaël Gobin (CEA Saclay) who were always ready to provide advice and assistance whenever we encountered a problem.

Without the help of Rémi Chipaux and François Daly (CEA Saclay), our γ calibration of the ionization chamber at CoCase would have been impossible.

Also Michał Pomorski (CEA Saclay) provided invaluable support and expertise during all tests of the diamond detectors.

And probably most importantly, I would like to thank my supervisor, Jacques Marroncle (CEA Saclay), who allowed me to develop my work in all the independence I could have wished for and who supported my work with all the expertise and encouragement I could have hoped for.

Last, but not least, I would like to express my gratitude towards my parents who always believed in me and my work, and who supported me whenever I was in need of encouragement.

The work was supported by the EU under contract PITN-GA-2008-215080.

Acronyms

AC	Alternate Current
ACCT	AC Current Transformer
ADC	Analog-to-Digital Converter
B3	CEA Bruyères-le-Châtel
BA	Broader Approach
BF_3	boron trifluoride
B_2H_6	diborane
BEM	Boundary Element Method
BIF	Beam Induced Fluorescence
BLM	Bunch Length Monitor
BLoM	Beam Loss Monitor
BPM	Beam Position Monitor
BNC	Bayonet Neill Concelman
BPM	Beam Position Monitor
CAD	Computer Aided Design
CAS	CERN Accelerator School
CEA	Commissariat à l'Énergie Atomique et aux Énergies Alternatives
CERN	Conseil Européen pour la Recherche Nucléaire
CID	Charge Injection Device
CIEMAT	Centro para Investigaciones Energéticas, Medioambientales y Tecnológicas
CMS	Compac Muon Solenoid
CoCase	Cobalt Casemate

cw	continuous wave
CVD	Chemical Vapor Deposition
D	Deuteron
DAQ	Data Acquisition System
DC	Direct Current
DCCT	DC Current Transformer
DITANET	DIagnostics Techniques for particle Accelerators NETwork
D-plate	diagnostics plate
DEMO	Demonstration Power Plant
dpa/fpy	displacements per atom per full power year
ECR	Electron Cyclotron Resonance
ELBE	Electron Linear accelerator with high Brilliance and Low Emittance
EU	European Union
Euratom	European Atomic Energy Community
EVEDA	Engineering Validation Engineering Design Activities
FC	Faraday Cup
FCC	face-centered cubic
FCT	Fast Current Transformer
FEE	Front-End Electronics
FEM	Finite Element Method
FP	Framework Program
FPM	Fluorescence Profile Monitor
Ganil	Grand accélérateur national d'ions lourds
GSI	Helmholtzzentrum für Schwerionenforschung
GUI	Graphical User Interface
HEBT	High Energy Beam Transport line
HV	high voltage
IC	Ionization Chamber
IFERC	International Fusion Energy Research Centre

IFMIF	International Fusion Material Irradiation Facility
IPM	Ionization Profile Monitor
IPHI	Injecteur de Protons à Haute Intensité
IRFU	Institut de Recherche sur les lois Fondamentales de l'Univers
ITER	International Thermonuclear Experimental Reactor
JAEA	Japan Atomic Energy Agency
JET	Joint European Torus
LEBT	Low Energy Beam Transport line
LHC	Large Hadron Collider
LHe	liquid helium
LN_2	liquid nitrogen
linac	linear accelerator
LIPAc	Linear IFMIF Prototype Accelerator
micromegas	micro-mesh gaseous detector
MCP	Multi Channel Plate
MEBT	Medium Energy Beam Transport line
MPS	Machine Protection System
pCVD	polycrystalline CVD
PPS	Personal Protection System
RF	Radio Frequency
RFQ	Radio Frequency Quadrupole
RMS	Root Mean Square
SAMES	Société Anonyme Machine ElectroStatique
SC	Space Charge
sCVD	single crystalline CVD
SEM	Secondary Electron Emission
SILHI	Source d'Ions Légers de Haute Intensité
SMD	Surface Mount Design
SPIRAL	Système de Production d'Ions Radioactifs Accélérés en Ligne

SRF	Superconducting Radio Frequency
SRIM	Stopping and Range of Ions in Matter
JT60-SA	Satellite Tokamak Programme
T	Tritium
TOF	time of flight
UNILAC	Universal Linear Accelerator
VME	Versa Module Eurocard

List of Figures

List of Tables

Appendices

Appendix A

Diamond Spectra

Spectra of the energy loss in diamond measured at B3 for various neutron energies.

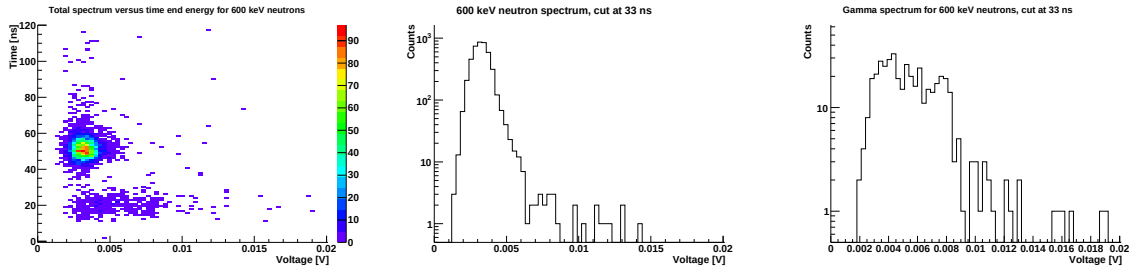

(a) Events versus diamond signal and TOF (b) Neutron spectrum (c) γ spectrum

Figure A.1: 600 keV neutron energy

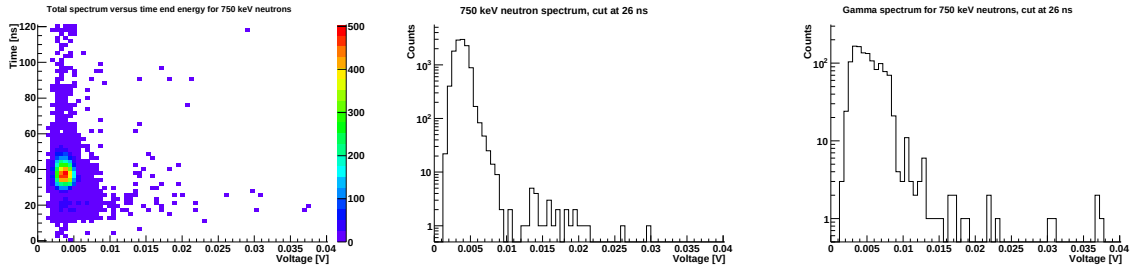

(a) Events versus diamond signal and TOF (b) Neutron spectrum (c) γ spectrum

Figure A.2: 750 keV neutron energy

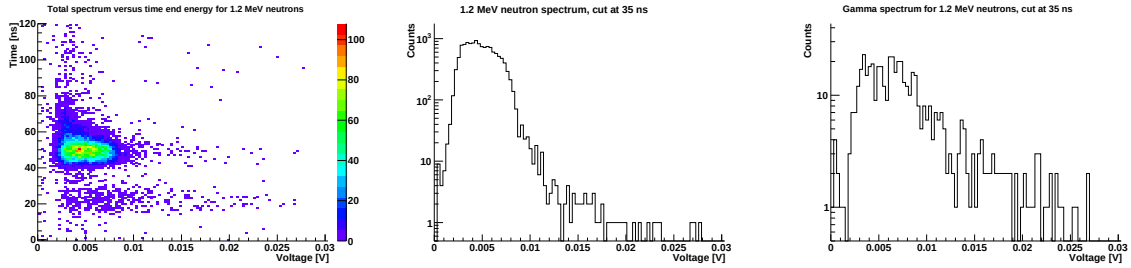

(a) Events versus diamond signal and TOF (b) Neutron spectrum (c) γ spectrum

Figure A.3: 1.2 MeV neutron energy

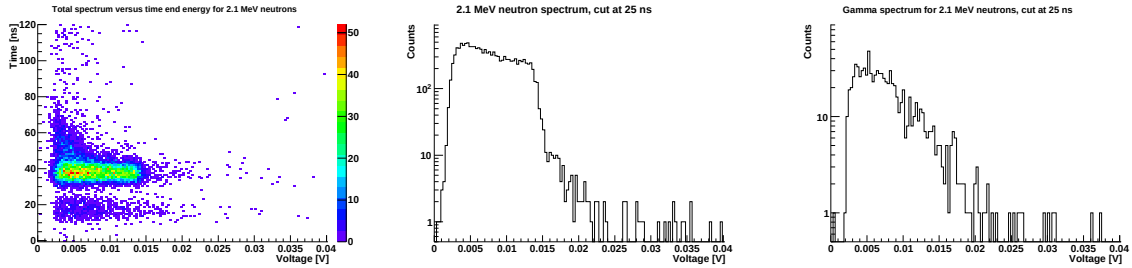

(a) Events versus diamond signal and TOF (b) Neutron spectrum (c) γ spectrum

Figure A.4: 2.1 MeV neutron energy

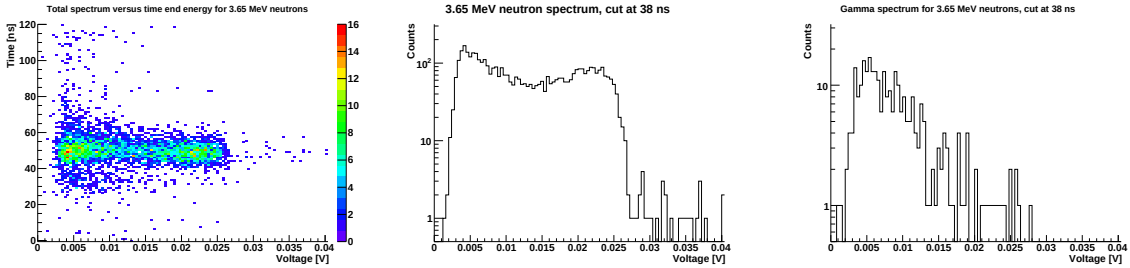

(a) Events versus diamond signal and TOF (b) Neutron spectrum (c) γ spectrum

Figure A.5: 3.6 MeV neutron energy

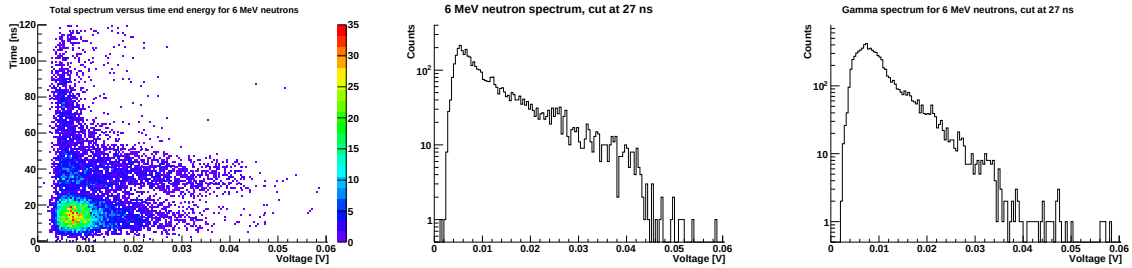

(a) Events versus diamond signal and TOF (b) Neutron spectrum (c) γ spectrum

Figure A.6: 6 MeV neutron energy

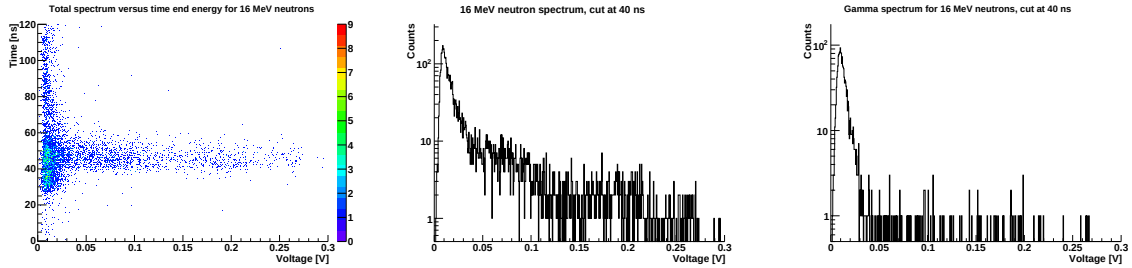

(a) Events versus diamond signal and TOF

(b) Neutron spectrum

(c) γ spectrum

Figure A.7: 16 MeV neutron energy

Appendix B

BIF Profile Comparison

Profiles of an 1 mA Xe^{21+} beam acquired at GSI by an IPM (blue) and a BIF monitor (red).

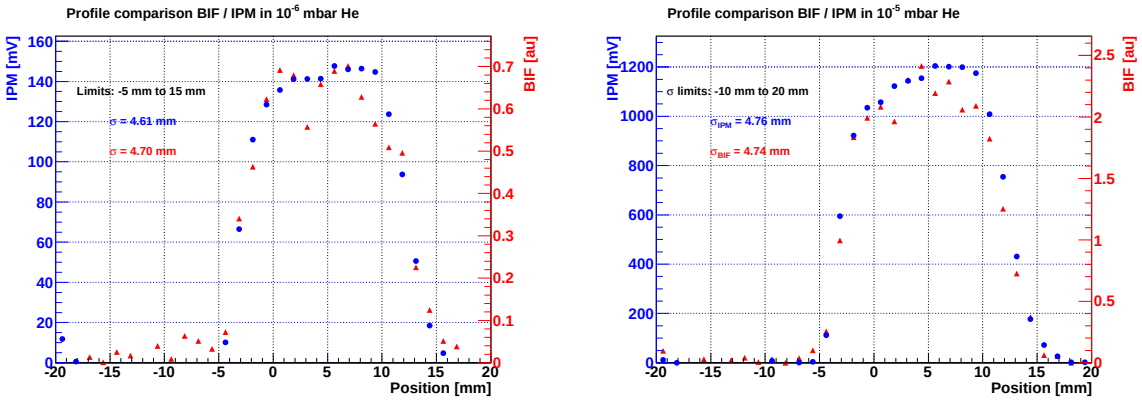

(a) Profiles at 10^{-6} mbar helium.

(b) Profiles at 10^{-5} mbar helium.

Figure B.1: Comparison of beam profiles acquired by the IPM (blue) and the GSI BIF monitor (red).

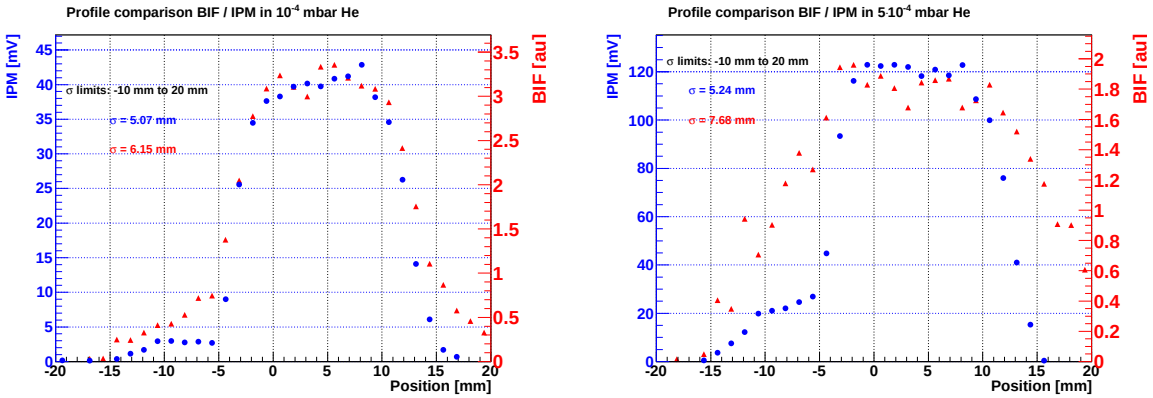

(a) Profiles at 10^{-4} mbar helium.

(b) Profiles at $5 \cdot 10^{-5}$ mbar helium.

Figure B.2: Comparison of beam profiles acquired by the IPM (blue) and the GSI BIF monitor (red).

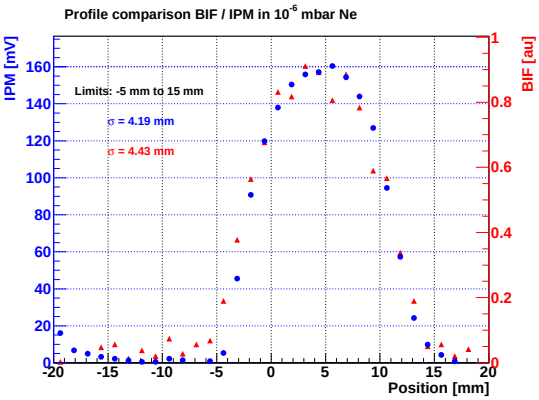

(a) Profiles at 10^{-6} mbar neon.

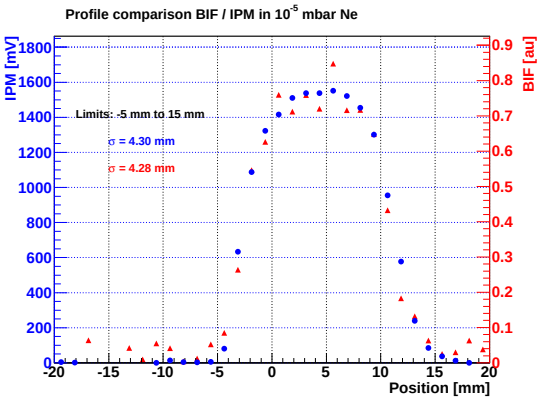

(b) Profiles at 10^{-5} mbar neon.

Figure B.3: Comparison of beam profiles acquired by the IPM (blue) and the GSI BIF monitor (red).

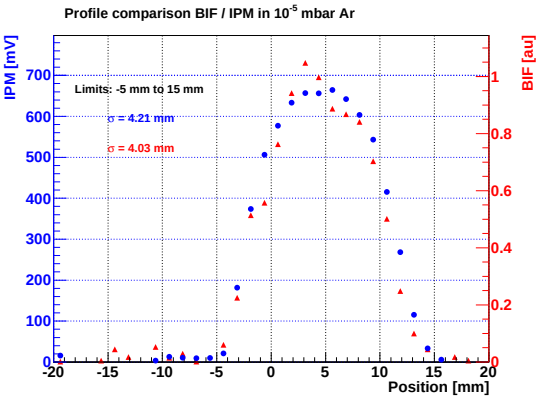

(a) Profiles at 10^{-5} mbar argon.

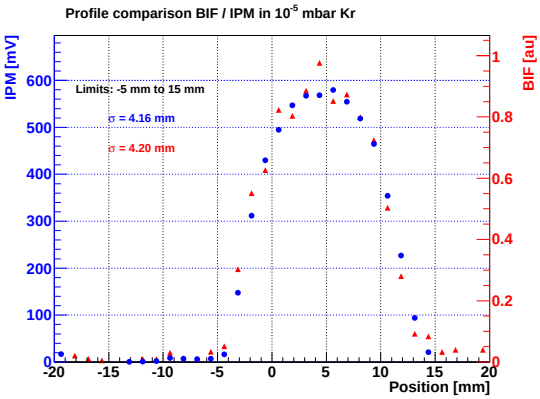

(b) Profiles at 10^{-5} mbar krypton.

Figure B.4: Comparison of beam profiles acquired by the IPM (blue) and the GSI BIF monitor (red).

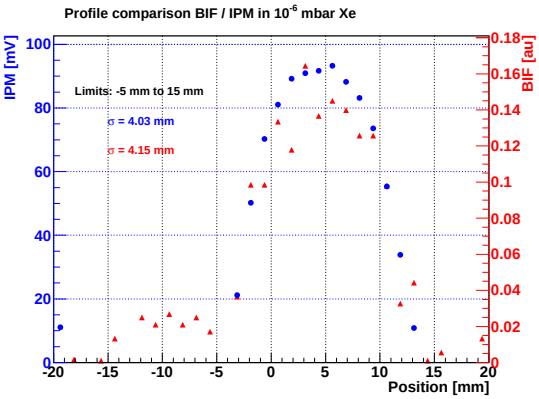

(a) Profiles at 10^{-6} mbar xenon.

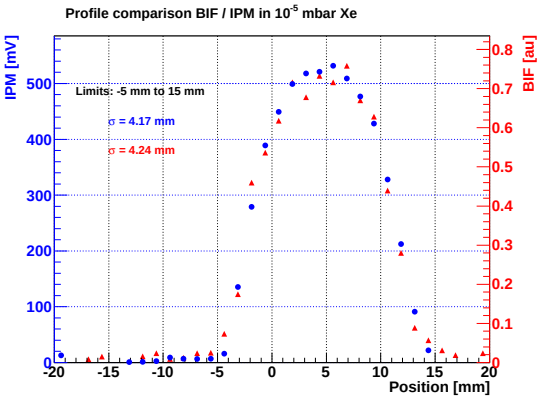

(b) Profiles at 10^{-5} mbar xenon.

Figure B.5: Comparison of beam profiles acquired by the IPM (blue) and the GSI BIF monitor (red).

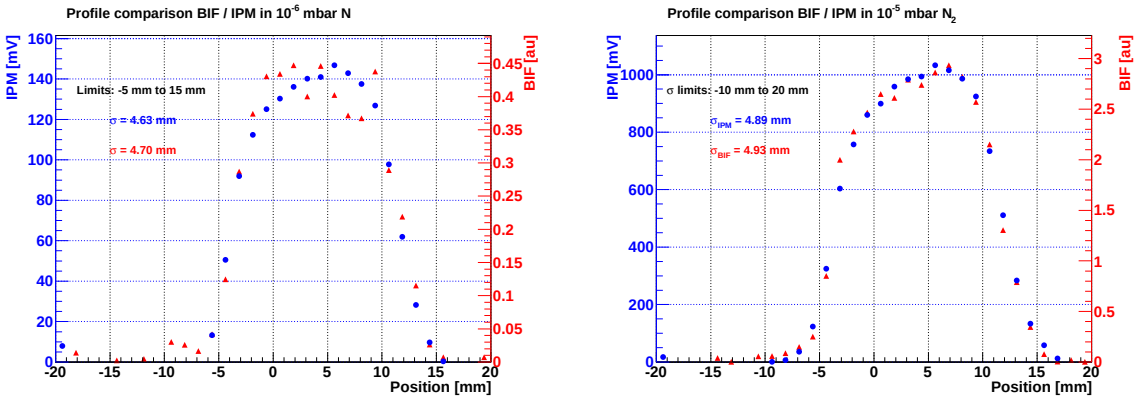

(a) Profiles at 10^{-6} mbar nitrogen.

(b) Profiles at 10^{-5} mbar nitrogen.

Figure B.6: Comparison of beam profiles acquired by the IPM (blue) and the GSI BIF monitor (red).

Appendix C

SC Correction Algorithm Test

Results of the SC correction algorithm test performed at the IPHI injector at CEA Saclay.

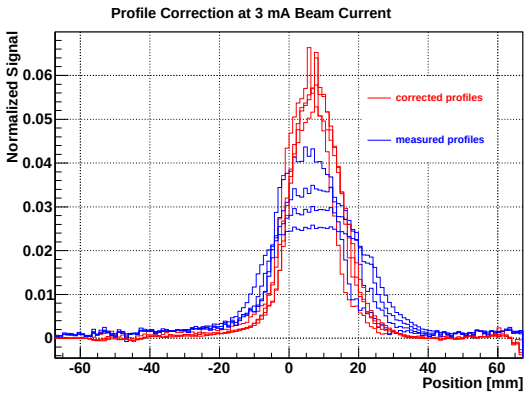

(a) All profiles are at their measured position.

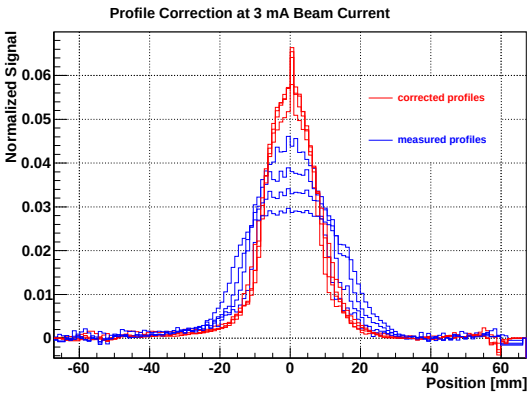

(b) All profiles are shifted to the center for a better comparison.

Figure C.1: SC correction algorithm tested at 3 mA beam current, measured profiles (blue) and corrected profiles (red).

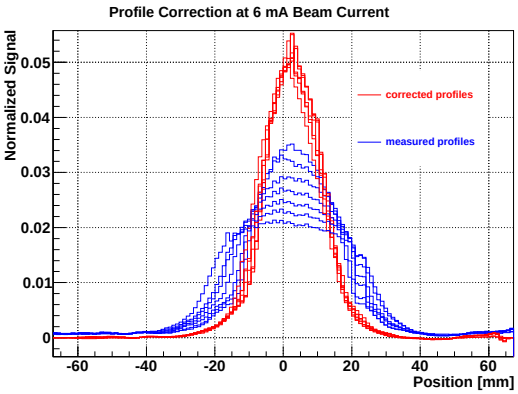

(a) All profiles are at their measured position.

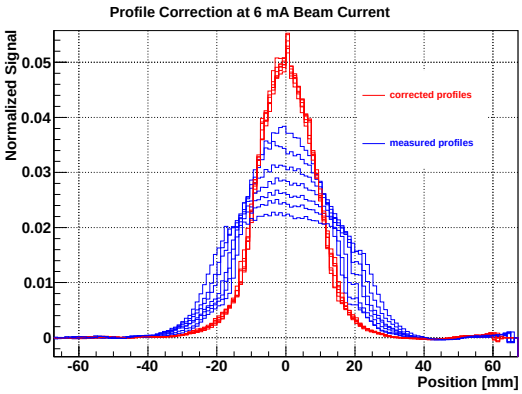

(b) All profiles are shifted to the center for a better comparison.

Figure C.2: SC correction algorithm tested at 6 mA beam current, measured profiles (blue) and corrected profiles (red).

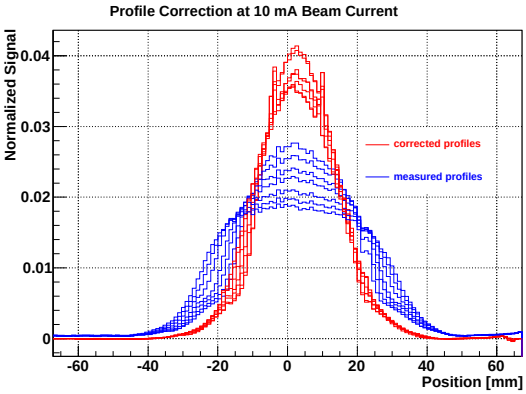

(a) All profiles are at their measured position.

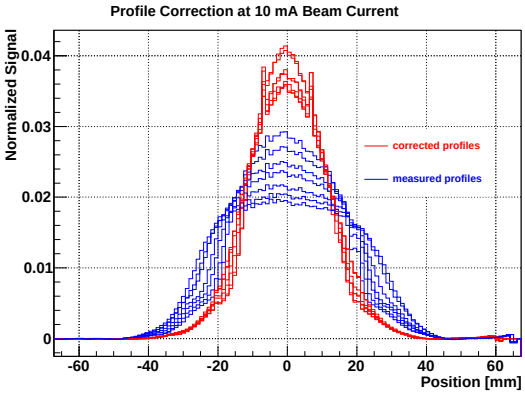

(b) All profiles are shifted to the center for a better comparison.

Figure C.3: SC correction algorithm tested at 10 mA beam current, measured profiles (blue) and corrected profiles (red).

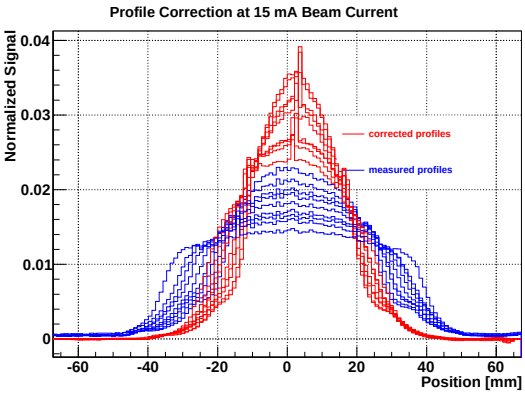

(a) All profiles are at their measured position.

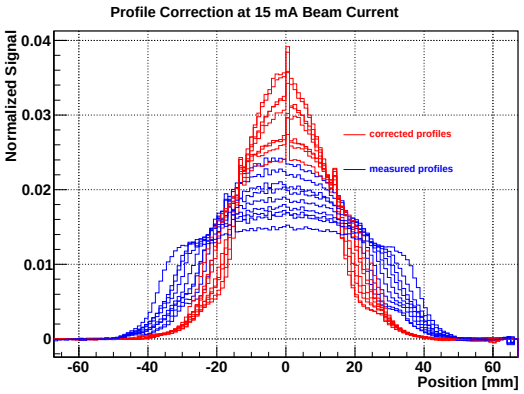

(b) All profiles are shifted to the center for a better comparison.

Figure C.4: SC correction algorithm tested at 15 mA beam current and the correction performed assuming a beam current of 15 mA as well, measured profiles (blue) and corrected profiles (red).

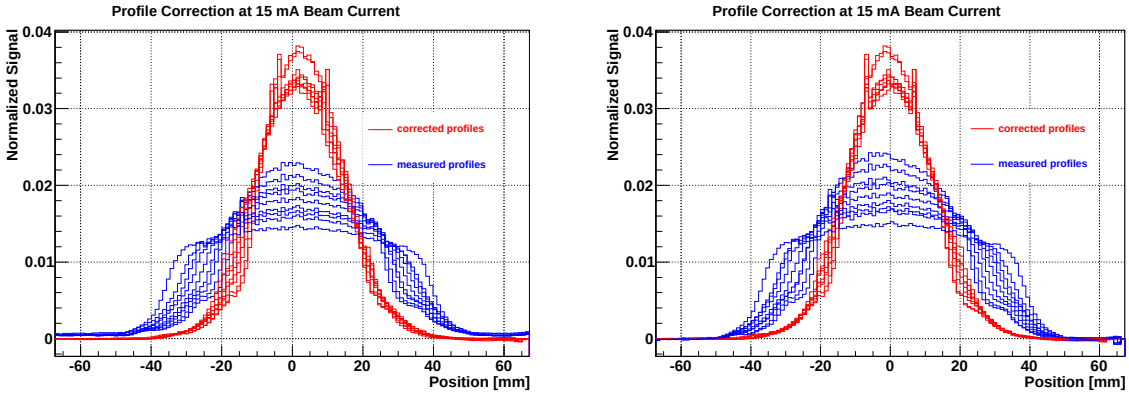

(a) All profiles are at their measured position.

(b) All profiles are shifted to the center for a better comparison.

Figure C.5: SC correction algorithm tested at 15 mA beam current and the correction performed assuming a beam current of 17 mA instead, measured profiles (blue) and corrected profiles (red).

Appendix D

IPM Design Drawings

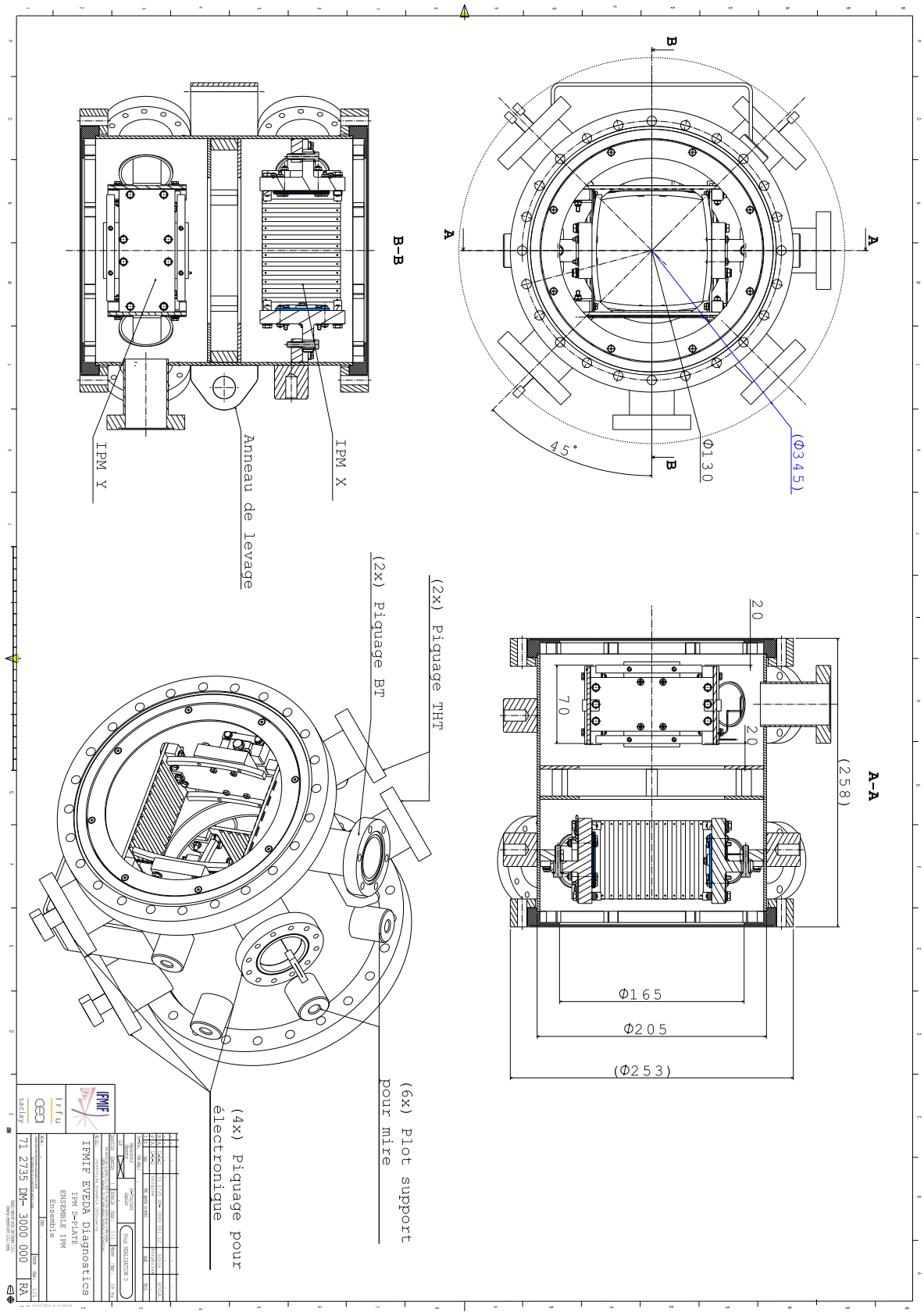

Figure D.1: Design drawing of the D-plate IPM.

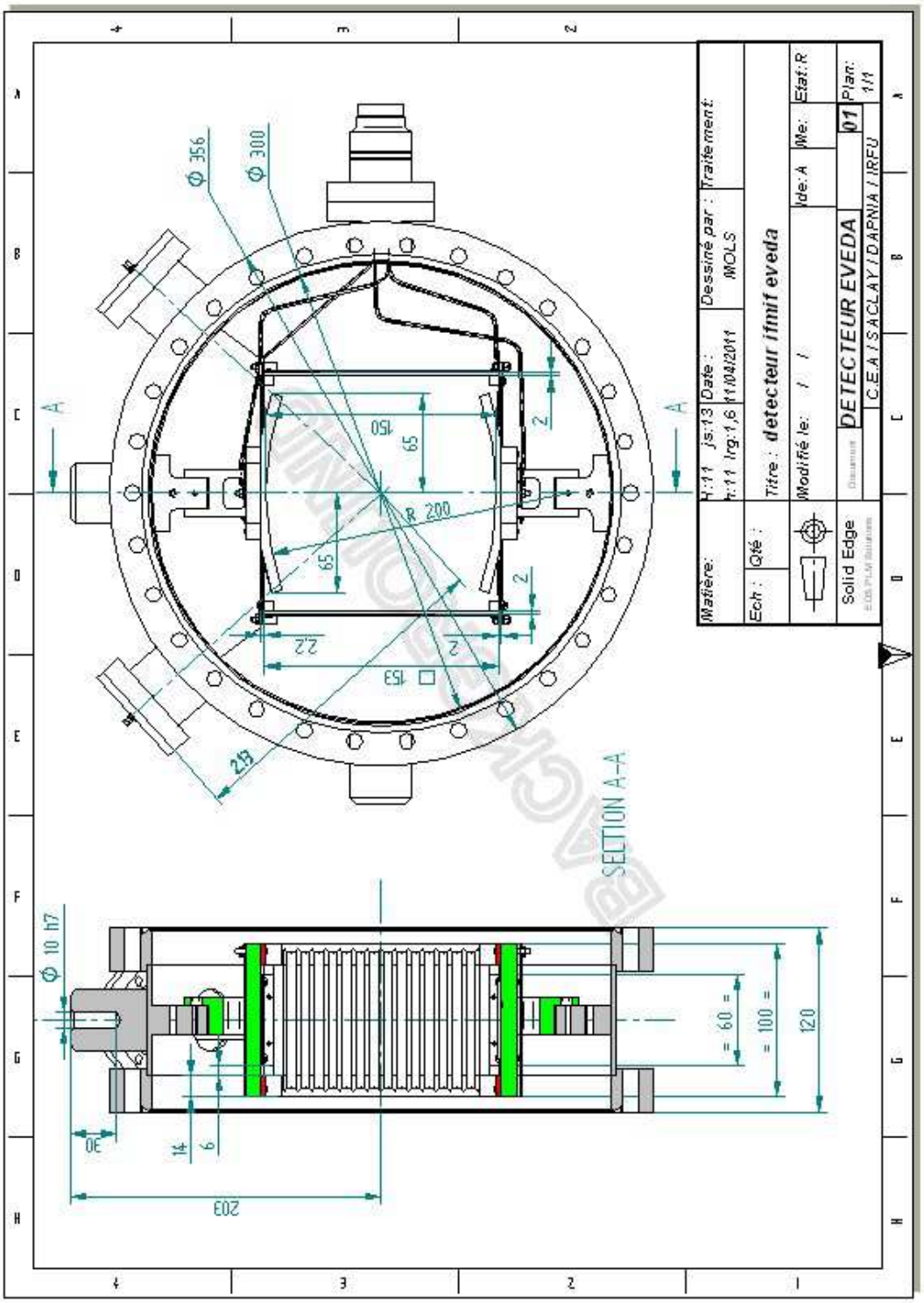

Figure D.2: Design drawing of the HEBT IPM.

Appendix E

SC Algorithm Overview

The SC correction algorithm applies a correction matrix on the vector given by the measured profile to calculate the real beam profile. The matrix element m_{ij} must thus consist of the probability to detect an ion, that is created by the beam at position i, on strip j. If the electric field inside the IPM field box and the beam distribution of the beam is known, such probability can be easily determined by a particle tracking.

Electric Field Calculations

The electric field inside the IPM field box was calculated by Lorentz-3E, the same software that was used to optimize the field box geometry. The IPM field box geometry was thus already implemented in the software and the x-, y- and z-components of the electric field is extracted in a text file for pre-defined raster points. This text file is then read by Root to perform the particle tracking.

For the calculation of the electric field of the beam, the assumption of an infinitely long linear charge density has been made. Gauss's Law can be used for this purpose for analytic beam distributions, for arbitrary distributions, a point summation method was applied, i.e. the beam cross section was screened and the electric field is calculated for single raster point assuming an infinitely long linear charge density. The total electric field at a given position is then calculated by summing up the contributions of all raster points.

Particle Tracking

Due to the rather low velocities of the ions, the tracking is performed based on classical mechanics. For each time step the velocity increase due to the electric fields is calculated and added to the velocity of the previous time step.

$$\vec{v}_i = \vec{v}_{i-1} + \frac{e\vec{E}}{m} \cdot \Delta t \tag{E.1}$$

From this velocity, the distance the particle has traveled in Δt can be easily derived.

$$\vec{x}_i = \vec{x}_{i-1} + \vec{v}_i \cdot \Delta t \tag{E.2}$$

Matrix Calculation

Particles are launched along a raster that covers the entire active area of the IPM and then tracked towards the read-out strips. For each ion, launched at its initial position i and collected on the read-out strips at position j, the matrix element m_{ij} is increased by the probability that an ion is created at position i. Finally, the matrix is normalized such that the magnitude of the profile vector remains constant under the matrix multiplication.

Search Algorithm

During the matrix calculation, it was assumed that the beam distribution is known. If this was the case, the profile monitor would not be required any more, since the beam profile can be derived from the beam distribution. A search algorithm is applied to find the matrix that provides a self-consistent solution, i.e. a solution where the profile corrected by a certain matrix is consistent with beam distribution used to calculate this matrix.

To improve the run time of the search algorithm, one takes advantage of the fact that positive ions are repelled by the beam and that the space charge effect thus always lead to profile broadening. In addition, the space charge becomes stronger the smaller the beam is. In a first step, the correction matrix is calculated for beam parameters corresponding to the measured profile P_0. Since this profile is greatly broadened, the space charge effect is underestimated. The resulting corrected profile P_1 is thus still broadened. In a second step, the correction matrix is calculated for beam parameters corresponding to this profile P_1. As this profile is still broadened, the space charge effect is still underestimated, but the correction is better than in the first step. This procedure can be repeated until the corrected profiles do not change any more. Tests show that this algorithm converges already after two or three iterations. The matrix that this search algorithm converged towards, should ideally correspond to the real beam profile. In reality there are two effects that lead to wrong matrices:

- The two parameters sigma and kurtosis
- The quantization of the matrix parameters

The previous considerations that the search algorithm is based on apply for the beam width and similarly for the kurtosis (the space charge increases the kurtosis) separately, but not necessarily for both combined, since both have an impact on the space charge effect and are thus coupled. In addition, the discrete values of the correction matrices at hand limit the precision with which the convergence point is found. Both effects can be eliminated by a second search that searches for the best solution in the proximity of the convergence point. For this purpose, a minimization parameter has been defined as the quadratic weighted sum over the discrepancy of the sigma and kurtosis values and the kurtosis as well. The kurtosis was added in the minimization parameter, since it was seen in the error analysis that the kurtosis reaches unreasonable values, if the algorithm fails. This, of course, means that the algorithm will always favor distributions with a low kurtosis, i.e. Gaussian shaped beams.

Bibliography

[1] Fusion for energy - annual report 2010. http://fusionforenergy.europa.eu/.

[2] Arnie Heller. How one equation changed the world. *Science & Technology Review*, 9:12–20, 2005.

[3] S. Atzeni and J. Meyer-ter Vehn. *The physics of inertial fusion: beam plasma interaction, hydrodynamics, hot dense matter*. International series of monographs on physics. Oxford University Press, 2004.

[4] http://www.iter.org/.

[5] R. J. Hawryluk. Results from deuterium-tritium tokamak confinement experiments. *Rev. Mod. Phys.*, 70:537–587, Apr 1998.

[6] ITER - FAQ, January 2012. http://www.iter.org/faq.

[7] C. Varandas. EURATOM strategy towards fusion energy. *Energy Conversion & Management*, 49:1803–1809, 2008.

[8] http://fusionforenergy.europa.eu/understandingfusion/broaderapproach.aspx, March 2012.

[9] IFMIF International Team. IFMIF Comprehensive Design Report. http://www.iea.org/techno/technologies/fusion/IFMIF-CDR_partA.pdf.

[10] P. Wilson. *Neutronics of the IFMIF neutron source: Development and analysis*. PhD thesis, Universität Karlsruhe, 1998.

[11] P. Garin et al. IFMIF specifications from the user point of view. *Fusion Engeneering and Design*, 86:611–614, 2011.

[12] Development of radiation resistant reactor core structural materials. In *51st IAEA General Conference (2007) Documents*, 2007.

[13] P. Garin. IFMIF: status and developments. In *Proc. of EPAC08, Genoa, Italy*, 2008.

[14] K. Ehrlich and A. Möslang. IFMIF - An international fusion meaterials irradiation facility. *Nuclear Instruments and Methods in Physics Research B*, 139:72–81, 1998.

[15] Frank Hinterberger. *Physik der Teilchenbeschleuniger und Ionenoptik*. Springer, 2008.

[16] F. Ruggiero et al. Cas basic course on general accelerator physics. CERN-2005-004, June 2005.

[17] N. Chauvin et al. Transport of intense ion beams and space charge compensation issues in low energy beam lines. *Review of Scientific Instruments*, 83:02B320, 2012.

[18] R. Duperrier, N Pichoff, and D Uriot. Cea saclay codes review for high intensities linacs computations. In *Proc. of ICCS 2002, Amsterdam, Netherlands*, 2002.

[19] P.A.P Nghiem et al. The IFMIF-EVEDA challenges in beam dynamics and their treatment. *Nuclear Instruments and Methods in Physics Research A*, 654:63–71, 2011.

[20] R. Gobin et al. Preliminary results of the international fusion materials irradiation facility deuteron injector. *Review of scientific instruments*, 83:02A345–1 – 4, 2012.

[21] R. Ferdinand et al. Deuteron beam test for IFMIF. In *Proc. of EPAC 2002, Paris, France*, 2002.

[22] A. Pisent et al. IFMIF-EVEDA RFQ design. In *Proc. of EPAC08, Genua, Italy*, 2008.

[23] A. Pepato et al. Engineering design and first prototype tests of the IFMIF-EVEDA RFQ. In *Proc. of IPAC'10, Kyoto, Japan*, 2010.

[24] A. Mosnier. The IFMIF 5MW linacs. In *Proc. of LINAC08, Vicoria, BC, Canada*, 2008.

[25] N. Grouas et al. Mechanical and cryogenic system design of the first cryomodule for the IFMIF project. In *Proc. of IPAC'10, Kyoto, Japan*, 2010.

[26] F. Orsini et al. Preliminary results of the IFMIF cavity prototypes tests in vertical cryostat and cryomodule development. In *Proc. of IPAC'10, Kyoto, Japan*, 2010.

[27] F. Orsini et al. Preliminary results of the IFMIF cavity prototypes tests in vertical cryostat and cryomodule development. In *Proc. of SRF2011, Chicago, IL, USA*, 2011.

[28] http://irfu.cea.fr/Sacm/.

[29] L. Arneudon et al. Linac4 technical design report. Technical report, CERN, 2006.

[30] K. Andersen et al. Conceptual design report. Technical report, European Spalation Source Lund, 2012.

[31] W. Barth et al. Technical design report FAIR proton-linac. Technical report, FAIR, 2008.

[32] S. Russenschuck and G. Vandoni, editors. *CERN Accelerator School - Superconductivity and cryogenics for accelerators and detectors*. CERN, Genève, 2004.

[33] H. KOndo et al. IFMIF/EVEDA litium test loop: design and fabrication technology of target assembly as a key component. *Nucl. Fusion*, 51:123008, 2011.

[34] J. Marroncle et al. IFMIF-LIPAc diagnostics and its challenges. In *Proc. of IBIC2012*, 2012.

[35] Ph. Cara, A. Mosnier, M. Sugimoto, and H Matsumoto. LIPAc Plant Integration Document.

[36] Ch. Vermare et al. Commissioning of the IFMIF/EVEDA accelerator prototype - objectives & plans. In *proc. of IPAC*, 2010.

[37] P. Nghiem et al. IFMIF-EVEDA beam comissioning. Technical report, February 2010.

[38] N. Chauvin et al. LIPAc beam commissioning plan, June 2012.

[39] I. Podadera et al. HEBT diagnostics for commissioning, control and characterization of the IFMIF-EVEDA accelerator. In *Proc. of Hadron Beam 2008, Nashville, Tennessee, USA*, 2008.

[40] http://www.cea.fr/, March 2012.

[41] http://www-centre-saclay.cea.fr/, March 2012.

[42] July 2012. http://www.liv.ac.uk/ditanet/.

[43] H. Takahashi. Function of MPS. Oct. 2010.

[44] P Abbon et al. Preliminary design of the ifmif-eveda beam instrumentation. Technical report, CEA Saclay, CIEMAT, INFN, 2010.

[45] D. Brandt, editor. *CERN Accelerator School Beam Diagnostics*. CERN, 2009.

[46] R. E. Shafer, E. Gerig, A. E. Baumbaugh, and C. R. Wegner. The tevatron beam position and beam loss monitoring system. In *Int. Conf. on High Energy Accelerators*, 1983.

[47] M. Stockner. *Beam Loss Calibration for High Energy Proton Accelerators*. PhD thesis, Technische Universität Wien, 2007.

[48] R. L. Witkover and D. Gassner. Design and testing of the new ion chamber looss monitor for sns. In *Proc. of the 2003 PArticle Accelerator Conference*, 2003.

[49] http://openticle.com/, March 2012.

[50] W. Friesenbichler. *Development of the Readout Electronics for the Beam Loss Monitors of the LHC*. PhD thesis, Fachhochschule Wien, 2002.

[51] M. Brugger, E. Lebbos, M. Sapiński, and M. Stockner. Response functions if ionisation chamber beam loss monitor. Technical report, CERN, 2010.

[52] J.F. Ziegler. Particle interactions with matter. www.srim.org, March 2012.

[53] Y. Calzavara, N. Authier, S. Wisniewski, and X. Jacquet. Experimental facilities for mixed field neutron / gamma; irradiation. In *Radiation and Its Effects on Components and Systems, 2005. RADECS 2005. 8th European Conference on*, 2005.

[54] L. Yasui et al. Boron neutron capture in prostate cancer cells. *Applied Radiation and Isotopes*, 1:6–12, 2012.

[55] Nuclear Science Deivision LBNL. The isotopes project home page. http://ie.lbl.gov/, March 2012.

[56] Rémi Chipaux. Cocase 2, le retour. *Scintillations*, 70:7, 2006.

[57] *Keithley Model 6485 Picoammeter - Instruction Manual*.

[58] M. Sapiński, M. Brugger, E. Lebbos, and M. Stockner. Response functions of ionisation chamber beam loss monitor. Technical report, CERN, 2010.

[59] Michał Pomorski. *Electronics Properties of Single Crystal CVD Diamond and its Suitability for Particle Detection in Hadron Physics Experiments*. PhD thesis, Johann-Wolfgang-Goethe Universität Frankfurt / Main, 2008.

[60] Tapper R.J. Diamond detectors in particle physics. *Reports on Progress in Physics*, 63:1273–1316, 2000.

[61] S. Ramo. Current induced by electron motion. *Proceedings of the IRE*, 27:584–585, 1939.

[62] CIVIDEC Instrumentation GmbH, Schottengasse 3A/1/41, A-1010 Vienna, Austria. *C3 Low-Noise Fast 40 dB Amplifi er*.

[63] CIVIDEC Instrumentation GmbH, Schottengasse 3A/1/41, A-1010 Vienna, Austria. *C6 Low-Noise Fast Charge Amplifi er (CSA1)*.

[64] M. Pillon, M. Angelone, and A.V. Krasilnikov. 14 MeV neutron spectra measurements with 4% energy resolution using a type IIa diamond detector. *Nuclear Instruments and Methods in Physics Research B*, 101:473–483, 1995.

[65] W. Adam et al. Pulse height distribution and radiation tolerance of CVD diamond detectors. *Nuclear Instruments and Methods in Physics Research A*, 447:244–250, 2000.

[66] M. Angelone et al. Thermal and fast neutron dosimetry using artificial single crystal diamond detectors. *Radiation Measurements*, 46:1686–1689, 2011.

[67] M. Angelone et al. Development of single crystal diamond neutron detectors and test at jet tokamak. *Nuclear Instruments and Methods in Physics Research A*, 595:616–622, 2008.

[68] C. Bauer et al. Radiation hardness studies of CVD diamond detectors. *Nuclear Instruments and Methods in Physics Research A*, 367:207–211, 1995.

[69] J. Hassard. The neutron radiation hardness of diamond detectors for future particle physics experiments. *Nuclear Instruments and Methods in Physics Research A*, 368:217–219, 1995.

[70] J. Isberg et al. Charge collection distance measurements in single and polycrystalline CVD diamonds. *Diamonds and related materials*, 13:872–875, 2004.

[71] M-M. Bé. Table of radionuclides (vol. 4 - A = 133 to 252), 2008.

[72] J-G. Marmouget. Van de Graaff 4 MV Accelerator.

[73] R. Brun and F. Rademakers. Root - an object oriented data analysis framework. In *Proc. of the AIHENP, Lausanne, Switzer;and*, 1996.

[74] R. A. Baragiola, E. V. Alonso, and A. Oliva-Florio. Electron emission from clean metal surfaces induced by low-energy light ions. *Physical Review B*, 19:121–129, 1979.

[75] Claus V. von Koch. Evidence of plasmons in secondary electron emission spectra. *Phys. Rev. Lett.*, 25:792–794, 1970.

[76] L.M. Kishinevsky. *Radiation Effects*, 19:23, 1973.

[77] R. A. Baragiola, E. V. Alonso, J. Ferron, and A. Oliva-Florio. Ion-induced electron emission from clean metals. *Journal of Surface Science*, 90:240–255, 1979.

[78] Yasushi Yamauchi and Ryuichi Shimizu. Secondary electron emission from aluminum by argon and oxygen ion bombardment below 3 keV. *Japanese Journal of Applied Physics*, 22:L227–L229, 1983.

[79] E.J. Sternglass. Theory of secondary electron emission by high-speed ions. *American Physical Society*, 108:1–12, 1957.

[80] O.W. Richardson. Xxii. the emission of electrons from tungsten at high temperatures: an experimental proof that the electric current in metals is carried by electrons. *Philosophical Magazine Series 6*, 26(152):345–350, 1913.

[81] S. Dushman. Electron emission from metals as a function of temperature. *Phys. Rev.*, 21:623–636, 1923.

[82] Ansys, inc. www.ansys.com, March 2012.

[83] T. Giacomini et al. Ionization profile monitors - IPM @ GSI. In *Proc. of DIPAC2011*, 2011.

[84] W. H. DeLuca. Beam detection using residual gas ionization. *Nuclear Science IEEE*, 16:3:813–822, 1969.

[85] C.D. Johnson. The CPS gas-ionization beam scanner. *Nuclear Science IEEE*, 13:3:909–913, 1969.

[86] M. E. Rudd, R. D. DuBois, L. H. Toburen, and C. A. Ratcliffe. Cross sections for ionization of gases by 5-4000-keV protons and for electron capture by 5-150keV protons. *Physical Review A*, 28:3244 – 3257, 1983.

[87] M. A. Plum, Bravin. E., J. Bosser, and R. Maccaferri. N_2 and Xe gas scintillation cross-section, spectrum, and lifetime measurements from 50 MeV to 25 GeV at the CERN PS and Booster. *Nuclear Instruments and Methods in Physics Research A*, 492:74–90, 2002.

[88] F. Becker. Beam induced fluorescence monitors. In *Proc. DIPAC2011*, 2011.

[89] F. Becker. *Zerstörungsfreie Profilmessung intensiver Schwerionenstrahlen*. PhD thesis, Technische Universität Darmstadt, 2010.

[90] C. Dimopoulou et al. Breakup of H_2 in singly ionizing collisions with fast protons: Channel-selective low-energy electron spectra. *Physical Review Letters*, 93:123203–1 – 123203–4, 2004.

[91] Igor D. Kaganovich, Edward Startsev, and Ronald C. Davidson. Scaling and formulary of cross-sections for ion-atom impact ionization. *New Journal of Physics*, 8:278, 2006.

[92] M. Bartelmann. Theoretische Physik II: Elektrodynamik. http://www.ita.uni-heidelberg.de/research/bartelmann/index.shtml?lang=en.

[93] R. Courant. Variational methods for the solution of problems of equilibrium and vibrations. *Bulletin of the American Mathematical Society*, 49:1–23, 1943.

[94] INTEGRATED ENGINEERING SOFTWARE. *INTEGRATED ENGINEERING SOFTWARE 3D Program Guide*, 8.0 edition, July 2009.

[95] David Meeker. *Finite Element Method Magnetics*, 4.2 edition, October 2010.

[96] http://www.integratedsoft.com/.

[97] http://www.comsol.com/.

[98] J. Egberts et al. Detailed experimental characterization of an ionization profile monitor. In *Proc. of DIPAC2011*, 2011.

[99] http://www.home.agilent.com.

[100] http://www.gsi.de.

[101] H. Luna et al. Dissociation of N_2 in capture and ionization collisions with fast H^+ and N^+ ions and modeling of positive ion formation in the titan atmosphere. *Journal of Geophysical Research*, 108:14, 2003.

[102] A.K. Edwards and R.M. Wood. Dissociation of N2+2 ions into N+ fragments. *AIP The Journal of chemical physics*, 76:2938–2942, 1982.

[103] A. K. Edwards, R. M. Wood, and M. F. Steuer. Dissociative ionization of N_2 produced by 1-MeV H^+ and He^+: Time-energy spectroscopy. *Physical Review A*, 15:48–52, 1977.

[104] F. Becker et al. Beam induced fluorescence monitor - spectroscopy in nitrogen, helium, argon, krypton and xenon gas. In *Proc. of BIW10*, 2010.

[105] F. Becker et al. Beam induced fluorescence monitor & imaging spectrography of different working gases. In *Proc. of DIPAC09*, 2009.

[106] K. G. Baldwin. Metastable helium: atom optics with nano-grenades. *Journal of Contemporary Physics*, 46:105–120, 2005.

[107] Pfeiffer Vacuum. *Compact FullRange Gauge PKR 251*, 2008.

[108] P.C. Zalm and L.J. Beckers. Ion-induced secondary electron emission from copper and zinc. *Journal of Surface Science*, 152:135–141, 1985.

[109] G.D. Magnuson and C.E. Carlson. Electron ejection from metals due to 1- to 10-kev noble gas ion bombardment. 1. polycrystaline materials. *Physical review*, 129:2403–2409, 1963.

[110] C. E. Carlston, G.D. Magnuson, and P. Mahadevan. Electron ejection form single crystals due to 1- to 10-keV noble gas ion bombardment. *Physical Review*, 139:A729–A736, 1965.

[111] J. Ferron, E. V. Alonso, R. A. Baragiola, and A. Oliva-Florio. Ion-electron emission: The effect of oxidation. *Journal of Surface Science*, 120:427–434, 1982.

[112] R. Gobin et al. Development of an H^- ion source based on the electron cyclotron resonance plasma generator at CEA/saclay. *Review of Scientific Instruments*, 75:1741–1743, 2004.

[113] J-M. Carmona, O. Nomen, and I. Podadera. Diagnostics plate: Integration and mechanical support, June 2012.

[114] W. S. Graves. *MEASUREMENT OF TRANSVERSE EMITTANCE IN THE FERMILAB BOOSTER*. PhD thesis, University of Wisconsin - Madison, 1994.

[115] J. Amundson et al. Calibration of the Fermilab Booster ionization profile monitor. *Phys. Rev. STAB*, 6:102801, 2003.

[116] A. A. Aleksandrov et al. Closeout remarks for the LIPAC DDR.

[117] R. Ferdinand and P.Y. Beauvais. The IPHI project. Technical report, CEA Saclay, 2004.